TECHNISCHE UNIVERSITÄT MÜNCHEN

Department Chemie

Lehrstuhl für Technische Chemie II

Innovative Pathways for Sustainable Diphenyl Carbonate Production

Navneet Kumar Gupta

Vollständiger Abdruck der von der Fakultät für Chemie der Technischen Universität München zur Erlangung des akademischen Grades eines

Doktors der Naturwissenschaften (Dr. rer. nat.)

genehmigten Dissertation.

Vorsitzender: Univ.-Prof. Dr. Klaus Köhler

Prüfer der Dissertation: 1. Univ.-Prof. Dr. Johannes A. Lercher

                            2. Jun.-Prof. Dr. Konrad Tiefenbacher

Die Dissertation wurde am 25.11.2015 bei der Technischen Universität München eingereicht und von der Fakultät für Chemie am 17.12.2015 angenommen.

To my family

„ Arise, awake, and stop not till the goal is reached! "

Swami Vivekananda

Acknowledgment

Abstract

Detailed kinetic and mechanistic analysis of activated carbons enabled the development of highly stable and selective functional catalysts for transient phosgene synthesis. Employing advanced spectroscopic techniques, various in situ formed crucial intermediates for phosgene production were identified and their involvement in different catalytic steps has been studied in detail. By careful selection of probe molecules, the electronic nature of reactive intermediates were differentiated. Alumina has been successfully identified as new selective and stable catalyst through these studies.

Kurzfassung

Detaillierte kinetische und mechanistische Untersuchungen an Aktivkohle haben die Entwicklung hochstabiler und selektiver Katalysatoren für die Phosgenherstellung ermöglicht. Durch spektroskopische Methoden wurden in situ gebildete Zwischenprodukte für die Phosgenherstellung identifiziert und ihre Beteiligung an unterschiedlichen katalytischen Schritten untersucht. Durch die Verwendung von Probemolekülen wurde zwischen den elektronische Eigenschaften der reaktiven Intermediate unterschieden. Durch die Untersuchungen wurde alumininumoxid als stabiler und selektiver Katalysator identifiziert.

Table of Contents

Chapter 1

General Introduction

Abstract

Polycarbonates have been proved to be one of the most important class of polymers. A facile route to achieve a high quality polycarbonate is considered from the reaction of diphenyl carbonate with bisphenol-A. In turn, diphenyl carbonate synthesis proceeds by using phosgene as a reactive building block. Herein, a general introduction into vast polymer chemistry highlighting the importance of transiently formed phosgene used for a wide range of chemical production is provided. Different possible catalytic routes for the phosgene synthesis are presented and existing catalytic systems in perspective of industrial importance are discussed in detail. In order to better understand the challenges and opportunities in the polymer chemistry, we present here general considerations and ideas that were the basis for developing a new innovative process for sustainable chemical production.

1   General Introduction

1.1   Polycarbonates

Polycarbonates (PCs) are one of the most widely used engineering thermoplastics due to their outstanding physical characteristics, such as, high thermal and electrical stability, light weight, excellent toughness and stiffness, biological inertness, cost effectiveness, ready recyclability, high resistance to fracture and impact.[1,2] Over the years, the global PCs market has served a wide range of application areas and has observed increasing importance. While the global demand for PCs in 2009 was around 2.8 million metric tons, it is likely to cross 6.0 million metric tons by 2020.[3,4]
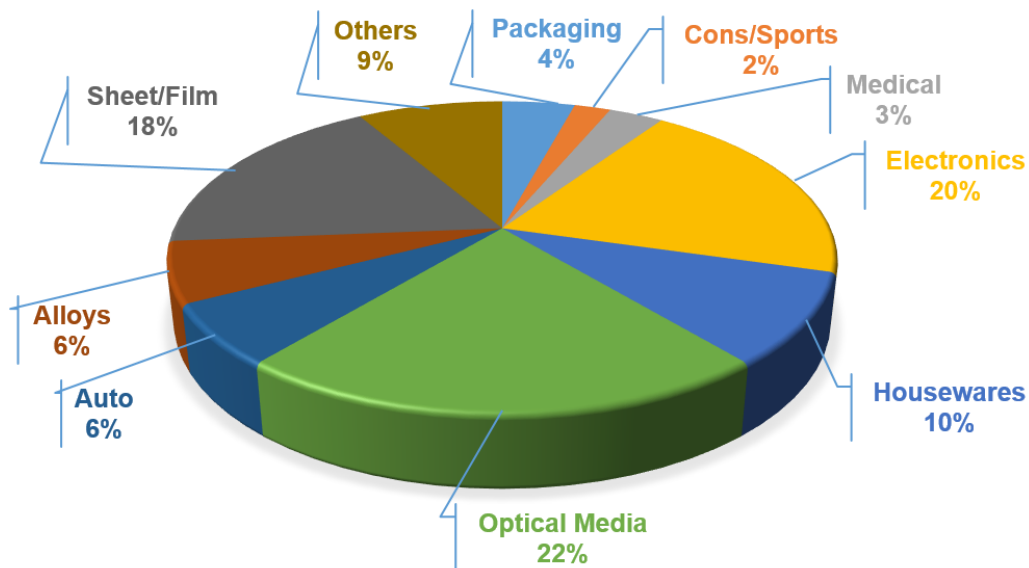
Figure 1-1. Application of polycarbonates.[3]

The main field of use are optical media, automotive components, electronics and sheet/film (Figure 1-1). In optical media, PCs are used in the production of CDs, DVDs, etc. It was recently implemented for making high quality windows for cars and motor vehicles. The use of PCs allow the weight savings compared to glass, providing more design options and easier handling.[5] Due to ecological and economic demand on sustainable development of processes for PCs production, innovative solutions are required. Therefore, revisions, evaluations of available synthetic methods form background research is needed at the first step in order to develop a tailored knowledge tool for innovative and sustainable PCs synthesis, with the ultimate goal of closing the knowledge-to-practice gap.

The first polycarbonate was synthesized in 1898, from the reaction of hydroquinone or resorcinol with phosgene.[6] In 1902, the same material was prepared by the transesterification of diols with DPC.[7] The polymer from hydroquinone was brittle, crystalline, insoluble in most of the solvents and had high melting points, >280 °C.[2] However, resorcinol produces the brittle and glassy polymers of low melting point (190-200 °C).[2] Due to the highly energy demanding processing and characterizations, both routes were afterwards not further considered. After 50 year in 1953, the research on aromatic carbonates were reevaluated as a topic for investigations. The independent researchers by H. Schnell (Bayer AG) in 1958 and D. W. Fox (GE) in 1960, discovered the polycarbonates of 2,2-bis(4-hydroxyphenyl)propane (called bisphenol-A or BPA), which affords PCs with high toughness, high glass transition temperature, optical clarity and high impact resistance.[8,9,10,11] This discovery again started the revolution for the development of new polycarbonate materials in polymer science and technologies. The solution based process using phosgene by Schnell and a melt transesterification technique by Fox is presented in detailed in the following sections.

Solvent based polycarbonate synthesis (interfacial process)

Interfacial process of polycarbonate was synthesized from the direct reaction of $COCl_2$ with BPA in aqueous base and methylene dichloride (a two phase system) using amines as a catalyst and mono-hydroxyl phenolic compound as chain stopper.[11] The general interfacial process is schematically illustrated in Scheme 1-1.
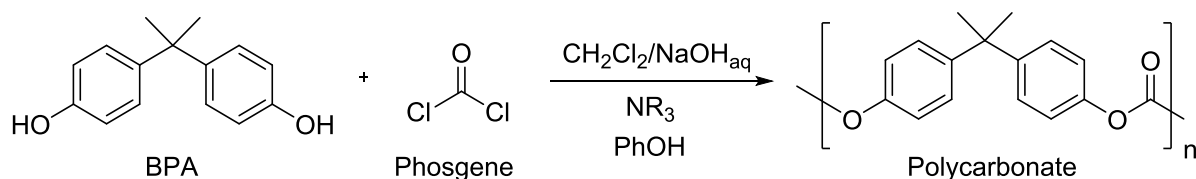
Scheme 1-1. Interfacial process to manufacture BPA-polycarbonate. (R = alkyl or aryl groups)

In a general synthetic procedure, $COCl_2$ is added to the mixture of aqueous NaOH, catalytic amine/CH_2Cl_2 and BPA. In this mixture, NaOH is used to generate the phenoxide of BPA which facilitates the phosgenation reaction.[12] The mono functional phenols such as phenol, *p*-t-butylphenol or *p*-cumylphenol were further considered to control the molecular weight of polymers. NaOH was similarly used as a quenching agent for in situ formed HCl. Accurate control of the pH is very important in order to avoid the hydrolysis of $COCl_2$ and effectiveness of the used amine catalysts. Further, a number of modifications and variations of the interfacial

polycarbonate process were attempted.[13] The use of triethylamine as catalyst was found to be convenient because of its accentuated nucleophilicity which forms activated acyl ammonium salts for the further reaction with aromatic alcohols.

Solvent free polycarbonate synthesis (melt process)

The melt process for the polycarbonate synthesis was carried out 100 years back from the reaction between hydroquinone with DPC.[14] The problem associated with its purity led to the modification of this synthesis by Fox (GE).[8] In the modified synthesis, BPA reacts with DPC in the presence of a basic catalyst, resulting in polycarbonate formation and phenol as byproduct *via* the transesterification reaction. The melt process for the BPA polycarbonate (BPA-PC) synthesis is shown in Scheme 1-2.
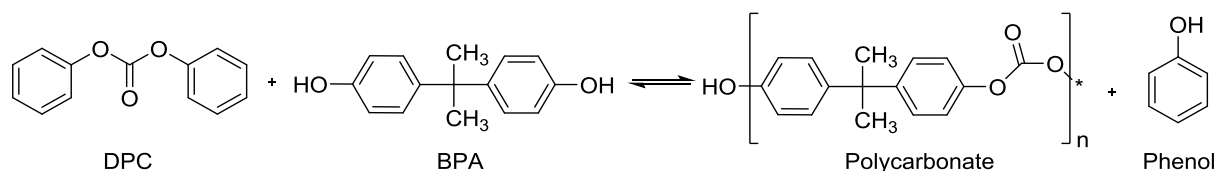
Scheme 1-2. Melt process for the synthesis of BPA-polycarbonate.

The transesterification is a reversible reaction. Therefore, the reaction by-product (phenol) must be distilled off continuously by applying a high vacuum to facilitate the forward chain-growth reaction. In the melt process, the slight excess of DPC is used, to control the molecular weight and to compensate any loss due to devolatilization from the reactor. The high molecular weight of the polymer is achieved by continuous removal of phenol as the equilibrium constant (K_{eq}) is one. The distillation of phenol is trivial at the beginning of the reaction, however, at final stage, the reaction becomes mass transfer limited by the high viscosity of the melt. The final polymer is end-caped with 60-90 % phenyl carbonate functionality and remaining hydroxyl groups. It was also possible to control the molecular weight of the polymers by addition of an extra end-capping molecule in the reaction mixture, although they were not generally used for this process.

In the melt process, DPC synthesis is energetically equivalent to the production of carbonates for the polymer chain reaction. It is further important to note, that the melt process is a thermodynamically controlled reaction. Hence, the formation of oligomeric cyclic products are less favored in the melt process compared to the interfacial phosgenation route. A comparison

of the main characterstic features of the two processes for the BPA-PC synthesis is shown in Table 1-1.

Table 1-1. Summary and comparison between interfacial and melt processes of PCs synthesis.[2]

Interfacial process	Melt process
Kinetically controlled reaction	Thermodynamically controlled reaction
Molecular weight control by addition of chain stopper	Molecular weight control possible by extent of the reaction time
Amine based catalysis	Base catalysis in condensed phase
Low temperature reaction	High temperature reaction
High molecular weight polymers	Low molecular weight polymers
100 % end-capping	60-90 % end-capping
Few by-products or side reaction	Side reaction may occur at high temperature
The use of phosgene and of solvents is required	Requires DPC and BPA
Washing and isolation is required	Direct isolation *via* extrusion

Advantages/disadvantages of the melt process over the interfacial process

Compared to the phosgene based interfacial process, the melt process for the synthesis of BPA-PC is more environmentally benign, hence attracting more industrial interest in the recent years.[8,11] A further advantage of the melt process is the ease of isolation. Melt process is also suitable for the synthesis of excellent quality polymers from low to high molecular weight for a wide range of applications. Due to high industrial demand of the BPA-PC from melt process more and more DPC is required. In sequence, DPC can be synthesized from different possible routes where $COCl_2$ is used as a reactive starting material. A detailed overview is shown in following section 1.2.

It is noteworthy to specify that independent of the both commercialized processes (interfacial and melt), $COCl_2$ is required for the BPA-PC production. However, the high toxicity of $COCl_2$ restrict its industrial importance. This can be, however, circumvented by the development of an adequated new synthetic approach, which could allow the transient formation of high purity

$COCl_2$ required for BPA-PC synthesis. The development of sustainable synthetic routes for $COCl_2$ are presented in Section 1.3.

1.2 Diphenyl carbonate

The main commercial value of DPC is its use as a monomer in the BPA-PC synthesis *via* melt polymerization process. DPC can be obtained by several synthetic routes, as described below. Mainly two processes are commercialized for large scale DPC synthesis (1) transesterification of dimethyl carbonate (DMC) by phenol and (2) phosgene reaction with phenol. Other processes such as methyl nitrite, dimethyl oxalate (DMO) decarbonylation, diphenyl oxalate (DPO) decarbonylation and cyclic carbonate are still under investigation for large scale production.[15,16]

Phosgene free DPC synthesis

DPC can be synthesized without the use of $COCl_2$ in numerous processes as indicated in Scheme 1-3.[2]
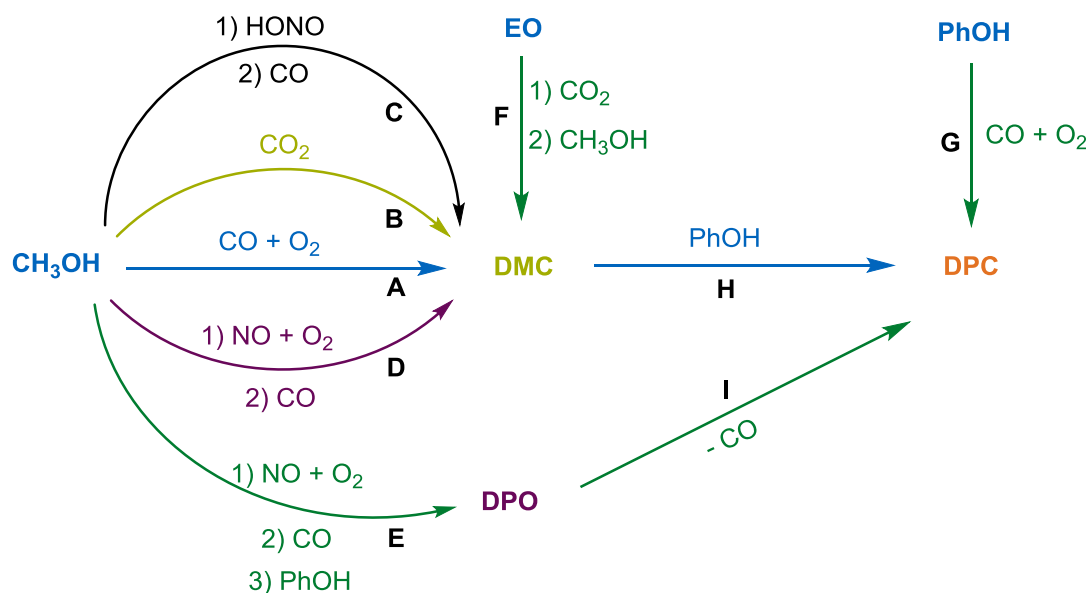
Scheme 1-3. Proposed pathways for phosgene free DPC synthesis. (DPO = diphenyloxalate, EO = ethylene oxide, PhOH = phenol)

Among the several phosgene free approaches the DMC process involving the direct carbonylation of methanol (CH_3OH) with CO and O_2 in liquid phase is one of the most

promising route for the synthesis of DMC (**A**, Scheme 1-3).[17] Consequently, the second step leads to DPC formation (**H**, Scheme 1-3).[18] The one step process for DPC synthesis by oxidative carbonylation of phenol is also receiving increasing attention from the industrial point of view (**G**, Scheme 1-3).[19] As conversion of DMC to DPC, the transesterification process with phenol is highly unfavorable from thermodynamic and kinetic point of view.[20]

DMC is a key intermediate in all the five DPC processes (**A-D and F**, Scheme 1-3). Pathway **C** and **E** (Scheme 1-3) includes the formation of dimethyl oxalate (DMO) as an intermediate. However, pathway **D** (Scheme 1-3) proceeds *via* methyl nitrite formation. The pathway **F** (Scheme 1-3) involves the formation of cyclic carbonate, which represents the sole commercially viable carbonate from CO_2 and ethylene oxide (EO) reaction.[21]

Due to the thermodynamic and kinetic limitation of DMC to DPC reaction, the yield and selectivity of final product is very low for a commercial utilization. Therefore, a highly efficient phosgene route is considered for industrial production of DPC.

Phosgene based DPC Synthesis

Industrial route for DPC synthesis involves the reaction between $COCl_2$ and PhOH in a catalytic process, as depicted in Scheme 1-4.
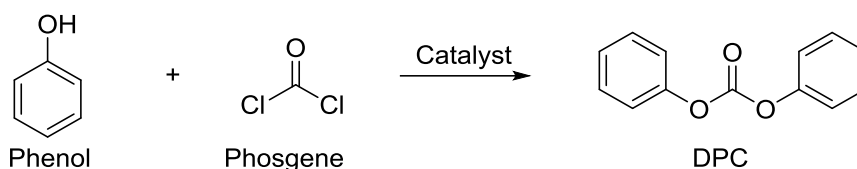
Scheme 1-4. Industrial route for large scale DPC synthesis.

Traditionally, aqueous NaOH is used to convert phenol to phenolate (high nucleophilicity on O) required for facial DPC synthesis.[22] Presently, Lewis acid based catalysts are successfully implemented for this tranfomation.[23] The use of solid Lewis acid catalysts (e.g. porous alumina, $AlCl_3$) over homogenous aq. $NaOH/amine/CH_2Cl_2$ mixture, attracting much attentions due to easy workup and high purity of the final product.[23] Industrially, $COCl_2$ is produced by passing purified CO and Cl_2 gas through a bead of porous solid catalysts, as described in section 1.3.

1.3 Phosgene

Phosgene,[24] retains the status of being a very unpleasant chemical, due to its high toxicity. Whilst undeniably toxicity, due to $COCl_2$ exposure can be avoided by immediate conversion into harmless value added products *i.e.*, DPC, which contribute to our quality of life. Using a nano-reactor, we may completely utilize this toxic intermediate for sustainable production of global demanding DPC, as well as in the synthesis of pharmaceuticals and agrochemicals mentioned in Section 1.4.

Phosgene synthesis

Large scale production of the $COCl_2$ in industry is carried out by the reaction of gaseous Cl_2 and CO due to the high atom efficiency (100 %) of the reaction.[25]

[1-1] $\quad\quad Cl_2 \quad + \quad CO \quad \longrightarrow \quad COCl_2 \quad\quad \Delta H \approx -108 \text{ KJ mol}^{-1}$
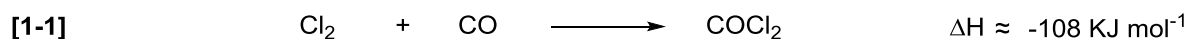
The modern industrial $COCl_2$ synthesis has not changed significantly since 1920s.[25] The entire process comprises the preparation of pure raw materials, Cl_2 and CO, the the quantification and mixing of these compounds, the reaction of the mixed gases over a solid catalyst bed and the purification and condensation of the $COCl_2$.

Precautions and safety issues at working place during $COCl_2$ synthesis

Due to the extremely poisonous nature of the $COCl_2$, following safety measures are mandatory to consider:

I. The preparation and handling must be conducted in well ventilated specially designed fume hoods for poisonous gases. According to the EH&S safety guidelines a floor level exhaust ventilation is needed at the working place because phosgene is heavier than air.

II. The appropriate sensors and indicator paper should be kept in fume hood in which the operation involving the $COCl_2$ synthesis are being carried out. Further, a gas mask made of special filter is mandotary to have next to the working area.

III. Special precautions should be taken in the complete neutralization of waste phosgene produced by the reactions. Therefore, the use of concentrated (basic KOH or NaOH) solution is necessary at the outlet of reactor.

IV.   Moreover, it was necessary to design a controlled experimental set-up, which can be used for the production and immediate conversion of very small amounts of corrosive and highly reactive gases.

1.3.1 Metal free phosgene synthesis

$COCl_2$ is readily synthesized by passing equimolar mixture of Cl_2 and CO through activated carbon beads placed into quartz tube at ambient temperature and pressure.[26,27] Since thermal dissociation of $COCl_2$ occurs already at 200 °C, it is necessary to respect this temperature as an upper limit for the temperature in the bulk catalyst.[28] Further, the effect of γ-irradiation on active carbon material has been examined for $COCl_2$ activity.[29] The rate constant for the γ-irradiated material was found smaller than that for the parent material. The radiation is considered to destroy the π-electron system consequently, the conjugation in the carbon get destroyed, through bond ruptures, resulting in decrease of the corresponding catalytic activity.[29] In this respect, it is believed that activation of Cl_2 on activated carbon is a key issue during $COCl_2$ production.[30] Beginning of the $COCl_2$ synthesis a large heat is generated. However, the produced heat was very less after passing mixture of Cl_2 and CO over pre chlorinated activated carbon.[30] Increasing the molar excess by 2.5 % of CO in the mixture of CO/Cl_2, the high yield of $COCl_2$ (97 %) is ensured.[31]

Detailed kinetic studies on the carbon catalyzed $COCl_2$ formation from Cl_2 and CO have been reported by various research groups.[32] However, the exact mechanism of the carbon catalyzed phosgene synthesis is still not well understood.[33] To a certain extent, this may be associated with the chemical complexity of the active carbon surfaces. The structural complexity of the carbon significantly restricts the elucidation of the active sites and consequently the identification of reactive intermediates.

In order to develop a new generation of stable and highly active catalyst for transient $COCl_2$ generation, the nature of active sites and of the elementary steps of $COCl_2$ synthesis from CO and Cl_2 on conventional activated carbon is required. Therefore, a fully understanding of each active and reactive sites located on activated carbon and model carbon mimicking their structures and sites involved in catalysis is important.

Industrial used activated carbon materials

Depending on the material's origin, thermal history, and chemical post-treatment of activated carbon materials layers contain different types of active and reactive sites,i.e., zig-zag and arm-

chair edges terminated by reactive -H atoms and reactive oxygen and nitrogen functional groups (Figure 1-2).[50] Beside these, the Stone-Wales defects (5–7 ring pair in a hexagonal network) are dominant and easily introduced on the graphitic planar surface by the thermal induced bond rearrangement of hexagons and by the structural distortions.[49] These are mainly responsible for the presence of fullerenic type of half shells in the material (Figure 1-2). Due to the structural complexity of activated carbon having multiple active sites, a clear understanding the effects of single sites in still not existing.
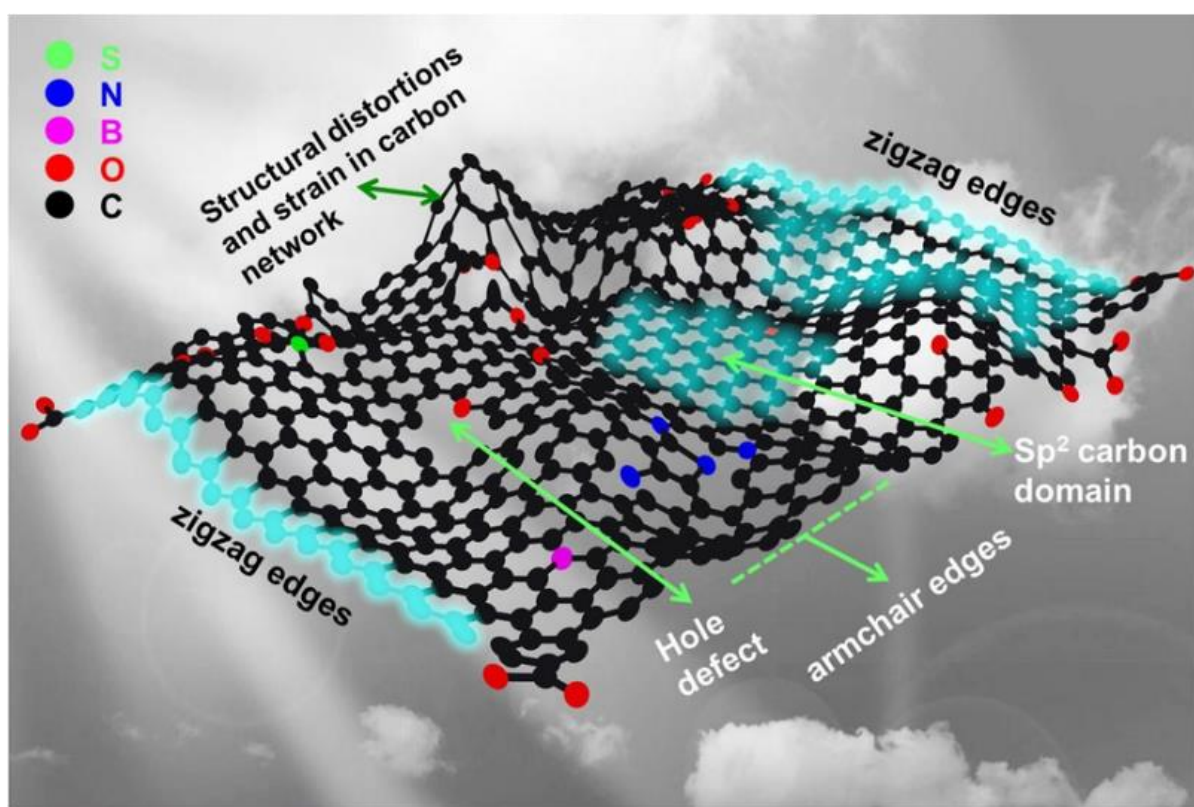
Figure 1-2. General schematic model illustrating the possible active sites on graphene. Black, red, magenta, blue and green balls represent carbon, oxygen, boron, nitrogen, and sulfur atoms, respectively.[50]

In this respect, the newly developed pure model carbon nano materials mimicking the active sites of activated carbons can provide a good platform to understand and explore the chemistry of carbon in catalysis. Further to evaluate the electronic influence of heteroatoms in diverse functionalities, the design and development of functional carbon materials is required. Therefore, systematically different type non-functionalized and functionalized model carbon materials were considered for the current study.

Model carbon materials

Carbon materials exist in different allotropic forms due to the structural versatility and bonding abilities of the carbon atoms.[33] Depanding on bonding types and structures, different type of hybridization on carbon, e.g., sp^2, sp^3 and mixed sp^2/sp^3 can be stabilized. Further by the heteroatoms modification the electronic properties of carbon can be altered. Based on the structural features and their modification each type of carbon material is discussed in detail as follows.

Fullerenes

In fullerenes, carbon atoms have a spherical arrangement similar to a soccer-ball. Since their discovery in 1985 by Robert Curl, Harry Kroto and Richard Smalley at Rice University, various research activities highlighting the unique physicochemical properties of fullerenes have been reported. [34] Generally, fullerenes have the form of hollow spheres or ellipsoids. The widely known fullerene "buckminsterfullerene", also known as C_{60} fullerenes, consists of 60 carbon atoms, arranged in pentagons and hexagons were intensively studied due to their unique chemistry and for their technological applications in the field of material science, electronics and nano-technology.[34-36] Till now, a large number of other fullerenes similarly exists, starting from C_{20} and reaching up to C_{540}.[35]
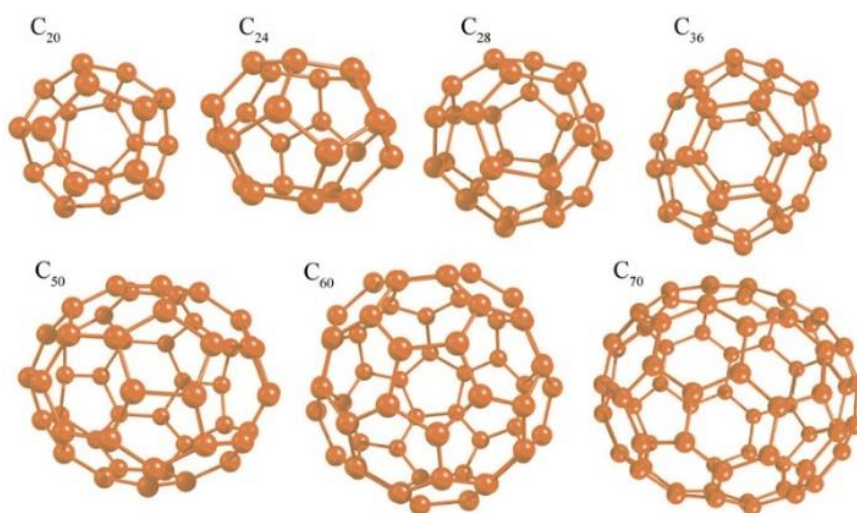
Figure 1-3. Structure of different fullerenes.[36]

Recently, "buckytubes" and "buckyeggs" were also discovered.[37]

Carbon nanotube

Carbon nanotubes are classified and well accepted as 1D carbon allotropes. Since their discovery in 1991,[38] single and multi-walled carbon nanotubes have been extensively investigated in a wide range of fields from academia to industry.

Single wall carbon nanotube (SWCNTs)

The highly pure SWCNTs were first isolated in 1993.[39] SWCNTs are proposed to consist of a seamless cylinder of a graphitic sheet capped by hemispherical ends composed by pentagons and hexagons.[40] The high tensile strength, high resilience, electronic properties ranging from metallic to semiconducting, high current carrying capacity, and high thermal conductivity makes them exceptionally attractive material for industrial applications.[40] In this type of curved materials, the higher electronic charge is located on the outer concentric tubes compared to inner tube of carbon.[39,40]
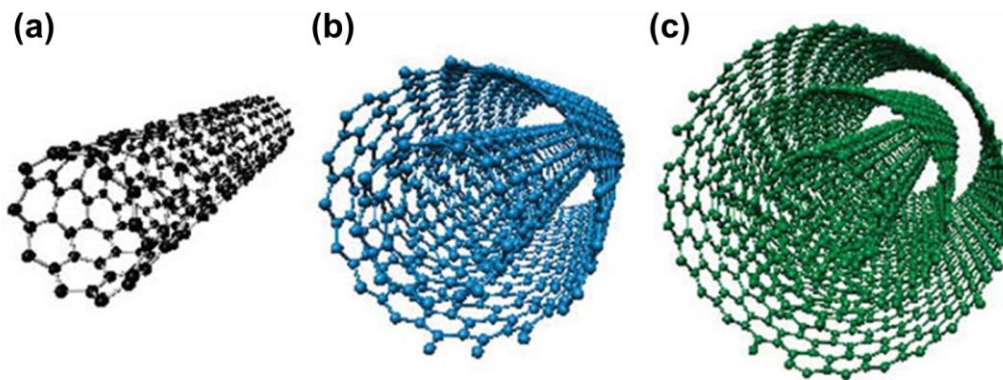
Figure 1-4. Structure of single wall carbon nanotube (a) double wall carbon nanotube (b) and multiwall carbon nanotube (c).

It has been shown that the higher electronic density on outer surface of curved surfaces are due to the rehybridization of sp^2 dangling bond states to mixed sp^2/sp^3.[34-40] Overall, CNTs exhibit extraordinary strength and unique electrical properties.[40]

Multiwall carbon nanotubes (MWCNTs)

MWCNTs, comprise of concentric nanotube shells, each shell apparently fitting inside the next with an inter-tube spacing to the van der Waals inter-plane distance of ~0.34 nm.[41] MWCNTs have very similar chemical properties to SWCNTs. Nevertheless, the MWCNTs can protect inner nanotube shell form chemical interactions. Due to the presence of multiple shells,

MWCNTs have a higher tensile strength than SWCNTs.[42] Beside this, MWCNTs exhibit extraordinary strength and efficient conductors of heat.[42]

Graphene

Graphene is fundamentally one single layer of carbons, where a layer of sp^2 bonded carbon atoms are arranged in a honeycomb (hexagonal) lattice.[43] Being a single atomic layer and having high electron mobility, graphene offers great electronic conduction due to the presence of movable π-electrons from each carbon atoms.
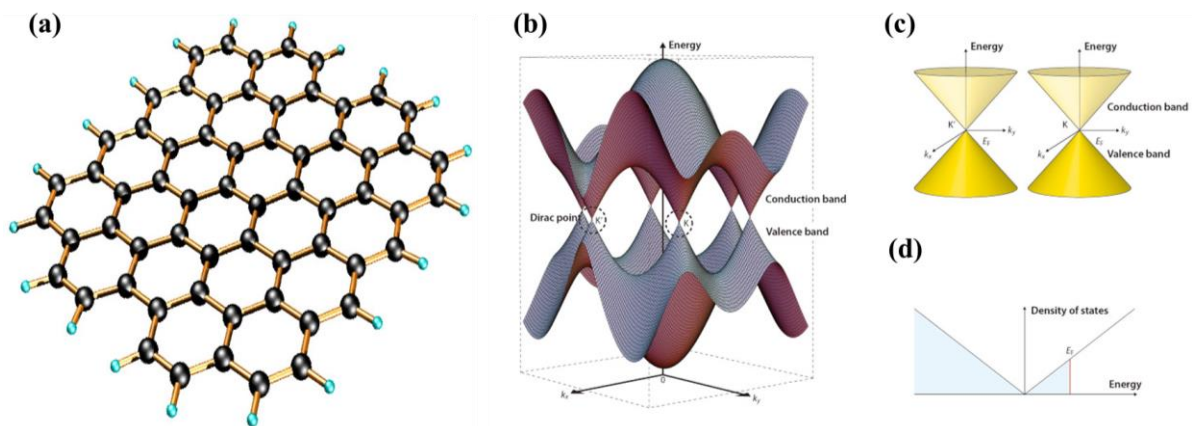
Figure 1-5. Structure of graphene (a) and electronic band structure of the graphene honeycomb lattice.[44,45]

In the graphene, three of the four valence electrons are involved in the σ-bonds formation and the fourth single electron occupies $2p_z$ orbital to form the π(HOMO) and π*(LUMO) band with neighbors for the delocalization. The valence band and the conduction band of graphene meet at a point which is known as Dirac point.[44-45] At this point, electrons and holes have zero effective mass (Figure 1-5b).[45] This occurs because the energy–movement relation (the spectrum for excitations) is linear for low energies near the six individual corners of the Brillouin zone. The Fermi level can be changed by doping or functionalization (with an appropriate electrons or holes) to design a material for future applications.

Graphite

Graphite [46] is a 3D, naturally occurring allotropes of carbon. It has a planar layered structure of carbon atoms linked in a hexagonal lattice with C-C separation of 0.14 nm and the distance between planes are 0.34 nm (Figure 1-6b). Each carbon atom (sp^2 hybridized) uses three of its valance electrons to form σ- bonds to the close neighboring carbons. The fourth electron of

each carbon atom is delocalized over the whole sheet of atoms in one layer. Principally, the crystalline flake of graphite, is basically hundreds to thousands individual layers of linked carbon atoms stacked together by van der Waals interactions.

Nano diamond

Nano diamond (ND)[47] was first produced in the USSR in 1960s. Later, in 1990s, a number of important breakthroughs led to wider interest in nano-scale diamond particles as nontoxic quantum dots for biomedical imaging, nanoscale magnetic sensors and in drug delivery.[47] The stability of various phases of nano carbons have been theoretically studied. The presented models have shown that, with size below 3-6 nm, tetrahedral hydrocarbons are more stable than polyaromatics. It has been proved that the morphology has an important role in the stability of ND by influencing surface reconstruction and re-hybridization of carbons from sp^3 to sp^2.
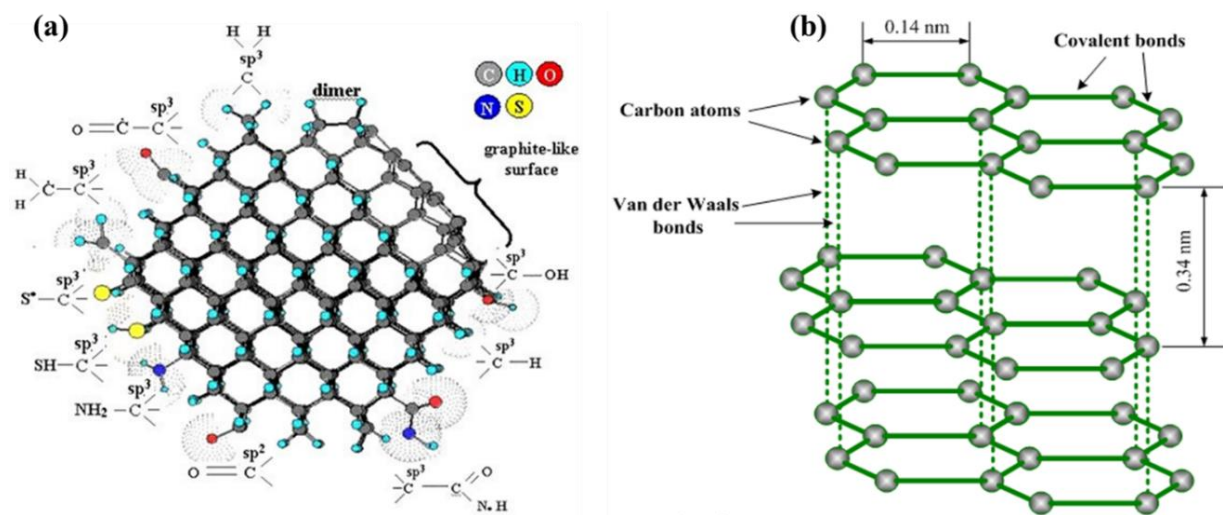
Figure 1-6. Systematic structural representation of nano diamond (a) and graphite (b).[48]

The bare ND surfaces of cubic crystals reveal similar structure to diamond, however, octahedral, cuboctahedral and spherical clusters show an adjustment from sp^3-C to sp^2-C. The surface of sp^3-C clusters must be either stabilized through termination with functional groups or reconstructed into sp^2-C as shown in Figure 1-2.[47]

Nitrogen modified carbon materials

In the part of nitrogen modified carbon materials, Triazine based polymers, representing a class of "covalent organic frameworks (COFs)" has recently attracted tremendous attention as a robust and stable semiconductor for photocatalysis, potential material for hydrogen storage, gas separation and catalysis.[51]
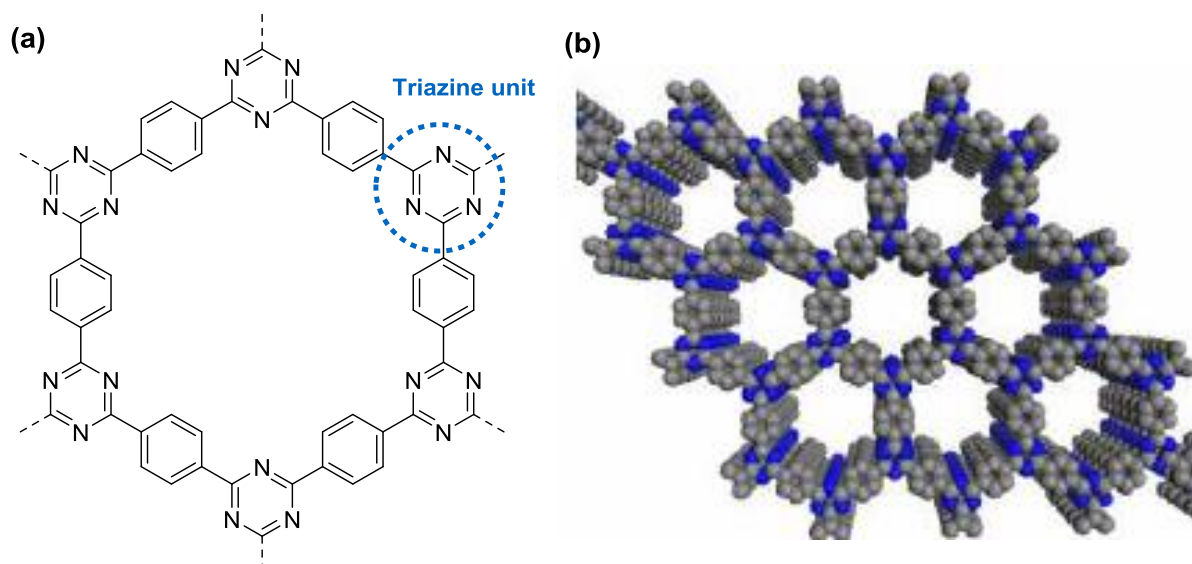
Figure 1-7. Proposed molecular structure of triazine based polymer (a) and schematic representation of the bulk polymer (C-gray, N-blue); H atoms are omitted for clarity.[52]

Further, N- modified material can acts as a multifunctional catalyst, either *via* its electronic properties (for the Friedel–Crafts and Diels–Alder reactions and the trimerisation of alkynes), its nucleophilic properties (for the activation of CO_2) or by its ability to form hydrogen bonds (for the trimerisation of nitriles).
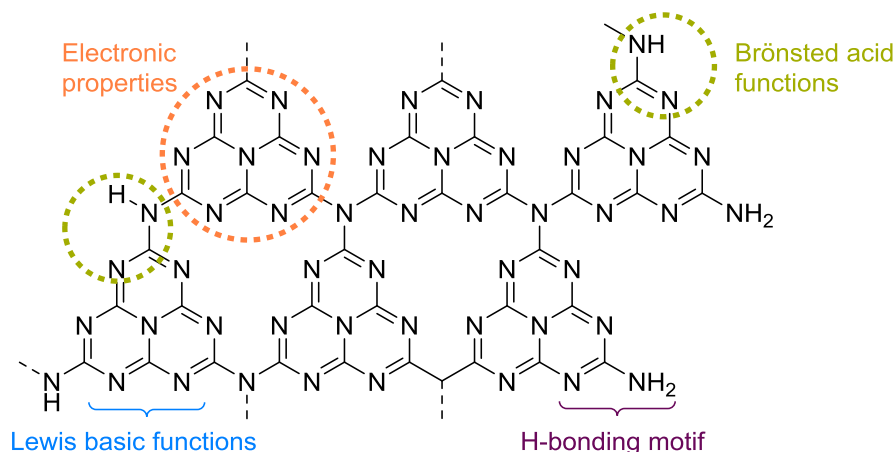
Figure 1-8. Multiple functionalities of C_3N_4 as a catalyst.[53]

Considering the stability and unique electronic properties of its well defined structural features, N-modified materials open the door for further investigation.

Active sites in carbon for catalysis

Each and every site (presented in Figure 1-2 and Figure 1-6) located on carbon materials have their unique electronic properties and thus able to act as catalytic component for various specific reactions shown in Table 1-2. Further, the materials could also be modified by suitable functional groups for enhanced catalytic activity. Table 1-2, summarizes the literatures which evidences the correlation between different intrinsic properties induced by functionalities and their influence on catalytic behavior.

Table 1-2. Short overview of carbon as metal free catalyst used for various reactions.

Reaction type	Material	Reactant	Active sites	Ref.
Reduction	Graphite	Hydrazine hydrate, nitro compound, ethanol	N/A	54
	Reduced graphene oxide	Nitrobenzene	Defects/edges	55
Hydrogenation	Fullerene	H_2, nitro compounds	N/A	56
Oxidative dehydrogenation	Surface modified CNTs	O_2 , butane	Keto and quinonic functional groups	57
Oxygen reduction reaction	N-modified graphene	O_2	Electron accepting ability of N atoms creates a net positive charge on adjacent carbon	58
	B-modified graphene	O_2	The electron deficient B atoms may function as active sites for O_2 activation.	59
Oxidative coupling	Chemically modified graphene	Amines	Synergistic effect of carboxylic acid groups and unpaired electrons at the edge/defect sites	60
Oxidation	Reduced graphene oxides	Benzene to phenol	Aromatic network and defects	61
Decomposition	Functional graphene	Nitromethane	Defect sites decorated with oxygen functional groups	62

Note: N/A denotes not available from the literature.

Various synthetic transformations can occur on carbon materials including reduction, oxidation, H_2 and O_2 activation, and oxygen reduction reaction (ORR). The nitrogen and oxygen functionalities are known to change the electronic properties of carbon for ORR type of reaction. Further, the functional groups and defects on surface of carbon showed a potential use for oxidative coupling of amines and decomposition of nitromethane.

1.3.2 Metal based phosgene synthesis

Although, the industrial process for $COCl_2$ synthesis involves the direct reaction of Cl_2 and CO on metal free activated carbon, several synthetic routes for $COCl_2$ production have been proposed when a metal based catalyst is used in a liquid phase reaction. These processes include oxychlorination of CO in the presence of Cu(II) catalyst, CO reaction with inorganic chlorides and transition metal chlorides, and organophosphines catalyzed Cl_2 and CO reaction.

Oxychlorination

This process was primarily developed to utilize HCl, a large volume by-product form several chemical industries. The oxychlorination of CO to $COCl_2$ has been accomplished over a catalyst composed of copper (II) chloride supported on metal oxides.[63,64]

[1-2] $\quad CO + HCl + 1/2\,O_2 \xrightarrow{\text{Metal}} COCl_2 + H_2O$
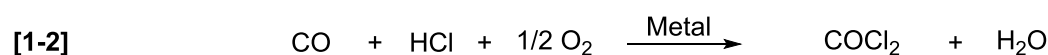
Using stoichiometric amounts of CO, HCl, and O_2 in a flow system at 393 °C and 1 bar, a conversion of CO corresponding to 42 % with selectivity to $COCl_2$ of 57.2 % was achieved.
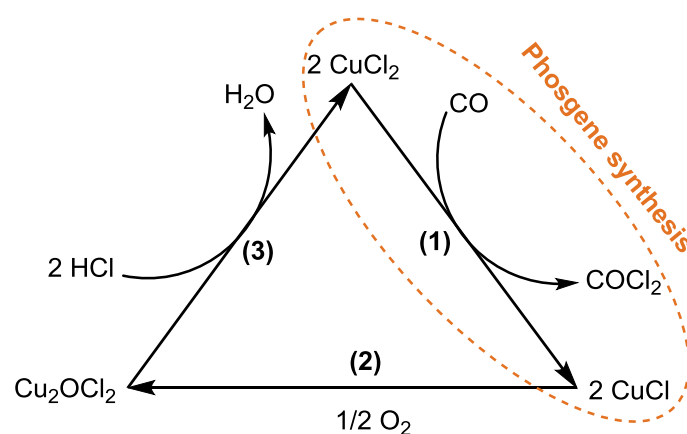
Scheme 1-5. Schematic representation of three-step reaction cycle of Cu (II) catalyzed $COCl_2$ synthesis and catalyst regeneration.[64]

Recently, a revised Cu(II) catalyzed $COCl_2$ formation and catalyst regeneration mechanism has been discussed in three steps (Scheme 1-5). The first step is the oxychlorination of CO which gives rise to $COCl_2$ and simultaneous reduction of $CuCl_2$ to CuCl. In the second step, the oxidation of CuCl with air generates Cu_2OCl_2, while in the third step the neutralization of Cu_2OCl_2 with HCl to $CuCl_2$ takes place.

The co-production of H_2O with $COCl_2$ in CO oxychlorination is one of the major disadvantage of this process and makes the process unfeasible. Although the hydrolysis of $COCl_2$ is thermodynamically favoured, the rates of reaction are found to be slow even at elevated temperatures, unless the reaction is suitably catalyzed.[32]

Inorganic chlorides

Next to the oxychlorination process, various inorganic chlorides have been investigated for the reaction with CO at 45-750 °C to obtain $COCl_2$.[32] For simplicity the results are presented and discussed in detail by their position in periodic table. Based on previous study it has been shown that CO combines with a variety of inorganic chlorides to generate $COCl_2$ in various yield. The synthesis of $COCl_2$ from group-13 metal chlorides occurs, from a reaction between CO and Cl_2 at 30-35 °C.[65] In the $AlCl_3/CHCl_3$ solution, this reaction occurs only in the presence of light.[67] Later, it has been shown that $AlCl_3$ material has no intrinsic effect on the generation of $COCl_2$ from CO and Cl_2 in trichloromethane or 1,1,2,2-tetrachloroethane solution in the presence of light.[68] However, recently a study suggested the occurrence of above reaction by the use of $AlCl_3$ in dark under harsh reaction conditions.[69]

Group-14 chlorides were also reported to react with CO to produce considerable amounts of $COCl_2$ (Equation 1-3 and 1-4).[66] It was speculated the that thermal decomposition of the lead salts give Cl_2, for CO reaction and consequently the $COCl_2$ formation.

$$\textbf{[1-3]} \qquad 2\,CCl_4 \quad + \quad 2CO \quad \xrightarrow{\;350\ °C\;} \quad C_2Cl_4 \quad + \quad COCl_2$$

$$\textbf{[1-4]} \qquad PbCl_2 \quad + \quad CO \quad \xrightarrow{\;650\text{-}750\ °C\;} \quad Pb \quad + \quad COCl_2$$
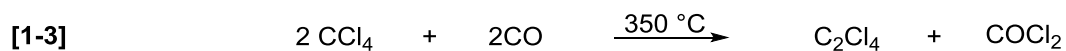
Beside group 14 chlorides, the reaction of CO with chlorides of group-15 elements (e.g. NOCl and $SbCl_5$) have been also described for $COCl_2$ synthesis (Equation 1-5 and 1-6).[66] The reaction between NOCl and CO occurs only in the presence of activated charcoal at 100 - 250 °C and also photo-chemically at ambient temperature.[66]

[1-5]   2 NOCl   +   CO $\xrightarrow{350\ °C}$ 2 NO   +   COCl$_2$

[1-6]   SbCl$_5$ +   CO $\xrightarrow{140\ °C}$ SbCl$_3$ +   COCl$_2$

Group-16 chlorides, namely sulfur dichloride (SCl$_2$), reacts with CO, yielding COCl$_2$ and S$_2$Cl$_2$. S$_2$Cl$_2$ can be converted again to the active SCl$_2$, clearly indicating an overall reaction between activated Cl$_2$ and CO.[66]

Altough the inorganic metal chlorides showed their potential application for phosgene synthesis, the formation of products from metal chlorides are genreally stable and need to be treated differently in Cl$_2$ atmosphere for regeneration of starting material for next catalytic cycles.[66] To overcome the high energy demands, transition metals chlorides were also explored for the reaction of CO and their regeneration in the presence of Cl$_2$.

Transition metal chlorides

The reaction of different transition metal chlorides with CO is presented in following equeations 1-7 to 1-8.[32]

[1-7]   2 AuCl   +   2 CO $\xrightarrow{50\text{-}110\ °C}$ AuCl   +   COCl$_2$

[1-8]   PdCl$_2$ +   CO $\xrightarrow{>\ 45\ °C}$ Pd   +   COCl$_2$

[1-9]   PtCl$_4$ +   CO $\xrightarrow{140\ °C}$ PtCl$_2$ +   COCl$_2$
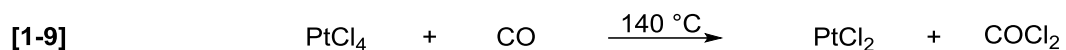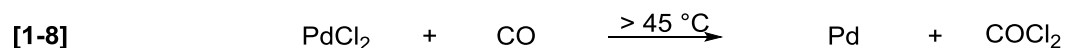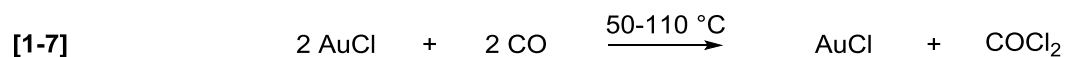
Generally the reaction of transition metal chlorides with CO leads to the in situ formation of the corresponding metal chloride-carbonyl complexes in intermediate step.[66] The reaction of surface -Cl and adsorbed CO led to the formation of COCl$_2$. This was experimentally proved by changing the transition metal with different binding strength with CO. High polarity of M—CO bond led to higher catalytic activity as proposed in following sequence.[66]

Au(CO)Cl   >   [Pd(CO)Cl$_3$]$^-$ >   [Pt(CO)Cl$_3$]$^-$
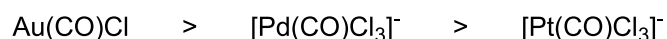
However, no apparent COCl$_2$ formation was observed using RhCl$_3$ and OsCl$_3$ at low temperature due to catalytic decomposition of eventually formed COCl$_2$.[66]

Organophosphines

Potential alternative to gas phase reaction, a new liquid phase COCl$_2$ synthesis process directly from Cl$_2$ and CO reaction using organophosphine chlorides at moderate temperature and

pressure has been published.[66] The liquid phase process has several advantages and disadvantage over gas phase conventional $COCl_2$ synthesis process. The liquid phase process conveys the advantages of better heat transfer characteristics relative to the traditional gas phase chemistry, which is prone to developing hot spots, resulting in depressed yields. In addition to that the $COCl_2$ is more readily separated from unreacted gases and, providing an excess of CO, the amount of residual Cl_2 in the solution is negligible. The disadvantages are that the process uses more costly and difficult-to-handle catalysts and that a solvent make-up is required. Therefore, the development of metal based catalysts is still required for efficient gas phase $COCl_2$ production from Cl_2 and CO reaction at ambient conditions.

Phosgene utilization in sustainable chemical synthesis

Due to its high reactivity $COCl_2$ is widely used as C_1 synthon in several other industrial processes such as for synthesis of isocyanates, acid cholorides, urea derivatives, N-carboxy anhydride and α-chlorinated chloroformate as shown in Scheme 1-6.[32] In particular, its organic chemistry is vast reflecting the compound versatility and general usefulness. Owing to its bad reputation, however, many industrial process are based on their use as in large number of important chemical transformations.
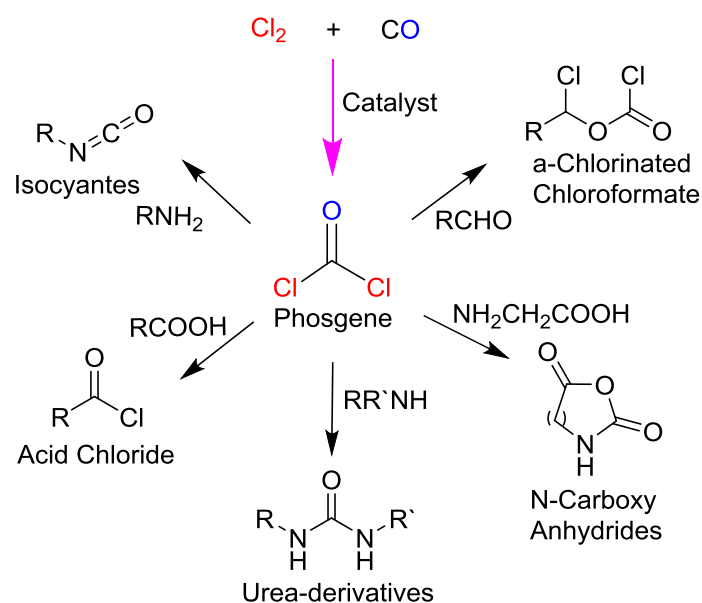
Scheme 1-6. Schemetic representation of wide phosgene utilitzation in industry.

Worldwide, it is used mainly in the manufacture of isocyanates (for urethane polymers and organic intermediates), polycarbonates (for speciality polymers), and monomeric carbonates and chloroformates (largely for the synthesis of pharmaceuticals and pest control chemicals).[32] Further, large number of phosgenation processes are additionally known for organic chemicals synthesis and their utilizations.[32]

1.4 Main challenges and opportunities facing the polymer industry

The main challenges of the polymer industry is the high purity $COCl_2$ production for the catalytic reaction with phenol. Further, the high toxicity of $COCl_2$ stricts its industrial importance. Therefore, a new opportunity towards innovative polymer production would involve the development of a concept based on the use of transiently generated $COCl_2$. In this respect, within the framework of the 7th European Project INCAS (Innovative pathways for sustainable chemical production) the possibility of the use of robust nano-reactor for the transient $COCl_2$ production has been proposed.
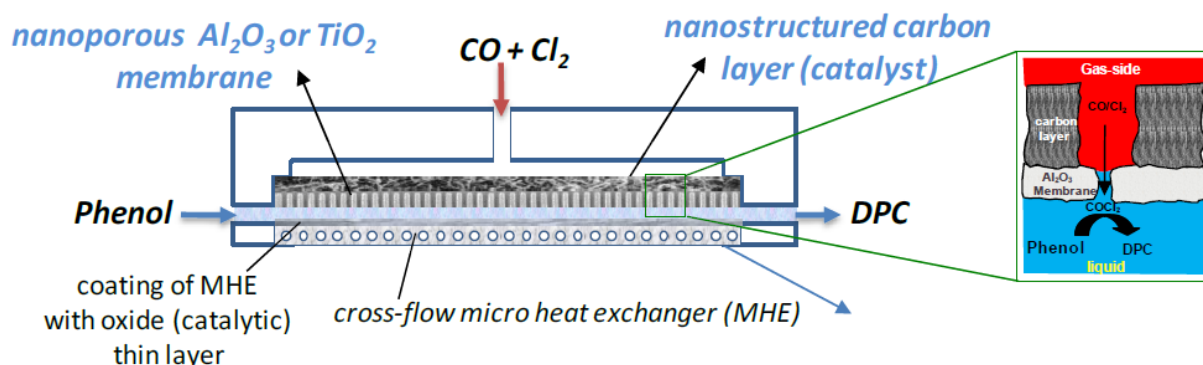
Figure 1-9. Concept of proposed nanoreactor for sustainable DPC production.

The nanoreactor is coupling the $COCl_2$ formation from CO and Cl_2 and its immediate further conversion to DPC by in situ phosgenation of liquid phenol. Contact between phenol and elementary Cl_2 has to be avoided and, therefore, complete Cl_2 conversion on passing the carbon catalyst is mandatory. Traditionally, activated carbon is used as a catalyst for $COCl_2$ formation because this material is not only cheap in costs but also highly active. Presence of multisite in carbon catalysts similarly favor various side reactions, which may arise doubts on their usability as constituent of the catalytically active materials. However, carbon remains to be highly attractive as catalyst due to the high and well known activity. Therefore, the research activities during this work had an emphasis on both investigations of the complex reaction network and

$COCl_2$ formation over carbon catalysts that might count for the observed product formation. It is also expected that deeper understanding of the reaction mechanism will help to define a sustainable catalyst with improved selectivity maintaining its activity for the timespan required for an industrial application.

In order to overcome the challenges for the sustainable DPC synthesis, several important chemical aspects need to be analysed, which includes:

1. Identification of active sites and their contribution to the product and by-products formation.
2. Understanding on thermal and chemical stability of carbon materials.
3. Development of stable catalyst for next generation catalysis.
4. Identify an alternative metal-based catalyst for sustainable chemical production.

1.5 Scope of the Thesis

The aim of the thesis is to provide a substantiated knowledge of the complex $COCl_2$ synthesis from gaseous Cl_2 and CO using carbon catalyst under conditions relevant for industrial process and finally to design a robust and stable catalyst for transient $COCl_2$ production aimed for the immediate conversion to DPC.

Chapter 2 and 3, describes the physicochemical properties of active carbon catalysts for phosgene synthesis. The role of different types of active sites operating under process relevant conditions are discussed in detail. Mechanistic and kinetic studies were performed during Cl_2 activation under He and CO atmosphere. The kinetically relevant steps of the reaction are identified by a kinetic approach and basic kinetic parameters are determined. For this study, highly pure structurally different model carbon materials were selected in order to elucidate the elementary steps of carbon catalyzed Cl_2 activation and $COCl_2$ synthesis. Extensive Cl_2 treatment of various carbon catalysts with different structural and textural properties proved that at low chlorine coverage the irreversible chlorine uptake occurs at energetically more favored sites, i.e., zig-zag and armchair edges, different types of defect sites, coordinatively unsaturated positions and at reactive terminal sp^3 hybridized atoms. The sp^2/sp^3 mixed hybridized carbon sites were identified of radical character of activated Cl_2 species formation during phosgene synthesis.

Within the Chapter 3, the influence of graphitized/well-ordered carbon versus amorphous carbon on catalytic performance for $COCl_2$ synthesis and by products formation was studied in

detail. Significantly, it could be demonstrated, that the majority of the sites favoring side-reactions are mainly located in the amorphous, less organized phase, of the implemented carbon catalyst. The thermal treatment of the considered catalysts enabled the selective removal of the amorphous part and improved the catalyst performance by the reduction of byproducts formation.

In Chapter 4, the synthesis and detailed characterization of N-modified carbon material is presented. The aim was to identify the effect of N- functionalization for the catalytic Cl_2 activation in order to deliver a knowledge and/or requirements for tailoring a stable and active material for transient $COCl_2$ production in DPC synthesis. By carefully analyzing the Cl_2 interaction with the active sites of the heteroatom functionalized carbon materials, it was possible to show, that the heteroatom doping has only an electronic influence on the catalytic reaction. It was shown that the 'real' catalytically active sites responsible for the transient Cl_2 activation and concomitant formation of $COCl_2$ are the carbon atoms in the close vicinity of electron withdrawing nitrogen functionalities. In the case of new N- functionalized model carbon materials, the formation of polarized (ionic) Cl_2 was experimentally evidenced by using in-situ Raman and ESR spectroscopic measurements. By using heteroatom modification, very stable and efficient catalysts for $COCl_2$ production were successfully developed.

In first part of Chapter 5, the design and development of alternative, non-carbon based catalysts for $COCl_2$ synthesis is presented, which could also enable the DPC formation from $COCl_2$ and phenol. An extensive kinetic and mechanistic studies have shown that γ-Al_2O_3 is one promising catalyst for the transient $COCl_2$ synthesis.

Finally, Chapter 6 will give a brief summary and draw the main conclusion of the overall thesis.

1.6   References

[1]   http://www.transparencymarketresearch.com/article/polycarbonate-market.htm
[2]   D. J. Brunelle, M. Korn, *Advances in Polycarbonates, American Chemical Society,* **2005.**
[3]   CMAI Global Plastics & Polymers Market Advisory Service – October **2009.**
[4]   Research and Markets: Global Market for Polycarbonate - Forecast, Trends & Opportunities 2014-2020.
[5]   http://www.wintergardenz.co.nz/glass-vs-poly-vs-film.html
[6]   A. Einhorn, *Liebigs Ann. Chem.* **1898**, *300*, 135.
[7]   C. A. Bischoff, A. V. Hedenstroem, *Berichte*, **1902**, *35*, 3431.
[8]   D. W. Fox, *U.S. Pat. 3, 144,432* assigned to the General Electric Company, **1964.**

[9]   (a) H. Schnell, *Angew. Chem.* **1956,** *68*, 633. (b) H. Schnell, *Ind. Eng. Chem.* **1959,** *51*, 157.

[10]   W. F. Christopher, D. W. Fox, *Polycarboantes, Reinhold Publishing Corporation, New York*, **1962**.

[11]   J. A. King, *Synthesis of Polycarbonates*, *Handbook of Polycarbonate Science and Technology*, Marcel Dekker Inc. New York, **2000**.

[12]   P. G. Kosky, J. M.´Silva, E. A. Guggenheim, *Ind. Eng. Chem. Res*. **1991**, *30*, 462.

[13]   H. Schnell, *The Chemistry and Physics of Polycarbonates*, Wiley Interscience, New York, **1964**.

[14]   C. A. Bischoff, A. V. Hedenstroem, *Berichte*, **1902**, *35*, 3431.

[15]   Y. Shiomi, T. Matsuzaki, K. Masunaga, *EP Patent 0,108,359*, **1987**.

[16]   K. Harada, R. Sugise, K. Kashiwagi, M. Nishio, T. Doi, *Jpn. Kokai Tokkyo Koho Patent 10,330,324*, **1998**.

[17]   G. Illuminati, U. Romano, R. Tesei, *U.S. Patent 4,182,726*, **1980**.

[18]   G. Illuminati, U. Romano, R. Tesei, *Rom. Patent 71,663*, **1980**.

[19]   H. Y. Song, E. D. Park, J. S. Lee, *J. Mol. Catal. A: Chem.* **2000,** *154*, 243.

[20]   J. Haubrock, W. Wermink, G. F. Versteeg, H. A. Kooijman, R. Taylor, M. van Sint Annaland, J. A. Hogendoorn, *Ind. Eng. Chem. Res.*, **2008**, *47*, 9862.

[21]   B. M. Bhanage, M. Arai, *Transformation and Utilization of Carbon Dioxide*, Springer-Verlag GmbH, **2014**.

[22]   W. S. Benedict, T. Sager, *U. S. Patent 2,362,865 A*, **1941.**

[23]   P. Ooms, N. Schon, H. J. Buysch, *U. S. Patent 5,473,094 A* , **1994.**

[24]   W. Schneider, W. Diller, *Phosgene*, *Ullmann's Encyclopedia of Industrial Chemistry,* Weinheim: Wiley-VCH, **2002**.

[25]   K. L. Dunlap, "*Phosgene" Kirk-Othmer Encyclopedia of Chemical Technology*, Wiley, **2001**.

[26]   R. H. Atkinson, C. T. Heycock, W. J. Pope, *J. Chem. Soc.*, **1920**, *117*, 1410.

[27]   E. E. Hardy, *Kirk-Othmer Encyclopaedia of Chemical Technology*, Wiley, **1982**, *17*, 416.

[28]   G. N. Jarman, *Kirk-Othmer Encyclopaedia of Chemical Technology*, Wiley, **1953**, *10,* 391.

[29]   A. Landsberg, F. E. Block, *U.S., Bur. Mines, Rep. Invest.*, **1970** [*Chem. Abstr.*, 73:40417].

[30]   N. C. Jones, *J. Phys. Chem.*, **1929**, *33*, 1415.

[31]   C. Potter, S. Baron, *Chem. Eng. Progress*, **1951**, *47*, 473.

[32]   T. A. Ryan, E. A. Seddon, K. R. Seddon, C. Ryan *Phosgene: And Related Carbonyl Halides*, Elsevier, **1996**.

[33]   P. Serp, J. L. Figueiredo, *Carbon Materials for Catalysis,* John Wiley & Sons **2009**.

[34]   H. W. Kroto, J. R. Heath, S. C. Obrien, R. F. Curl, R. E. Smalley, *Nature*, **1985**, *318*, 162.

[35]   P. Calaminici, J. C. Espindola, G. Geudtner, A. M. Koster, *Int. J. Quantum Chem*, **2012**, *112*, 3252.

[36]   http://eng.thesaurus.rusnano.com/wiki/article1931

[37]   E. Osawa, *Perspectives of Fullerene Nanotechnology*, Kluwer Academic Publisheres, **2002**.

[38]   S. Iijima, *Nature*, **1991**, *354,* 56.

[39]   S. Iijima, T. Ichihashi, *Nature*, **1993**, *363*, 603.

[40]   M. S. Dresselhaus, G. Dresselhaus, P. Avouris, *Carbon Nanotubes Synthesis, Structure, Properties, and Applications*, Springer-Verlag GmbH, **2001**.

[41]   A. Vaseashta, I. N. Mihailescu, *Functionalized Nanoscale Materials, Devices and Systems*, Springer, **2007**.

[42]   K. K. Kar, J. K. Pandey, S. K. Rana, *Handbook of Polymer Nanocomposites. Processing, Performance and Application*, Springer, **2015**.

[43]   S. K. Pati, T. Enoki, C. Nagesa, *Graphene and Its Fascinating Attributes*, World Scientific Publishing, **2011**.

[44]   H. Gu, X. Zhang, H. Wei, Y. Huang, S. Wei, Z. Guo, *Chem. Soc. Rev.*, **2013**, *42*, 5907.

[45]   A. H. C. Neto, F. Guinea, N. M. R. Peres, K. S. Novoselov, A. K. Geim, *Rev. Mod. Phys.*, **2009**, *81*, 109.

[46]   D. D. L. Chung, *J. Mater. Sci.,* **2002***, 37,* 1475*.*

[47]   V. N. Mochalin, O. Shenderova, D. Ho, Y. Gogotsi, *Nat. Nanotechnol*, **2012**, *7*, 11.

[48]   Y. Gogotsi, V. Presser, *Carbon Nanomaterials*, Taylor & Francis, **2006**.

[49]   L. D. Carr, M. T. Lusk, *Nat. Nanotechnol,* **2010**, *5*, 316.

[50]   H. Hu, J. H. Xin, , H. Hu, X. Wang, Y. Kong, *Appl. Catal., A: Gen*, **2015**, *492*, 1.

[51]   (a) X. Zhu, C. Tian, S. M. Mahurin, S. H. Chai, C. Wang, S. Brown, G. M. Veith, H. Luo, H. Liu, S. Dai, *J. Am. Chem. Soc.*, **2012**, *134*, 10478. (b)

[52]   P. Kuhn, M. Antonietti, A. Thomas, *Angew. Chem. Int. Ed.,* **2008**, *47*, 3450.

[53]   A. Thomas, A. Fischer, F. Goettmann, M. Antonietti, J. O. Müller, R. Schlögl, J. M. Carlssonc, *J. Mater. Chem.*, **2008**, *18*, 4893.

[54]   H. H. Byung, H. S. Dae, Y. C. Sung, *Tetrahedron Lett.* **1985**, *26*, 6233.

[55]   Y. Gao, D. Ma, C. Wang, J. Guan, X. Bao, Chem. Commun. 47 (2011) 2432–2434.

[56]   B. Li, Z. Xu, *J. Am. Chem. Soc.,* **2009**, *131*, 16380.

[57]   J. Zhang, X. Liu, R. Blume, A. Zhang, R. Schlögl, D. S. Su, *Science,* **2008**, 322, 73.

[58]   L. Qu, Y. Liu, J. B. Baek, L. Dai, *ACS Nano*, **2010**, *4*, 1321.

[59]   Z. H. Sheng, H. L. Gao, W. J. Bao, F. B. Wang, X. H. Xia, *J. Mater. Chem.*, **2012**, *22*, 390.

[60]   C. Su, M. Acik, K. Takai, J. Lu, S. J. Hao, Y. Zheng, P. Wu, Q. Bao, T. Enoki, Y. J. Chabal, K. P. Loh, *Nat. Commun.,* **2012**, *3,* 1298.

[61]   J. H. Yang, G. Sun, Y. J. Gao, H. B. Zhao, P. Tang, J. Tan, A. H. Lu, D. Ma, *Energy Environ. Sci.,* **2013**, *6*, 793.

[62]   L. M. Liu, R. Car, A. Selloni, D. M. Dabbs, I. A. Aksay, R. A. Yetter, *J. Am. Chem. Soc.*, **2012**, *134*, 19011.

[63]   J. C. Daumas, *U.S. Patent, 3,996,273*, **1976**.

[64]   T. Zhang, C. Troll, B. Rieger, J. Kintrup, O. F. K. Schlüter, R. Weber, *J. Catal*. **2010**, *270*, 76.

[65]   F. Calderazzo, D. B. Dell'Amico, *lnorg. Chem.*, **1982**, *21*, 3639.

[66]   T. A. Ryan, C. Ryan, E. A. Seddon, K. R. Seddon, *Top. Inorg. Gen. Chem.,* **1996,** *24*, 223.

[67]   F. Calderazzo and D. B. Dell'Amico*, lnorg. Chem*., **1982**, *21*, 3639.

[68]   (a) M. J. Parkington, K. R. Seddon and T. A. Ryan, *J. Chem. Soc., Chem. Commun.,***1989**, 1823; (b) M. J. Parkington, *D. Phil. Thesis*, University of Sussex, **1987**.

[69]   H. Eckert, B. Gruber, J. Auerweck, *US20020065432 A1*, **2002**.

Chapter 2

Bent Carbon Surface Moieties as Active Sites on Carbon Catalysts for Phosgene Synthesis

Abstract

Active sites in carbon catalyzed phosgene synthesis from gaseous CO and Cl_2 have been identified using C_{60} fullerene as model catalyst. The carbon atoms distorted from sp^2 coordination in non-planar carbon units are concluded to generate active Cl_2. Experiments and density functional theory calculations indicate the formation of a surface bound $[C_{60}\cdots Cl_2]$ chlorine species with radical character as key intermediate during phosgene formation. It reacts rapidly with physisorbed CO in a two-step Eley-Rideal type mechanism.

2 Bent Carbon Surface Moieties as Active Sites on Carbon Catalysts for Phosgene Synthesis

2.1 Introduction

The synthesis of phosgene ($COCl_2$) by a catalyzed reaction between gaseous chlorine (Cl_2) and carbon monoxide (CO) is one of the oldest, most reliable, and efficient large-scale chemical processes.[1] Since catalytic $COCl_2$ synthesis has replaced earlier processes based on photolysis,[2] the activated carbon used as catalyst has remained basically unchanged. While several kinetic studies on phosgene formation have been reported,[3] mechanistic insight into carbon catalyzed $COCl_2$ synthesis and the associated active sites is largely lacking.[4] In part this may be associated with the diversity and chemical complexity of carbon surface structures rendering the identification of the active sites on carbon catalysts highly challenging.

In order to initiate the development of a new generation of stable and highly active catalysts the nature of active sites and of the elementary steps of $COCl_2$ synthesis from CO and Cl_2 on activated carbon have been studied. Insight is critical not only to optimize catalytic properties *via* maximizing the concentration of active sites, but also to minimize production of chlorinated side products.

2.2 Experimental

2.2.1 Selected carbon nano materials

C_{60} fullerenes (>99.5%) with a $S_{BET} < 5$ m^2/g were purchased from Sigma-Aldrich. $C_{60}Cl_{30}$ was obtained from Nanofluor GmbH.

2.2.2 Catalytic Cl_2/CO activation and $COCl_2$ synthesis

The catalytic activity of the carbon materials (≤ 80 µm particle size) was tested in a quartz pulse reactor (0.4 cm ID, SI Figure S2-2). A six-port valve was used for the automated dosage of Cl_2. C_{60} was packed in a quartz tube reactor and thermally treated under inert conditions (150 °C, temperature ramp: 5 °C min^{-1}, 10 cm^3 s^{-1} He flow; 99.996 % He, Westfalen) during 1.0 h prior to measurements. Cl_2 pulses, 60 µL each, ($Cl_2 > 99,996\%$, Westfalen) were performed at intervals of 230 s, under atmospheric pressure. The gaseous products were characterized in situ

by MS using a PFEIFFER OmniStar quadrupole mass spectrometer (QMS 200). For testing the reactivity of activated Cl_2 at 200 °C, pre-mixed 5 % CO and 5 % CH_4 in He (> 99.9 %, Westfalen) were used. The rate of $COCl_2$ formation was evaluated at a temperature range of 100 – 350 °C. The Cl_2 and $COCl_2$ containing gaseous residue was decomposed in two interconnected KOH containing bottles. An active carbon filter finally retained reactive components from the exiting stream.

2.2.3 Experimental set-up and safety issues

The schematic representation of the experimental setup for Cl_2 and CO activation study is shown in supporting information, Figure S2-1. Pulse mode experiment is a powerful technique to understand the mechanism and kinetics in heterogeneous catalytic system. The transient measurements with high time resolution, it is possible to determine single reaction steps during a complex reaction over real catalysts. One major advantage of this setup designed for Cl_2 activation studies is the possibility to use minimal amounts of toxic and corrosive gases. Thereby, a six-port valve connected to an on-line mass spectrometer (MS) was used for the automated dosage of Cl_2. All the gaseous residues were neutralized in two interconnected concentrated KOH and Cu^{+2} solution containing bottles. Additionally, an activated carbon containing filter finally accounts for the retention of any generated toxic gaseous intermediates left.

Special attention was paid to the safety issues; two different types of Cl_2 and CO detectors were placed under the fume hood to constantly monitor the Cl_2 and CO concentration at the working place. To avoid contamination with CO, two additional filters for CO entrapment were installed at the outlet of the six-port valve and of the reactor. The maximum amount of $COCl_2$ which could theoretically be formed in the pulse reactor (0.025 ppm) is lower than the permissible exposure limit (0.1 ppm averaged over a work shift of up to 10 hours a day, 40 hours per week with a ceiling level of 0.2 ppm averaged over a 15 min period).

2.3   Catalyst characterization

BET surface area

The specific surface area and pore volume was determined by N_2 physisorption and Brunauer-Emmett-Teller (BET) using PMI automated Sorptomatic 1990 instrument.

Elemental analysis

Elemental compositions of the carbon nano-materials were determined by CHN analysis at TU-München. The quantity of oxygen was estimated at Mikroanalytisches Labor Pascher, Germany.

Scanning electron microscope (SEM)

The topographical images of all carbon samples were recorded on a JEOL JSM-5900LV and Hitachi S3500N SEM operating at 10-25 kV.

Transmission electron microscope (TEM)

High resolution TEM images of the carbon nano-materials were recorded with a JEM-2010 JEOL transmission electron microscope operating at 120 kV. Before transferring to the vacuum system, the samples were finely ground, suspended in ethanol and ultrasonically dispersed for 2-5 minute and drops of the dispersions were applied on a copper grid supported carbon film.

Ramann spectroscopy

The in situ Raman spectra were measured under isothermal conditions at 40 °C, and the samples were analyzed inside a quartz flow reactor in order to maintain Cl_2 atmosphere, Cl_2 containing gas (25% Cl_2 in He, Westfalen) was used. Prior Cl_2 treatment the samples were activated at 150 °C for 1 h in N_2 flow (99,996%, Westfalen). The Raman spectra at 514.5 nm (2.41 eV, Ar^+ laser) were taken with Renishaw spectrometer in a backscattering configuration every 43 s. To exclude the possibility of Raman spectral changes due to the laser irradiation the blank test was performed under pure N_2 flow.

Electron Spin Resonance (ESR) spectroscopy

ESR spectra were recorded in perpendicular mode on an X-band Joel Jes Fa 200 spectrometer. The measurements were performed in high-pressure quartz tube at 25 °C (9.45 GHz, 1mW microwave power).

Density functional theory (DFT)

DFT calculations were carried out using the B3LYP exchange-correlation functional as implemented in Gaussian 09 D.01.[15] Dispersion interactions were accounted with the D3 version of Grimme's dispersion with Becke-Johnson.[16] Full geometry optimizations were carried out using the 6-31G(d,p) basis set. The energies obtained at this step were further refined by single point electronic energies computed using the larger TZVP basis set.[17] Reaction enthalpies were calculating by correcting the electronic energies for zero-point energies and finite temperature contributions calculated from the results of the normal mode analysis at 298.15K and 1 atm. The accuracy of the selected method is confirmed by a close agreement between the computed and experimental energetics.

2.4   Results and discussions

In a first step, transmission electron microscopy has been used to exemplify the characteristic features of a typical activated carbon catalyst, i.e., the ample presence of bent carbon layers, semi-spheres, and carbon cages (Figure 2-1). Bending of the carbon structures is usually induced by the presence of 5-membered rings or the combination of 5- and 7-membered rings (Stone-Wales defects).[5]
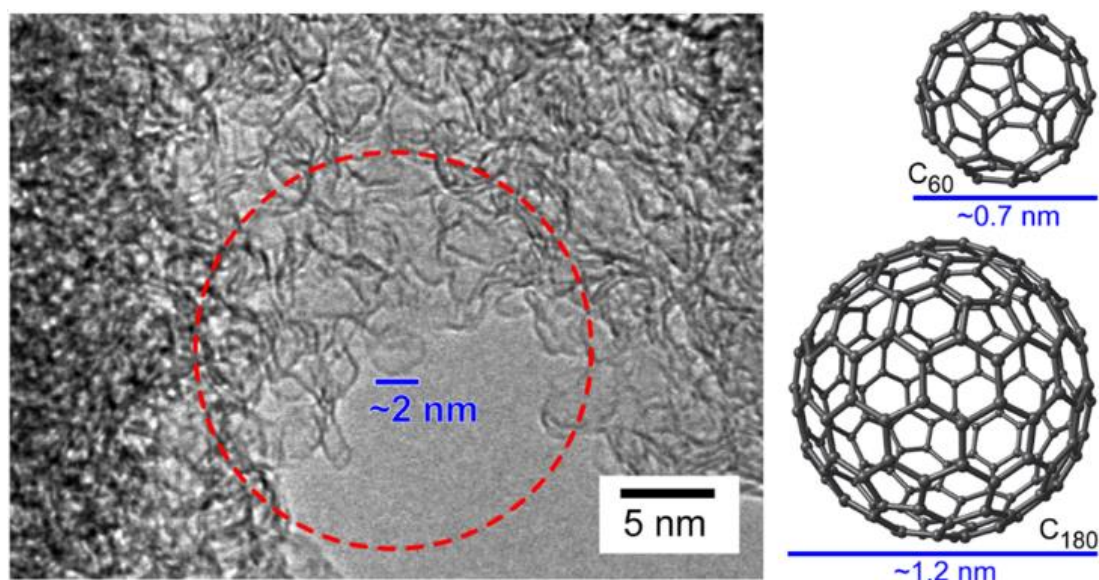
Figure 2-1. (Left) HR-TEM micrograph of an activated carbon catalyst for $COCl_2$ synthesis from CO and Cl_2 showing curled carbon layers and carbon semi-spheres that resemble (right) fullerene-type structures.

The diameters of these bent structural units (Figure 2-1, blue bar) approximate the diameter of fullerenes, which range from 0.71 (C_{60}) to 1.2 nm (C_{176}) [6,7]. The structural analogy between the curved surfaces of activated carbon and the molecular structure of fullerenes stimulated us, in consequence, to select fullerenes as well-defined model catalysts. These models lack defect sites, edges, and functional groups. It allows to explore the mechanism of carbon catalyzed Cl_2 activation and conversion with CO in absence of various more reactive but less defined carbon species.

Table 2-1 compares DFT-computed reaction energies for $COCl_2$ formation and the Cl_2 addition to unsaturated moieties in several model structures with distinct structural characteristics, *i.e.*, a planar $C_{32}H_{14}$ graphene model, 2-butene and C_{60}. Only in the case of C_{60}, the reaction energy is lower than that of the reaction of Cl_2 with CO. The reaction of Cl_2 with graphene is highly endothermic and addition to graphene has not been observed.[8] Chlorination of butene is strongly exothermic, suggesting the formation of strong and stable C-Cl bonds. We hypothesize, therefore, that the curved structure of the conjugated fullerene π-system provides the appropriate balance between the loss of conjugation energy and the energy gain in reactive coordination of Cl_2 (SI, Figure S2-1), in line with the relatively low exothermicity of Cl_2 addition to C_{60}.

Table 2-1. DFT-computed reaction energies (B3LYP-D3/TZVP//6-31G(d,p)) of Cl_2 addition *via* X + Cl_2 → XCl_2.

X	Graphene[a]	C_{60}	CO[b]	2-Butene[b]
ΔE [kJ mol^{-1}]	+227	-18	-124	-189

[a] The structure of graphene was approximated by a $C_{32}H_{14}$ fragment in this calculation (SI, for further details).
[b] The experimental ΔH_r values for CO and 2-butene chlorination are -109.6 and -191.2 kJ mol^{-1}, respectively.[1e]

To test the suitability of C_{60} as a model catalyst for $COCl_2$ synthesis, the material was exposed to CO and Cl_2 pulses at 200°C (SI, Figure S2-2). Once the reversible adsorption of Cl_2 was established, the stable catalytic formation of $COCl_2$ was detected by online mass-spectrometry (m/z = 63, Figure 2-2a), corresponding to $[COCl]^{+\cdot}$. Without catalyst only negligible concentrations of $COCl_2$ formed (Figure 2-2b).
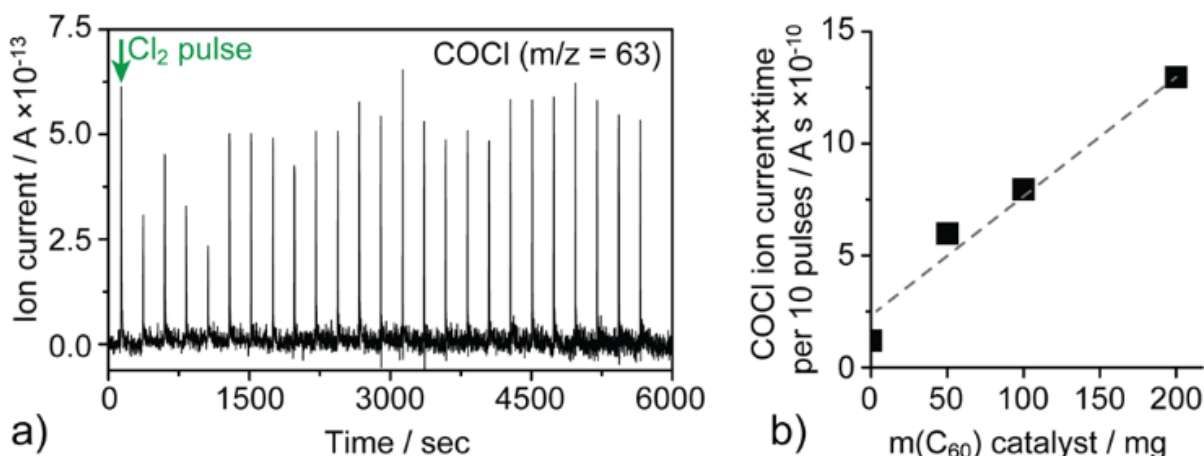
Figure 2-2. (a) $COCl_2$ formation on applying Cl_2 pulses over solid C_{60} at 200°C in 5 % CO in He. (b) Comparison of the $COCl_2$ formation in the presence of various amounts of C_{60} fullerene.

To probe the hypothesis that Cl_2 has to be weakly adsorbed to be successfully activated and converted to $COCl_2$, in situ Raman spectroscopy was used to study the interaction of Cl_2 with the C_{60} fullerene (Figure 2-3a). The pentagonal pinch mode A_2g at 1465 cm^{-1} was used to monitor the electronic environment of the carbon atoms.[8,9,10]
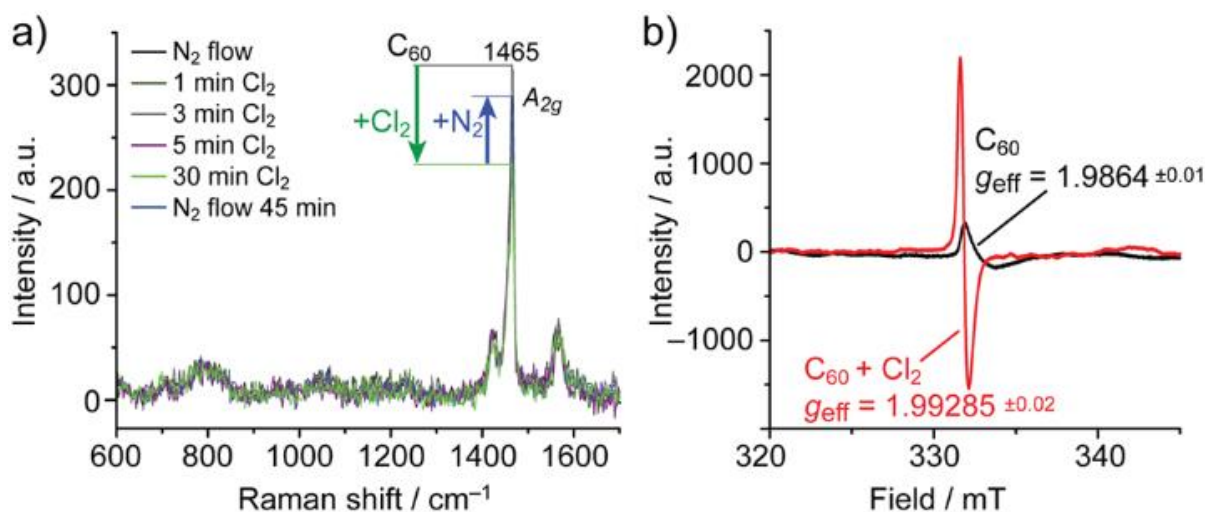
Figure 2-3. (a) In situ Raman spectra of C_{60} contacted with Cl_2 at 40 °C. (b) Comparison of the ESR spectra of C_{60} under inert conditions (black) and in a Cl_2 atmosphere (red) recorded at ambient temperature.

In the presence of Cl_2 the intensity of the A_2g band decreased, rapidly reaching a new equilibrium (Figure 2-3a). Purging with an inert gas reverted the spectral changes induced by Cl_2 addition. This demonstrates a reversible interaction between Cl_2 and C_{60} involving the

42

formation of a $[C_{60}\cdots Cl_2]$ complex, presumably *via* a charge transfer from C_{60} to Cl_2.[11] Reduction of the spherical symmetry upon C-Cl bond formation eliminates the A_{2g} band and results in new Raman bands at 650-850 cm^{-1} (C-Cl vibration in $C_{60}Cl_{30}$, Figure S2-3a). Combined Raman (Figure 2-3a) and elemental analysis (Table S2-1) of the Cl_2 treated C_{60} further show that the $[C_{60}\cdots Cl_2]$ interaction has neither led to the formation of covalent C-Cl bonds nor significantly changed the symmetry of fullerene.

To characterize the reversibly adsorbed $[C_{60}\cdots Cl_2]$ species, ESR spectroscopy was used (Figure 2-3b). Neutral C_{60} has no unpaired electrons and is, therefore, ESR inactive. However, in our studies an ESR signal at g = 1.9864 ± 0.01 was observed for the nominally neutral C_{60} due to the presence of small amount ($5.4 \cdot 10^{17}$ spin g^{-1}) of paramagnetic defects generated during the synthesis procedure or the purification. The ESR line patterns indicate that these defects are delocalized an all the C atoms of the C_{60} cage, so that the contributions to the ESR line are dynamically averaged over all sites on C_{60}.[12] Upon Cl_2 exposure a new strong signal was observed at g_{eff} = 1.9928 ± 0.02 indicating the localized Cl_2 adsorption and formation of strong paramagnetic $[C_{60}\cdots Cl_2]$ charge transfer complex.[12] The singlet line, an isotropic doublet without zero-field splitting peaks, indicates that the symmetry of the C_{60} fullerene cage was not changed by exohedral functionalization.

DFT calculations were performed to rationalize these experimental observations. Figure 2-4 shows the calculated reaction energy diagram for the activation of Cl_2 in the presence of C_{60}.
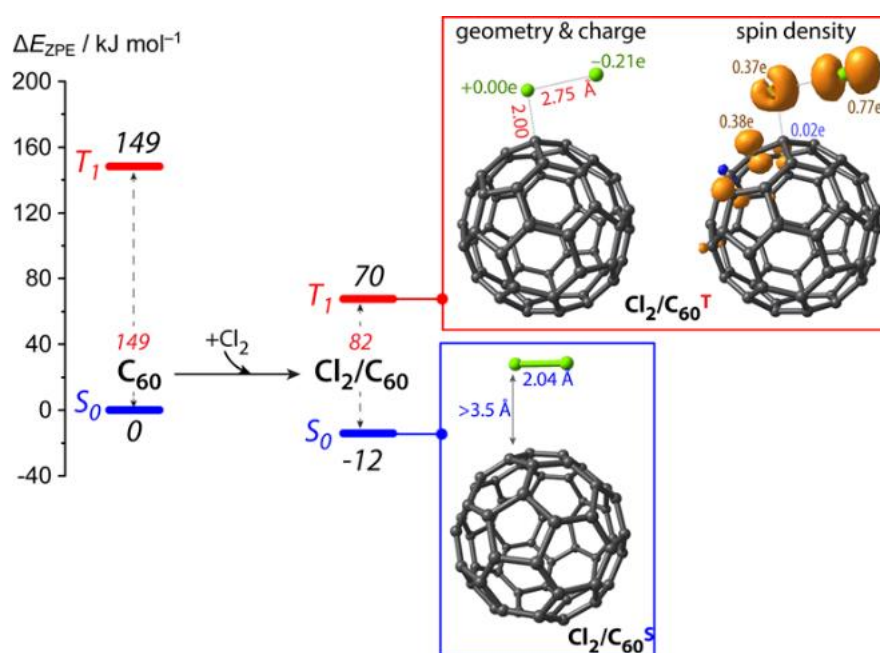
Figure 2-4. Reaction energy diagram and optimized structures (selected bond lengths are given in Å, Mulliken atomic charges and spin density are given for the open-shell Cl_2 adsorption

complex Cl_2/C_{60}^T) of intermediates involved in Cl_2 adsorption and activation by C_{60} in the singlet (S_0) and triplet (T_1) electronic configurations.

The activation of Cl_2 by C_{60} leading to C_{60}/Cl_2^S in the ground singlet state (S_0) proceeds with a prohibitively high-energy barrier (exceeding 400 kJ mol^{-1}, as estimated by relaxed potential energy scan calculations). Therefore, we conclude that a direct activation of Cl_2 on a C_{60} in the singlet state is not possible in the reaction space explored. Cl_2 activation becomes favorable when the reaction proceeds over the triplet excited potential energy surface. DFT-computed energy differences between the singlet (S_0) and triplet (T_1) electron configurations of C_{60} is 149 kJ mol^{-1}, i.e., in excellent agreement with the reported experimental values (150-155 kJ mol^{-1}).[13] In the presence of Cl_2, the triplet electronic configuration (T_1, Figure 2-4, Cl_2/C_{60}^T) becomes strongly stabilized and is only 70 kJ mol^{-1} higher in energy than the respective ground state of a Cl_2 and C_{60} mixture. The T_1 adsorption complex Cl_2/C_{60}^T can be regarded as a biradical species featuring a Cl radical anion coupled with the $C_{60}Cl$ unit in which the spin density is delocalized, as shown in Figure 2-4. This is in line with the ESR spectra (Figure 2-3), showing the formation of Cl_2 radicals when Cl_2 is adsorbed on C_{60}. Such radical Cl_2/C_{60}^T species are hypothesized to be the key species for the catalytic conversion of CO to $COCl_2$. DFT calculations indicate a very favorable catalytic path (Figure 2-5, Scheme 2-1). The cycle starts with the facile reaction (E_{act} = 7 kJ mol^{-1}) of CO with a Cl radical moiety of Cl_2/C_{60}^T yielding $COCl^.$ (CO$\cdots Cl_2/C_{60}^T$ → $COCl\cdots ClC_{60}^T$, Figure 2-5). The favorable path proceeds *via* a barrierless reaction of $COCl^.$ with another Cl_2 to yield $COCl_2$ (Figure 2-5) and regenerate Cl_2/C_{60}^T (Scheme 2-1, path A). However, the direct recombination of the $COCl^.$ and adjacent Cl· radicals (Scheme 2-1, path B) resulting in $COCl_2$ and transient C_{60}^T that is readily stabilized by Cl_2 to form Cl_2/C_{60}^T also cannot be completely ruled out. The off-cycle spin-crossing S_0 →T_1 relaxation path (Figure 2-5) is less likely and would give a catalytic cycle with an apparent E_{act} over 70 kJ mol^{-1} needed for the transition to the active T_1 state (Figure 2-4). This is in a strong contrast to the observed barrier 18 kJ mol^{-1} (SI, Table S2-2).
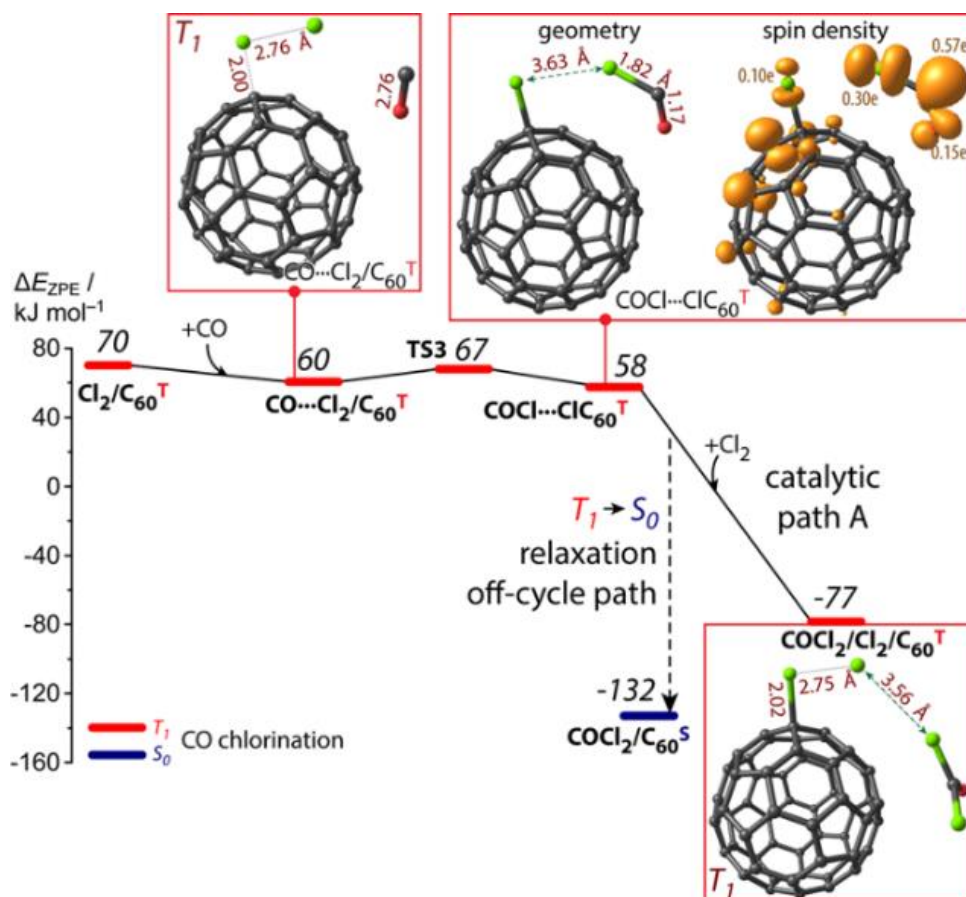
Figure 2-5. Reaction energy diagram and structures of key intermediates and transition states involved in phosgene synthesis over C_{60}.

The proposed reaction sequence is in line with the observed reaction order of one (SI, Table S2-2) in Cl_2 and CO. The apparent activation energy was significantly lower (18 kJ mol^{-1}) than the one measured for an activated carbon catalyst (56 kJ mol^{-1}, SI, Table S2-2)[3] clearly indicating the subtle effect of the local environment of the active sites on the structure and energy of the transition state. At this point, we would like to highlight that the proposed active site, the triplet [Cl_2….C_{60}] will increase in concentration with temperature, as it lies 70 kJ mol^{-1} higher than the ground state of isolated C_{60} and Cl_2.
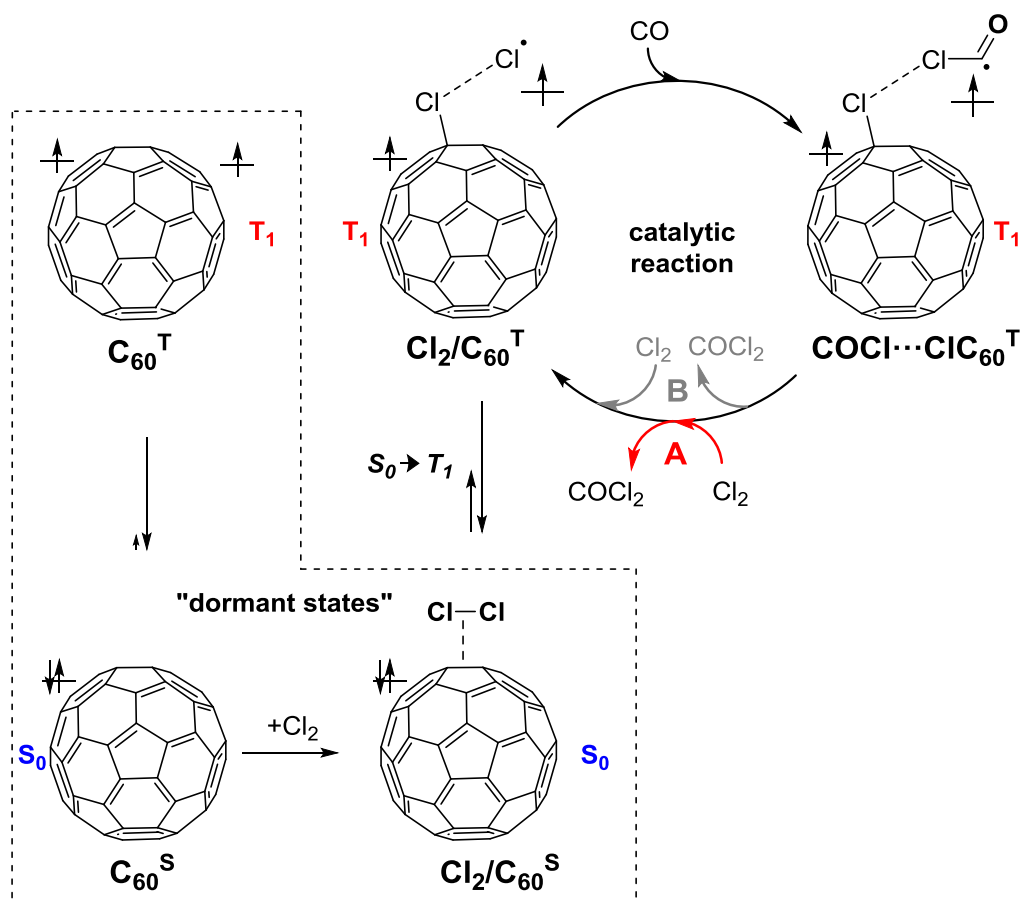
Scheme 2-1. Proposed mechanism for Cl_2/C_{60}^T catalyzed $COCl_2$ formation following an Eley-Rideal mechanism. The potentially dormant off-cycle species are shown in the dashed rectangle, while alternative paths for the regeneration of the catalytic species Cl_2/C_{60}^T are indicated as paths A and B.

To independently probe the presence of radicals, $[C_{60}{\cdots}Cl_2]$ was reacted with CH_4, which is known to be chlorinated by radical substitution. The reaction led to a mixture of CH_3Cl, CH_2Cl_2, $CHCl_3$ and CCl_4. In presence of C_{60} a five-fold rate increase compared to the non-catalytic thermal chlorination of CH_4 was observed at 200 °C (Figure 2-6) evidencing unequivocally the presence of surface bound $Cl\cdot$ radicals.

$$CH_4 \xrightarrow[-HCl]{Cl_2} CH_3Cl \xrightarrow[-HCl]{Cl_2} CH_2Cl_2 \xrightarrow[-HCl]{Cl_2} CHCl_3 \xrightarrow[-HCl]{Cl_2} CCl_4$$
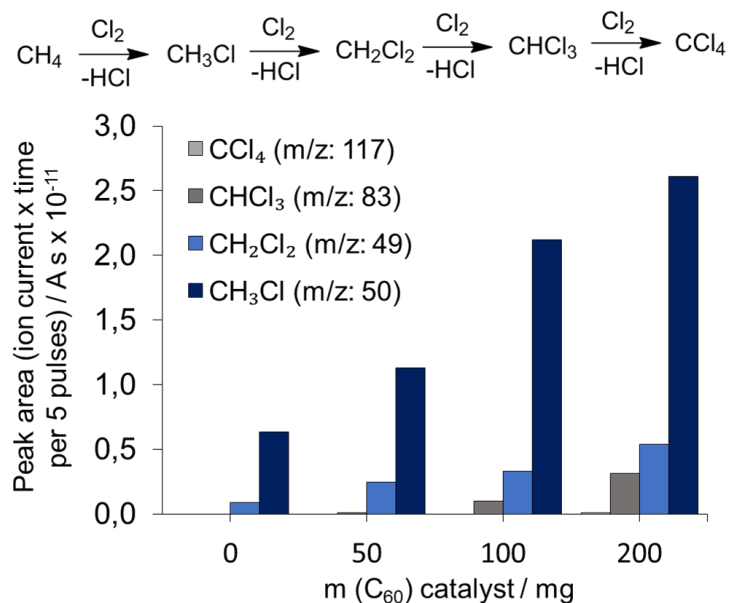
Figure 2-6. CH_4 chlorination in the absence (0 mg) and in the presence of variable amounts (50 – 200 mg) of C_{60} catalyst at 200 °C.

2.5 Conclusions

Thus, combining ESR and Raman spectroscopic analysis and reactivity data, we conclude that a reversible surface bound radical $[C_{60}\cdots Cl_2]$ species is formed, which reacts with CO to form $COCl_2$ and with CH_4 to form $CH_{4-n}Cl_n$. The $COCl_2$ formation is suggested to occur most likely *via* stepwise addition of Cl atoms. A second Cl_2 restitutes the reactive $[C_{60}\cdots Cl_2]$ species, as the $COCl_2$ desorbs. The quite marked dependence of the Cl_2 reactions with carbon surfaces of various strain on the sp^2 hybridized carbons, allows us to conclude that $COCl_2$ synthesis requires carbon catalysts with an intermediate strain to form a sufficient concentration of the critical reversibly bound radical $[C_{60}\cdots Cl_2]$ species.

2.6 References

[1]   (a) W. Schneider, W. Diller, *Phosgene*, *Ullmann's Encyclopedia of Industrial Chemistry*, Weinheim: Wiley- VCH **2005**; (b) K. L. Dunlap, *Phosgene, Kirk-Othmer Encyclopedia of Chemical Technology* **2010**, 1; (c) T. A. Ryan, E. A. Seddon, K. R. Seddon, C. Ryan, *Top. Inorg. Gen. Chem.* **1996**, *24*, 3; (d) *www.phosgenesafety.info,* accessible after registration by the International Isocyanate Institute (III) in Manchester, GB; (e) NIST Chemistry WebBook, accessed 16.04.2015, http://webbook.nist.gov.

[2]   T. A. Ryan, E. A. Seddon, K. R. Seddon, C. Ryan, *Top. Inorg. Gen. Chem.* **1996**, *24*, 167.

[3]   (a) C. J. Mitchell, W. v. d. Borden, K. v. d. Velde, M. Smit, R. Scheringa, K. Ahrikaa, D. H. Jonesa, *Catal. Sci. Technol.* **2012**, *2*, 2109; (b) C. Potter, S. Baron, *Chem. Eng. Prog.* **1951**, *47*, 473; (c) Z. Csũrös, R. Soós, I. Petneházy, G. T. Szabó, *Period. Polytech., Chem. Eng.* **1970**, *14*, 3; (d) E. N. Shapatina, V. L. Kuchaev, M. I. Temkin, *Kinet. Catal.* **1977**, *18*, 968; (e) E. N. Shapatina, V. L. Kuchaev, M. I. Temkin, *Kinet. Catal.* **1978**, *20*, 972.

[4]   P. Serp, J. L. Figueiredo, *Carbon Materials for Catalysis*, John Wiley & Sons, **2009**.

[5]   (a) A. J. Stone, D. J. Wales *Chem. Phys. Lett.* **1986**, *128*, 501; (b) P. A. Thrower, *Chemistry and Physics of Carbon* **1969,** *5*, 217.

[6]   J. Sloan, R. E. Dunin-Borkowski, J. L. Hutchison, K. S. Coleman, V. C. Williams, J. B. Claridge, A. P. E. York, C. Xu, S. R. Bailey, G. Brown, S. Friedrichs, M. L. H. Green, *Chem. Phys. Lett.* **2000,** *316,* 191.

[7]   A. Goel, J. B. Howard, J. B. Vander Sande, *Carbon* **2004***, 42,* 1907.

[8]   F. N. Tebbe, J. Y. Becker, D. B. Chase, L. E. Firment, E. R. Holler, B. S. Malone, P. J. Krusic, E. Wassermann, *J. Am. Chem. Soc.* **1991**, *113*, 9900.

[9]   H. Kuzmany, M. Matus, B. Burger, J. Winter, *Adv. Mater.* **1994**, *6*, 731.

[10]   D. S. Bethune, G. Meijer, W. C. Tang, H. J. Rosen, *Chem. Phys. Lett.* **1990**, *174*, 219.

[11]   M. Kalbac, L. Kavan, M. Zukalova, L. Dunsch, *Small* **2007**, *3*, 1746.

[12]   (a) N. G. Spitsina, M. V. Motyakin, I. V. Bashkin, K. P. Meletov, *J. Phys.: Condens. Matter* **2002**, *14*, 11089; (b) A. I. Mikhaylov, V. A. Pakhomova, S. I. Kuzina, S. A. Baskakov, Y. M. Shul'ga, A. A. Volodin, V. E. Muradyan, *Nato Sci. Ser. II Math.* **2007**, 155; (c) L. Khachatryan, B. Dellinger, *Chemosphere* **2003**, *52*, 709; (d) M. S. Dresselhaus, G. Dresselhaus, P. C. Eklund, *Science of Fullerenes and Carbon Nanotubes: Their Properties and Applications.* Elsevier Science (USA), **1996**.

[13]   M. G. Giuffreda, F. Negri, G. Orlandi, *J. Phys. Chem. A* **2001,** *105,* 9123.

[14]   R. Deng, M. Treat, O. Echt, K. Hansen, *J. Phys. Chem.* **2003**, *118*, 8563.

[15]   M. J. Frisch, Gaussian 09, Revision D.01, Gaussian, Inc., Wallingford CT, **2009** (full reference is given in the supporting information).

[16]   S. Grimme, S. Ehrlich, L. Goerigk, *J. Comp. Chem.* **2011**, *32*, 1456.

[17]   (a) A. Schaefer, H. Horn, R. Ahlrichs, *J. Chem. Phys.* **1992**, *97*, 2571; (b) A. Schaefer, C. Huber, R. Ahlrichs*, J. Chem. Phys.* **1994**, *100*, 5829.

2.7 Supporting information
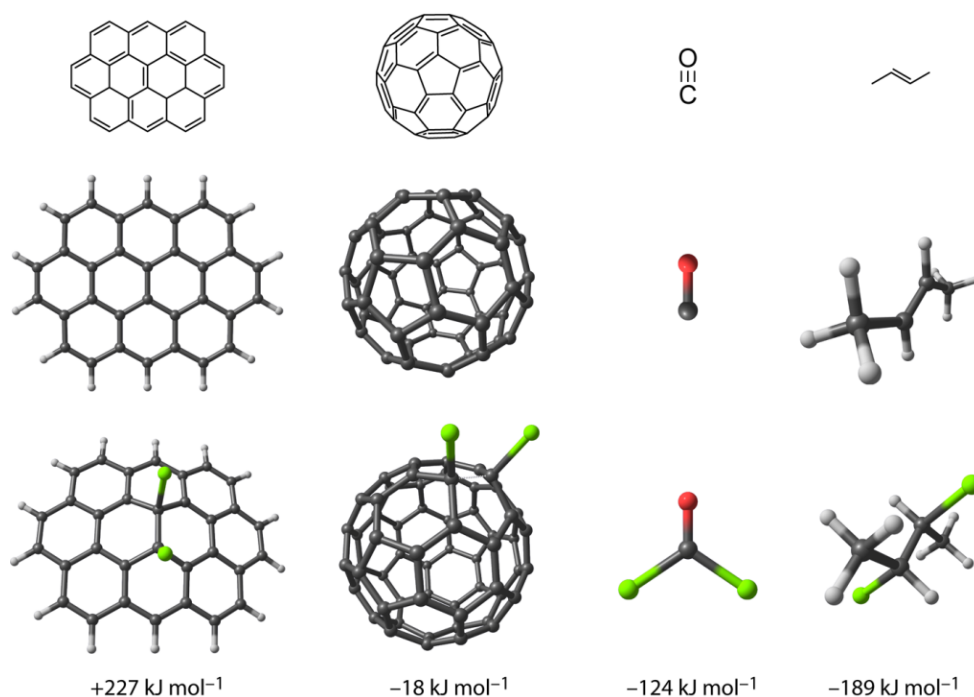
Figure S2-1. Comparison of Cl_2 addition enthalpies to different carbon structures as determined by DFT.
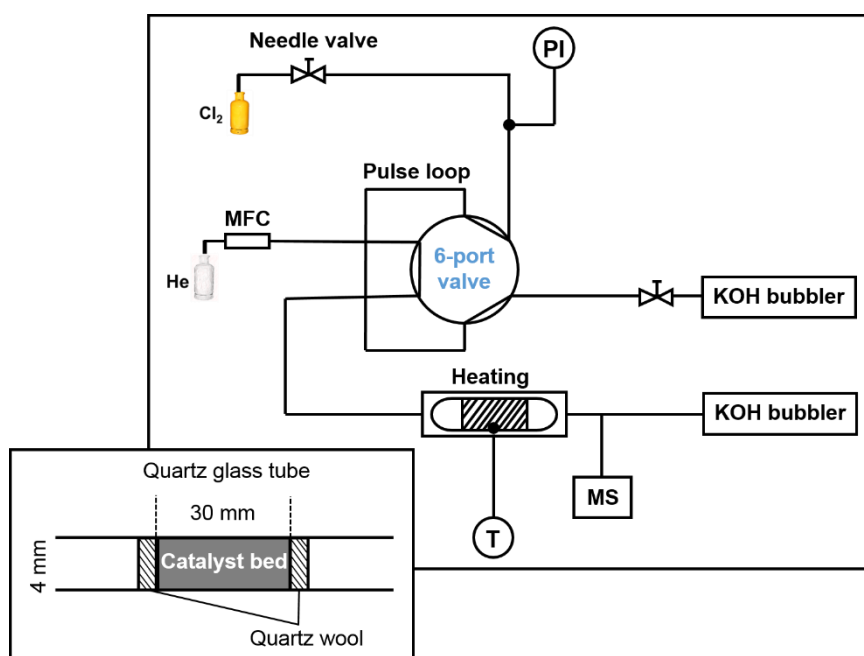
Figure S2-2. Pulse setup for Cl_2 and CO activation study.

To illustrate the changes in the Raman spectra of C_{60}, which would be induced by the formation of covalent C-Cl bonds, the Raman spectrum of the chlorinated analog $C_{60}Cl_{30}$ is shown in Figure S2-3a. Reduction of the spherical symmetry on C-Cl bond formation leads to the appearance of several Raman bands, which were not observed in the in situ Raman experiment (Figure S2-3b). Thus, we conclude that the charge complex $[C_{60}\cdots Cl_2]$ formed during Cl_2 interaction has neither led to the formation of covalent C-Cl bonds nor significantly changed the symmetry of C_{60} fullerene.

In order to further prove that the observed change in the A_{2g} Raman band intensity during Cl_2 treatment (shown in Figure 2-3) are due to the associative adsorption of Cl_2 on the C_{60} surface, in-situ Raman measurements were repeated by using silicon (111 phase, 99.99 %, Sigma Aldrich) as an internal standard that give a strong Raman line at 521 cm^{-1} with almost no background. As shown in Figure S2-3b, in the presence of Cl_2, the only changes are observed at A_{2g} band, while the band intensity at 521 cm^{-1} is not affected by chlorine treatment.
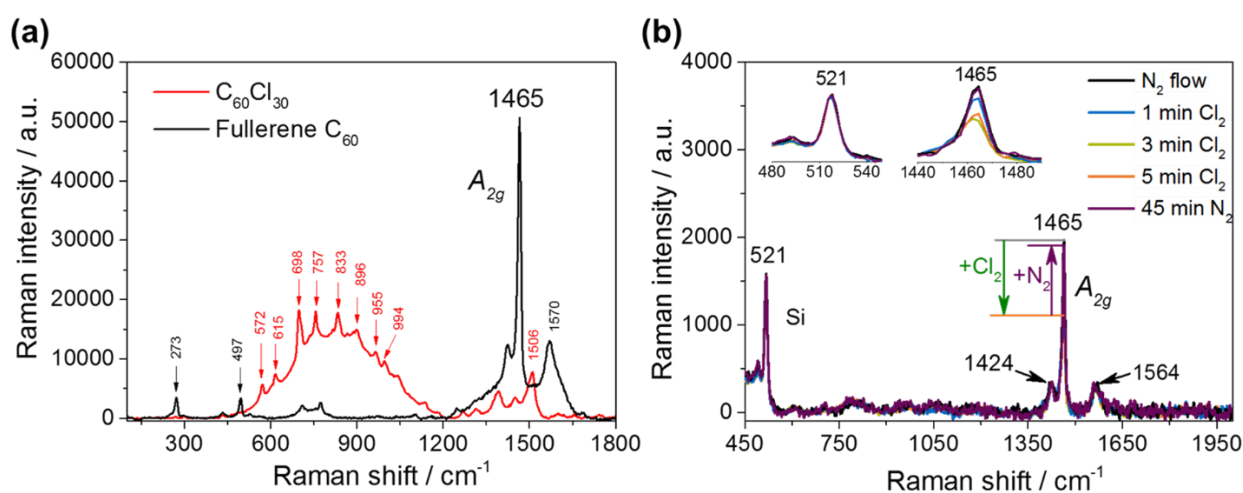
Figure S2-3. In situ Raman spectra of $C_{60}Cl_{30}$ (a) and of C_{60} fullerene (b) contacted with Cl_2 at 40 °C.

Vibrational analysis of the A_{2g} band in the in situ Raman spectra of C_{60} under inert conditions and in the presence of Cl_2 similarly confirm the formation of a charge transfer complex where the C_{60} cage structure is preserved. The observed phonon softening $\Delta\omega$ for the mode is about -9 cm^{-1} (Figure S2-4) indicating the one electron is transferred per C_{60} molecule. This phonon softening is attributed to the C-C bond expansion in the C_{60} molecule due to the charge transfer in the antibonding t_{1u} bond.[6] Similar small shifts were observed in the case of TDAE (tetrakis(dimethylamino)ehylene) C_{60} complex.[6]
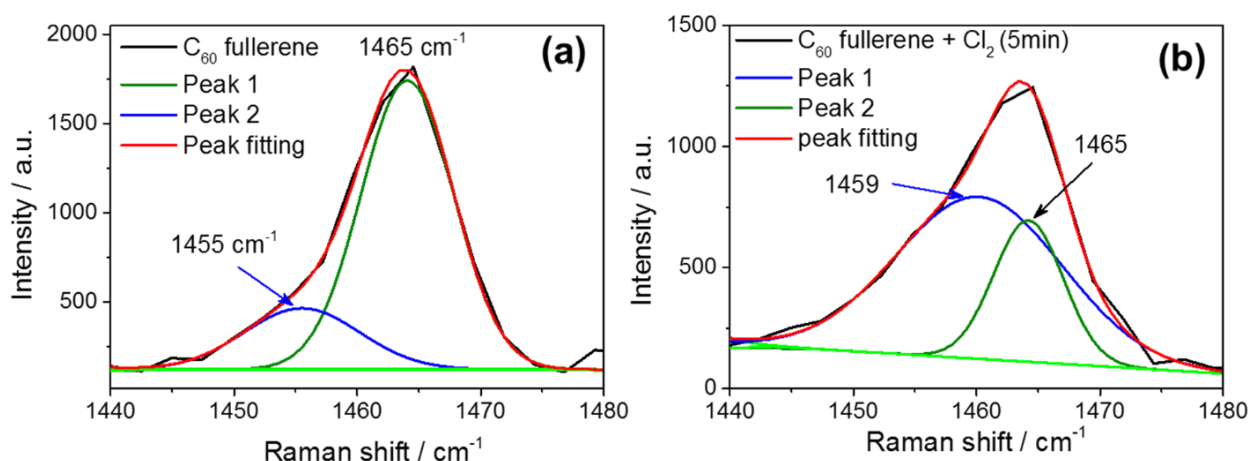
Figure S2-4. Vibrational analysis of the Raman spectra of C_{60} (a) and of C_{60} fullerene (b) contacted with Cl_2 at 40 °C.

After the exposure of C_{60} to Cl_2 at 40 °C, the elemental analysis of the material was carried out to support the assumption of reversible formation of a $[C_{60}\cdots Cl_2]$ charge transfer complex. CHNS analysis results of pristine C_{60} and of the Cl_2 treated material are summarized in Table S2-1.

Table S2-1. Elemental analysis of Cl_2 treated C_{60} fullerene.

Material	Elemental analysis (wt. %)					
	C	**H**	**N**	**S**	**Cl**	**Others***
C_{60}	99	<1	<1	-	-	-
C_{60} after exposure to Cl_2	98.6	<1	-	-	-	1-2 (SiO_2)

*EDX analysis

The elemental analysis of materials clearly indicate that no chlorination of C_{60} occurs during the Cl_2 treatment. For example, at a very low chlorination degree of C_{60} such as in the case of $C_{60}Cl_2$, where two chlorine atoms are covalently bounded to C_{60} would result in a theoretical elemental value of 91.04 wt. % C and 8.96 wt. % Cl.

Neutral C_{60} molecules do not have unpaired electrons and are, therefore, ESR inactive. However, in our studies an ESR signal at g = 1.9864 ± 0.01 was observed for the nominally neutral C_{60} sample due to the presence of small amount ($5.4 \cdot 10^{17}$ spin g^{-1}) of paramagnetic defects generated during the synthesis procedure or the purification. The ESR line patterns indicate that the hole or the electron defects are delocalized an all the carbon atoms of the C_{60}

cage, so that the contributions to the ESR line are dynamically averaged over all the sites on the C_{60} ion.[2]

During the contact of C_{60} with Cl_2 another narrow signal with $g = 1.99285 \pm 0.02$, very close to the free electron value, arises. In independent studies and in line with our experimental results, the localized adsorption and formation of strong paramagnetic carbon-chlorine charge transfer complex is assumed to take place during the contact of C_{60} with Cl_2.[12c,3,4,5] The singlet line, an isotropic doublet without zero-field splitting peaks, in the ESR spectra of C_{60} in a Cl_2 atmosphere demonstrates that reduction in the symmetry of the fullerene cage due to exohedral functionalization did not take place. The strong analogy with the depicted ESR spectra of paramagnetic carbon chlorine *C-Cl_2 charge transfer complex[5] led us to conclude that the charge transfer complex stabilized on the active surface of a C_{60} molecule has an unpaired electron located on the chlorine atom. The extreme reactivity of nanomaterials in solid-state reactions forming active charge transfer complexes with radical character has been demonstrated for various multi-center carbons to proceed under direct interaction of Cl_2.[12c,4,5,7] A control ESR measurement using $C_{60}Cl_{30}$, having all the 30 highly reactive sites already chlorine substituted,[8] showed that chlorination of C_{60} did not take place in Cl_2 atmosphere under the studied reaction conditions (Figure S2-5).
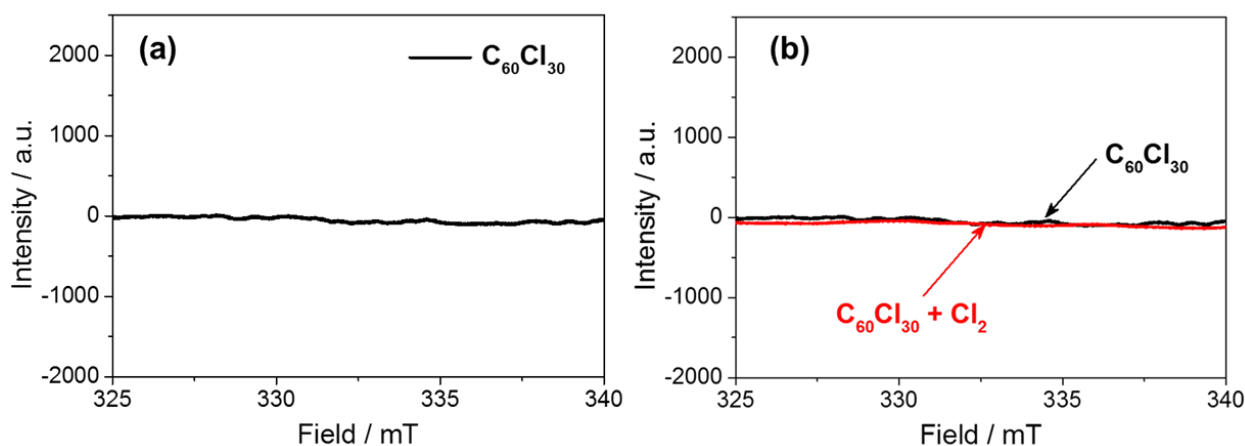
Figure S2-5. ESR spectra of $C_{60}Cl_{30}$ contacted with Cl_2 at 40 °C.
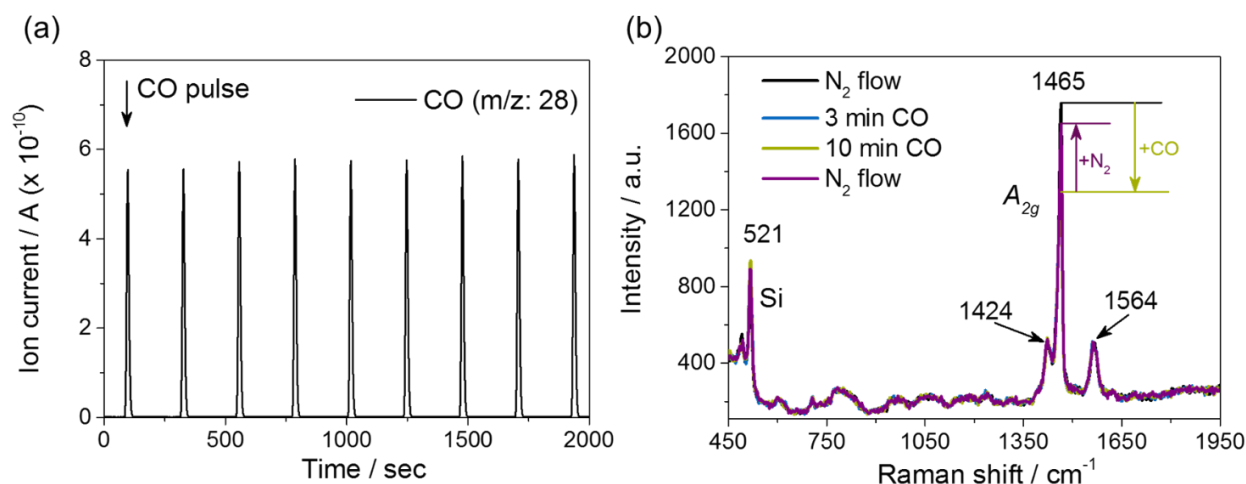
Figure S2-6. CO pulses to C_{60} at 200 °C indicate full reversibility of adsorption (left), while in situ Raman spectra of the CO in contact with C_{60} at 40°C indicates a minor concentration adsorbed (right).

Table S2-2: Measured rate constants (k) and activation energies for phosgene formation on selected carbon catalysts bearing active sites with different pyramidalization degrees.[a]

Catalysts	$COCl_2$ formation rate at 200 °C [μmol s^{-1} m^{-2}]	E_a[b] [kJ mol^{-1}]	Heat of Cl_2 adsorption [kJ mol^{-1}][c]	Reaction order
Activated carbon	0.036	56	43[d]	1
C_{60} fullerene	0.120	18	10	1

[a] All catalysts were activated in situ in He (10 ml / min) for 1 h at 150 °C.

[b] ± 2 kJ mol^{-1}. All the catalytic reactions were performed in a temperature range of 60 – 350 °C.

[c] ± 3 kJ mol^{-1}. All the carbon materials were activated at 150 °C for four hours prior calorimetric measurements. All the measurements were performed in the presence of 50 – 200 mg of carbon by using 0.2 – 2.7 μmol Cl_2 diluted in He at ambient temperature.

[d] In the case of irreversible Cl_2 adsorption on the most reactive sites of an activated carbon, 134 kJ mol^{-1} was detected.

Supplementary References:

[1]   Gaussian 09 Revision D.01, M. J. Frisch, G. W. Trucks, H. B. Schlegel, G. E. Scuseria, M. A. Robb, J. R. Cheeseman, G. Scalmani, V. Barone, B. Mennucci, G. A. Petersson, H. Nakatsuji, M. Caricato, X. Li, H. P. Hratchian, A. F. Izmaylov, J. Bloino, G. Zheng, J. L. Sonnenberg, M. Hada, M. Ehara, K. Toyota, R. Fukuda, J. Hasegawa, M. Ishida, T. Nakajima, Y. Honda, O. Kitao, H. Nakai, T. Vreven, J. A. Montgomery, Jr., J. E. Peralta, F. Ogliaro, M. Bearpark, J. J. Heyd, E. Brothers, K. N. Kudin, V. N. Staroverov, R. Kobayashi, J. Normand, K. Raghavachari, A. Rendell, J. C. Burant, S. S. Iyengar, J. Tomasi, M. Cossi, N. Rega, N. J. Millam, M. Klene, J. E. Knox, J. B. Cross, V. Bakken, C. Adamo, J. Jaramillo, R. Gomperts, R. E. Stratmann, O. Yazyev, A. J. Austin, R. Cammi, C. Pomelli, J. W. Ochterski, R. L. Martin, K. Morokuma, V. G. Zakrzewski, G. A. Voth, P. Salvador, J. J. Dannenberg, S. Dapprich, A. D. Daniels, Ö. Farkas, J. B. Foresman, J. V. Ortiz, J. Cioslowski and D. J. Fox, Gaussian, Inc., Wallingford CT, **2009.**

[2]   (a) R. S. Lee, H. J. Kim, J. E. Fischer, A. Thess, R. E. Smalley, *Nature*, **1997**, *388*, 255; (b) R. Voggu, C. S. Rout, A. D. Franklin, T. S. Fisher, C. N. R. Rao, *J. Phys. Chem. C*, **2008**, *112*, 13053.

[3]   (a) W. Schneider; W. Diller, *Phosgene*, Ullmann's Encyclopedia of Industrial Chemistry, Weinheim: Wiley- VCH, **2005**; (b) K. L. Dunlap, *Phosgene*, Kirk-Othmer Encyclopedia of Chemical Technology, **2010**, 1; (c) T. A. Ryan, E. A. Seddon, K. R. Seddon, C. Ryan, *Top. Inorg. Gen. Chem.* **1996**, *24*, 3.

[4]   M. S. Dresselhaus, G. Dresselhaus, P. C. Eklund, *Science of Fullerenes and Carbon Nanotubes: Their Properties and Applications.* Elsevier Science (USA), **1996**.

[5]   (a) A. A. Fedorov, *Russ. J. Appl. Chem.* **1997**, *70*, 44; (b) S. I. Koltsov, E. P. Smirnov, V. B. Aleskovskii, *Zhurnal Obsshchei Khimii* **1973**, *8*, 1643.

[6]   Y. A. Serguchev, G. A. Stetsyuk, V. V. Strelko, E. I. Tomilenko, *Theor. Exp. Chem.* **1996**, *32*, 313.

[7]   B. E. Shenfel'd, A. D. Belozovskii, A. N. Ketov, A. A. Fedorov, *Izv. Vyssh. Uchebn. Zaved., Khim. Tekhnol.* **1972**, *15*, 1563.

[8]   D. S. V. Muthu, M. N. Shashikala, A. K. Sood, R. Seshadri, C. N. R. Rao, *Chem. Phys. Lett.* **1994**, *217*, 146.

[9]   S. Filippone, N. Martin, *Encyclopedia of Polymeric Nanomaterials*, Springer-Verlag Berlin Heidelberg, **2014**, 1.

Chapter 3

Onion-like graphene carbon nanospheres as stable catalysts for CO and CH$_4$ chlorination

Abstract

Thermal treatment induces a modification in the nanostructure of carbon nanospheres generating ordered hemi fullerene-type graphene shells arranged in a concentric onion-type structure, which catalytic reactivity is studied in comparison with that of the parent carbon material. The change in the surface reactivity induced by the transformation of the nanostructure, characterized by TEM, XRD, XPS, Raman and porosity measurements, is investigated by multi-pulses of Cl$_2$ in inert gas or in the presence of CH$_4$ or CO. The strained C-C bonds (sp^2-type) in the hemi fullerene-type graphene shells induce unusually strong, but reversible, chemisorption of Cl$_2$ in molecular form. This is the active species in CH$_4$ and CO chlorination, probably in the radical-like form. Highly strained C-C bonds in parent carbon materials instead reacts irreversibly with Cl$_2$, inhibiting further reaction with CO. In addition, the higher presence of sp^3-type defect sites promotes the formation of HCl with deactivation of the reactive C-C sites. The nano-ordering of the hemi fullerene-type graphene thus reduces the presence of defects and transforms strained C-C bonds, giving irreversible chemisorption of Cl$_2$ to catalytic sites able to perform selective chlorination.

3 Onion-like graphene carbon nanospheres as stable catalysts for CO and CH₄ chlorination

3.1 Introduction

Carbon has been widely used as support for metal nanoparticles, particularly for hydrogenation reactions,[1] but recently the possibility to use it directly as catalyst is emerging as an interesting option.[2-4] The catalytic performances of carbon materials depend on their nanoscale structure[5-7] as well as on the presence of functional groups, both aspects reliant on preparation, doping and functionalization.[2,3] Significant advances have been made recently in this direction on nanocarbon materials such as carbon nanotubes (CNT), graphene, fullerene and other type of nanocarbon catalysts (-fibers, -coils, -horns, -etc.).[8,9] However, onion-type carbon materials, for their intrinsic more complex structure and presence of different type of sites, remain still less understood, notwithstanding the relevant progresses in this area.[10] Critical aspects to be further analyzed regard the role of nano-ordering and the formation of fullerene-type nano-structures. Thermal annealing allows to increase the degree of ordering (graphitization) and it may be possible to create fullerene-type nano-structures, depending on the nature of the starting carbon.

While the research on the catalytic properties of nanocarbon materials such as CNT, graphene etc. is exponentially increasing,[11-16] the catalytic use of onion-type carbon materials is largely unexplored. The materials may be visualized as hemi fullerene-type graphene shells arranged in a concentric onion-type layered structure.[11] It is known that the strain of C-C (sp^2-type) bonds may activate their reactivity due to the curvature present in these nanostructures, enabling coordination and activation of reactants ranging from O_2 to Cl_2.[3,11] They thus have in principle interesting catalytic properties, which may be tuned by nano-ordering and suitable control of the parent amorphous carbon material, which in contrast, does frequently not show such a type of catalytic properties.[17]

In general, the unique catalytic features of nanocarbons derive from their atomic arrangement, i.e., linear, trigonal, planar or tetrahedral geometries,[18] and the presence of sp, sp^2, and sp^3 hybridized carbon bonds.[19,20] In addition, the presence of surface strains, point defects, dangling bonds, curvatures etc. further enhance the catalytic performance.[21,22] Onion-like structure combines several of these features,[23-26] making it difficult identifying and characterizing the specific sites responsible for a particular catalytic behavior. It was suggested that the "surface roughness" influences the reactivity of onion-like carbon materials, facilitating

redox reaction and desorption of reaction products, but without providing more precise indications.[24,27,28]

The presence of curvature and strains in C-C bonds may activate adsorbed reactants decreasing the activation energy, but it is not disclosed whether the activation leads to irreversible chemisorption or is effective in promoting catalytic reactions. It may be expected that the nano-ordering induced by thermal treatment of carbon materials, which are precursors of surface nano-onion-type structures, can thus provide an useful approach to understand better this question, and at the same time a good way to create specific catalytic sites. In presence of disordered nanostructures, carbon is more reactive at the edges, showing lower bond energies (ca. 7 kcal/mol), but mainly giving rise to irreversible reactions with adsorbed reactants. More ordered carbon nanostructures will have a larger energy barrier for chemisorption, although would allow in principle to transform sites giving stoichiometric chemisorption into catalytic ones.[2]

It has to be remarked that the catalytic behavior of strained C-C (sp^2-type) bonds is still largely unexplored. In nanocarbons materials such as graphene and CNTs, which have been extensively studied from the catalytic perspective,[3] the reactive sites are associated essentially to edges or defects. Fullerenes, due to curvature of C-C sp^2-type bonds, are known to readily react with various biatomic molecules, but in a stoichiometric way only.[11] The possibility of utilization of these reactive sites for the catalytic activation of small biatomic molecules is thus highly challenging. Nano-onion-type carbon materials have the double feature of high presence of strained C-C sites, but also to allow the tuning of their characteristics. From the catalytic perspective, therefore, these materials have the potential of being of high interest, especially when combined with a low-cost preparation method as that used here.

As reaction to probe the surface chemistry, the catalytic activation of Cl_2 is used. The reaction is relevant to understand the utilization of these catalysts in chlorination reactions, e.g., synthesis of chloroform from methane or the synthesis of phosgene from CO, two structure-dependent reactions realized on large scale (about 5-6 Mtons/y).[29,30] Phosgene is produced industrially by catalytic chlorination of CO, a strongly exothermic reaction.[31-33] The formation of by-products (hydrochloric acid, and carbon tetrachloride[34]) depends strongly on the type of activated carbon catalysts used in the process. In fact, the extensive chlorination of the carbon material leads to weakening of the carbon-carbon bond and the formation of gas-phase chlorination products, with a concomitant loss of catalyst material and decrease of the available active sites. The gas phase chlorinated hydrocarbons can further polymerize in the gas-phase and form high-molecular by-products, which re-adsorb on the surface and deactivate the

catalyst by blocking the active sites. Therefore, carbon properties have to be optimized to minimize both HCl and CCl_4 formation, as well as irreversible chlorine adsorption, while maintaining a rate of phosgene synthesis as high as possible.[35,36] While the reaction of graphene-type materials with chlorine atoms has been previously reported,[37-40] results on the uptake rather than on the catalytic behavior have not been shown. In addition, the dependence of these properties on the nanostructure is unclear.

The selective synthesis of halogenated compounds from CH_4 over carbon catalysts helps to understand the radical chemistry of Cl_2. It should be noted that large interest on the conversion of methane to olefins and gasoline *via* mono halogen-alkanes exists, as alternative route to methanol conversion.[41-45] Carbon materials offer an interesting alternative to metal oxides, which may form volatile halogenides[46] and have problems of long-term stability related to volatility of $MeCl_x$ species.

In previous works[47,48] we showed a method to obtain carbon nanospheres characterized by stacks of sp^2 graphene-like nanosheets starting from an amorphous carbon obtained by controlled pyrolysis of glucose. These materials showed an onion-like carbon structure, i.e., spherical closed carbon graphene shells arranged in a concentric layered structure, resembling that of an onion.[49-51] Following the acronym suggested by Zhang et al.[52] we indicated these materials here as onion-like carbon nanospheres (OCNSs). The resulting material shows high surface area and a structural order in the stacking of the graphitic layers. These results evidence the possibility to prepare different type of nanostructure of sp^2-sp^3 mixed carbon system, having different degree of nano-ordering. The aim of this work is to compare two carbon nanomaterials with analogous nanostructure, but different degree of ordering, in the reaction with Cl_2, CO and CH_4. The combined experiments help to understand how the local nanostructures influence the surface reactivity.

3.2   Experimental

3.2.1 Experimental set-up and safety issues

One major advantage of the experimental setup designed for Cl_2 activation studies is the possibility to use minimal amounts of toxic and corrosive gases. A six-port valve connected to an on-line mass spectrometer (MS) was used for the automated dosage of Cl_2. All the gaseous residues were neutralized in two interconnected concentrated KOH and Cu^{2+} solution

containing bottles. An active carbon containing filter finally accounts for the retention of any generated toxic gaseous intermediate left.

Special attention was paid to the safety issues. Two different types of Cl_2 and CO detectors were placed under the fume hood to constantly monitor the Cl_2 and CO concentration at the working place. To avoid contamination with CO, two additional filters for CO entrapment were installed at the outlet of the six-port valve and of the reactor. The maximum amount of $COCl_2$ which could theoretically be formed in the pulse reactor (0.025 ppm) is lower than the permissible exposure limit (0.1 ppm averaged over a work shift of up to 10 hours a day, 40 hours per week with a ceiling level of 0.2 ppm averaged over a 15 min period).

3.2.2 Material syntheses

Powder carbon synthesis. Sample hereinafter indicated as CHT was obtained by dissolution of pure glucose in distilled water (180 mL) to form a clear solution, and placed in a Teflon-lined autoclave at 200°C for 20 h. The product was then separated by filtration, washed several times with hot water, acetone, and ethanol. Then it was dried at 100°C and further treated at 200°C for 2 h. The quantitative yield was about 20 wt.%.

Thermal annealing procedure. For each thermal annealing procedure, an amount of sample (ca. 200 mg) was placed in a vertical fixed bed reactor. The sample underwent to graphitization at an annealing temperature of 1000°C for 6 h under a bottom-up N_2 gas flow (100 STP mL/min). This sample is named CHT-tr.

3.2.3 Activity tests

Multipulse experiments were carried out to investigate the interactions of carbon materials with Cl_2 and to identify the transiently formed intermediates when reacting with CO and CH_4. All gaseous residues were neutralized in two interconnected concentrated KOH and Cu^{2+} solution containing bottles. An active carbon-containing filter finally accounts for the retention of any generated toxic gaseous intermediate left. Two different types of Cl_2 and CO detectors were placed under the fume hood to monitor constantly the Cl_2 and CO concentration. Two additional filters for CO entrapment were installed at the outlet of the six-port valve and of the reactor. The maximum amount of $COCl_2$ which could theoretically be formed in the pulse reactor (0.025 ppm) is lower than the permissible exposure limit (0.1 ppm averaged over a work shift of up to

10 hours a day, 40 hours per week with a maximum level of 0.2 ppm averaged over a 15 min period).

For each experiment, the solid carbon material (10 mg, particle size ≤ 80 μm) packed in a quartz reactor (0.4 cm ID) was activated in He flow (10 mL/min) at 150°C for 1h prior to catalysis. The schematic representation of the experimental setup constructed for the Cl_2 activation study is shown in supporting material, Figure S3-2. Multiple Cl_2 pulses (3.6 μmol Cl_2/pulse, pulses length 230 s) were performed in order to understand the catalytic activation of Cl_2 on the multiple active sites in the selected carbons. To probe the nature of activated Cl_2 species in separate experiments, 5 % CO and CH_4 in He carrier (flow rate 10 mL/min) were exposed to the Cl containing carbon sample. All the gaseous products were analyzed by on-line mass spectrometry (PFEIFFER OMNIstar/TM mass-spectrometer, QMS 200). For the identification of the surface bound species, temperature-programmed desorption (TPD) was performed until 800°C with a temperature increment of 5°C/min in He flow (flow rate 10 mL/min).

3.3   Carbon characterization

Carbon morphology structure was investigated by transmission electron microscopy (TEM) using a Philips CM12 microscope (resolution 0.2 nm) equipped with a high-resolution camera, at an accelerating voltage of 120 kV. Suitable specimens for TEM analyses were prepared by ultrasonic dispersion in *i*-propyl alcohol adding a drop of the resulting suspension onto a holey carbon supported grid.

Samples were characterized by X-ray powder diffraction (XRD) using a Philips X-Pert diffractometer with a monochromatic CuKα (λ = 1.54056 Å) radiation at 40 kV and 30 mA. Data were collected over a 2θ range of 10-100 degrees, with a step size of 0.04° at a time per step of 3s. The graphitization degree of onion-like carbon nanospheres was quantitatively determined by using LiF as a standard material (in a ratio from 1 to 5). For quantification, the peak area and the intensity were used and analyzed comparatively to the standard sample. Results are presented in Table 3-1 and shown in Figure S3-1.

The specific surface areas were calculated using the Brunauer Emmett Teller (BET) equation from the adsorption branch of the isotherms, obtained at -196 °C on a Quantachrome sorption

analyser. Prior to the measurements, samples were heated in N_2 flow at 350°C for 1h1h. The micropore volume was evaluated by t-plot method.

X-ray Photoelectron Spectroscopy (XPS) data were measured using a Physical Electronics GMBH PHI 5800-01 spectrometer operating with a monochromatized Al-K_α radiation with a power beam of 300W. The pass energy for determination of the oxidation state and concentration of surface species was 11.0 eV and 58.0 eV, respectively. The BE regions of C_{1s} (280-300 eV) and O_{1s} (524-544 eV) were investigated, taking the Al_{2p} line (73.0 eV) of aluminum standard as reference for signal calibration. Ar^+ 2 kW voltage small beam sputtering was performed in order to remove adventurous carbon.

Raman spectra at 514 nm (2.41 eV, Ar^+ laser) were recorded with a Renishaw (Series 1000) spectrometer equipped with a 50x objective. All Raman spectra were obtained following the thermal activation of the carbon materials under inert conditions at 150°C for 1h. After Cl_2 treatment further measurements under inert conditions (in N_2 flow) were performed. For in situ Raman measurements a temperature regulated quartz reactor (1.62 mm ID) was used.

3.4   Results and discussions

3.4.1 Physicochemical characterization

TEM micrographs of CHT and CHT-tr samples are shown in Figure 3-1. It should be remarked that similar samples have been also earlier studied by us.[47] Although the samples reported here were prepared again choosing optimized conditions, the results are quite similar, confirming the reproducibility of the preparation. The hydrothermal procedure used to prepare CHT sample gives rise to a uniform distribution of spherical-shaped carbon nanoparticles, with an average main diameter in the 200-400 nm range. After thermal annealing, the spherical shape and morphology is almost retained, although a different degree of ordering is noted by TEM characterization (Figure 3-1).
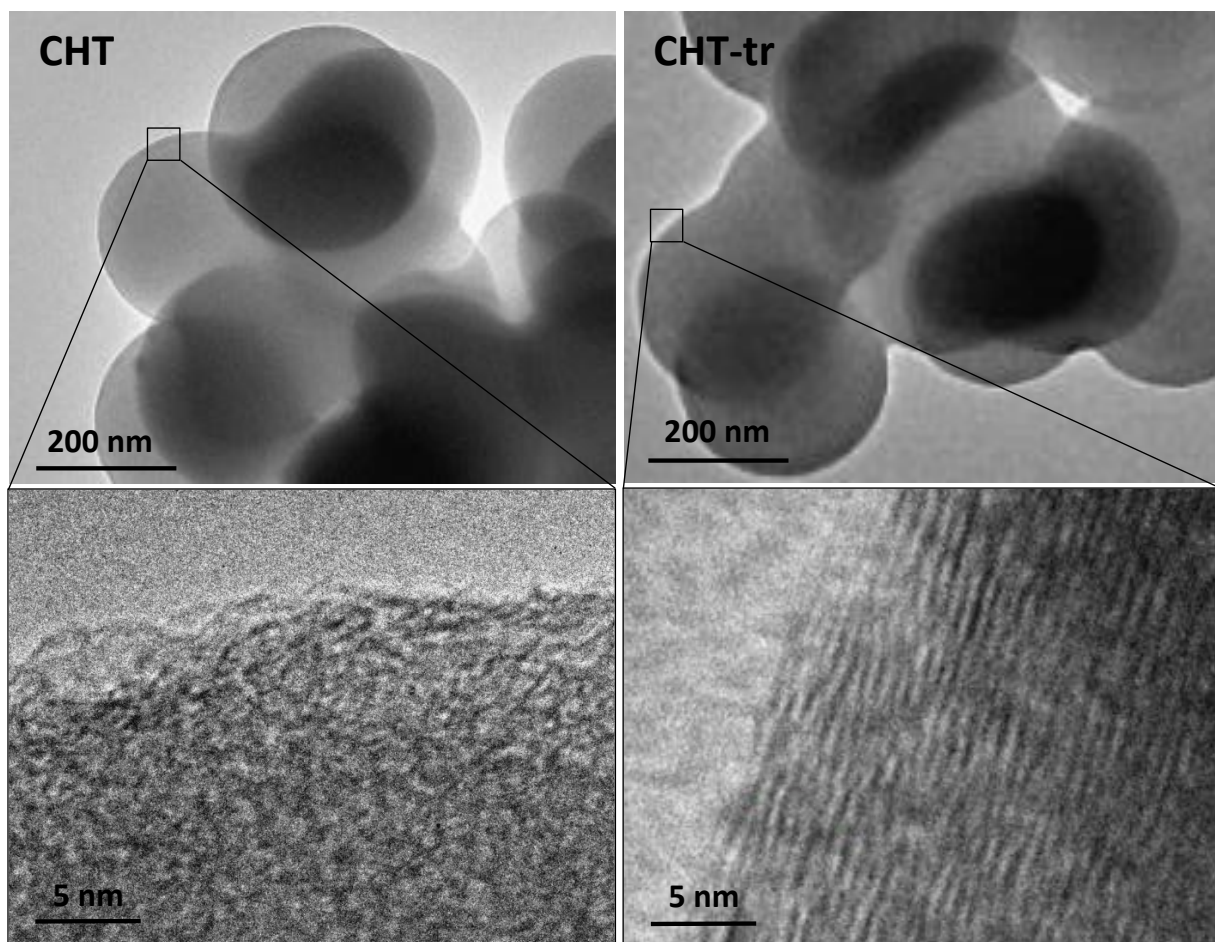
Figure 3-1. TEM images of CHT and CHT-tr catalysts at different magnifications.

CHT-tr shows the presence of graphitic like structure, with a characteristic nano-onion rearrangement, initiating at the surface and propagating inside the nanoparticles, forming concentric shells of C sp^2-bonded atoms from the spherical or cylindrical shape of the original amorphous precursor.

Table 3-1 reports the crystallographic parameters determined by XRD patterns for CHT and CHT-tr samples.

Table 3-1. Crystallographic parameters (from XRD measurements) of CHT and CHT-tr (see text for description).

Sample	d_{002}(nm)	L_a(nm)	L_c(nm)	L	G_I (LiF as reference)	relative G_I (100% for CHT-tr)
CHT	0.376	-	0.79	-	5.5	27,3
CHT-tr	0.349	4.5	1.04	0.34	20.1	100

The calculated d_{002} spacing for CHT-tr was 0.349 nm, suggesting the formation of quasi-ordered graphitic layer, although with larger interlayer spacing (as reference, d_{002} for graphite is 0.335).This d_{002} value is instead significantly larger in CHT sample, due to the presence of a highly disorganized situation. In CHT the (110) reflection is so weak, that does not allow estimating L_a, and as consequence, L. The L_c value indicates the presence of some ordering along this crystallographic direction, but not in the orthogonal direction, as expected from a disordered organization, characteristic for the precursor of an onion-type nanostructure. This indication is well in agreement with the TEM data (Figure 3-1).

The textural characteristics of the CHT and CHT-tr samples have been determined by nitrogen sorption isotherms (Table 3-2).

Table 3-2. Textural properties of the samples: surface area determined by BET and Langmuir methods, area of the micropores (by t-plot method), total pore volume and volume of micropores (also by t-plot method).

Sample	S.A.$_{BET}$ – S.A.$_{Lang}$ (m^2/g$_{cat}$)	Micropore Area* (m^2/g$_{cat}$)	Tot. P.V. (cm^3/g$_{cat}$)	Micropore vol.* (cm^3/g$_{cat}$)
CHT	635-840	503	0.31	0.23
CHT-tr	585-770	550	0.26	0.25

* determined by t-plot method

The CHT sample has a very high surface area (about 640 m^2/g$_{cat}$) with a major contribution of the micropore fraction (about 500 m^2/g$_{cat}$). Upon annealing in N$_2$ at 1000 °C for 6 h, there is a decrease both in S.A. and pore volume (-20% and -16%, respectively), with a corresponding increase in the microporosity (about 10%). This increase in microporosity after annealing is surprising, because typically microporosity decreases. An explanation could be the presence of hydrocarbon impurities in the carbon micropores, filling them and making not accessible during the determination of the microporosity. The desorption of these adsorbed organic species during the annealing procedure leads thus to the apparent increase of the microporosity. However, thermogravimetric (coupled with mass spectrometer analysis of the gas evolution) and FTIR data on similar samples[47] also showing an increase of the microporosity after annealing, excluded that the increase of microporosity is related to desorption of the organic species present in the carbon micropores. Therefore, we may conclude that the effect is related to a

structural reorganization, which is consistent with the TEM and XRD results and previous literature indications.[53-56]

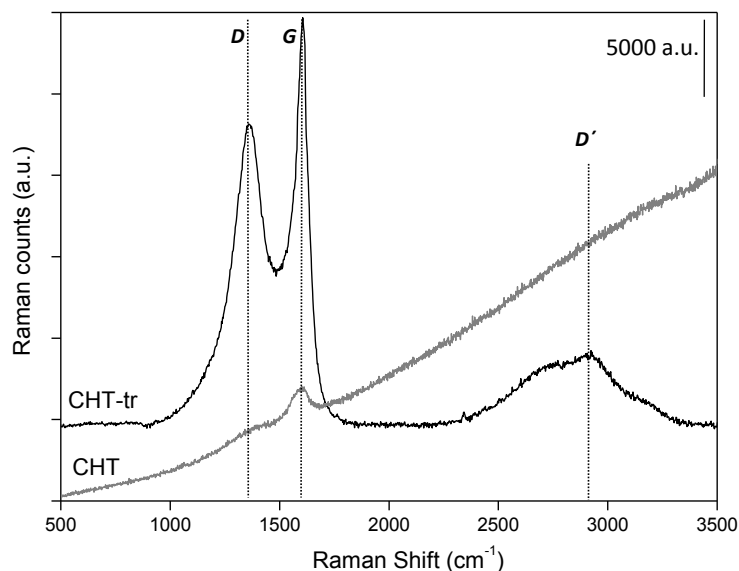Raman spectroscopy illustrates further the differences between CHT and CHT-tr samples (Figure 3-2).

Figure 3-2. Raman spectra of CHT and CHT-tr.

CHT shows a broad fluorescence background. This could be due to the presence of organic impurities and/or surface defects. Thermogravimetric data cited above indicate the absence of significant organic adsorbed species, but do not allow to exclude the presence of traces of adsorbed species, enough to give the fluorescence effect. However, likely the fluorescence is related to the strongly defective situation, as indicated by TEM data. It is known that strong fluorescence originates in nanocarbon materials from the electronic transitions among/between the non-oxidized carbon regions and the boundary of oxidized carbon atom regions, where different functionalized groups C-O, C=O and O=C-OH are present.[57] This is well in agreement with the indication by EDS that the amount of oxygen in CHT is about 10%.

Raman spectrum of CHT-tr exhibits two main bands at 1586 and 1344 cm^{-1}, respectively. These bands are also present in the CHT sample, but are broader and weaker. The G (1580-1600 cm^{-1}) and the D (1350 cm^{-1}) peaks are usually assigned to zone center phonons of E_{2g} symmetry and K-point phonons of A_{1g} symmetry, respectively. They can be attributed to many forms of sp^2-bonded carbons with various degrees of graphitic ordering, ranging from microcrystalline graphite to amorphous carbon.[5] While the G peak involves the in-plane bond-stretching motion of pairs of all sp^2 sites (not necessarily only those arranged in six fold rings), the D peak is

forbidden in perfect graphite and becomes active in presence of more disordered structure.[54-56] The intensity ratio between these two bands (I_D/I_G) is usually indicative of the relative degree of disorder.[53] In case of CHT-tr, the I_D/I_G is equal to 0.77. According to the Tuinstra and Koenig equation:[58]

[3-1]
$$\frac{I_D}{I_G} = \frac{c(\lambda)}{L\alpha}$$

a correlation between I_D/I_G ratio and L_a value obtained from XRD measurement exists. In our case, values lies within the range where I_D/I_G is proportional to $1/L_a$, i.e, analogous to the case of graphite or nanocrystalline graphite with uniform crystallization (see S3-3 and Table S3-1).[53,59] It should be noted that some authors argued that the absolute intensity of the G-band may be a more suitable quality parameter than the D/G ratio.[60,61] However, this estimation requires a more complex procedure, for example, measuring the G-band intensity of liquid suspensions of SWCNT samples as a function of solid concentration.[61] This procedure is necessary to quantify the purity of SWCNT, but is not necessary to have an indication on the degree of disorder, as in our case.

The presence of oxygen functionalities in CHT and CHT-tr was analyzed by XPS measurements of C_{1s} and O_{1s} signals. The C_{1s} spectra of CHT and CHT-tr are shown in Figure 3-3a.
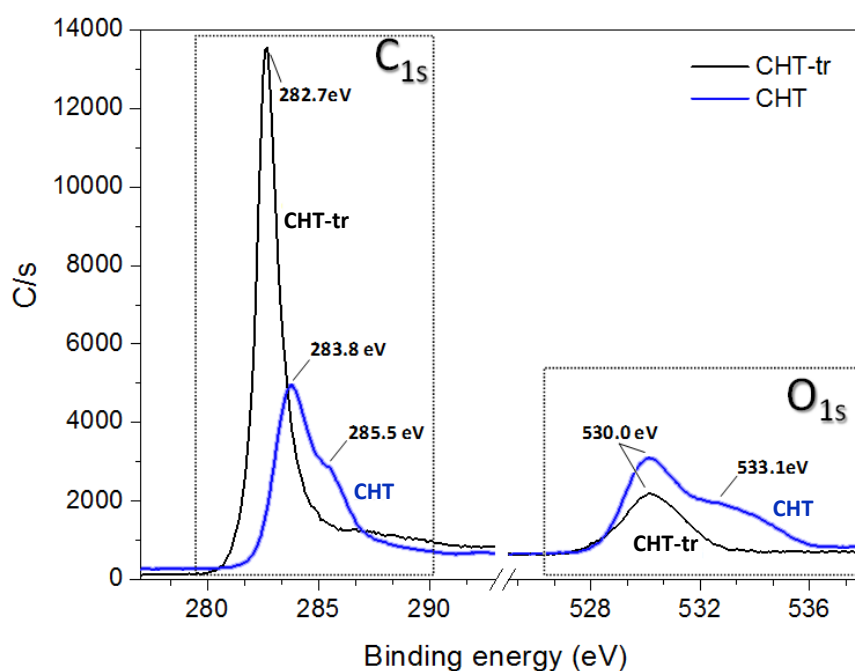

Figure 3-3. XPS of C_{1s} and O_{1s} for CHT and CHT-tr.

CHT shows a right shoulder in comparison with the sharp and symmetric graphitic C_{1s} peak present in CHT-tr reasonably due to the removal of functional C-OH, C=O and COOH groups[62] during the annealing process. The main C_{1s} peak shifts from about 283.8eV in CHT to 282.7 eV in CHT-tr which is consistent with the change from a prevalent sp^3 to a sp^2 configuration after thermal annealing.[59] The transformation during annealing process is confirmed by the analysis of the O_{1s} region (Figure 3-3b), presenting a main peak centered at 530.03 eV with a right shoulder centered at about 533 eV which disappears after thermal annealing. This shoulder position is consistent with that expected for -COOH type surface species, while that at around 530 eV is typical for quinones and C=O species, which are known to be thermally more stable than -COOH type oxygen functional groups present in carbon materials.[63]

3.4.2 Catalytic reactivity

Cl_2 reversible and irreversible uptake by CHT and CHT-tr

The surface reactivity of CHT and CHT-tr towards Cl_2 was studied by sequential multipulse method at 200 °C. HCl was the only product observed in the reactor outlet stream, in addition to Cl_2. From the difference of Cl_2 content in the inlet and outlet streams, the amount of reacted Cl_2 can be determined. By subtracting the HCl formed, it is possible to determine then the amount of irreversible chemisorbed Cl_2. In addition, from the difference in the peak shape of the single Cl_2 peaks with respect to those observed when the catalyst is absent, an indication of the type of reversible chemisorption of Cl_2 can be deduced.

Typical profiles recorded during Cl_2 sequential pulses on CHT and CHT-tr are shown in Figure 3-4a and 3-4b, respectively.
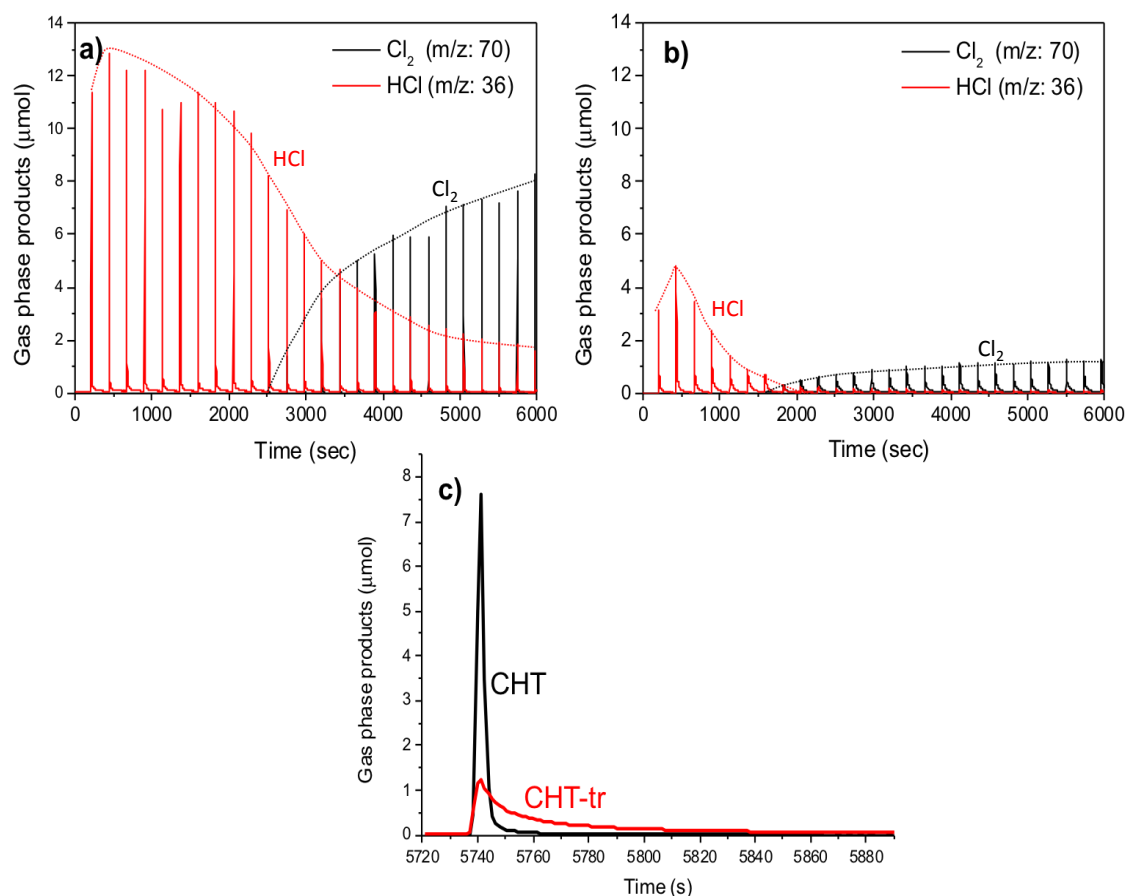
Figure 3-4. Cl_2 multi-pulse experiments on CHT (a) and CHT-tr (b) in He continuous flow. (c) Comparison of the reactor outlet Cl_2 pulses for CHT and CHT-tr. *Experimental conditions:* 30-50 Cl_2 pulses (230 s pulse length) (3.6 µmol Cl_2 / pulse), He flow: 10 ml / min, 10 mg of material, T = 200 °C.

HCl is the major product formed initially, up to about 3000s for CHT and about 1500s for CHT-tr, respectively. Cl_2 starts to be detected when the formation of HCl begins to end. However, the formation of HCl does not correspond to the total amount of converted Cl_2. From the amount of Cl_2 converted and that of HCl detected in the gas phase, the total irreversible Cl_2 uptake is calculated (Table 3-3).

Table 3-3. Cl_2 multipulse experiments on CHT and CHT-tr at 200°C in continuous He flow. Experimental error in the ±5-10% range

Sample	Irreversible Cl_2 uptake (mmol/g_{cat})	HCl formation (mmol/g_{cat})
CHT	7.36	9.70
CHT-tr	2.16	3.90

The amount of irreversible uptake of Cl_2 by CHT is three times higher than the amount calculated for CHT-tr. Similarly, HCl formation is about 2-3 times higher in CHT with respect to CHT-tr. After approximately 6000s, Cl_2 pulse intensity at reactor outlet reaches an intensity nearly corresponding to the inlet value. It should be noted that the formation of HCl requires the presence of H-donor species on carbon sites nearlying those of chlorine activation, as discussed in a more detail later.

The difference in peak shape between inlet and outlet Cl_2 pulses, as a consequence of the interaction of Cl_2 with the catalyst, provides further interesting indications. While for CHT catalyst the difference is minor and the peak remains sharp (Figure 3-4c), a relevant difference is noted for CHT-tr which shows a long tail. This indicates an unusually strong, but reversible, interaction of Cl_2 with the more ordered catalyst. Therefore, CHT-tr is characterized by a high amount of reversible adsorption of Cl_2, while CHT shows a high irreversible uptake of Cl_2 as well as higher formation of HCl.

After equilibration with Cl_2 at 200°C (e.g. after 6000s), the temperature of catalyst was increased linearly (TPD experiments) to analyze the type of surface species present of the catalyst (Figure 3-5) and their energy of interaction with the catalyst. Both CHT and CHT-tr show a very broad, structured desorption profile of HCl between 200 and 800°C.
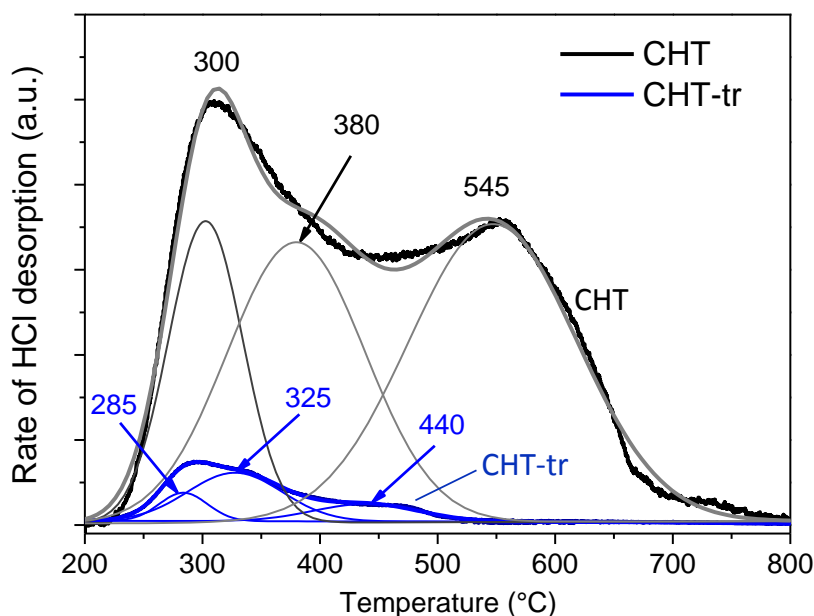

Figure 3-5. Temperature program desorption of CHT and CHT-tr after exposure to multiple pulses of Cl_2 (6000s, experimental conditions as in Figure 3-4).

The total amount of HCl (8.2 mmol/g), desorbing at three different temperatures (300 °, 380 ° and 545 °C) from CHT was about 14 times higher than in the case of CHT-tr (0.6mmol/g). For both catalysts, no other chlorinated species were detected during TPD experiments. Also CHT-tr sample shows three desorption peaks, but with maxima shifted to lower temperatures (285°, 325° and 440°C) and the peak relative to intermediate temperature becoming the more intense. These results confirm that thermal treatment not only induces a strong decrease of the sites responsible for HCl chemisorption, but also a slightly change in their nature.

However, it may be argued whether the three peaks correspond to three types of chemisorbed HCl species, with different energy of interaction with the surface sites or a different interpretation is possible. It may be anticipated part of discussion made more extensive later, that HCl derives from the reaction of Cl atoms produced by dissociative chemisorption of Cl_2 and H-donor sites, related to defective sp^3-type C atoms. When these site are nearlying to a Cl atom coordinated to carbon, desorption of HCl may occur. Otherwise, it may be necessary a surface migration of hydrogen atoms to the carbon atom coordinating Cl, and then HCl may form and desorbs. The three observed peaks for HCl desorption in TPD experiments after multipulse of Cl_2 (Figure 3-5) may be thus alternatively interpreted as deriving from three different energy paths necessary for surface diffusion of the hydrogen to reach the carbon atom coordinating Cl. It should be also recalled that neither on CHT or CHT-tr samples desorption of Cl_2 is detected during TPD experiments. Therefore, all chemisorbed (intact) Cl_2 desorbs reversibly at 200°C (even if peak shape analysis discussed before evidences the presence of a strong chemisorption on CHT-tr), while dissociative chemisorbed Cl_2 requires higher temperatures for the desorption, explaining also why may lead to progressive catalyst deactivation.

The structural changes on the active sites of CHT-tr caused by Cl_2 treatment were monitored by in situ Raman spectroscopy.
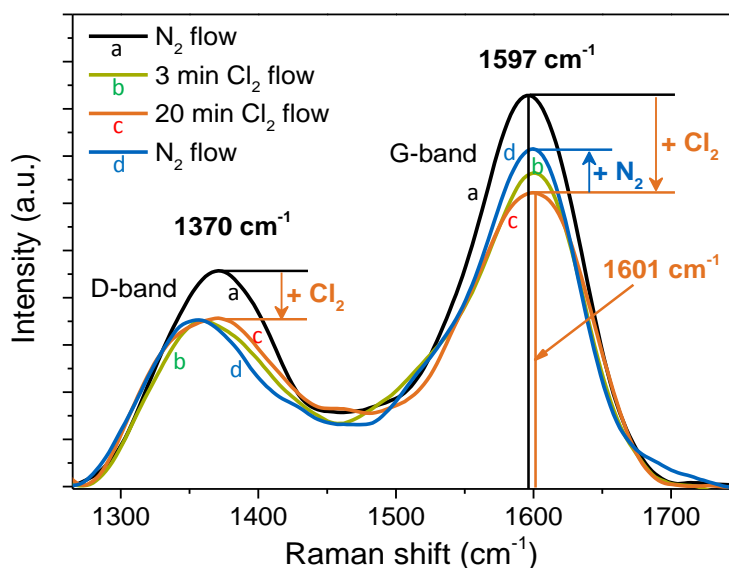
Figure 3-6. In situ Raman spectra of CHT-tr contacted with Cl_2 at 40°C.

Raman spectra recorded during the interaction of Cl_2 with CHT-tr (Figure 3-6) show that after short time of Cl_2 exposure (3 min) both **D** and **G** bands decreased in intensity, indicating a marked interaction of sp^3 and sp^2 hybridized carbons with adsorbed Cl_2. On increasing the time of exposure, the **D** band does not change further, whilst the **G** band intensity continued to decrease. Replacing the Cl_2 stream with N_2, the **D** band intensity is not affected, while the **G** band recovered part of the intensity, indicating the reversibility of the adsorption processes on Cl_2 in CHR-tr, according to the results reported in Figure 3-4. As commented before, the D-band is a second-order Raman scattering process that is enhanced by the presence of defects, while the G band involves the in-plane bond-stretching motion of pairs of all sp^2 sites. These in-situ Raman results thus indicate that defect sites (sp^3 like) irreversibly interact with Cl_2, while C-C bonds (sp^2 type) can give reversible chemisorption of Cl_2. However, pure graphene does not interacts with Cl_2 (excpect at the edges) neither is active in phosgene generation, and highly strained C-C bonds as in fullerene give only irreversible dissociative chemisorption.[64,65]

Reactivity of the surface chlorine species

The reactivity of surface chlorine species in the two catalysts was studied by multipulse Cl_2 experiments in the presence of a continuous flow of He-CO (5 vol. % CO) or He-CH_4 (5 vol. % CH_4).

CO as a probe molecule

The reactivity of chemisorbed chlorine species towards CO is investigated by sending pulses of Cl_2 while continuously feeding a mixture of 5 vol. % CO in He over the catalyst. The results for CHT and CHT-tr catalysts are reported in Figure 3-7.
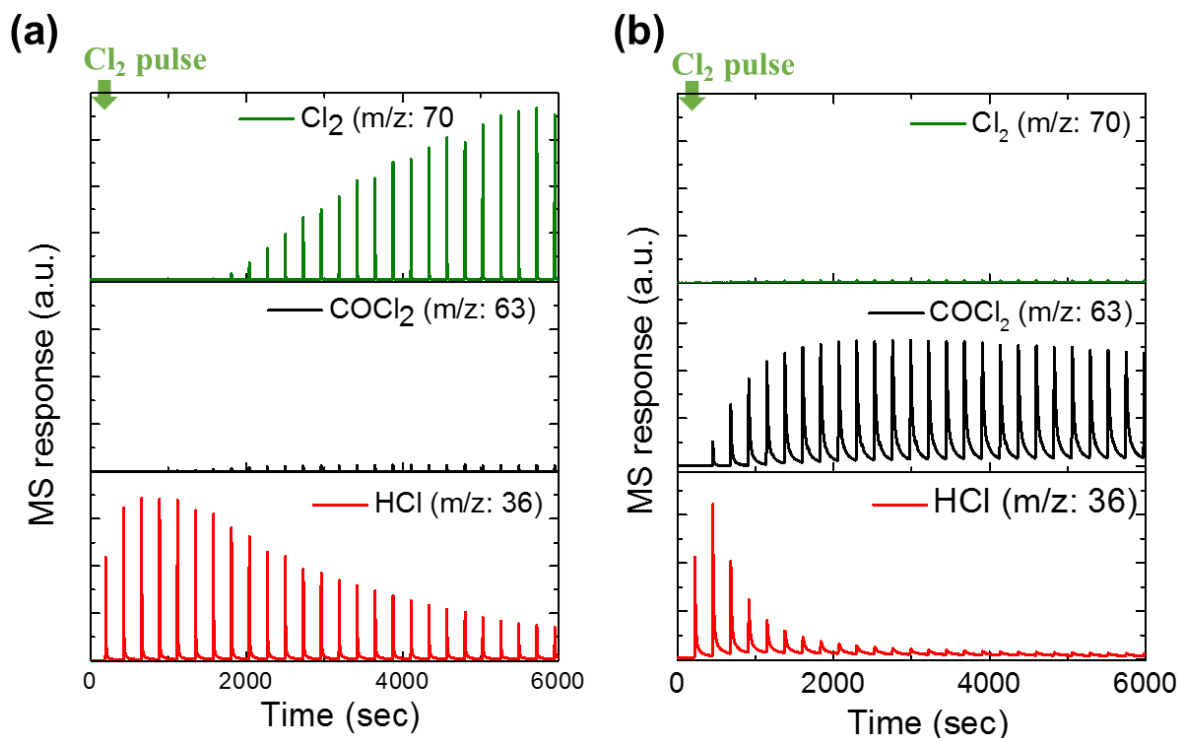

Figure 3-7. Cl_2 multipulse tests at 200°C on CHT (a) and CHT-tr (b) in He-CO (5 vol. % CO) continuous flow. *Experimental conditions* as in Figure 3-4.

Differences can be observed with respect to the equivalent tests, but feeding continuously only an inert gas over the catalyst (Figure 3-4). Cl_2 starts to be detected in the reactor stream after about 2000s for CHT, but is not detected for CHT-tr, differently from the case without CO. The irreversible Cl_2 uptake was estimated to be 10.5 mmol/g and 3.7 mmol/g for CHT and CHT-tr, respectively. These values are slightly higher of those measured in the absence of CO (Table 3-3), although the difference is not considered relevant and within an experimental error which can be estimated in the ±5-10% range. In fact, the ratio of the irreversible Cl_2 adsorption of CHT with respect to that of CHT-tr remained nearly constant, e.g. around threefold. We may conclude that the concentration of irreversibly adsorbed Cl_2 remains nearly identical in presence and absence of CO indicating that the reaction of the irreversible chlorine chemisorbed species with CO does not occur.

While $COCl_2$ does not form on CHT catalyst, a significant formation of $COCl_2$ is detected using CHT-tr catalyst. There is an initial delay in $COCl_2$ formation, which starts when HCl formation

ends on CHT-tr. On the contrary, much larger HCl formation is detected over all the time frame investigated over CHT. Note that the formation of HCl passes through a maximum for both catalysts, suggesting that the mechanism of formation of HCl involves first the dissociative chemisorption of Cl_2 and then the reaction of the formed species with the H-donor species, thus generating HCl. Note also that TPD experiments allowed to exclude the presence of chemisorbed water or hydrocarbons over the catalysts surface, and therefore these H-donor species are necessarily those associated to sites present on the catalyst.

The conversion of Cl_2 and formation of $COCl_2$ on the CHT and CHT-tr catalysis and the relative graphitization index (G_I), i.e. the graphitic degree in respect to CHT-tr sample (which has been put equal to 100%), are summarized in Figure 3-8.
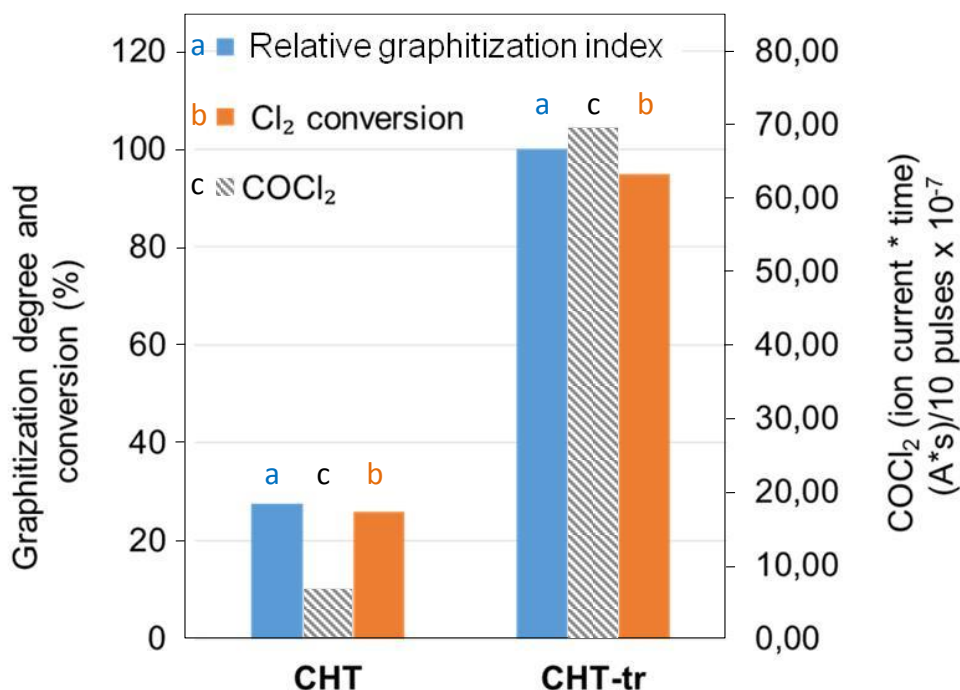

Figure 3-8. Relationship between graphitization degree, Cl_2 conversion and $COCl_2$ formation on CHT and CHT-tr.

The latter index characterizes the transition from sp^3 to sp^2 carbon and the formation of the onion-like structure.

CH$_4$ as a probe molecule

In order to explore the radical nature of chemisorbed chlorine species, their reactivity with CH_4 was investigated over a CHT-tr sample and in an empty reactor, as reference. The results obtained are summarized in Figure 3-9.
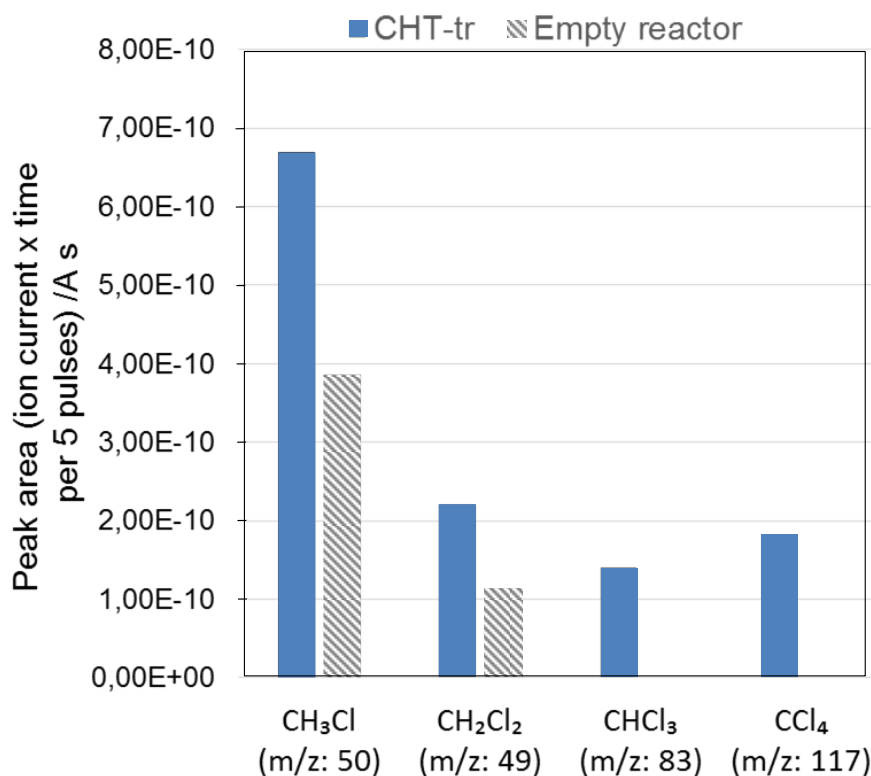
Figure 3-9. Total amount of CH_3Cl, CH_2Cl_2, $CHCl_3$ and CCl_4 formed in 6000s during Cl_2 multipulse experiments at 200°C on empty reactor and in presence of CHT-tr under continuous He-CH_4 (5 vol. % CH_4) flow. *Experimental conditions* as in Figure 3-4.

The reaction, known to occur with radical-type chlorine species,[66] was conducted at 200 °C pulsing Cl_2 in a continuous flow of He and CH_4 (5vol%), and in dark conditions (light may promote the halogenation). Halogenated methane species, i.e., CH_3Cl, CH_2Cl_2, $CHCl_3$ and CCl_4, are the products of reaction, with a distribution consistent with the presence of radical-type chlorine species on the surface of the catalyst. These products were also observed without the catalyst (empty reactor), albeit in minor amounts, and were considered in the evaluation of the catalyzed reaction. The fact that the distribution of the products, however, does not significantly change in the tests with and without the catalyst is in accordance with the radical-type mechanism and proves that the onion-type catalyst was active in producing chlorine-radicals, which reacted with methane to give chloromethanes with a distribution in agreement with that expected for radical-type reactions.

3.4.3 Nature of the reactive sites

Overall, spectroscopic, structural characterization and kinetic measurements show that the thermal treatment creates an unique carbonaceous species, a nanoscopically defined hemi-fullerene-type structure. The combination of the layered carbon structure and the specific bending of the hemisphere create highly active sp^2 hybridized carbon atoms, which are suggested to be the site responsible of Cl_2 reversible activation. Carbon terminating defects (sp^3 hybridized) are instead responsible for irreversible chemisorption, similarly to highly strained C-C bonds. Raman in-situ experiments (Figure 3-3 to 3-6) well support this conclusion, while tests with methane as probe molecule suggests a radical-like character of this reversible chemisorbed (undissociated) Cl_2 species.

The results reported in Figures 3-4 and 3-7 show that CHT and CHT-tr differ in terms of reversible and irreversible uptake of chlorine species on the surface. Cl_2 uptake was mainly irreversible in CHT, while CHT-tr shows less irreversible chemisorption (as well as HCl formation) and the presence of a reversible chemisoption, although strongly interacting with carbon surface sites. Based on previous comments, Raman and other characterization results, it is reasonable to attribut to moderate strained C-C bonds (sp^2-type) the sites able to reversibly activate Cl_2. Nano-ordering during thermal treatment induces the conversion of sites giving irreversible (dissociative) chemisorption of Cl_2, to sites which still chemisorb Cl_2 strongly, but in molecular (reversible) form. Dissociatively chemisorbed Cl_2 may then react with surface H-donor sites to generated HCl. The formation of the latter hence requires the presence of H-donor sites. Since TPD data exclude the presence of possible hydrogen donor species, such as water or hydrocarbons adsorbed on the carbon surface, these H-donor species are associated to hydrogen atoms saturating carbon defects, or present as -OH or -COOH surface groups.

Catalysts characterization data have pointed out that these H-donor sites may be associated to sp^3 carbons at defect sites (carbon terminating sites). When these H-donor sites are no longer available, CO reacts with molecular chemisorbed Cl_2 leading to $COCl_2$. However, notwithstanding that HCl maximum formation in CHT is detected at about 1000s, $COCl_2$ formation is not detected over this catalyst, at least up to 6000s. This suggests that desorption of HCl does not allow to restore the original active site and thus surface reactivity toward Cl_2 decreases progressively (Figure 3-7a). Reasonably, this is due to the fact that the other Cl atom deriving from dissociative chemisorption of Cl_2 remains chemisorbed on the catalyst, blocking further the site. Only at higher temperatures, mobility of hydrogen on the surface allows the complete desorption of HCl, as shown from TPD results (Figure 3-5). Data in Figure 3-4c

evidenced also that sites strongly chemisorbing Cl_2, although still in a reversible molecular form, are present in CHT-tr, but not in CHT.

These observations may be rationalized considering that different types of C-C (sp^2-type) bonds are present in the catalysts:

- highly strained C-C bonds, deriving from disordered nano-onion type structures, which can irreversibly react with Cl_2 giving rise to homolytic dissociation of Cl-Cl bond; these sites are similar to those present in fullerene-type carbon materials sites having a high bending (pyramidalization) degree and showing similar irreversible uptake of Cl_2.[11,67-69]

- strained C-C bonds, reasonably deriving from the first during the nano-ordering process, and able to strongly chemisorb Cl_2, but in a molecular reversible form; these sites are those responsible for $COCl_2$ formation, in presence of CO; these sites are also those promoting CH_4 chlorination.

- C-C bonds with moderate to weak straining which do not interact or only weakly with Cl_2.

It is thus reasonable that HCl forms when H-donor sites, associated to defective sp^3 carbon sites, are present nearlying to the first two types of sites. In such configuration, the other Cl atom (deriving from Cl_2 dissociative chemisorption) remains strongly chemisorbed, but not in a position nearlying to a H-donor site, thus resulting in the inhibition of that site. Nano-ordering occurring during the thermal treatment leads to the elimination of these defect sites, in agreement with the significantly lower formation of HCl in CHT-tr compared to CHT. The larger formation of $COCl_2$ in CHT-tr derives thus from both the modification of the characteristics of C-C bond (sp^2-type) and the elimination of carbon defects (sp^3-type).

This indication is further supported from the data reported in Figure 3-8, where the Cl_2 conversion and $COCl_2$ formation on the two catalysts are compared with respect to the relative graphitization index. The latter index characterizes the transition from sp^3 to sp^2 carbon and thus the formation of the onion-like structure. This result gives further support to the above interpretation. However, further experiments are necessary for a better understanding of the unusually high strength of interaction with Cl_2 of CHT-tr and the exact nature of these sites in onion-type nanostructure. The relation between HCl formation and concentration/nature of defect sites in carbon deserves also further clarification.

The irreversible chemisorbed Cl_2 species, due to their strong interaction, are instead not reactive towards CO, neither are in equilibrium with the reversible ones. This is well consistent with the hypothesis that irreversible adsorbed species are those homolytically dissociated (e.g. ClC-CCl), while those reversibly chemisorbed are the molecular ones. Thermal treatment, by inducing nano-ordering, minimizes the concentration of defects (sp^3-type carbon sites) and

amount of strongly bend C-C bonds (sp^2-type), limiting in this way irreversible Cl_2 chemisorption and HCl formation. To further support this indication, Figure 3-10 reports the inverse correlation between the graphitization index (G_I) of the carbons, the total amount of HCl formed and the concentration of irreversibly chemisorbed Cl_2.
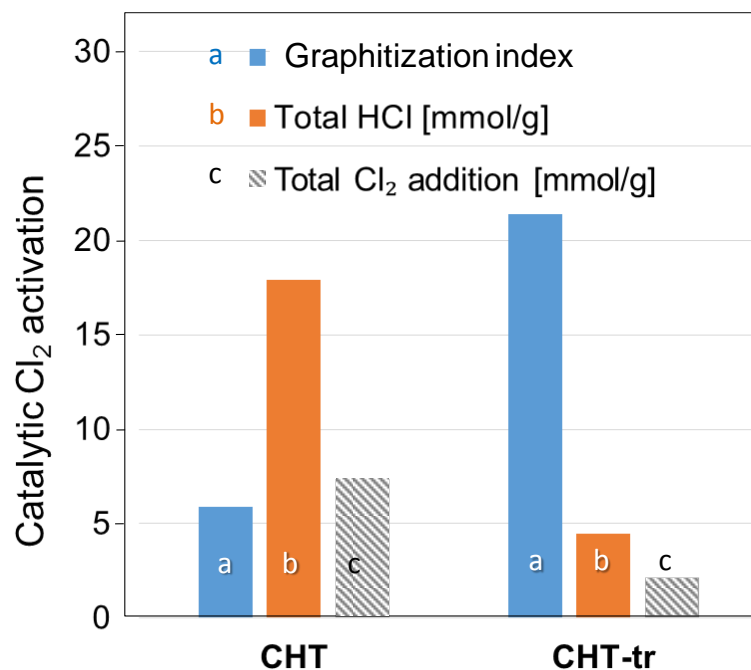

Figure 3-10. Relationship between the graphitization index (G_I) of carbon materials and the catalytic Cl_2 activation.

Note that CHT-tr contains only one fourth of the sp^3 carbon compared to the parent CHT. This is paralleled by an approximatively four times lower Cl_2 uptake and HCl formation.

3.4.4 Reaction mechanism

The tentatively catalytic cycle for $COCl_2$ formation, which describes the experimental evidences discussed above, is presented in Scheme 3-1.
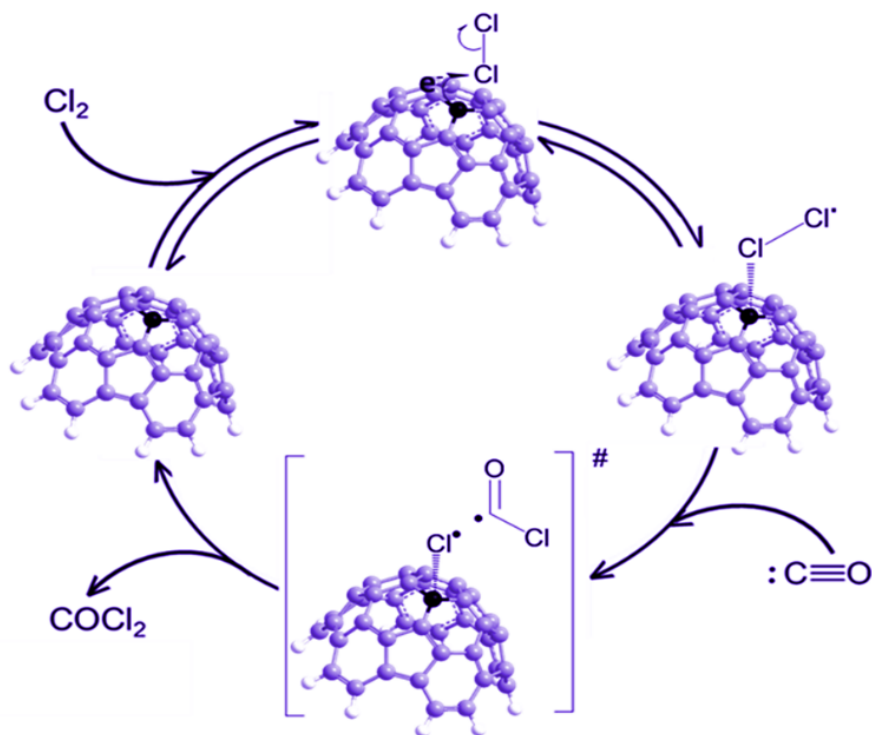
Scheme 3-1. Proposed $COCl_2$ synthesis mechanism on CHT-tr carbon materials.

Although in part speculative, deserving thus further demonstrations, we believe that it may be useful to analyze better the discussed experimental results. During Cl_2 interaction with sp^2 carbon sites, labile charge-transfer complexes $[^*C\cdots Cl_2]$ are formed. Raman in-situ spectra confirm this type of interaction, while reactivity data show that only when a relatively strong interaction, although reversible and reasonable involving undissociated Cl_2 molecules, subsequent reaction with CO to form phosgene may occur. Following the subsequent charge transfer from carbon material to Cl_2, a new chlorine radical $[^*C\text{-}Cl_2^\bullet]$ species is generated, which reacts with CO, forming $COCl_2$ *via* acylchloride radical $[^\bullet COCl]$. The presence of such a radical-like chlorine chemisorbed species is confirmed by the tests with CH_4 as probe molecule. In fact, the product distribution of methylchlorides is in agreement with the presence of radical like species at the active carbon surface.

The key in the reaction mechanism is the type of carbon sites responsible for the first step of labile charge-transfer complex formation. According to what discussed in the previous section, C-C sp^2-type bond is not enough active in this activation of Cl_2. Bending of the bond (strained C-C bonds) reduces activation energy allowing the coordination and relative strong chemisorption, although still in a reversible molecular form (equation 3-4a). A higher bending degree (highly strained C-C sites), as present in more disordered onion-type materials and

fullerene-type carbons as well, further decrease the activation energy, leading to dissociative chemisorption (equation 3-2b).

[3-2a] $*C=C*$ + Cl_2 $\longrightarrow$ $*C-C*(--Cl_2)$

[3-2b] $*C=C*$ + Cl_2 $\longrightarrow$ $(Cl)*C-C*(Cl)$

Formation of HCl occurs either consecutively to the formation of these dissociatively chemisorbed Cl_2 (equation 3-2b) by reaction with carbon sites terminating defects ($*C-H$) (equation 3-3a) or alternatively by direct heterolytic chemisorption on these sites (equation 3-3b). We believe that equation 3a is more likely and in better agreement with experiments, in particular with Raman data (Figure 3-6), despite this is an aspect deserving further studies.

[3-3a] $(Cl)*C-C*(Cl)$ + $*C-H$ $\longrightarrow$ $(Cl)*C-C*$ + HCl + $C*$

[3-3b] $*C-H$ + Cl_2 $\longrightarrow$ $*C-Cl$ + HCl
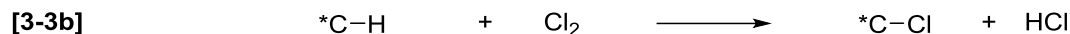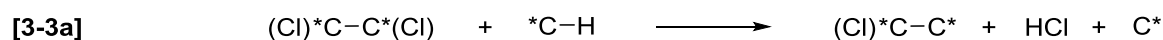
3.4.5 Generation of the active sites

The results show how two carbon samples, with the nearly identical round-shaped macroscopic morphology and similar surface area/porosity, change significantly their reactivity towards Cl_2 activation and further catalytic CO and CH_4 chlorination by variation of their structural order. Using thermal annealing, onion-type carbon nanospheres showing on the surface hemi fullerene-type ordered nanoshells have been prepared. The latter are obtained by thermal reordering of the precursor, highly defective, carbon material, but likely already having the suitable structure to form this specific surface nanostructure upon annealing. The catalyst obtained after the thermal treatment, with respect to the parent carbon material, shows sp^2 carbon sites with unusually high strength of adsorbing Cl_2 molecularly (in a reversible way), leading to high catalytic activity in phosgene generation, significantly higher than in many other type of carbon materials (although not shown here). The annealing at the same time lowers the amount of sp^3 type defect carbon sites, responsible for Cl_2 conversion to HCl. Possibly, the thermal ordering process, indicated by the increase of G_I, also cause a modifications of highly strained sp^2 carbon sites responsible for irreversible Cl_2 chemisorption, although there are not definitive evidences on this aspect.

This special carbon nanostructure requires, to be created by thermal treatment, a suitable and specific carbon arrangement in the (quasi-amorphous) precursor. The synthesis of these precursor nanospheres depends not only on the precursors and the heat treatment conditions, but also on the environment in which carbon spheres are generated. In the case of CHT synthesis, the solid/liquid interface between carbon source and the surrounding water during the thermal decomposition plays a key role in the concentric growth of the spherical carbon.[48] As for macro-shape, the nano-order in this material resembles that of nano-onion, but with a great disorder and the presence of sp^3-sp^2 mixed coordination, with the curvature process leading to about 200 nm-size nanospheres favoring the formation of disordered stacking planes with various terminations and defects (sp^3-type carbon atoms). Thermal annealing, however, rearranges these layers into materials ordered at the nanoscopic level, according to the description outlined above.

3.5   Conclusions

A novel nano structured carbon was synthesized by a combination of thermal decomposition in an aqueous environment and subsequent thermal annealing. This carbon shows a unique strain on the graphene sheets, inducing carbon sites for strong chemisorption of Cl_2.

In the parent carbon material, the high degree of bending of C-C sp^2-type bonds induces irreversible dissociative chemisorption of Cl_2, while the high concentration of defects carbon atoms (sp^3-type, to which H-atoms are coordinated to saturate the valence) favors further reaction of chemisorbed Cl species to generate HCl. Thermal annealing forms a nano-ordered hemi spherical graphene shell structures (hemi-fullerene type) with a decrease of strain in C-C sp^2-type bonds, as well as the reduction of defect (sp^3-type) carbon atoms. The reorganization transforms sites able to irreversibly (dissociatively) chemisorb Cl_2 to sites able to strongly, but reversibly and in a molecular form, coordinate Cl_2. These sites react with CO to generate catalytically $COCl_2$, and also promote CH_4 chlorination. Reorganization also reduces the concentration of carbon defects (sp^3-type), decreasing HCl formation and catalyst deactivation. During interaction with these sites, the formation of [*C-Cl_2] adducts with radical character is enabled. By using CO and CH_4 as reactive probe molecule, it was possible to show that this is the only species able to contribute to $COCl_2$ synthesis and $CH_{4-n}Cl_n$ formation. The properties and catalytic potential of this new material are currently being further explored.

3.6   References

[1]   (a) Y. Qin, L. He, J. Duan, P. Chen, H. Lou, X. Zheng, H. Hong, *ChemCatChem.* **2014**, *6*, 2698.(b) V. Calvino-Casilda, A.J. Lopez-Peinado, C.J. Duran-Valle, R.M. Martin-Aranda, *Catal. Reviews - Science and Eng*. **2010**, *52*, 325. (c) T.J. Bandosz, in *Carbon Materials for Catalysis*, P. Serp, J.L. Figueiredo (Eds.), John Wiley & Sons, Inc., Hoboken, NJ, **2008**, p. 45.

[2]   (a) W. Qi, D. Su, *ACS Catal.***2014**, *4*, 3212. (b) D. C.Sorescu, K. D Jordan, P. J. Avouris, *Phys. Chem. B* **2001**, *105*, 11227. (c) Z. Y Zhu, S. M. Lee, Y. H. Lee, T. Frauenheim, *Phys. Rev.Lett.* **2000**, *85*, 2757. (d) J. Zhang, X. Liu, R. Blume, Z. Zhang, R. Schlögl, D. Su, *Science* **2008**, *322*, 73.

[3]   (a) D. S. Su, G. Centi, S. Perathoner, *Chem. Rev*. **2014**, *113*, 5782. (b) G. Centi, S. Perathoner, D.S. Su, *Catal. Survey Asia*, **2014**, *18*, 149. (c) D.S. Su, G. Centi, S. Perathoner, *Catal. Today* **2012**, *186*, 1.

[4]   (a) J.H. Bitter, *J. Mater. Chem*. **2010**, *20*, 7312. (b) X. Pan, X. Bao, *Acc. Chem. Res*. **2011**, *44*, 553.

[5]   R. Arrigo, M. Hävecker, S. Wrabetz, R. Blume, M. Lerch, J. McGregor, E. P. J. Parrott, J. A. Zeitler, L. F. Gladden, A. Knop-Gericke, R. Schlögl, D. S. Su, *J. Am. Soc.* **2010**, *132*, 9630.

[6]   L. Mleczko, G. Lolli, *Angew. Chemie – Int. Ed.***2013**, *52*, 9372-9387.

[7]   J.-W. Shi, X. Zong, X. Wu, H.-J. Cui, B. Xu, L. Wang, M.-L. Fu, *ChemCatChem.* **2012**, *4*, 488-491.

[8]   D. S. Su , J. Zhang, B. Frank, A. Thomas, X. Wang, J. Paraknowitsch, R. Schlögl, *ChemSusChem* **2010**, *3*, 136.

[9]   R. Chakravarti, M. L. Kantam, H. Iwai, S. S. Al-deyab, K. Ariga, D.-H. Park, J.-H. Choy, K. S. Lakhi, A. Vinu, *ChemCatChem.* **2014**, *6*, 2872.

[10]   D. S. Su, J.-O. Müller, R. E. Jentoft, D. Rothe, E. Jacob, R. Schlögl *Topics in Catal*. **2004**, *30-31*, 241.

[11]   V. Georgakilas, J. A. Perman, J. Tucek, R. Zboril, *Chem. Rev.* **2015**, 115, 4744.

[12]   T. J. Bandosz, M. Seredych, *Chin. J. Catal.* **2014**, *35*, 807.

[13]   J. Matthiesen, T. Hoff, C. Liu, C. Pueschel, R. Rao, J.-P. Tessonnier, *Chin. J. Catal.* **2014**, *35*, 842.

[14]   L. R. Radovic, C. Mora-Vilches, A. J. A. Salgado-Casanova, *Chin. J. Catal.* **2014**, *35*, 792.

[15]   G. Centi, S. Perathoner, *ChemSusChem.* **2011**, *4*, 913.

[16]   M. Godino-Ojer, A. J. López-Peinado, R. M. Martín-Aranda, J. Przepiórski, E. Pérez-Mayoral, E. Soriano, *ChemCatChem.* **2014**, *6*, 3440.

[17]   W. Zhang, L. Theil Kuhn, *ChemCatChem.* **2013**, *5*, 2591.

[18]   Y. Zhu, Y. Lin, B. Zhang, J. Rong, B. Zong, D. S. Su, *ChemCatChem.* **2015**,10.1002/cctc.201402930.

[19]   R. Wang, X. Sun, B. Zhang, X. Sun, D. Su, *Chem. Eur. J.* **2014**, *20*, 6324.

[20]   J. Zhu, A. Holmen, D. Chen, *ChemCatChem.* **2013**, *5*, 378.

[21]   A. Ramos, I. Cameán, A. B. García, *Carbon* **2013**, *59*, 2-.

[22]   D. Tasis, N. Tagmatarchis, A. Bianco, M. Prato, *Chem. Rev.* **2006**, *106*, 1136.

[23]   C. T. J. Low, F. C. Walsh, M. H. Chakrabarti, M. A. Hashim, M. A. Hussain, *Carbon* **2013**, *54*, 1.

[24]   S. Stankovich, D. A. Dikin, R. D. Piner, K. A. Kohlhaas, A. Kleinhammes, Y. Jia, Y. Wu, S. T. Nguyen, R. S. Ruoff, *Carbon* **2007**, *45*, 1558.

[25]   S. Y. Sawant, R. S. Somani, A. B. Panda, H. C. Bajaj, *Mater. Lett.* **2013**, *94*, 132.

[26]   D. R. Dreyer, H.-P. Jia, C. W. Bielawski, *Angew. Chemie – Int. Ed.* **2010**, *49*, 6813.

[27]   Y. Z. Jin, C. Gao, W. K. Hsu, Y. Zhu, A. Huczko, M. Bystrzejewski, M. Roe, C. Y. Lee, S. Acquah, H. Kroto, D. R. M. Walton, *Carbon* **2005**, *43*, 1943.

[28]   C. Su, K. P. Loh, *Acc. Chem. Res.* **2013**, *46*, 2275.

[29]   B. Keggenhoff, H. Lokum, J. Münnig, *Process and apparatus for the production of phosgene*, **2008**, Patent US7442835.

[30]   C. J. Mitchell, K. s van der Velde, M. Smit, R. Scheringa, K. Ahrika, D. H. Jones, *Catal. Sci. Technol.* **2012**, *2*, 2109.

[31]   J.-P. Senet, *Comptes Rendus de l'Académie des Sciences - Series IIC - Chemistry* **2000**, *3*, 505.

[32]   L. Cotarca, H. Eckert, *Phosgenations - A Handbook* **2005**,Wiley Online Library.

[33]   V. A. Volodina, A. A. Kozlovskii, S. I. Kuzina, A. I. Mikhailov, *High En.Chem.* **2008**, *42*, 311.

[34] T. Zhang, C. Troll, B. Rieger, J. Kintrup, O. F. K. Schlüter, R. Weber, *J. Catal.* **2010**, *270*, 76.

[35] J. Heuser, H. Kauth, C. Kords, *Phosgene having low content of carbon tetrachloride*, **2005**, Patent US6930202.

[36] F. A. Via, G. L. Soloveichlk, P. G. Kosky, W. V. Cicha, *Method for producing phosgene*, **2002**, Patent US6500984.

[37] H. Şahin, S. Ciraci, *J. Phys. Chem. C* **2012**, *116*, 24075.

[38] B. Li, L. Zhou, D. Wu, H. Peng, K. Yan, Y. Zhou, Z. Liu, *ACS Nano* **2011**, *5*, 5957.

[39] K. Gopalakrishnan, K. S. Subrahmanyam, Prashant Kumar, A. Govindaraj, C. N. R. Rao, *RSC Adv.* **2012**, *2*, 1605.

[40] M. Yang, L. Zhou, J. Wang, Z. Liu, Z. Liu, *J. Phys. Chem. C* **2012**, *116*, 844.

[41] S. Abate, G. Centi, S. Perathoner, *National Science Review*, **2015**, doi:10.1093/nsr/nwv017

[42] I. M. Y. A. M. Rabiu, *J. Power and Energy Eng.* **2013**, *1*, 41.

[43] C. Hammond, S. Conrad, I. Hermans, *ChemSusChem* **2012**, *5*, 1668.

[44] Y. Wei, D. Zhang, Z. Liu, B.-L. Su, *Cuihua Xuebao* **2012**, *33*, 11.

[45] Z. Guo, B. Liu, Q. Zhang, W. Deng, Y. Wang, Y. Yang, *Chem. Soc. Rev.* **2014**, *43*, 3480.

[46] J. He, T. Xu, Z. Wang, Q. Zhang, W. Deng, Y. Wang, *Angew. Chemie, Int. Ed.* **2012**, *51*, 2438.

[47] K. Barbera, L. Frusteri, G. Italiano, L. Spadaro, F. Frusteri, S. Perathoner, G. Centi, *Chinese J. Catal.* **2014**, *35*, 869.

[48] L. Frusteri, C. Cannilla, K. Barbera, S. Perathoner, G. Centi, F. Frusteri, *Carbon* **2013**, *59*, 296.

[49] X.-Y. Liu, J.-M. Zhang, K.-W. Xu, *Physica B: Condensed Matter* **2014**, *436*, 54.

[50] J. Zhang, D.S. Su, R. Blume, R. Schlögl, R. Wang, X. Yang, A. Gajovic, *Angew. Chemie, Int. Ed.* **2010**, *49*, 8640.

[51] Z. Wang, L. Yu, W. Zhang, Z. Zhu, G. He, Y. Chen, G. Hu, *Phys. Lett. A* **2003**, *307*, 249-252.

[52] W. Zhang, M. Yao, X. Fan, S. Zhao, S. Chen, C. Gong, Y. Yuan, R. Liu, B. Liu, *J. Chem. Phys.* **2015**, *142*, 034702.

[53] (a) J. Robertson, *Phys.Rev. B* **2000**, *61*, 14095. (b) S. E. Rodil, J. Robertson, *Phys. Rev. B* **2003**, *67*, 155306.

[54] P. K. Chu, L. Li, *Mater. Chem. Phys.* **2006**, *96*, 253.

[55] N. A. Marks, D. W. M. La *Phys. Rev. B* **2009**, *79*, 075430.

[56]   A. C. Ferrari, *Solid State Comm*. **2007**,*143*, 47.

[57]   J. Shang, L.Ma, J. Li, W. Ai, T. Yu, G.G. Gurzadyan, *Scientific Reports* **2012**, *2*, 792.

[58]   F. Tuinstra, J. L. Koening, *J. Chem. Phys*. **1970**, *53*, 1126.

[59]   P. K. Chu, L. Li, *Mat. Chem. and Phys*. **2006**,*96*, 253.

[60]   D. Nishide, H. Kataura, S. Suzuki, K. Tsukagoshi, Y. Aoyagi, Y. Achiba. *Chem Phys Lett* **2003**, *372*, 45.

[61]   V. M. Irurzun, M. Pilar Ruiz, D. E. Resasco, *Carbon* **2010**, 48, 2873.

[62]   S. Yumitori, *J. Mater. Sci*. **2000**, *35*, 139.

[63]   R. Arrigo, M. Havecker, S. Wrabetz, R. Blume, M. Lerch, J. McGregor, E. P. J.Parrott, J. A. Zeitler, L.F. Gladden, A. Knop-Gericke, R.Schlögl, D.S. Su, *J. Am. Chem. Soc.* **2010**, *132*, 9616.

[64]   Y. Ling, G. K. Koyanagi, D. Caraiman, V. Baranov, D. K. Bohme, *Int. J. Mass Spectrometry* **1999**, *182/183*, 349.

[65]   I.-Y. Jeon, H. M. Kim, I. T. Choi, K. Lim, J. Ko, J. C. Kim, H.-J. Choi, M. J. Ju, J.-J. Lee, H. K. Kim, *Nano Energy* **2015**, *13*, 336.

[66]   G. Czako, J. M. Bowman, *J. Chem. Phys.* **2012**, *136*, 044307/1.

[67]   Z. Chen, W. Thiel, A. Hirsch *ChemPhysChem* **2003**, *4,* 93.

[68]   I. H. Campbell, D. L. Smith *Solid State Physics 55* **2000** (Eds.: H. Ehrenreich, F.Spaepen), Academic Press, New York, NY,.

[69]   P. A. van Hal, M. P. T. Christiaans, M. M. Wienk, J. M. Kroon, R. A. J. Janssen, *Phys. Rev B*. **1999**, *103*, 4352.

3.7 Supporting information

Determination of domain size

The parameters relative to domain size reported in Table 3-1:

- the average values of the interlayer spacing d_{002},
- the height of layered stacking (L_c)
- the basal plane length (La)

were determined using the XRD patterns of CHT and CHT-tr samples, after correction for background baseline and instrumental broadening, following the approach of Ungár et al.[1] The average interlayer spacing is measured through the position of the (002) peak by applying Bragg's equation. The height of layered stacking is estimated from the (002) and the basal plane length from (110) peaks, respectively, using the Scherrer formula. The layer dimension in the plane of the layer was calculated from the peak width at half of the maximum intensity (B) using the following formulas:

[S3-1]
$$La = \frac{1.84\,\lambda}{B\,\cos\theta} \quad \text{and} \quad Lc = \frac{1.89\,\lambda}{B\,\cos\theta}$$

The effective dimension L of the graphitic microcrystallites were determined as follows:[2]

[S3-2]
$$L = \sqrt[3]{\frac{\pi}{4L_a^{\,2}L_c}}$$

Table 3-1 also reports the the graphitization index (G_I) and the relative G_I. The ratio of the area of (002) reflection for both CHT and CHT-tr samples with respect to that of LiF added as internal standard (see below) allows to estimate the graphitization index (G_I). The relative G_I is instead estimated but normalizing to 100% the G_I value of CHT-tr sample.
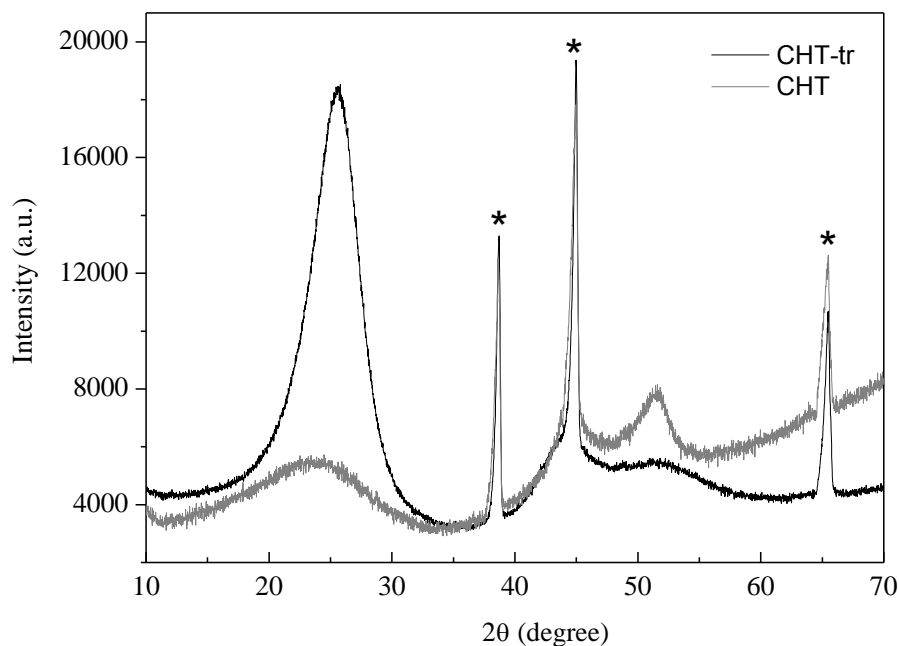
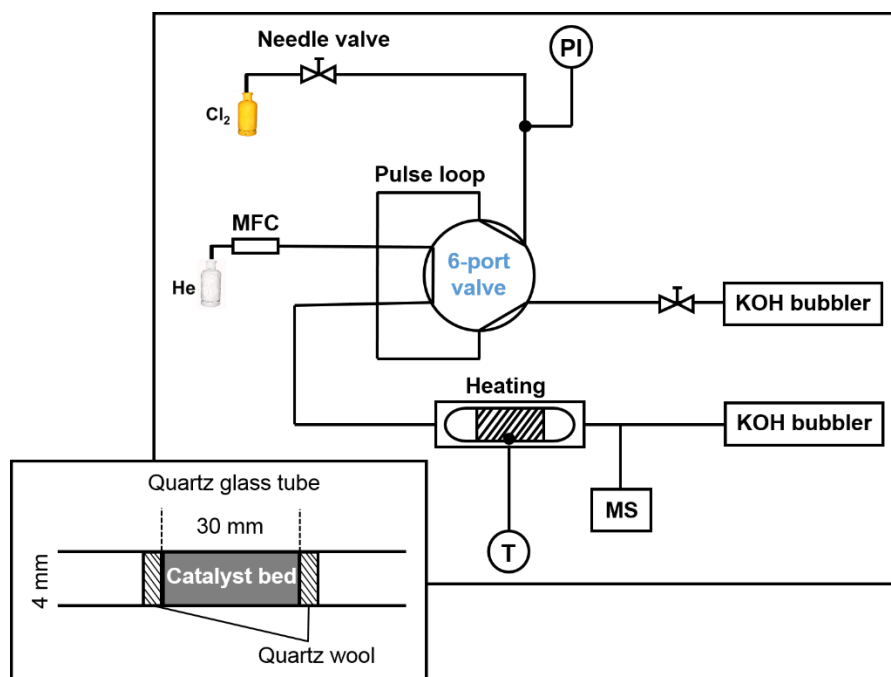**Figure S3-1.** XRD patterns of samples. * reflection of internal standard (LiF)

Figure S3-2. Pulse set-up for Cl_2 interaction and $COCl_2$ synthesis study. (PI = pressure indicator, MFC = mass flow controller, MS = Mass spectrometer, T = temperature controller)
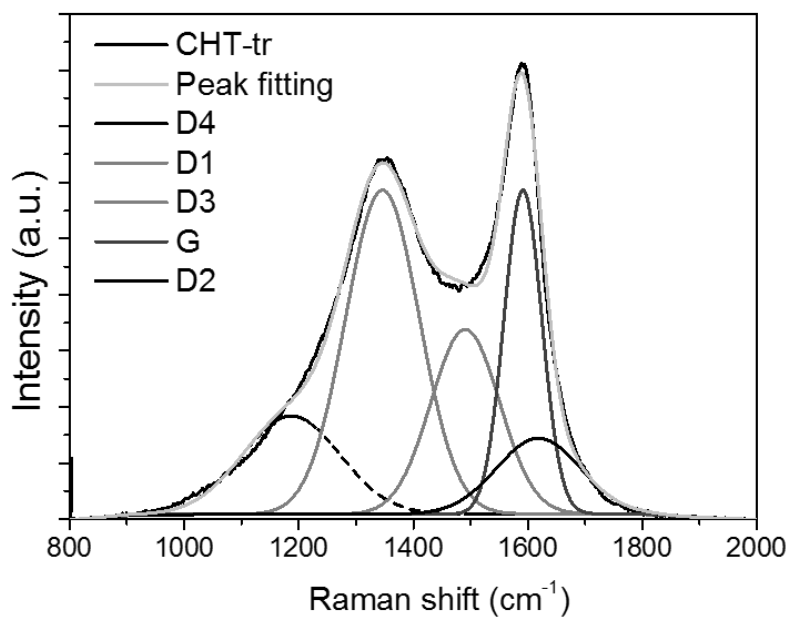
Figure S3-3. Raman spectra deconvolution for CHT-tr sample.

Table S3-1. Quantitative Raman peak areas and heights derived from deconvolution of spectra (see S3-3).

Band	G	D1	D2	D3	D4	G/D1
Center, cm^{-1}	1594	1346	1619	1451	1187	-
Height	11545	11551	2697	6577	3506	0.999
Area	952612	1865854	495288	988286	749371	0.511

Supplementary reference:

[1]   T. Ungár, J. Gubicza, G. Ribárik, C. Pantea, T. W. Zerda, *Carbon* **2002**, *40*, 929.

[2]   R. H. Hurt, A. F. Sarofim, J. P. Longwell, *Fuel* **1991**, *70*, 1079.

Chapter 4

Nitrogen Modified Carbon Nano-Materials as Stable Non-Metal Catalysts for Phosgene Synthesis

Abstract

The carbon catalyzed reaction of Cl_2 and CO constitutes a synthetic route to a versatile compound phosgene ($COCl_2$) successfully used for a variety of chemical transformations. One attractive scenario for the development of stable carbon catalysts for the selective formation of $COCl_2$ is the use of nitrogen modified well-ordered porous carbon materials. The interplay between the electron donating and withdrawing ability of incorporated nitrogen substituents on the formation and stabilization of active sites was examined by using X-ray photoelectron and Raman spectroscopies. Mechanistic studies indicate the intermediacy of ionic polarized chlorine obtained by direct interaction of Cl_2 with a strong electron deficient carbon site located in close proximity of a nitrogen substituent. We demonstrate here that the successful modification of ordered carbon materials to generate active carbon catalysts for $COCl_2$ with remarkable long-term operational stability even under harsh reaction conditions.

4 Nitrogen Modified Carbon Nano-Materials as Stable Non-Metal Catalysts for Phosgene Synthesis

4.1 Introduction

Carbon based materials have received increasing attention as metal-free catalysts,[1-3] because different hybridizations e.g. sp^2, sp^3 and mixed sp^2/sp^3 hybridization of the carbon, yield inhomogeneous surfaces and/or structures[4] and enables divers modes of adsorption.[5,6,7] Fairly recently it was shown, that by the insertion of various heteroatoms, i.e. N, O, P and B, carbon can be made attractive for a wide number of applications by tuning the electronic properties of the active sites.[8-11] The most widely introduced heteroatom after oxygen is nitrogen, which has been successfully used in carbon modification. In the case of nitrogen, many different nitrogen-doped materials, such as N-doped carbon nanotubes,[12,13,14] colloidal graphene quantum dots[15] and carbon sub-micrometer spheres have been successfully synthesised.[16] Several studies have described that nitrogen can influence the spin density and charge distribution on neighboring carbon atoms[17,18] enhancing their catalytic activity and providing long-term durability and tolerance to poisoning / deactivation as metal-free catalysts.[19,20,21] Generally, nitrogen heterocyclic rings consist of three main nitrogen types, as pyridinic, pyrrolic and quaternary nitrogen, and it is expected that the modified electronic structure on adjacent carbon is different depending on the electronic environment of the nitrogen and types of C-N bonding configurations. It is well known that pyridinic nitrogen possesses a strong electron affinity and creates a substantially high net positive charge density on the adjacent carbon atoms[18,22] while pyrrolic nitrogen induces a high electron density on the carbon sites.[23] However, quaternary-N substitutions in aromatic compounds stabilize carbenes by push-pull mesomeric and inductive synergetic effects.[24] How the different nitrogen modifications determine the catalytic activity is, however, still controversial due to the lack of experimental results. Therefore, a good understanding of diverse effects of N-modification on carbon deserves diligent and urgent attention in view of rapid progress in conventional carbon catalyzed processes.

Here, we report a detailed mechanistic study of the catalytic synthesis of $COCl_2$, one of the oldest carbon catalyzed large-scale processes, directly from Cl_2 and CO under mild conditions. In a recent report the ample presence of bent carbon layers, semi-spheres and carbon cages has been shown for typical carbon catalysts, that in the case of non-modified carbon catalyst, provides the appropriate balance between the loss of conjugation energy and the energy gain in the reactive coordination of Cl_2.[25] Planar carbon surfaces were proved to be inactive for $COCl_2$

formation. The initial interaction of Cl_2 with the bent surfaces and fullerenic structures activates the Cl-Cl bond and results in the formation of activated Cl_2 with radical character. The subsequent attack of physisorbed CO results in the transient formation of [COCl]$^.$, which further reacts to $COCl_2$. The key challenge by the use of conventional activated carbon catalyst during $COCl_2$ synthesis is, however, the low material stability due to the involvement of radicalic type of reactive chlorine containing species formed during the carbon chlorine interactions.[26] Therefore, it is of fundamental interest to investigate the electronic (inductive as well as mesomeric) effect of different N-modifications on the generation of active sites in carbon materials for $COCl_2$ synthesis, in order to develop a stable and highly active metal free catalyst. Spectroscopic studies have been successfully applied for the identification and characterization of the active sites responsible for the transient production of reactive chlorine intermediates on the active surface of a N-modified carbon during $COCl_2$ synthesis. With the purpose gaining a better understanding of the structural and electronic requirements of an active carbon catalyst for stable $COCl_2$ production, different types of N-dopants were selected for the preparation of carbon materials and studied by using various spectroscopic techniques.

4.2   Experimental

4.2.1 Nitrogen containing carbon materials

All the well-ordered nitrogen modified mesoporous carbon materials were prepared by following the published procedures.[27] The proposed polymeric structures are presented in Figure 4-1.
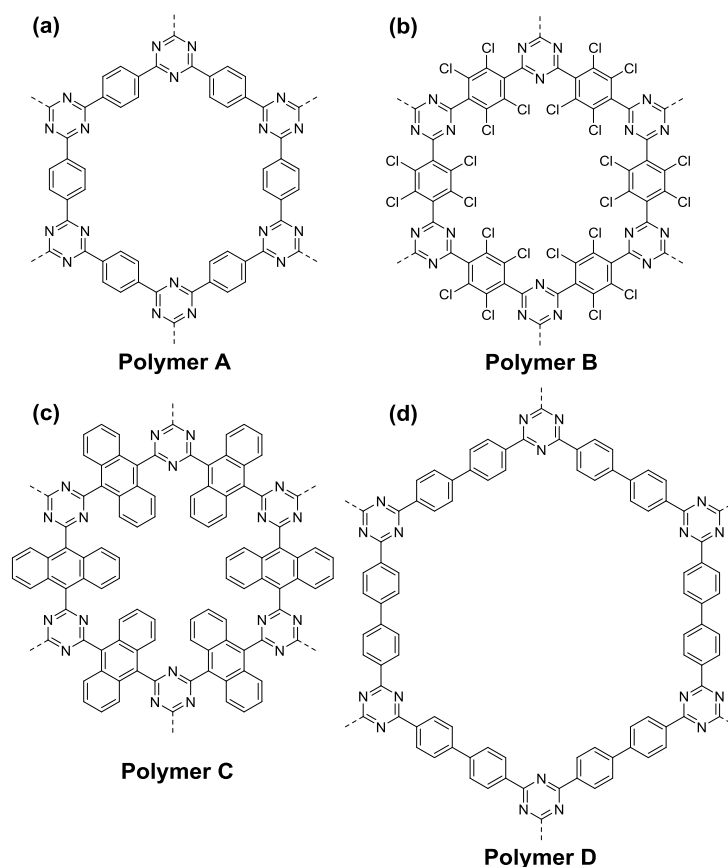
Figure 4-1. Proposed structures of N-modified mesoporous ordered carbon materials synthesized from 1,4-dicyanobenzene (a, Polymer A), tetrachloroterephthalonitrile (b, Polymer B), 9,10-anthracenedicarbonitrile (c, Polymer C) and 4,4′-biphenyldicarbonitrile (d, Polymer D).

For the preparation of 1,3,5-triazine based polymer A shown in Figure 4-1, a mixture of 1,4-dicyanobenzene (98 % from Sigma Aldrich) and anhydrous $ZnCl_2$ (5 mole equivalents, 97 % from Sigma Aldrich) was transferred and sealed in a glass ampule under inert conditions. The ampule was heated to 673 K (heating ramp 1K / min). After standing at this temperature for 40 h the ampule was cooled to ambient temperature and carefully opened (high pressure ampule due to the thermal generation of gaseous degradation products). The solid reaction mixture was ground and washed thoroughly with small aliquots of bi-distilled H_2O and diluted HCl. The resulting black powder was refluxed at 373 K in 1 M HCl for 48 h to remove the remaining excess of $ZnCl_2$. Finally, the polymer was further purified by washing with 1 L of bi-distilled H_2O followed by THF (99.9 %, Sigma Aldrich, 15 ml). The resulting solid was dried in vacuum at 350 K overnight.

To understand the influence of different physico-chemical properties of nitrogen substituted carbons on the adsorption and interaction ability with Cl_2 and CO during the catalytic $COCl_2$

synthesis, the same reaction was repeated by using 9,10-anthracenedicarbonitrile (97 % from Sigma Aldrich), and 4,4′-biphenyldicarbonitrile (97 % from Sigma Aldrich) as building units. These precursors yield 1,3,5-triazine rings interconnected with different aromatic spacers (biphenyl and anthracene, respectively) resulting in texturally different carbons. By using tetrachloroterephthalonitrile (95 % from Sigma Aldrich) as reagent resulted in a mesoporous carbon (Figure 4-1, structure B) where all sp^2 carbon atoms are blocked by covalently bonded –Cl.

In a comparative study on the Cl_2 activation ability, following pyridinic (type A) and quaternary nitrogen containing molecules (type B) were selected and are shown in Figure 4-2 and 4-3. All the materials with a purity higher than 97 % were purchased from Sigma Aldrich and used without any further purification under inert conditions.
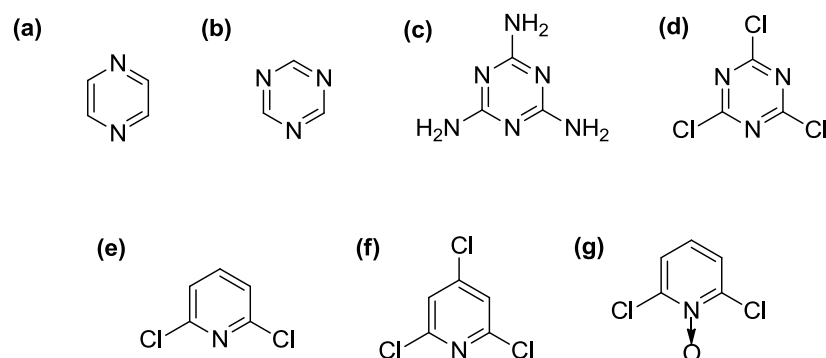
Figure 4-2. Overview of studied pyridinic nitrogen containing molecules (Type A): pyrazine (a), 1,3,5-triazine (b), melamine (c) cyanuric chloride (d), 2,6-dichloropyridine (e), 2,4,6-trichoropyridine (f) and 2,6-dichloropyridine N-oxide (g).
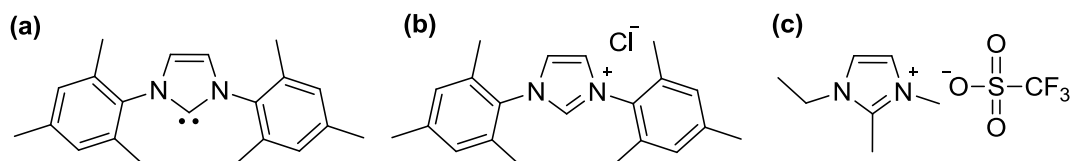
Figure 4-3. Overview of studied quaternary nitrogen containing molecules (Type B): 1,3-bis(2,4,6-trimethylphenyl)-1,3-dihydro-2H-imidazol-2-ylidene (a, BTDIY), 1,3-bis(2,4,6-trimethylphenyl) imidazolium chloride (b, BTIC), 1-Ethyl-2,3-dimethylimidazolium-trifluoromethanesulfonate (c, EDITM).

4.2.2 Catalytic Cl₂/CO activation and COCl₂ synthesis

Cl_2 activation on all the synthesized N-modified carbons along with selected well-defined nitrogen containing substances was studied in a temperature range from 300 to 473 K. The obtained results were compared with non-modified carbon, *e.g.* high-surface area graphite (HSAG, specific surface area of 300 m^2/g, received from Timcal®). For each experiment 10 − 100 mg of solid catalyst (particle size ≤ 80 µm) was placed in a quartz reactor (0.4 cm ID) and activated at 423 K and 1 bar for 1 h prior to multiple Cl_2 pulses (1.8 µmol Cl_2 / pulse, pulse length 230 s) in He (10 cm^3 STP per min) were applied. All the gaseous materials were analyzed by on-line mass spectrometry (OMNIstar/TM mass-spectrometer). For the identification of the surface bound species, temperature programmed desorption (TPD) of catalyst was performed from 300 to 993 K. CO interaction on fresh and Cl_2 exposed catalysts was also studied under conditions similar to Cl_2 activation. To test the catalytic performance for $COCl_2$ synthesis, repetitive Cl_2 pulses were conducted with 5 vol. % CO in He (10 cm^3 STP per min).

4.2.3 Experimental set-up and safety issues

A schematic representation of the experimental setup constructed for the Cl_2 activation and CO interaction study is shown in supporting material, Figure S4-1. One major advantage of this setup designed for Cl_2 activation studies is the possibility to use minimal amounts of toxic and corrosive gases. A six-port valve connected to an on-line mass spectrometer (MS) was used for the automated dosage of Cl_2. All the gaseous residues were neutralized in two interconnected concentrated KOH and Cu^{2+} solution containing bottles. An active carbon containing filter finally accounts for the retention of any generated toxic gaseous intermediates that remain. Special attention was paid to the safety issues; two different types of Cl_2 and CO detectors were placed under the fume hood to constantly monitor the Cl_2 and CO concentration at the working place. To avoid contamination with CO, two additional filters for CO entrapment were installed at the outlet of the six-port valve and of the reactor. The maximum amount of $COCl_2$ which could theoretically be formed in the pulse reactor (0.025 ppm) is lower than the permissible exposure limit (0.1 ppm averaged over a work shift of up to 10 hours a day, 40 hours per week with a ceiling level of 0.2 ppm averaged over a 15 min period).[28]

4.3 Catalyst characterization

BET surface area

For the determination of the characteristic textural properties of the targeted carbon catalysts, N_2 physisorption measurements were performed on a PMI automated Sorptomatic 1990 instrument operated at liquid N_2 temperature (77 K). Prior to the experiments, 200 mg of the N-modified C samples were outgassed and activated under vacuum (10^{-4} mbar) at 473 K for 2 h. After activation, the samples were weighed and cooled to 77 K. Specific surface areas were estimated by applying the BET-formalism to the adsorption branch of the isotherms over the relative pressure range p/p^0 from 0.05 to 0.25. The pore size distributions (PSD) were obtained by applying the Barret–Joyner–Halenda (BJH) model[29] to the adsorption branch of the isotherm. Pore volumes were evaluated from the α_s comparative plot with nonporous hydroxylated silica as the reference adsorbent.[30] The t-plot method was used to discriminate micro- from mesoporosity.[31]

Elemental analysis

Elemental compositions of the materials were determined by CHN analysis at TU-München. The quantity of oxygen was estimated at Mikroanalytisches Labor Pascher, Germany.

Scanning electron microscope (SEM)

Topographical imaging of the materials were performed using a JEOL JSM-5900LV and Hitachi S3500N SEM. The SEM was operated at acceleration voltages between 10 and 25 kV, using a working distance of 9 mm for imaging.

Ramann spectroscopy

The Raman measurements were performed with a Renishaw Raman spectrometer Series 1000. After calibration of the Raman setup using an Si(111) single crystal the Raman spectra were recorded using the green line of an Ar-ion laser (514.53 nm, 2.41 eV) at elevated temperature under inert conditions. For ex situ measurement the thermally activated (423 K, 1h) samples were prepared over glass slits. The final spectra were 1-10 accumulations in a range of $100-4000$ cm^{-1}. Similar conditions were applied for in situ Raman measurements. In situ Raman measurements were performed by placing materials between quartz wool in a quartz reactor of diameter 1.62 mm ID. Spectra were recorded after thermal induced desorption of small molecules from the carbon surfaces (N_2 flow at 423 K and 1 h). Subsequently, the surface

active species were probed by Cl_2 at elevated temperature, until a consistent spectrum was achieved. The Cl_2 reversibility on the surface was checked by switching back to inert gas (N_2) flow.

Electron Spin Resonance (ESR) spectroscopy

ESR spectra of N-modified materials were recorded in the perpendicular mode on an X-band Joel Jes Fa 200 spectrometer equipped with a cylindrical mode cavity and a liquid He cryostat. The ESR measurements were performed, by taking spectra of samples inside a quartz tube in a temperature range of 298−473 K using 9.45 GHz, 1mW microwave power. The analysis and simulation of the data was done with the Jes-Fa Series software package Version 2.2.0.

X-ray photoelectron spectroscopy (XPS)

For the quantitative analysis of the surface chemical composition and bonding, X-ray photoelectron spectroscopic measurements were performed on ULVAC-PHI, Type Versa Probe 5000 spectrometer using monochromatic Al Kα radiation. All the samples were ground (particle size < 80 μm) and mounted on a double sided adhesive tape before introduction in the measuring chamber. The detection depth is 5 to 10 nm and the identification limit is around 0.1 atom %. The overall XPS spectra was recorded with a 187.8 eV pass energy analyser and an increment of 1eV. High-resolution individual spectra were obtained by using a 23.5 eV pass energy and an increment of 0.1 eV. The data analysis has been performed by using MultiPak software version 9.4.1.2. All the recorded spectra were calibrated to a 284.8 eV C1s binding energy. The binding configuration of the studied elements were identified based on the chemical shifts in the photoemission spectra and by a direct comparison with the reported literature values.[32] The XPS peaks were fitted to Voigt functions having 60 % Gaussian and 40 % Lorentzian character, after performing a Shirley background subtraction. Deconvolution of the XPS spectra was done by applying fixed binding energy values for the different N- and C- types and allowing the full width at half maximum to vary in order to obtain the best possible fit.

4.4   Results and discussions

4.4.1 Physicochemical properties of materials

Due to their unique structural and electronic properties, several N-doped carbon materials formed in a Lewis acid catalyzed one-pot multicomponent reaction, by using various aromatic nitriles as precursors, were used as porous organocatalytic materials (Figure 4-1). In a typical temperature controlled polymerization reaction, depending on the monomer architecture, the formation of well-ordered layered materials bearing various nitrogen and oxygen based substituents on the aromatic rings located at terminal positions (supporting material, Table S4-1 and Figure S4-2) takes place. The textural properties of synthesized materials varied markedly with the carbon precursors used in the synthesis. Detailed analysis results of the main textural properties of the carbon polymers presented in Figure 4-1 are summarized in Table 4-1.

Table 4-1. Specific surface areas and pore volumes of N-modified mesoporous carbon polymers.

Precursors	Textural analysis of the mesoporous carbon polymers			
	S_{BET} [m²/g]	Medium pore diameter [Å]	Mesopores V [cm³/g]	Micropore V [cm³/g]
1,4-Dicyanobenzene	775	21	0.096	0.374
Tetrachloroterephthalonitrile	285	22	0.026	0.012
9,10-Anthracenedicarbonitrile	746	42	0.429	0.063
4,4′-Biphenyldicarbonitrile	1558	28	0.912	0.186

The porous 1,3,5-triazine based polymers obtained from 1,4-dicyanobenzene and 9,10-anthracenedicarbonitrile show comparable specific surface area ranging from 775 to 746 m²/g, respectively, as well as a broad pore size distribution. The cross-linked networks in the polymer A (shown in Figure 4-1) synthesized from 1,4-dicyanobenzene had a significantly higher micropore volume (Vmicropore = 0.374 cm³/g) compared to the material synthesized by using 9,10-anthracenedicarbonitrile (Vmicropore = 0.063 cm³/g). However, the use of carbon involving the bulkier group anthracene compared to benzene as spacer resulted in an increase of the material mesoporosity from Vmesopore = 0.096 cm³/g (for benzene) compared to 0.429 cm³/g (for 9,10-anthracenedicarbonitrile) due to the induced deviations in planarity by anthracene molecules located between the triazine rings (for further information, see SI Figure S4-3). In contrast, the use of tetrachloroterephthalonitrile resulted in notable reduction of the specific surface area of the triazine based polymer A from 775 to 285 m²/g and a considerable decrease in the material porosity (Vmesopore = 0.096 to 0.026 cm³/g, Vmicropore = 0.374 to

0.012 cm^3/g, respectively). The decrease in surface area, mesoporosity and microporosity were attributed to the presence of covalently bound −Cl on the benzene linker located between triazine groups. HR-SEM images of the materials obtained by using tetrachloroterephthalonitrile evidenced the three dimensional layered structure of the materials similar to the case of the material resulting from 1,4-dicyanobenzene (Figure S4-3 (a) and (b)). The carbon material with the highest surface area and mesoporosity was, however, obtained by using 4,4′-biphenyldicarbonitrile as the starting precursor (1558 m^2/g). It is hypothesized that the larger distance between the -C≡N groups of the 4,4'-bisphenyldicarbonitrile compared to 1,4-dicyanobenzene materials is the cause for the two times higher specific surface areas of the resulting carbon.

The electronic structure of the synthesized materials was evaluated by use of Raman spectroscopy.
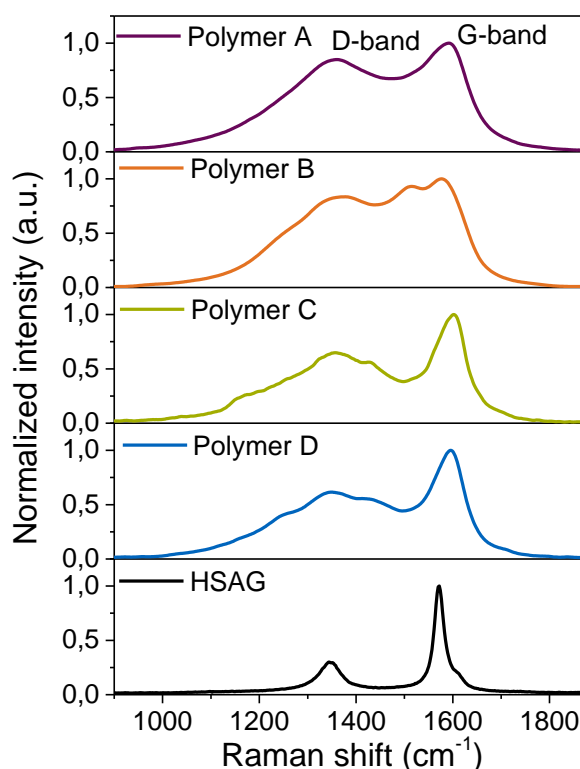
Figure 4-4. Ex-situ Raman spectra of the synthesized carbon polymers A, B, C and D and selected carbon material HSAG. Spectral analysis results are shown in Figure S4-4 and S4-5 as well as in Table S4-3 and S4-4.

All the N-modified carbon materials showed two distinct bands at ~1350 cm^{-1} (D-band) and ~1580 cm^{-1} (G-band), corresponding to the defected amorphous and well order crystalline phase [33,34] in the compound (Figure 4-4). In order to determine the well-ordered graphitic

carbon and the surface structural defects, the intensity ratios of D- to G-bands (I_D/I_G) were estimated by using the method published by Haghseresht et al. and Sadezky et al. and the deconvoluted spectra of Figure S4-4. The I_D/I_G ratio of synthesized materials ranged from 0.75 (for the 1,3,5-triazine based polymer D synthesized from 4,4′-biphenyldicarbonitrile) to 1.55 (for the polymer B obtained from tetrachloroterephthalonitrile, shown in Figure S4-4 and Table S4-3). Comparing the structural properties of the N-modified carbons to HSAG ($I_D/I_G = 0.28$,) a higher density of structural defects of the nitrogen containing carbon materials was evidenced. In comparison to the triazine-based polymers, the selected N-containing small molecule shows sharp molecular vibrational bands (Figure 4-5), but no collective vibrations of an extended solid (phonon modes).
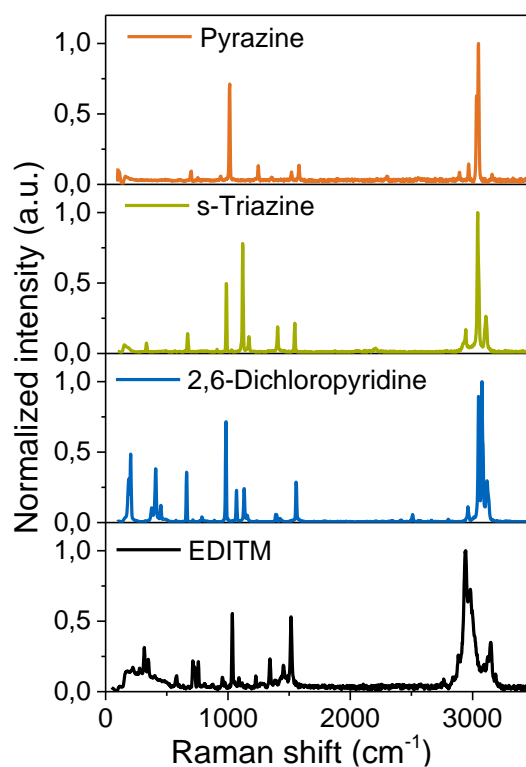
Figure 4-5. Ex-situ Raman spectrum of N-containing small molecules.

The chemical compositions of the synthesized carbons varied by changing the precursors (additional information in supplemental material Table S4-1 and S4-2). For this study, high variation in C to N atom ratios from 3.04 for the polymeric material B synthesized from tetrachloroterephthalonitrile to 21.28 for the polymeric material C obtained by using 9,10-anthracenedicarbonitrile was achieved. A more accentuated increase in the chlorine content (6.81 at. %) was observed for the material synthesized from tetrachloroterephthalonitrile (Supporting Information, Table S4-1 and S4-2). High temperature acid hydrolysis of nitrile

groups resulted in all the carbon materials in 3.72 to 8.07 at. % oxygen containing functional group formation.

Nitrogen 1s X-ray photoemission spectra were used to probe the nature of different N-functionalization of synthesized materials. The deconvoluted XPS spectra of N1s bonding state (shown in supporting information Figure S4-7) provided evidence for the existence of N in six different chemical environments in synthesized N-modified carbons. These include pyridinic-N (BE = 398.62 ± 0.11 eV), amine (BE = 399.83 ± 0.10 eV), pyrrolic-N (BE = 400.62 ± 0.11 eV), quaternary nitrogen (BE = 401.82 ± 0.11 eV), N-oxides of pyridinic-N (BE = 403.32 ± 0.11 eV) and NOx (BE = 404.72 ± 0.11 eV).[35,36] The relative content of each N bonding configuration is summarized in Table 4-2 for the four triazine based polymers shown in Figure 4-1.
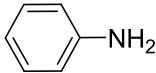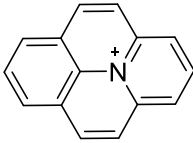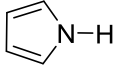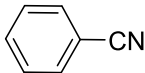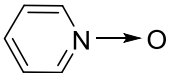
Table 4-2. XPS analysis of N1s binding state for synthesized different N-modified carbons.

Precursor	N 1s binding states (%)						Atom % of N
	Pyridine	Amine/ nitrile	Pyrrole/ amide	Quart.	Pyr.- NO	- NOx	
1,4-Dicyanobenzene	55.3	9.6	31.2	0	4.0	0	10.6
Tetrachloroterephthalonitrile	62.6	9.6	27.2	0.3	0	0.2	14.7
9,10-Anthracenedicarbonitrile	53.6	11.4	25.3	3.2	5.6	1.0	3.6
4,4`-Biphenyldicarbonitrile	40.5	15.4	38.0	3.4	2.8	0	5.5

The deconvolution and quantification of XPS spectra showed that the relative distribution of all N bonding configurations is quite similar in those four materials. Thus, in all cases the most abundant sites are pyridinic-N, with 40.5-62.6 % of all nitrogen, followed by pyrrolic-N and/or amides (25.3-38 %) and amine/nitrile functionality (9.6-15.4 %). Aromatic sp^2 hybridized nitrogen, i.e., pyridine, is electronegative and therefore, induces a substantially high electron deficiency on the aromatic ring.[37] In contrast, the N-atom in amine is bonded to one sp^2 C and carries hydrogen (C–N(H)–H). The basic lone pair on the nitrogen in this case is enhancing the electron-donating ability of the ring. Materials from 1,4-dicyanobenzene and tetrachloroterephthalonitrile contain about 9.6 ± 0.4 % amine/nitrile functionalities. However, this was slightly higher (11.4 - 15.4 %) in materials synthesized from 9,10-anthracenedicarbonitrile and 4,4`-biphenyldicarbonitrile. It should be noted, that based on XPS analysis, a clear distinction between the aromatic amine and nitrile functionalities can not be made.[42] Pyrrolic-N refers to two N atoms that are each bonded to two carbon atoms and

contribute to the aromatic system with two π-electrons. For 9,10-anthracenedicarbonitrile and tetrachloroterephthalonitrile 27.2 and 25.2 % pyrrolic-N, respectively, were found that is about 1.2 -1.5 times higher than the amounts found in materials synthesized from 1,4-dicyanobenzene and 4,4`-biphenyldicarbonitrile. All samples excluding the material synthesized from 4,4`-biphenyldicarbonitrile contained 0.3-3.4 % of quaternary-N, in which the N-atom is replacing a C-atom in the polymer layers. N-oxides were also found in all material in the range of 0.2 to 5.6 %, which is pyridinic-N ($-N^+-O^-$) with a bond to one or two C atoms and the O atoms. Considering the electronic effects exerted by the diverse nitrogen modifications on the neighboring aromatic carbon atoms, nitrogen substituents can be divided into two classes, as indicated in Table 4-3.

Table 4-3. Classification of N-functional groups based on their electronic effect (R-Resonance/mesomeric, I-inductive) towards aromatic C.

Electron withdrawing effect (-I/-R)	Electron donating effect (+I/+R)
Pyridinic (-R)	Amine (+R)
Quaternary (-I)	Pyrrolic (+R)
Nitrile (-R)	Pyridinic-N oxides (+I)

The pyridinic-N induces -R effect and stabilizes the electrophilic sp^2-carbon site.[38] In contrast, the amine and pyrrolic-N groups promote a more accentuated +R effect rather than -I and, therefore, induce a higher electronic density (nucleophilicity) on the adjacent carbon in an aromatic ring. However, in the case of pyridinic-N oxides the dominating effect is +I and contribute to the stabilization of the negative charge on highly electronegative oxygen atom. The quaternary-N modification possess –I effect and significantly contribute to the stabilization of electrophilic C.[39] Additional substitution promotes an extra electronic effect and outcome in stable carbenes.[24]

Further details about the chemistry of the N-modified carbon materials was obtained from C1s X-ray photoemission (Figure S4-8). The deconvoluted XPS spectra are shown in supporting information Figure S4-8 and binding energies summarized in Table 4-4.

Table 4-4. XPS analysis of C1s binding state for synthesized different N-modified carbon materials.

Precursor	C1s binding states (%)				
	-C=C-, -C-H	Ph-Cl, -C=N-	-C-O-	-C=O, -O-C-O-	-O-C=O
1,4-Dicyanobenzene	68.1	9.1	13.7	3.8	5.2
Tetrachloroterephthalonitrile	59.2	20.8	14.7	3.5	1.9
9,10-Anthracenedicarbonitrile	66.6	9.8	14.5	1.7	7.4
4,4`-Biphenyldicarbonitrile	72.8	7.4	12.0	0.4	7.4

Deconvolution of the C1s peak of the materials showed a main peak at 284.5±0.31 eV, attributed to the graphitic C, in agreement with photoemission studies on carbon materials.[40] The peak at 285.5 ± 0.2 eV is assigned to the combination of aryl carbon bonded to –Cl and / or double bonded to N,[41] whereas the peaks at 286.15 ± 0.25, 287.55 ± 0.31 and 288.65 ± 0.26 eV are due to the existence of carbon atoms attached to different O-moieties in the form of ether/alcohol, ketone, and carboxylic acids, respectively.[42,43]

Quantitative analysis of the XPS data showed the presence of 59.2-72.8 % of graphitic C in all N-modified carbon materials. From C1s line of carbon derived from tetrachloroterephthalonitrile, the decrease of the sp^2 graphitic C contribution (by ~ 10 %) and concomitantly the increase of contribution from the C–Cl groups was observed. The -Cl incorporation (1-2 wt. %) in other carbons was due to the use of $ZnCl_2$ as catalyst. The aryl-OH (12-14.7 %), C=O (≤ 3.8 %) and RCOOH (carboxylic acid) (≤ 7.4 %) groups in all materials were due to acid hydrolysis reaction, at high temperature and pressure (simultaneously generated in the synthesis ampule).[44,45]

4.4.2 Cl₂ activation study

In the attempt to find a correlation between the chemical configuration of the N substituent in the composition of various carbon materials, the surface reactivity, and the potential of this

material in carbon catalyzed $COCl_2$ synthesis, the Cl_2 activation study has been performed by using a pulse quartz reactor (schematic view of the setup is available in supplemental material, Figure S4-1). Following the thermal activation of the selected carbon materials it was shown that the immediate formation of HCl (m/z: 36) takes place (Figure 4-6).
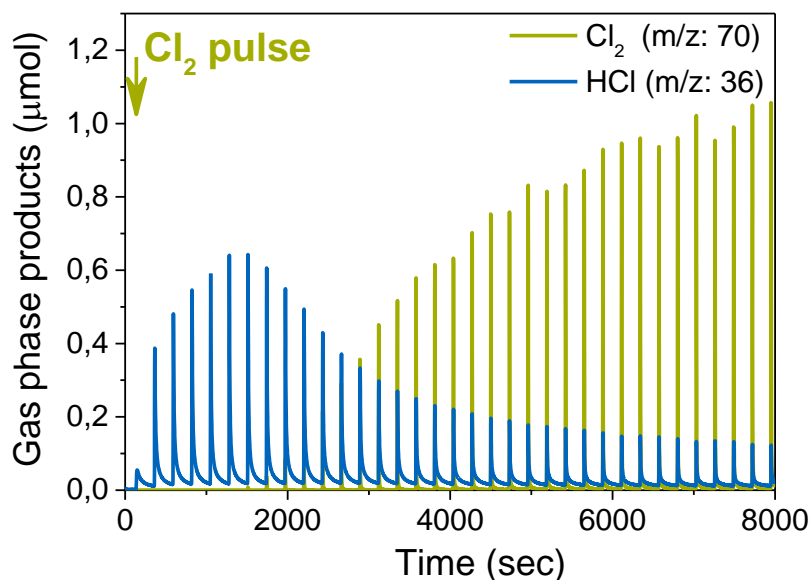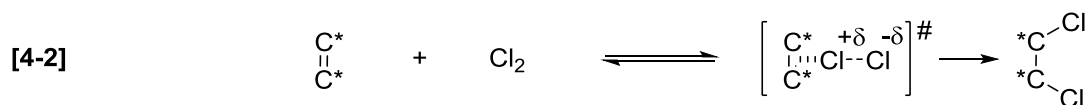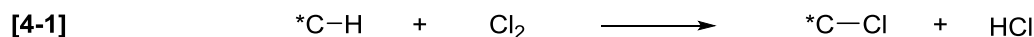

Figure 4-6. Cl_2 activation study. Experimental conditions: 35 Cl_2 pulses (230 s pulse length, 1.8 μmol Cl_2 / pulse), He flow: 10 ml/min, 10 mg of polymer A synthesized from 1,4-dicyanobenzene.
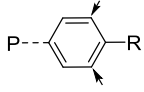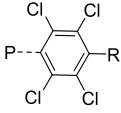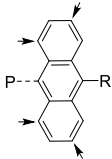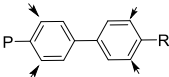
In that time no molecular Cl_2 (m/z: 70) is detected in the gas phase, indicating irreversible surface processes are probable (equation 4-1 and 4-2).

[4-1] $*C{-}H$ + Cl_2 $\longrightarrow$ $*C{-}Cl$ + HCl

[4-2] $\begin{matrix} C^* \\ \| \\ C^* \end{matrix}$ + Cl_2 $\rightleftharpoons$ $\left[\begin{matrix} C^* \\ \vdots \\ C^* \end{matrix} {\overset{+\delta}{Cl}}{\cdots}{\overset{-\delta}{Cl}} \right]^{\#}$ $\longrightarrow$ $\begin{matrix} *C \\ *C \end{matrix}\begin{matrix} {\diagup}Cl \\ {\diagdown}Cl \end{matrix}$

The irreversible addition and substitution of Cl_2 is hypothesized to primarily occur on the most reactive sites, i.e., the defect sites and unsaturated carbons located at zig-zag edges and terminating positions.[46]

The amount of irreversible Cl_2 uptake and HCl formed on the investigated carbon materials during Cl_2 treatment at 473 K are summarized in Table 4-5.

Table 4-5. Cl_2 adsorption on N-modified carbon materials at 473 K.

Polymer	Defect/edge sites	Nr. of available sites per aromatic linkage for irreversible adsorption	Irreversible Cl_2 uptake (mmol/g)				HCl formation (mmol/g)	
			N-functionalities		Accessible "C" sites		R-NH$_2$	Accessible "C" sites
			A[a]	S[b]	A	S		
A		2	0.45	0.21	1.09	1.00	0.21	1.00
B		0	0.73	0.29	0	0	0.29	0
C		4	0.14	0.08	4.23	2.11	0.084	2.11
D		4	0.12	0.17	4.13	1.78	0.17	1.78

P = polymeric network as proposed in Figure 4-1, R = N and O-based substituents. [a]A = Addition reaction, [b]S = substitution reaction.

The obtained results show clearly that there is no correlation between the amount of total Cl_2 uptake and the specific surface area of catalysts. However, in general, the amount of irreversible Cl_2 uptake is proportional to that of HCl formed, although it is invariably less than the initial H content of materials (27.9 - 30 mmol / g for polymer A, C and D and 18 mmol / g for polymer B) indicating that on the active surface of the carbon various addition reactions at unsaturated positions are similarly favored.

Terminal positions of the polymers mainly comprises $-C{\equiv}N$ or $-C-NH_2$ groups (Table 4-2), that are strongly activating the aromatic rings by increasing the electron density of the π-system making it concomitantly more nucleophilic. These are considered to be responsible for the facile irreversible oxidative addition and substitution reactions with Cl_2.[47] To experimentally prove this hypothesis, 1,4-dicyanobenzene was used as a well-defined probe molecule (experimental measurement details summarized in supporting information Figure S4-9). Cl_2 pulses conducted in the presence of aromatic nitriles resulted in the irreversible Cl_2 addition and HCl formation.

In separate control experiments, the role of the aromatic amines in the Cl_2 activation has been tested. In the case of 1,4-diaminobenzene, a model molecule having two amine substituents on the aromatic ring, show a fast interaction with Cl_2 and results in immediate formation of chlorination products (detailed information provided in Table 4-6 and supplemental material, see Figure S4-9).

In line with previous experimental observations made for the polymers, experimental results clearly evidence that aromatic amines are promoting the irreversible consumption of Cl_2 on secondary reaction pathways.[50,51] Chlorination of aromatic amines may be accomplished without the need for highly polar solvents or of an added catalyst, which is often employed for electrophilic aromatic substitutions.[52] In this reaction, the formation of a N-chloramine as a reaction intermediate is assumed to occur before the intramolecular delivery of electrophile chlorine *via* the heterolytic cleavage of N-Cl bond takes place and leads to the formation of halogenated aromatic compounds. In the current experiment, a direct correlation was found between the initial Cl_2 uptake and the number of free accessible aromatic sp^2 carbon sites located at vicinal ortho and para positions of an electron directing amine or nitrile functionality (Figure 4-7 (a)).
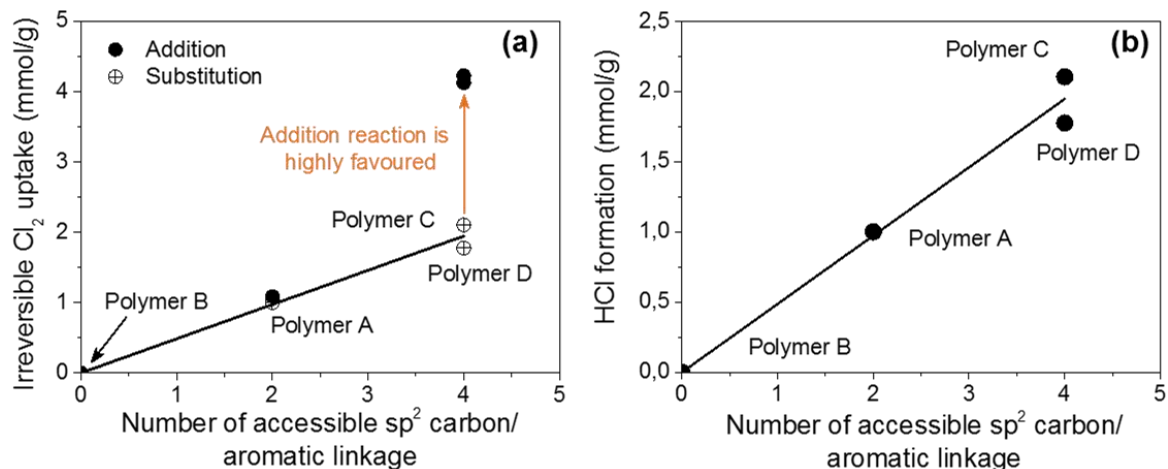
Figure 4-7. Correlation between free accessible sp^2 C sites in the aromatic ring in the terminal polymer structure and initial Cl_2 uptake at 473 K (a) and amount of HCl formed at 473 K (b).

In case of polymer B, a material having all the active carbon sites blocked by Cl_2, the irreversible Cl_2 uptake and HCl formation takes preferentially place on the amine functional groups leading to the formation of chloroamines and HCl as specified in the general Eq. 4-3.[60]

[4-3] $R\text{-}NH_2$ + Cl_2 $\longrightarrow$ $R\text{-}NHCl$ + HCl
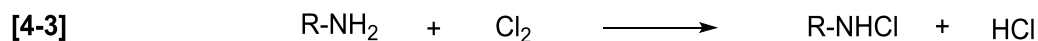
Furthermore, the 3.5 times higher Cl_2 uptake as HCl release indicate the further contribution of the lone electron pair of the N-atoms in triazine to the formation of a non-covalent chlorine adduct, as suggested by previous DFT calculations of Cl_2 interactions with triazine.[53]

The irreversible Cl_2 uptake on the amine functionalities and triazine units located in polymer A, C and D are listed in Table 4-5.

The observed linear dependence of irreversible Cl_2 uptake from the availability of nucleophilic carbons located at the ortho and para positions of the aromatic linkages in polymer A, C and D suggests that these sites due to their electronic environment are favoring the transiently formed electrophile Cl_2 adsorption and formation of strong carbon chlorine covalent bonds as depicted in Scheme 4-1.[48,49,50]
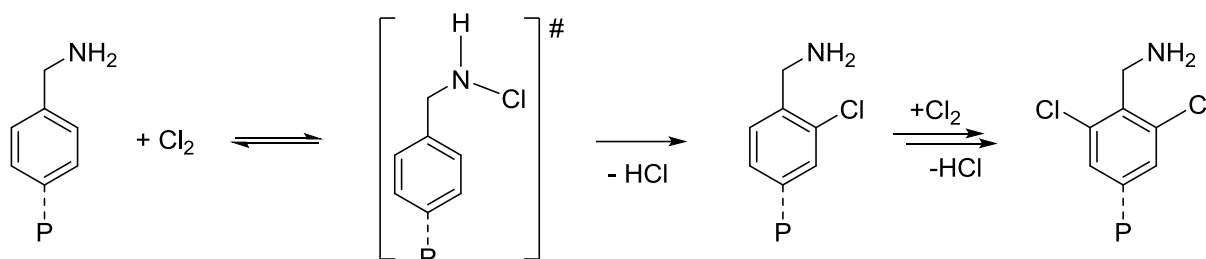
Scheme 4-1. Proposed reaction sequence that would account for the aromatic amine promoted irreversible Cl_2 interaction and HCl formation.

Direct reaction with the adjacent carbon favors the formation of mono-chlorinated aromatic compounds and HCl. Compared to polymer A, Cl_2 addition to polymer C and D results in about four times higher Cl_2 uptake and two time higher HCl formation since the aromatic linkers used in these two materials have a larger fraction of accessible sites (Figure 4-7 (a) and (b)). Accurate analysis of the irreversible Cl_2 consumption on diverse reaction routes (addition and substitution reactions) in polymer C and D evidenced that about two times greater Cl_2 (4.37 mM Cl_2 / g for polymer C and 4.26 mM Cl_2 / g for polymer D) is preferentially adsorbed / added to the active polymer surface as used in substitution reactions (2.19 mM Cl_2 in polymer C and 1.95 mM Cl_2 in polymer D) as shown in Table 4-5 and Figure 4-7.

After the saturation of these most reactive surface sites, Cl_2 interacts reversibly in a dynamic equilibrium with the surface (Scheme 4-2).

$$*C \;+\; Cl_2 \;\rightleftharpoons\; *C\text{---}\overset{\delta-}{Cl}\text{---}\overset{\delta+}{Cl}$$
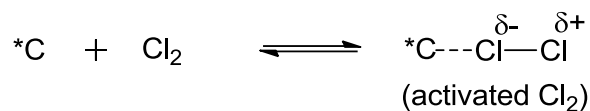
$$\text{(activated } Cl_2\text{)}$$

Scheme 4-2. Schematic representation of the transient formation of activated Cl_2.

The Cl_2 activation mechanism and the formation of reactive Cl_2 intermediates on N-modified material (polymer A) synthesized from 1,4-dicyanobenzene was further studied using in situ Raman spectroscopy (Figure 4-8).
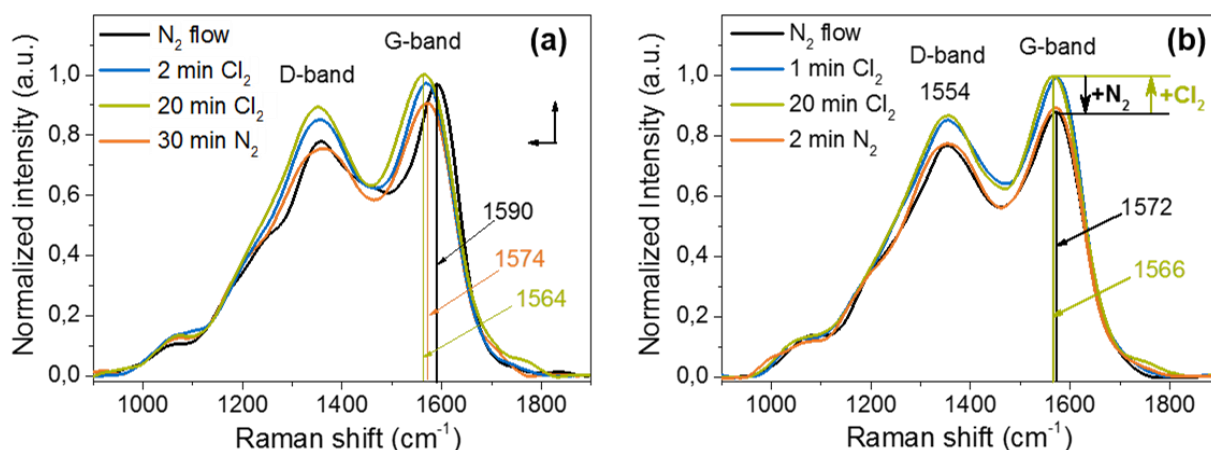

Figure 4-8. In situ Raman spectroscopic study of Cl_2 activation on triazine based polymer A (for structural information see Figure 4-1). In (a) is shown the first cycle of Cl_2 addition. In (b) the second one.

The equal contribution of the active sites located in the amorphous bulk and graphitic well-ordered mixed phase was attributed to the increase in both D- and G- Raman band intensity by Cl_2 addition. Notably, there is a good correlation between the pulse experimental results and the in situ Raman studies referring to the irreversible chemical processes taking primarily place on the various active sites located in material A. In the first cycle of recorded Raman spectra, the irreversible addition and substitution reactions on the more active sites of the carbon material will lead to irreversible changes in the Raman spectra of the mesoporous carbon (Figure 4-8 (a)), while following the saturation of these sites, the reversible interactions are enabled as revealed in the second cycle (Figure 4-8 (b)). Comparison of Cl_2 activation results obtained with the same procedure on non-modified planar HSAG (shown in Figure 4-9) resulted in clear experimental evidence for the enhanced adsorption and activation ability of nitrogen functionalized carbon materials.
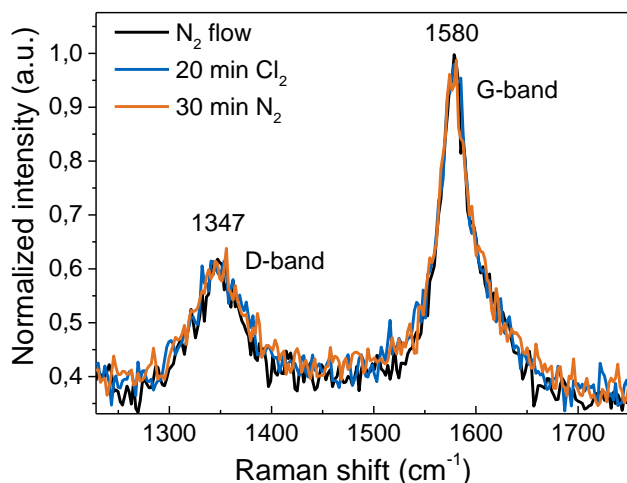
Figure 4-9. Cl_2 activation study on HSAG using in situ Raman spectroscopy.

The electronic nature of the surface activated Cl_2 under steady state conditions was probed by in situ electron spin resonance (ESR) spectroscopy. The transient formation of radical Cl_2 species on N-modified C has been excluded on the basis of the unchanged signal in the ESR spectra obtained after the Cl_2 addition to the N-modified materials (Supporting Information, Figure S4-10).

To further discriminate the ionic from radical nature of the activated Cl_2 the chlorination of CH_4 was used as probe reaction, because it is well-known that the multiple C-H bond substitution proceeds *via* a radical mechanism.[52]
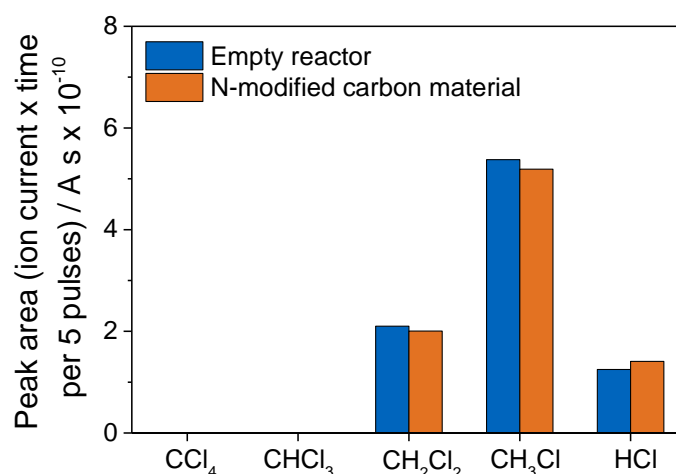
Figure 4-10. Probing activated Cl_2 with CH_4. Experimental conditions: 100 pulses (first 50 Cl_2 pulses till steady state conditions, 230 s pulse length, 1.8 μmol Cl_2 / pulse), 5 vol. % CH_4 in He flow: 10 ml/min, T = 473 K, 10 mg of mesoporous carbon A (shown in Figure 4-1).

The experiments showed clearly that during the Cl_2 activation processes enabled on the active sites of the nitrogen modified carbon material A no substitution in CH_4 in excess to what is observed in the empty reactor (Figure 4-10) is taking place. Thus, we conclude that with the 1,4-dicyanobenzene derived carbon did not activate Cl_2 in a radical pathway.

Similarly, the Cl_2 activation study on the N-modified carbons C and D obtained from 9,10-anthracenedicarbonitrile and 4,4`-biphenyldicarbonitrile using Raman and ESR spectroscopy, confirmed the ionic type of reversibly activated surface species formation as depicted in Scheme 4-2.

However, Cl_2 activation processes on materials with a high content of amine and pyrrolic-N functionalities that mainly promote aromatic *C-H bond substitution by Cl_2 and lead to the formation of covalently bound –Cl on sp^2 carbon site showed a more accentuated shift and change in D and G- bands intensity as shown in Figure 4-11.
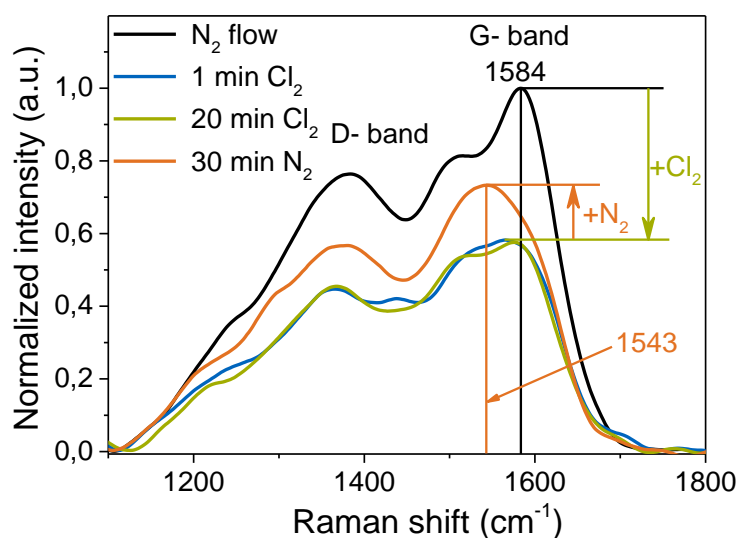
Figure 4-11. In situ Raman spectra of activated Cl_2 on material B obtained from tetrachloroterephthalonitrile.

The material B derived from tetrachloroterephthalonitrile includes sp^2-C hindered by the covalently bound –Cl and results in a different type of Cl_2 interaction. Therefore, the site for the reversible Cl_2 interaction with the catalyst obtained from tetrachloroterephthalonitrile may be is the lone electron pair of the N-atom resulting in the formation of a non-covalent adduct, as depicted in Scheme 4-3. This adduct has been suggested by previous DFT calculations of Cl_2 interactions on triazine.[53]
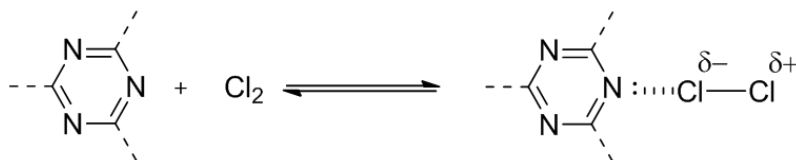
Scheme 4-3. Proposed Cl_2 activation on material from tetrachloroterephthalonitrile.

To demonstrate the Cl_2 activation process at the molecular level, the N-containing model molecules were examined using in situ Raman spectroscopy at 313 K (Table 4-6).

Table 4-6. Summary of Cl_2 activation study on well-defined N-modified model molecules using in situ Raman spectroscopy.

Selected model molecules	N-type[a]		Cl_2 activation			Adsorption
	Py-N (wt.%)	Quart-N (wt.%)	Typical Raman bands (cm^{-1})			
2,6-Dichloropyridine	9.46	-	160, 274, 398	743	907	Reversible
2,4,6-Trichloropyridine	7.68	-	-	-	-	Weak physisorption
2,6-Dichloropyridine N-oxide	8.54	-	-	-	-	No interaction
Melamine	66.64	-	-	-	-	No interaction
Cyanuric chloride	22.79	-	-	-	-	No interaction
BTIC	-	8.22	307, 352, 399	-	-	Reversible
BTDIY	-	9.20	272	-	-	Reversible
EDITM	-	10.21	-	-	-	No interaction

Type-1: 2,6-Dichloropyridine, 2,4,6-Trichloropyridine, 2,6-Dichloropyridine N-oxide, Melamine, Cyanuric chloride. Type-2: BTIC, BTDIY, EDITM.

[a] Calculated based on structure.

First, the role of pyridinic-N was studied by considering two model compounds, i.e., pyrazine and s-triazine. The band at 1013 cm^{-1} corresponds to a pyrazine ring vibration and the band around 3000 cm^{-1} is due to C-H bond vibration (supporting information, Figure S4-11). Cl_2 addition to the pyrazine increased the intensities of Raman bands and further resulted in the irreversible Cl_2 adsorption of activated Cl_2 species. Irreversible chlorination caused a change in the physical state from solid pyrazine to liquid mono and dichloro pyrazine as confirmed by

liquid state ^{1}H and ^{13}C-NMR (shown in supporting information Figure S4-12). The new bands at 678 cm^{-1} and 1224 cm^{-1} (supporting information, Figure S4-11) in the Raman spectra of the Cl$_2$ treated pyrazine indicate the formation of new covalent C-Cl bonds.[54] In the case of triazine, the Cl$_2$ interaction caused primarily an increase in the Raman band intensity due to the activation of Cl$_2$ on the electron deficient carbon sites as depicted in Scheme 4-4.
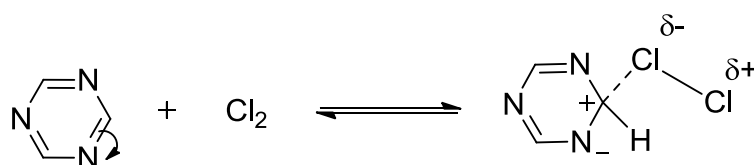
Scheme 4-4. Proposed Cl$_2$ interaction with s-triazine.

In this case Cl$_2$ is activated on the carbon site next to the pyridinic N-atom by the formation of a *C····Cl$_2$ adduct of ionic character. The electron deficient site is generated by the electronic resonance as shown in Scheme 4-5.
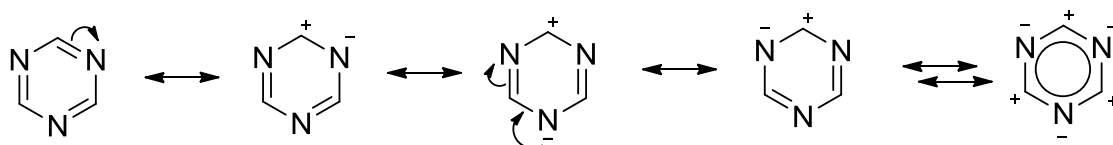
Scheme 4-5. Resonance structures of s-triazine.

In the presence of transiently generated ionic Cl$_2$ a more accentuated decrease in Raman bands intensity is caused by the consecutive reaction of the activated Cl$_2$ intermediates with the nitrogen functionalities (supporting information, Figure S4-13). This experimental observation is in good agreement with the literature reported data.[56]

To gather better insight for the location of the active sites responsible for the Cl$_2$ activation, melamine and cyanuric chloride were selected as model molecules. In melamine and cyanuric chloride all the carbon atoms adjacent to a pyridinic nitrogen are functionalized by covalently bound electron donating –NH$_2$ and electron withdrawing –Cl, respectively.

Raman spectra of Cl$_2$ interacting with melamine and cyanuric chloride showed no change in Raman bands because the sites for the Cl$_2$ activation were highly hindered by the covalently bound amine (-NH$_2$) groups in melamine and chlorine (-Cl) in cyanuric chloride (supporting information, Figures S4-14 and S4-15). It is interesting to note that the cyanuric chloride can better stabilize electron deficient C (Huckel charge: 0.463953) proximate to pyridinic-N

(Huckel charge: -0.487611, calculated by using Chem 3D Pro, Version 12.0.2.1076). Importantly, these experiments indicate that the site for Cl_2 activation is an electron deficient C-atom and not the pyridinic N-atom itself. Pyridinic N-modification only enhances the electron delocalization and creates a new site on sp^2-C of electrophilic character for the Cl_2 activation significantly enhancing the adsorption of Cl_2.

The requirement for a site in N-modified carbon for the reversible Cl_2 activation was explored by selection of three further model materials; 2,6-dichloropyridine, 2,4,6-trichoropyridine and 2,6-dichloropyridine N-oxide. Cl_2 activation on 2,6-dichlropyridine was studied under analogous experimental conditions using in situ Raman spectroscopy (Raman spectrum of 2,6-dichlropyridine recorded in N_2 is shown in the supporting information Figure S4-16a). Cl_2 addition resulted initially in an increase in the Raman band intensities with exposure duration. Continuous Cl_2 treatment (over 7 min continuous Cl_2 flow) showed the decrease in the bands intensity with consequent appearance of various new bands at 160, 274, 398, 743, 884 and 907 cm^{-1} (Table 4-6 and Figure S4-16b). The more intense band at 398 cm^{-1} is assigned to the symmetrical mode vibration of the polarized Cl_2 while the bands at lower wavenumbers belong to the bending mode of the activated Cl_2. The asymmetric vibration modes of the polarized chlorine are observed at higher wavenumbers, at 884 and 907 cm^{-1}. Based on the new band formation the Cl_2 activation mechanism is proposed in Scheme 4-6.
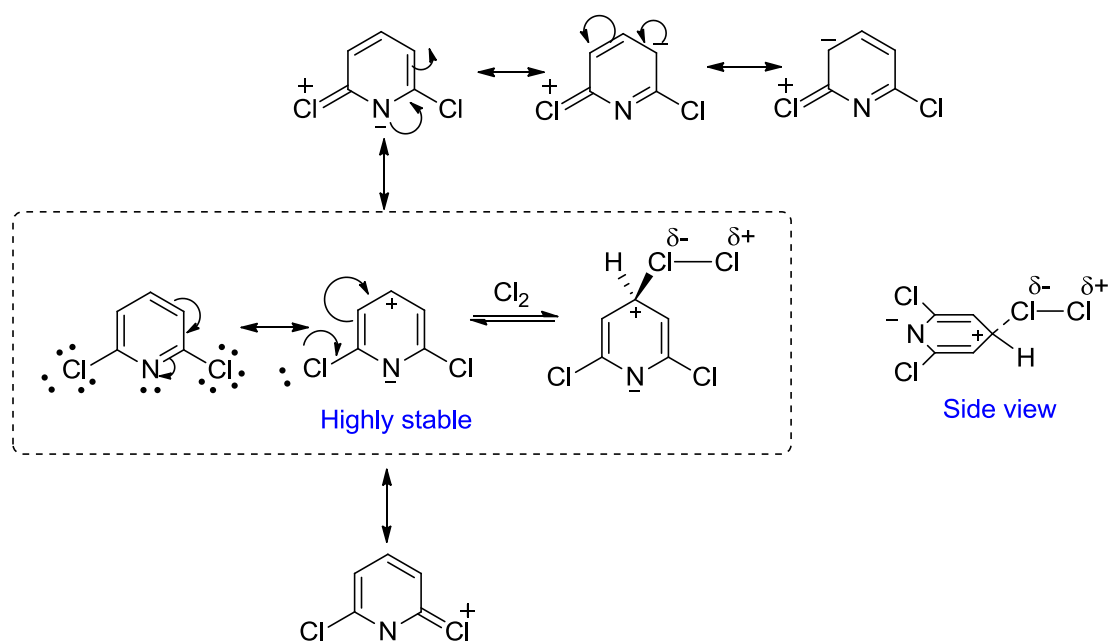
Scheme 4-6. Proposed Cl_2 activation mechanism on resonance stabilized 2,6-dichloropyridine.

The proposed Cl_2 activation takes place at the para-position of 2,6-dichloropyrdine, where the positive charge on the carbon is stabilized by the negative charge on highly electronegative N (Scheme 4-4) by the formation of non-covalent C*····Cl_2 adduct of ionic character. The location of the Cl_2 activation site on the para-position of 2,6-dichloropyridine was further verified by using 2,4,6-trichloropyridine, a molecule having the para-position already blocked by covalently bound –Cl. In the case of 2,4,6-trichloropyridine molecule can stabilize the electron deficient carbon on the para-position, but steric hindrance of covalently bound –Cl blocks the accessibility of the site for Cl_2 interaction. Further experimental evidence for the lack of a Cl_2 interaction ability in the case of 2,4,6-trichloropyridine was provided by the in situ Raman spectroscopic study was performed at 313 K. Recorded Raman spectra during the Cl_2 addition to the materials showed only a weak reversible interaction without any new band formation (shown in supplemental information Figure S4-17). Additionally, the selection 2,6-dichlropyridine N-oxide provides the facts about the generation of a new active carbon site under the electronic effect of pyridine N-atom, not due to the inductive effect of –Cl substituents. Cl_2 interaction on 2,6-dichlropyridine N-oxide using in situ Raman spectroscopy displayed unchanged spectral features (supporting information, Figure S4-18). These experiments support the fact that the activity of the electron deficient carbon site is induced by electronic resonance by the lone pair on pyridine-N atoms. The N^+–O^- groups are highly stable under a Cl_2 atmosphere.

N-modified materials contain not only the pyridinic N-modification but also quaternary N-modification as evidenced by the XPS analysis (Table 4-1). In order to understand the role of quaternary N-modification into N-modified carbon, 1,3-bis(2,4,6-trimethylphenyl)-1,3-dihydro-2H-imidazol-2-ylidene (BTDIY) was selected. The possible Cl_2 and BTDIY interaction was studied using in situ Raman spectroscopy (Figure 4-12). The reversible new band at 272 cm^{-1} by Cl_2 addition was due to the formation of [BTDIY····Cl_2] adduct as shown in Figure 4-12, see also Scheme 4-7.
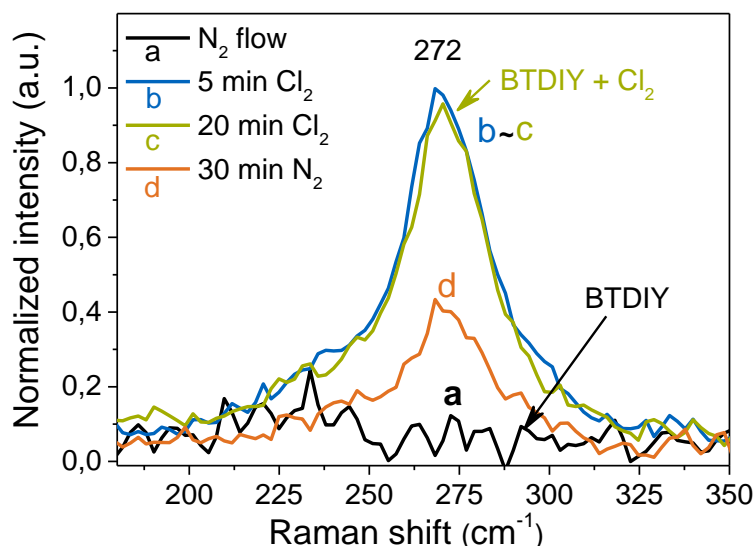
Figure 4-12. In situ Raman spectroscopy of Cl_2 interaction with BTDIY.

To gain knowledge on the electronic nature of activated Cl_2 on carbene in situ ESR spectroscopy was employed. The recorded ESR spectrum under ambient conditions (313 K, 101 kPa and Ar) showed a strong signal at g value 1.9882 ± 0.0012 confirming the presence of quaternary-N stabilized paramagnetic sites on BTDIY (Figure 4-13). The two quaternary N atoms stabilize the carbene through σ-electron acceptor and π-electron donor synergy.[24] Changing the gas from Ar to Cl_2 diminishes the ESR signal intensity, indicating the [BTDIY····Cl_2] adduct formation of ionic character.
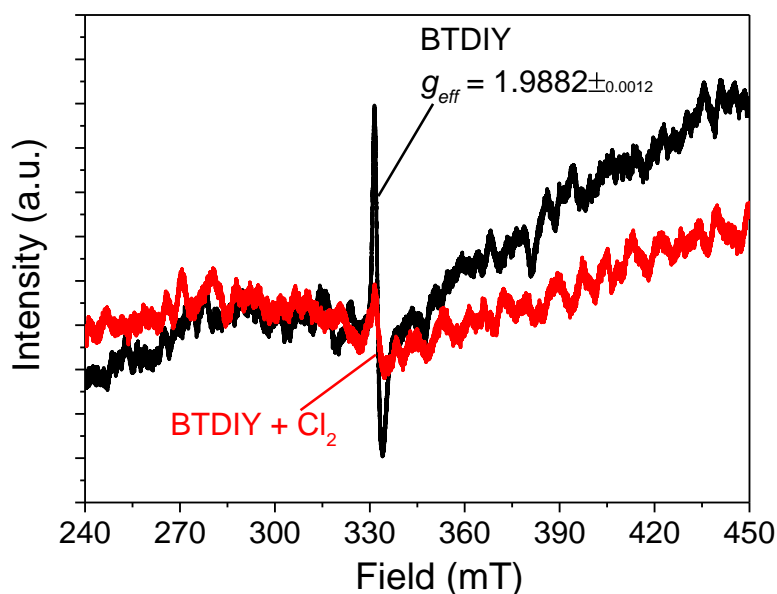
Figure 4-13. In situ ESR spectra of BTDIY recorded under inert conditions at ambient temperature (black) and in Cl_2 atmosphere (red).

Materials characterization using ^{1}H and ^{13}C NMR spectroscopy after Cl_2 interaction at 313 K evidenced the surface modification and substitution of -H from the 4th and 5th positions by covalently bound –Cl. This results in the generation of air stable carbene and in a better stabilized activated ionic Cl_2 intermediate.[56,57] The proposed Cl_2 activation mechanism of BTDIY is depicted in Scheme 4-7.
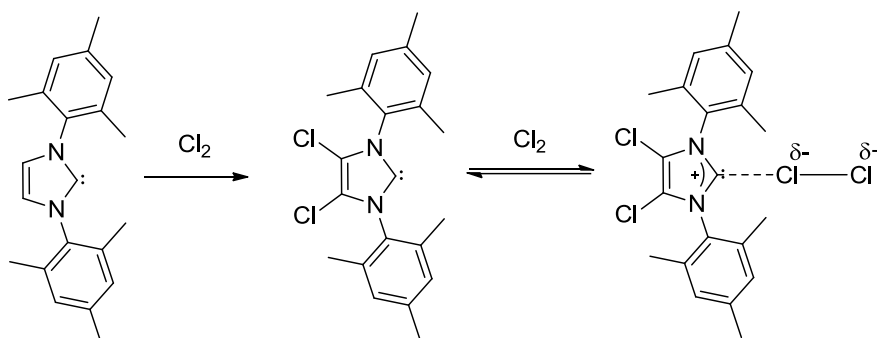
Scheme 4-7. Proposed Cl_2 interaction with BTDIY.

The catalytic Cl_2 activation on other possible quaternary N- containing molecules was studied by using another imidazolium based material, 1,3-bis(2,4,6-trimethylphenyl)imidazolium chloride (BTIC, Figure 4-3b). Cl_2 addition results in additional new band at 352 cm^{-1}, corresponding to the activated Cl_2 on BTIC (see SI, Figure S4-20). The broad band at 352 cm^{-1} is the combination of three Raman bands (two prominent bands at 307, 352 and one weak at 399 cm^{-1}) as shown in Figure 4-14.
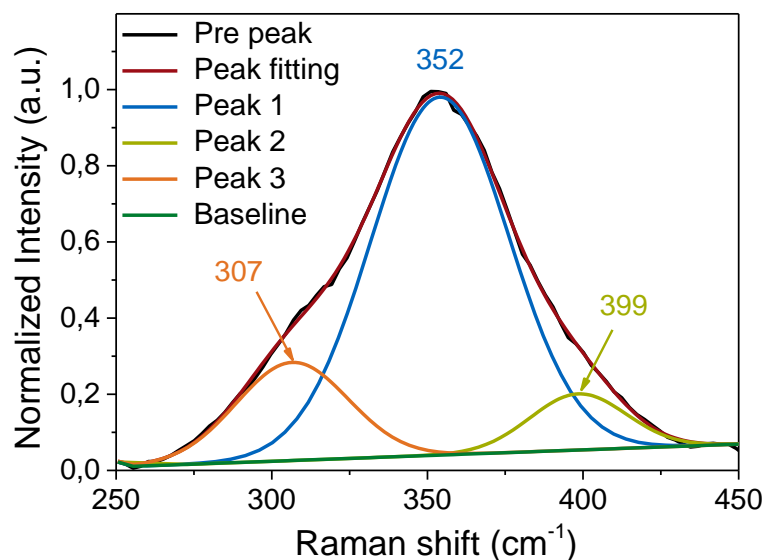
Figure 4-14. Deconvolution of Raman spectra of activated Cl_2 on BTIC.

Further N_2 flow, after discontinuing Cl_2 flow, confirmed the reversibility of the species formed. The development of the multiple Raman bands is indicative of the trichloride monoanion (Cl_3^-) formation as previously studied by Riedel et al.[58] The major band at 352 cm^{-1} is indicative of a connected Cl_2 unit, whereas the weak Raman bands at 307 and 399 cm^{-1} are assigned to Cl^-•••Cl_2 weak interactions. The transiently formed activated Cl_2 of ionic character was confirmed by using in-situ ESR spectroscopy. Extensive Cl_2 exposure (~20 minute) did not induce any ESR signal (supporting information, Figure S4-20).

To further test the assignment of the site on a carbon atom of imidazolium, 1-ethyl-2,3-dimethylimidazolium-trifluoromethanesulfonate (EDITM, Figure 4-3c) was studied for its ability to activate Cl_2. EDITM contains carbon sites substituted by a methylene group, situated in-between two quaternary N-atoms using in situ Raman spectroscopy (supporting information, Figure S4-21). Cl_2 addition did not induce spectral changes during exposure for 1200 s, demonstrating the importance of accessible, non-substituted, C atoms between quaternary N-atoms in catalysts.

4.4.3 CO activation study

In order to rigorously analyze any enabled interactions of CO with the nitrogen doped carbon materials, CO pulses were injected in He on N-modified material synthesized from 1,4-dicyanobenzene at 473 K (Figure 4-15a).
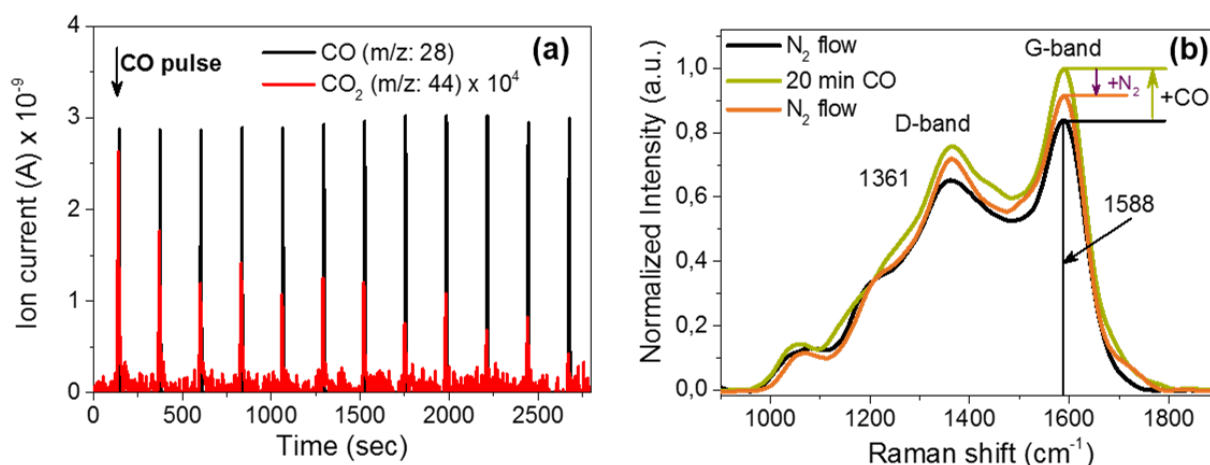
Figure 4-15. CO interaction study on N-modified material synthesized from 1,4-dicyanobenzene, (a) transient MS analysis, (b) in situ Raman spectroscopic study.

Transient MS analysis of repetitive CO pulses showed a weak reversible interaction and a small amount of CO_2 (0.1 μmol/g) formation (Figure 4-15(a)). In situ Raman spectroscopic measurements further confirmed the weak reversible interactions of CO, a weak nucleophile, (Figure 4-15(b)) with the electrophilic carbon sites leading to the formation of electron donor-acceptor adducts as proposed in Scheme 4-8.

C*   +   CO   ⇌   C*◄----:C꞊Ö:

Electrophilic C   [Lewis acid$_{(s)}$-Lewis base$_{(g)}$ adduct]
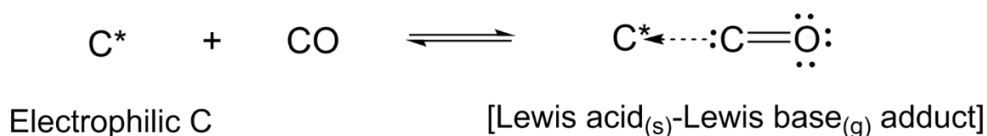
Scheme 4-8. Proposed CO interaction with N-modified carbons, C* represent to the electrophilic carbon.

The resistance to chemical poisoning of the materials during the activation processes has been studied by HR-SEM, and XPS. In this way it was possible to demonstrate that the surface bulk structure and elemental compositions of N-modified material is hardly affected by CO interaction at 473 K (Figure 4-16).
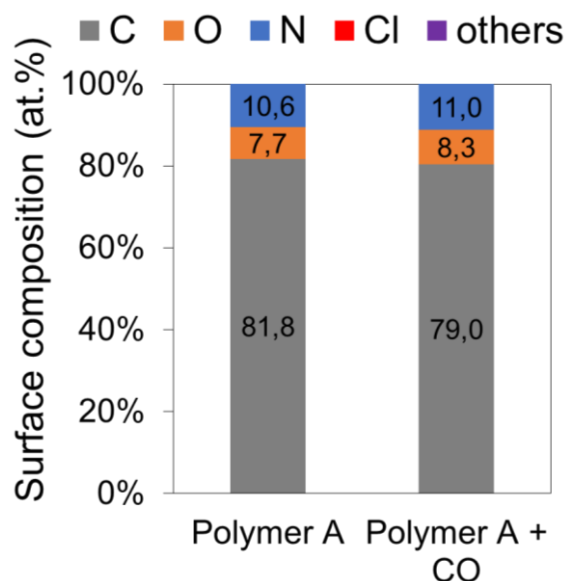
Figure 4-16. Comparisons of surface compositions using XPS of sample before and after CO interaction.

The change in N- containing functional groups of the polymer A during CO treatment was studied by the deconvolution of N1s and C1s-XPS peaks applying Shirley background

correction and using Gauss-Lorentz peak shape with setting the minimum to 60 %. The contributions of different nitrogen species to the N 1s peaks are summarized in Figure 4-17(a).
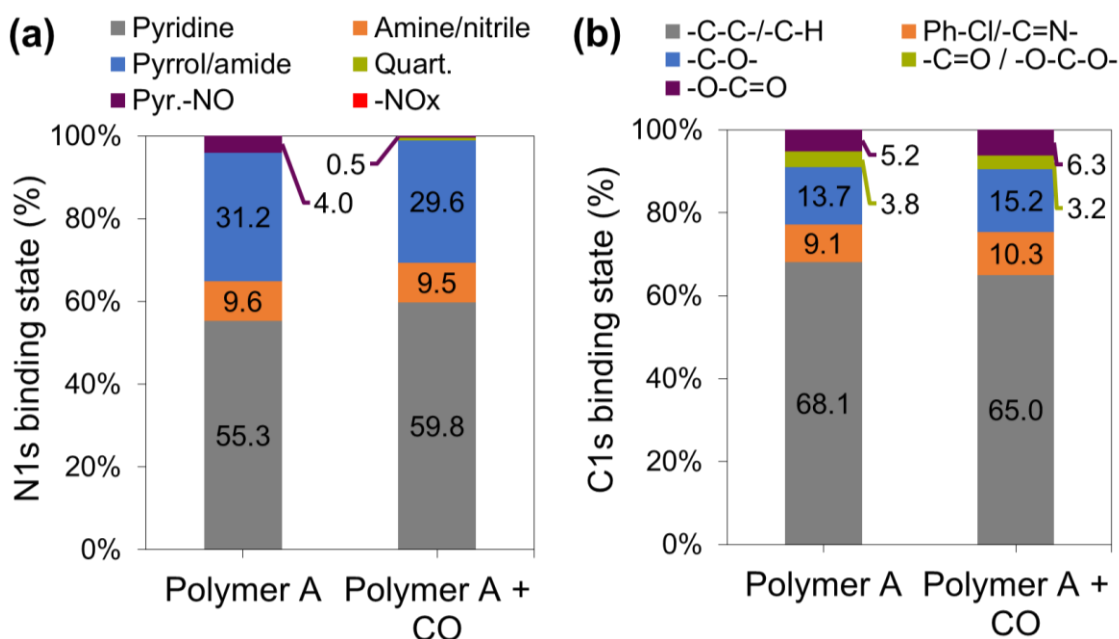
Figure 4-17. Change in binding state by CO interaction of material from 1,4-dicyano benzene, (a) N1s and (b) C1s.

The N 1s spectra for fresh and CO adsorbed samples shows no significant change in amine, pyrrol, and quaternary N-functionalities. However, decrease in pyridinic-N oxides content by 3.5 % with subsequent increase in pyridinic-N of 4.5 % during CO interaction was considered due to the surface oxidation reaction as shown in Scheme 4-9.
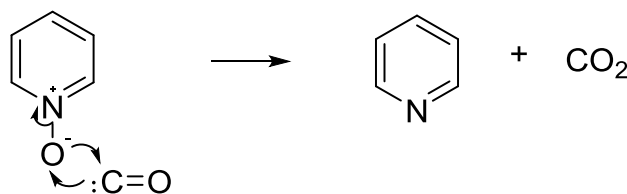
Scheme 4-9. Proposed mechanism of pyridine N- oxides to pyridine during CO interaction.

Deconvolution of C1s binding state indicates the presence of highly stable oxygen functional groups in CO atmosphere which is proven by only marginal (± 1 %) changes on surface oxygen groups after CO treatment at 473 K (Figure 4-17b).

4.4.4   CO interaction on Cl_2 exposed N-modified carbon

For a better understanding of the underlying reactions taking place during $COCl_2$ synthesis, temperature dependent in-situ Raman experimental investigations were performed for the CO interaction with Cl_2 treated polymer A (Figure 4-18).
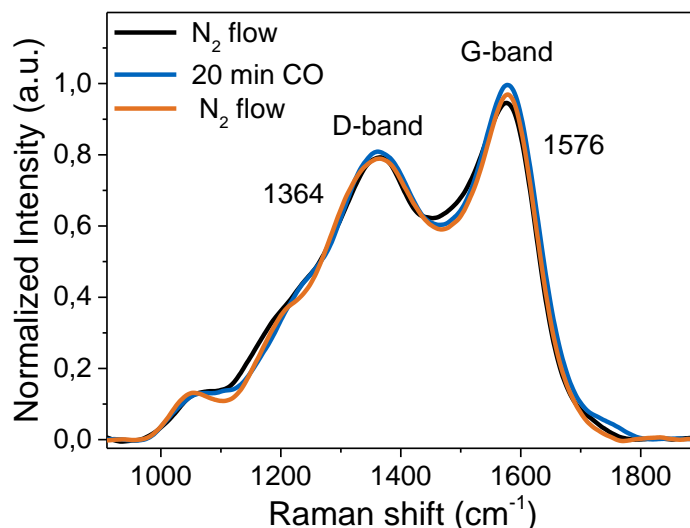
Figure 4-18. In situ Raman spectroscopic study of CO interaction on Cl_2 treated N-modified carbon material from 1,4-dicyanobenezene.

Detailed analysis of the CO interaction with material A synthesized from 1,4-dicyanobenzene under analog conditions reveal only a weak CO adsorption because of preferential adsorption of Cl_2 on the surface, demonstrating a similar nature of sites that are responsible for CO interaction and Cl_2 activation. However, the extensive CO treatment did not affect the active carbon surfaces responsible for Cl_2 activation. Based on these results the electrophilic carbon site is considered to be of importance for both CO and Cl_2 molecule activation. Nevertheless, the Cl_2 activation is dominant in the presence of both molecules in the system.

4.4.5   Mechanistic study for $COCl_2$ synthesis on nitrogen modified carbon

To understand how the surface N-modification influences the catalytic activity of the selected materials, the $COCl_2$ formation was studied by using the material synthesized from 1,4-dicyanobenzene (Figure 4-19).
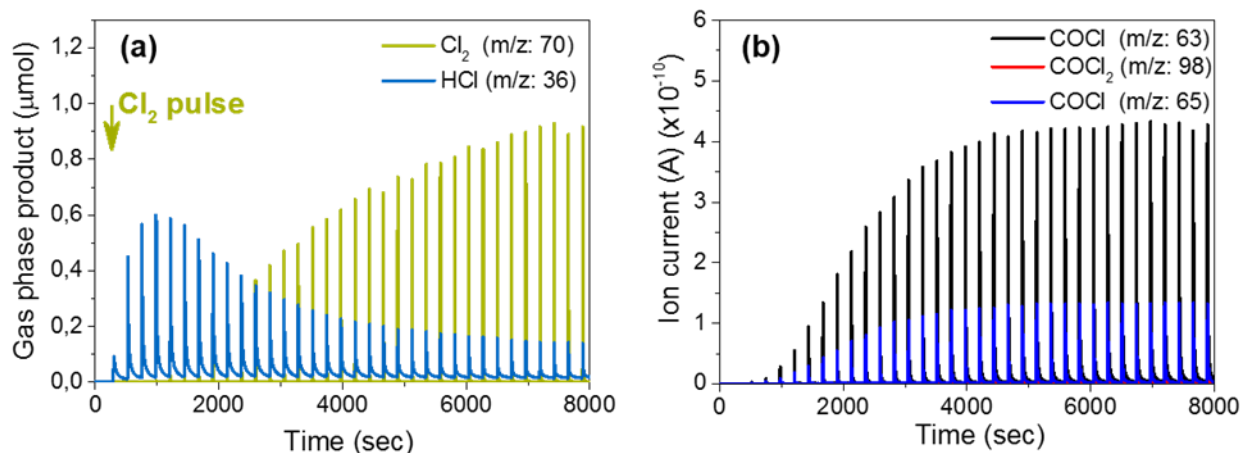
Figure 4-19. (a) Cl_2 adsorption at 473 K in 5 vol. % CO and (b) $COCl_2$ synthesis. Experimental conditions: 35 Cl_2 pulses (230 s pulse length, 1.8 μmol Cl_2 / pulse), 5 vol. % CO in He flow: 10 ml/min, 10 mg of N-modified carbon material.

At the beginning, the Cl_2 pulses resulted in HCl (1.17 mmol/g) formation. The amount of HCl formed by Cl_2 pulsing in CO atmosphere was very similar in amount to the HCl formed from Cl_2 pulses only in He (1.210 mmol/g, Figures 4-19 and 4-6) clearly indicating that the most reactive sites located on N-modified material selectively interact with Cl_2 without an effect of CO. Following the partial saturation of these reactive sites after about 1000 s, Cl_2 was detected in gas phase. At the same time, $COCl_2$ was also detected by gas phase MS analysis noticeably showing that after the irreversible Cl_2 interaction on the reactive sites, Cl_2 is reversibly activated on the electrophilic carbon sites of the N-modified carbon material. The reversibly activated Cl_2 reacts with CO resulting in $COCl_2$ formation. The $COCl_2$ formation occurred only in the presence of Cl_2 in the gas phase system, indicating the importance of non-dissociative activated Cl_2 for $COCl_2$ synthesis.

To explore the impact of electronic variations in the N-functionalization for $COCl_2$ synthesis, several N-modified carbon materials synthesized from different precursors including 1,4-dicyanobene, tetrachloroterephthalonitrile 9,10-anthracenedicarbonitrile and 4,4`-biphenyldicarbonitrile were used. The comparisons of $COCl_2$ formed in pulse mode on N-modified materials from Cl_2 and CO is presented in Figure 4-20.
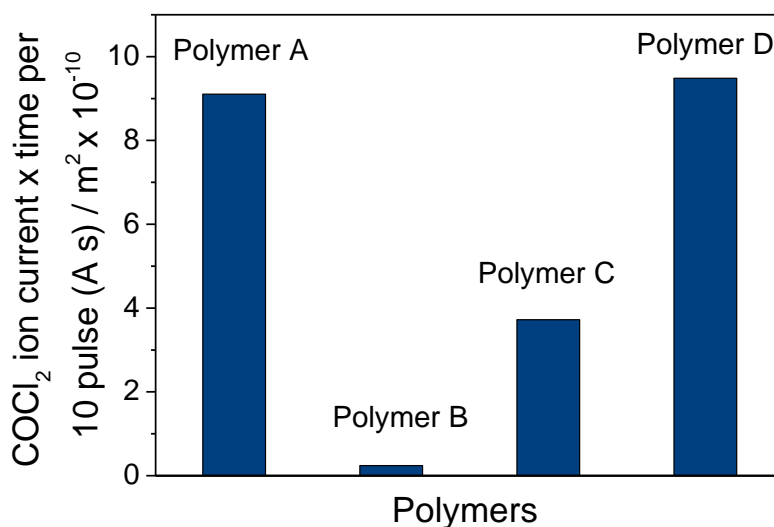
Figure 4-20. Comparisons of phosgene formation on N-modified carbon catalysts. Experimental conditions: 50-100 Cl_2 pulses (230 s pulse length, 1.8 µmol Cl_2 / pulse), 5 vol. % CO in He flow: 10 ml/min, 10 mg of N-modified carbon material. $COCl_2$ estimated after steady-state is achieved.

The materials A and D synthesized from 1,4-dicyanobenzene and 4,4`-biphenyldicarbonitrile catalyzed $COCl_2$ formation to a similar extent (0.10 µmol/$m^2 \times$ s and 0.116 µmol/$m^2 \times$ s, respectively). The material synthesized from the tetrachloroterephthalonitrile precursor had almost no catalytic activity in $COCl_2$ synthesis. The tetrachloroterephthalonitrile-derived carbon generates a material with carbon sites on the aromatic C_6 ring hindered with covalently bound –Cl and intact interconnected triazine rings. The activity test for $COCl_2$ synthesis showed that the covalently surface bound –Cl blocked the site for Cl_2 activation and consequently hindered the $COCl_2$ formation.

All the studied nitrogen carbon materials show high operational stability during $COCl_2$ synthesis. The long-term stability test results in the case of material A is shown in Figure 4-21.
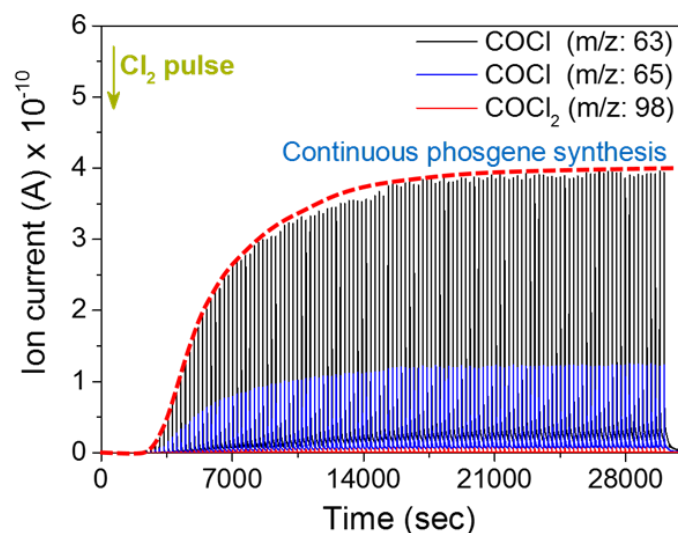
Figure 4-21. COCl$_2$ synthesis; Experimental conditions: 140 Cl$_2$ pulses (230 s pulse length, 1.8 µmol Cl$_2$ / pulse), He flow: 10 ml/min, 25 mg of material A synthesized from 1,4-dicyanobenzene.

The investigation of the long-term operational stability of the triazine based polymer A has confirmed the exceptional stability of the catalyst over COCl$_2$ synthesis duration. Similarly, an exceptional stability under operational conditions was observed for polymer C and D, respectively.

By accurate evaluation of all the spectroscopic analysis and reaction data obtained in the case of nitrogen substituted carbon materials, the following sequential reactions can be proposed for COCl$_2$ formation (Scheme 4-10).
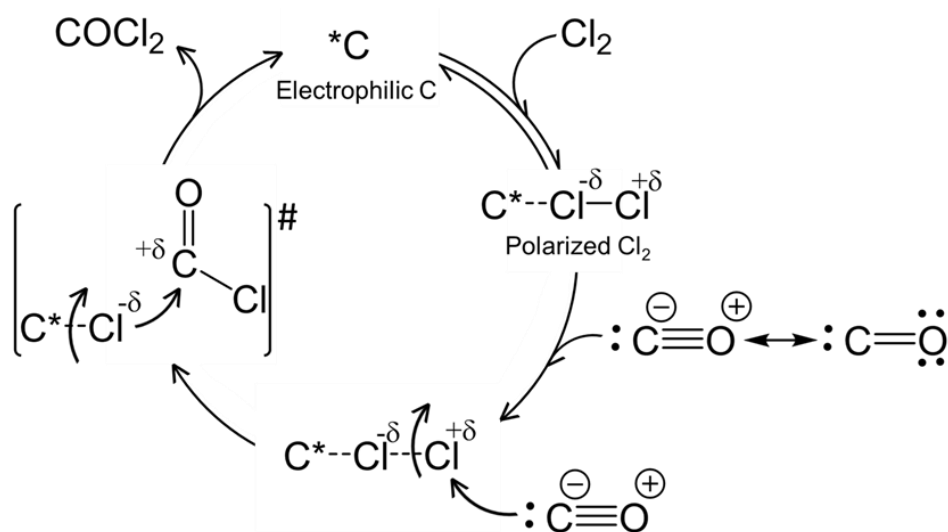
Scheme 4-10. Proposed reaction sequence that counts for COCl$_2$ formation on N-modified carbon materials.

The exposure of nitrogen functionalized carbon materials to Cl_2 results, thus, in associative adsorption of Cl_2 on the electron deficient active carbon sites and the concomitant formation of intermediate activated ionic Cl_2. The subsequent attack of physisorbed CO is hypothesized to lead to the transient formation of acylchloride cation $[^{+\delta}C(O)Cl]$ and weakly bound $Cl^{-\delta}$. Further reactive species $[^{+\delta}COCl]$ react with $Cl^{-\delta}$ and yield $COCl_2$. The proposed reaction sequence is in line with the observed reaction order of one (shown in Table 4-7) for Cl_2 and CO.

Table 4-7. Measured apparent activation energies for $COCl_2$ formation on carbon catalysts.[a]

Polymer precursor	Ea^b [kJ/mol]	Reaction order for Cl_2 and CO
1,4-Dicyanobenzene	34	1
9,10-Anthracenedicarbonitrile	29	1

[a]All catalysts were activated in He (10 cm^3 min^{-1}) for 1 h at 423 K. [b]±3 kJ/mol.

Overall, the apparent activation energy experimentally determined for the two most significant nitrogen modified carbon materials (shown in Table 4-7) was considerably lower (30 kJ/mol) than the one measured for activated carbon (56 kJ/mol[59]) clearly indicating the subtle effect of the local environment of the active sites on the structure and energy of the transition state. In general, the incorporation of nitrogen functionalities with electron withdrawing abilities in heterocyclic moieties, which are stabilized by resonance with the π-electron system, will preferentially contribute to the formation and stabilization of new electron deficient active carbon sites with enhanced adsorption and activation abilities. The selective associative adsorption of Cl_2 on these sites results in the favored intermediate formation of active ionic chlorine species able to further interact with CO and lead to the stable formation of $COCl_2$.

4.5 Conclusions

Combining spectroscopic results and reaction data it was shown that the N modification of C materials is crucial for the formation and stabilization of new active sites for stable $COCl_2$ production. The insertion of nitrogen substituents with electron withdrawing effect enables the formation of new active carbon sites with enhanced adsorption ability for gaseous molecules. The reversible weak associative adsorption of Cl_2 results in the intermediate formation of active chlorine species with ionic character. The ability to generate ionic type of intermediates during

the $COCl_2$ formation is the main reason for the long-term operational stability of the functionalized carbon materials.

4.6 References

[1]   P. Serp, J. L. Figueiredo, *Carbon Materials for Catalysis*; John Wiley & Sons: Hoboken, NJ, **2009**.

[2]   P. Trogadas, T. F. Fuller, P. Strasser, *Carbon* **2014**, *75*, 5.

[3]   M. M. Titirici, R. J. White, N. Brun, V. L. Budarin, D. S. Su, F. d. Monte, J. H. Clark, M. J. MacLachlan, *Chem. Soc. Rev.* **2015**, *44*, 250.

[4]   T. D. Burchell, *Carbon materials for advanced technologies*, Pergamon Press, **1999**.

[5]   N. P. Wickramaratne, M. Jaronie, *ACS Appl. Mater. Interfaces* **2013**, *5*, 1849.

[6]   D. Bégina, G. Ulrichb, J. Amadoua, D. S. Su, C. Pham-Huua, R. Ziessel, *J. Mol. Catal. A: Chem.* **2009**, *302*, 119.

[7]   B. R. Puri, R. C. Bansal, *Carbon* **1966**, *3*, 523.

[8]   P. Zhang, Y. Gong, H. Li, Z. Chen, Y. Wang, *Nat. Commun.* **2013**, *4*: 1593.

[9]   F. Zheng, Y. Yang, Q. Chen, *Nat. Commun.* **2014**, *5*: 5261.

[10]   J. Zhang, X. Liu, R. Blume, Z. Zhang, R. Schlögl, D. Su, *Science* **2008**, *322*, 73.

[11]   L. Yang, S. Jiang, Y. Zhao, L. Zhu, S. Chen, X. Wang, Q. Wu, J. Ma, Y. Ma, Z. Hu, *Angew. Chem. Int. Ed.* **2011**, *50*, 7132.

[12]   K. Chizari, A. Deneuve, O. Ersen, I. Florea, Y. Liu, D. Edouard, I. Janowska, D. Begin, C. Pham-Huu, *ChemSusChem* **2012**, *5*, 102.

[13]   K. P. Gong, F. Du, Z. H. Xia, M. Durstock, L. M. Dai, *Science* **2009**, *323*, 760.

[14]   Y. Tang, B. L. Allen, D. R. Kauffman, A. Star, *J. Am. Chem. Soc.*, **2009**, *131*, 13200.

[15]   Q. Li, S. Zhang, L. Dai, L. S. Li, *J. Am. Chem. Soc.*, **2012**, *134*, 18932.

[16]   K. Ai, Y. Liu, C. Ruan, L. Lu, G. M. Lu, *Adv. Mater.* **2013**, *25*, 998.

[17]   L. Zhang, Z. Xia, *J. Phys. Chem. C*, **2011**, *115*, 11170.

[18]   K. P. Gong, F. Du, Z. H. Xia, M. Durstock, L. M. Dai, *Science* **2009**, *323*, 760.

[19]   H. T. Chung, J. H. Won, P. Zelenay, *Nat. Commun.* **2013**, *4*:1922.

[20]   D. Yu, E. Nagelli, F. Du, L. Dai, *J. Phys. Chem. Lett.* **2010**, *1*, 2165.

[21]   K. Chizari, A. Deneuve, O. Ersen, I. Florea, Y. Liu, D. Edouard, I. Janowska, D. Begin, C. Pham-Huu, *ChemSusChem* **2012**, *5*, 102.

[22]   D. Yu, Y. Xue, L. Dai, *J. Phys. Chem. Lett*. **2012**, *3*, 2863.

[23]   E. Baltazzi, L. I. Krimen, *Chem. Rev.* **1963**, *63*, 511.

[24]   W. A. Herrmann, C. Kocher, *Angew. Chem. Int. Ed.* **1997**, *36*, 2162.

[25]   N. K. Gupta, A. V. Pashigreva, E. A. Pidko, E. J. M. Hensen, L. Mleczko, S. Roggan, E. E. Ember, J. A. Lercher *Unpublished results*.

[26]   L. Khachatryan, B. Dellinger *Chemosphere* **2003**, *52*, 709.

[27]   P. Kuhn, A. Thomas, M. Antonietti, *Macromolecules* **2009**, *42*, 319.

[28]   American Conference of Governmental Industrial Hygienists: "Phosgene", Documentation of the Threshold Limit Values for Substances in Workroom Air (3rd ed., 2nd printing), Cincinnati, **1974.**

[29]   E. P. Barrett, L.G. Joyner, P. P. Halenda, *J. Am. Chem. Soc.*, **1951**, *73*, 373.

[30]   S. J. Gregg, S. W. S. Kenneth, *Adsorption Surface Area and Porosity* ed. 2, Academic Press Inc.,U.S., London, **1982**.

[31]   B. C. Lippens, J. H. Deboer, *J. Catal.* **1965,** *4*, 319.

[32]   NIST X-ray Photoelectron Spectroscopy Database, Database 20, Version 3.5, http://srdata.nist.gov/xps/Default.aspx

[33]   A. C. Ferrari, J. Robertson, *Phil. Trans. R. Soc. Lond. A* **2004**, *362*, 2477.

[34]   S. Reich, C. Thomsen, *Phil. Trans. R. Soc. Lond. A* **2004**, *362*, 2271.

[35]   Y. Lin, X. Pan, W. Qi, B. Zhang, D. S. Su, *J. Mater. Chem. A* **2014**, *2*, 12475.

[36]   E. Jagst, , *PhD thesis*, Freien Universität Berlin, Germany **2010**.

[37]   W. Shen, W. J. Fan, *Mater. Chem. A* **2013**, *1*, 999.

[38]   Z. Luo, S. Lim, Z. Tian, J. Shang, L. Lai, B. MacDonald, C. Fu, Z. Shen, T. Yu, J. Lin, *J. Mater. Chem.* **2011**, *21*, 8038.

[39]   S. Wang, D. Yu, L. Dai, *J. Am. Chem. Soc.* **2011**, *133*, 5182.

[40]   I. Retzko, W. E. S. Unger, *Adv. Eng. Mater.* **2003**, 5, 519.

[41] C. H. Schmitz, C. Rang, Y. Bai, I. Kossev, J. Ikonomov, Y. Su, K. Kotsis, S. Soubatch, O. Neucheva, S. Tautz, I. S. Neese, H. -P. Steinrück, J. M. Gottfried, K. H. Dötz, M. Sokolowski, *J. Phys. Chem. C* **2009**, *113,* 6014.

[42] E. Jagst, *PhD thesis*, Freien Universität Berlin, Germany **2010**.

[43] D. Yanga, A. Velamakannia, G. Bozoklub, S. Parka, M. Stollera, R. D. Pinera, S. Stankovichc, I. Junga, D. A. Fieldd, C. A. Ventrice, R. S. Ruoffa, *Carbon* **2009**, 47, 145.

[44] C. P. Wilgus, S. Downing, E. Molitor, S. Bains, R. M. Pagni, G. W. Kabalka, *Tetrahedron Lett.* **1995**, *36*, 3469.

[45] V. K. Krieble, C. I. Noll, *J. Am. Chem. Soc.* **1939**, *61*, 560.

[46] J. P. Chen, R. T. Yang, *Surf. Sci.* **1989**, *216*, 481.

[47] (a) L. Watts, *US3816505,* **1974**. (b) E. Baciocchi, F. Cacace, G. Ciranni, G. Illuminati, *J. Am. Chem. Soc.*, **1972**, *94*, 7030.

[48] A. C. Legon, J. M. A. Thumwood, *Phys. Chem. Chem. Phys.* **2001**, *3*, 1397.

[49] G. A. Olah, *Angew. Chem. Int. Ed.* **1973***, 12,* 173.

[50] J. L. O'Connell, J. S. Simpson, P. G. Dumanski, G. W. Simpson, C. J. Easton, *Org. Biomol. Chem.* **2006**, *4*, 2716.

[51] P. G. Gassman, G. A. Campbell, *J. Am. Chem. Soc.* **1971**, 93, 2567.

[52] (a) B. Dayid, *US2839589 A*, **1958.** (b) O. W. Cass, *US2406195 A*, **1946**.

[53] D. S. Akićand, V. J. Vrcek, *Phys. Chem. A* **2012**, *116*, 1298.

[54] A. A. Bernussi, G. M. Gualberto, *J. Raman Spectrosc.* **1987**, *18*, 93.

[55] C. Grundmann, A. Kreutzber, *J. Am. Chem. Soc.*, **1955**, *77*,44.

[56] A. J. Arduengo, F. Davidson, H. V. R. Dias, J. R. Goerlich, D. Khasnis, W. J. Marshall, T. K. Prakasha, *J. Am. Chem. Soc.* **1997**, *119*, 12742.

[57] N. Kuhn, J. Fahl, R. Fawzi, C. Maichle-Mößmer, M. Z. Steimann, *Naturforsch. B Chem.* **2014**, *53*, 1865.

[58] R. Brückner, H. Haller, M. Ellwanger, S. Riedel, *Chem. Eur. J.* **2012**, *18*, 5741.

[59] L. Abrams, W. V. Cicha, L. E. Manzer, S. Subramoney, *Stud. Surf. Sci. Catal*., **2000**, *130*, 455.

[60] R. L. Jenkins, J. E. Haskins, L. G. Carmona, R. B. Baird, *Arch. Environm. Contain. Toxicol.* **1978**, *7*, 301.
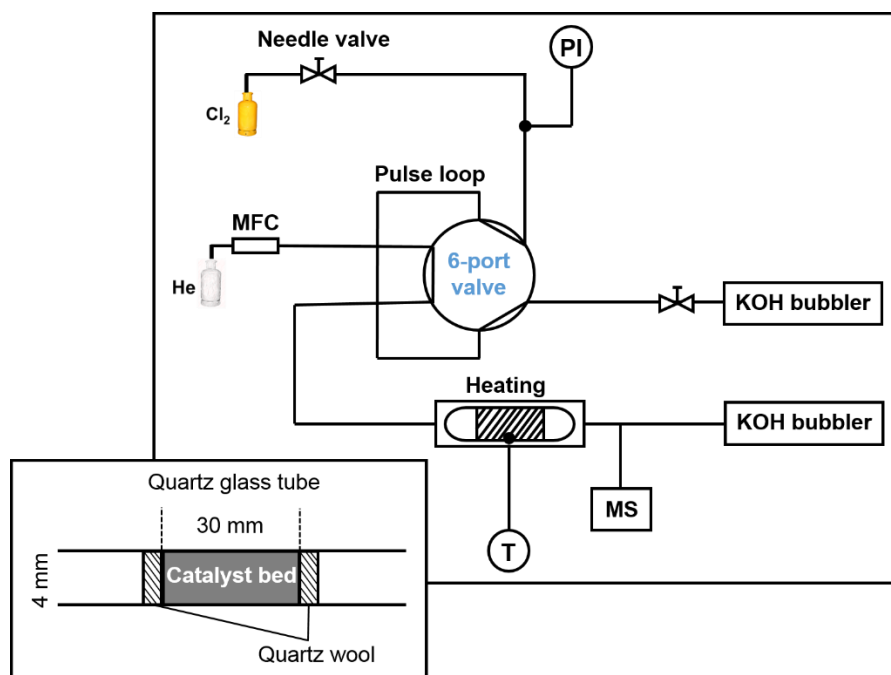
4.7 Supporting information

Figure S4-1. Pulse set-up for Cl_2 interaction and $COCl_2$ synthesis study. (PI = pressure indicator, MFC = mass flow controller, MS = Mass spectrometer, T = temperature controller)

Table S4-1. Elemental compositions from CHNS analysis of synthetic N-modified C materials.

Precursors	Element (atom %)					C/N
	C	H	N	O	Cl	
1,4- Dicyano benzene	56.63	27.76	9.37	5.79	0.44	6.04
Tetrachloroterephthalonitrile	46.7	23.07	15.34	8.07	6.81	3.04
9,10-Anthracenedicarbonitrile	65.54	25.73	3.08	5.37	0.27	21.28
4,4′-Biphenyldicarbonitrile	64.39	27.79	3.83	3.72	0.26	16.81

Table S4-2. Elemental analyses of synthetic N-modified C materials by XPS.

Precursors	Surface composition (atom %)					C/N
	C+H	N	O	Cl	Others	
1,4- Dicyano benzene	81.8	10.6	7.7	-	-	7.72
Tetrachloroterephthalonitrile	68.7	14.7	9.3	6.8	0.5 (Zn)	4.67
9,10-Anthracenedicarbonitrile	90.7	3.6	5.2	-	-	25.19
4,4′-Biphenyldicarbonitrile	86.0	5.5	6.4	-	1.9 (F)	15.64
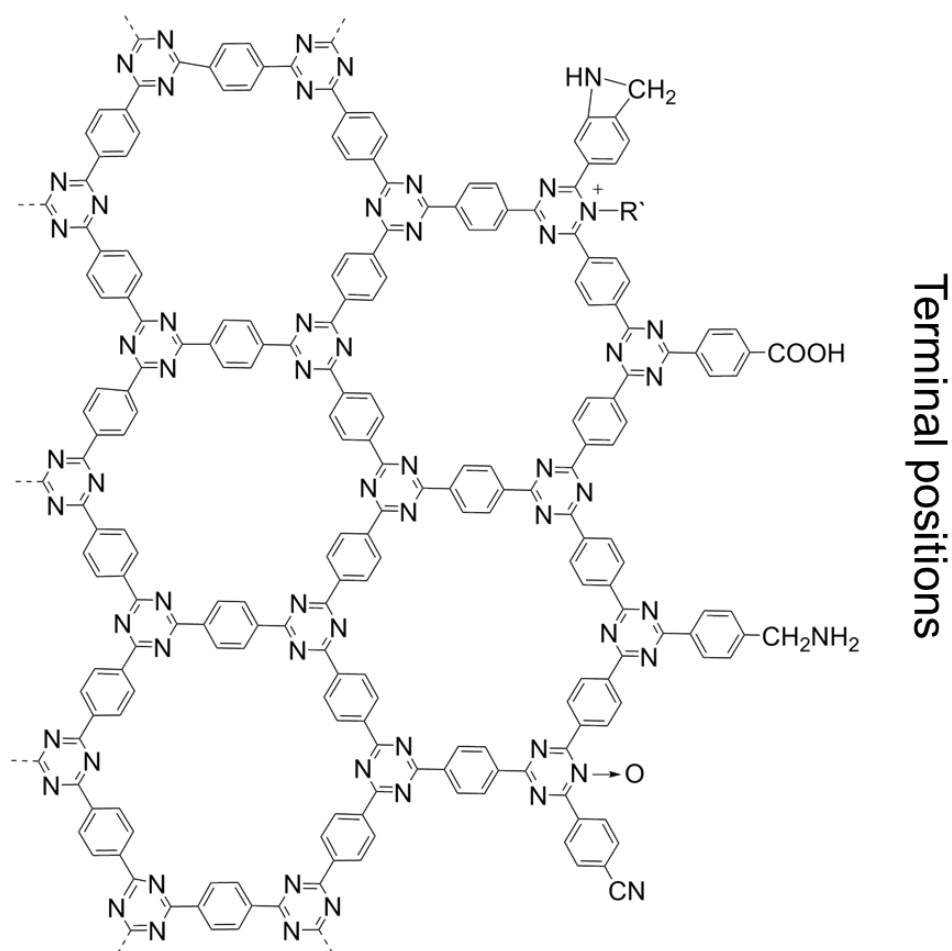
Figure S4-2. Overview of polymeric structure from 1,4-dicyano benzene precursor proposed based on XPS analysis.
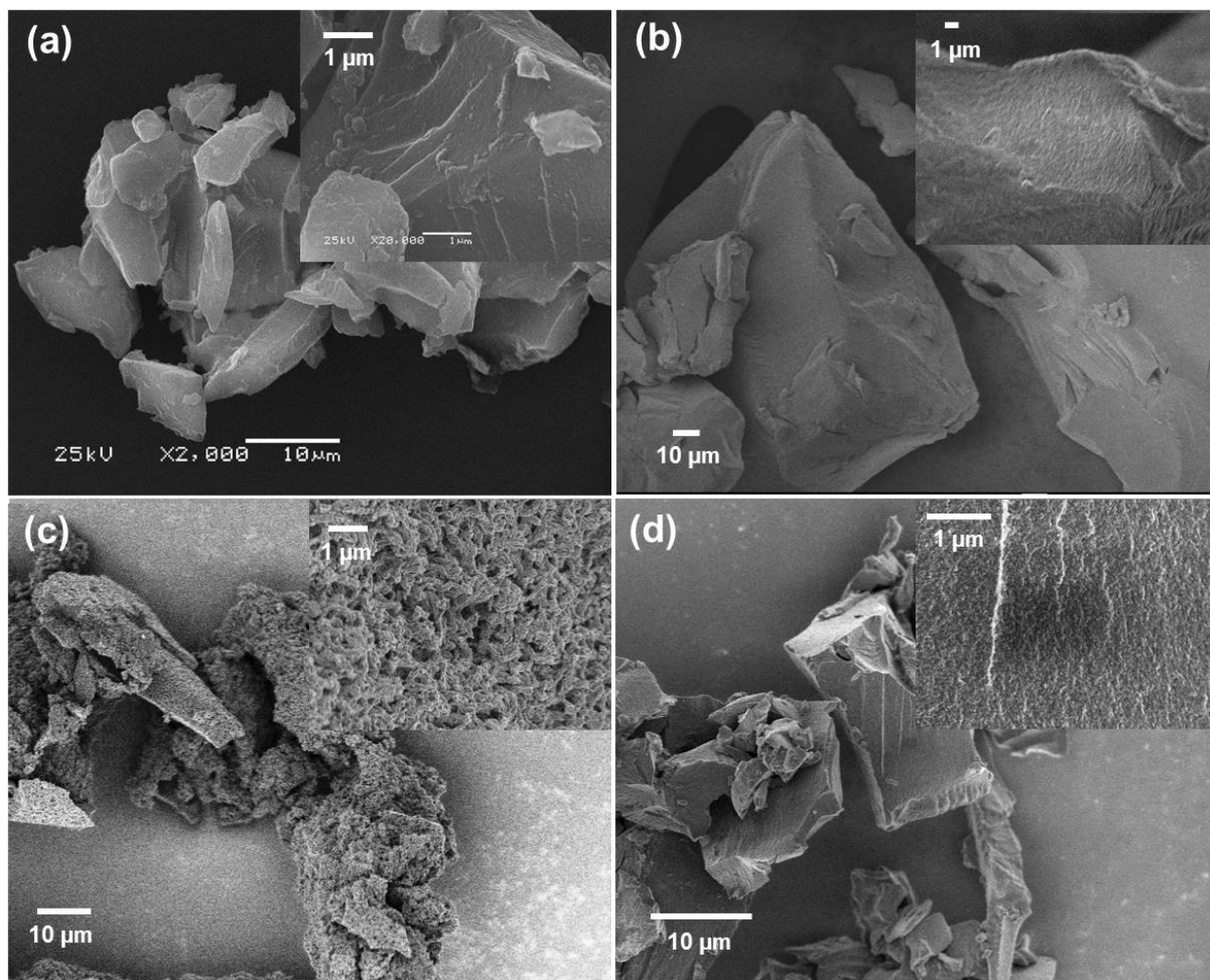
Figure S4-3. HR-SEM image of N-modified carbon materials synthesized by precursors (a) 1,4-dicyanobenzene, (b) tetrachloroterephthalonitrile, (c) 9,10-anthracenedicarbonitrile and (d) 4,4′-biphenyldicarbonitrile.
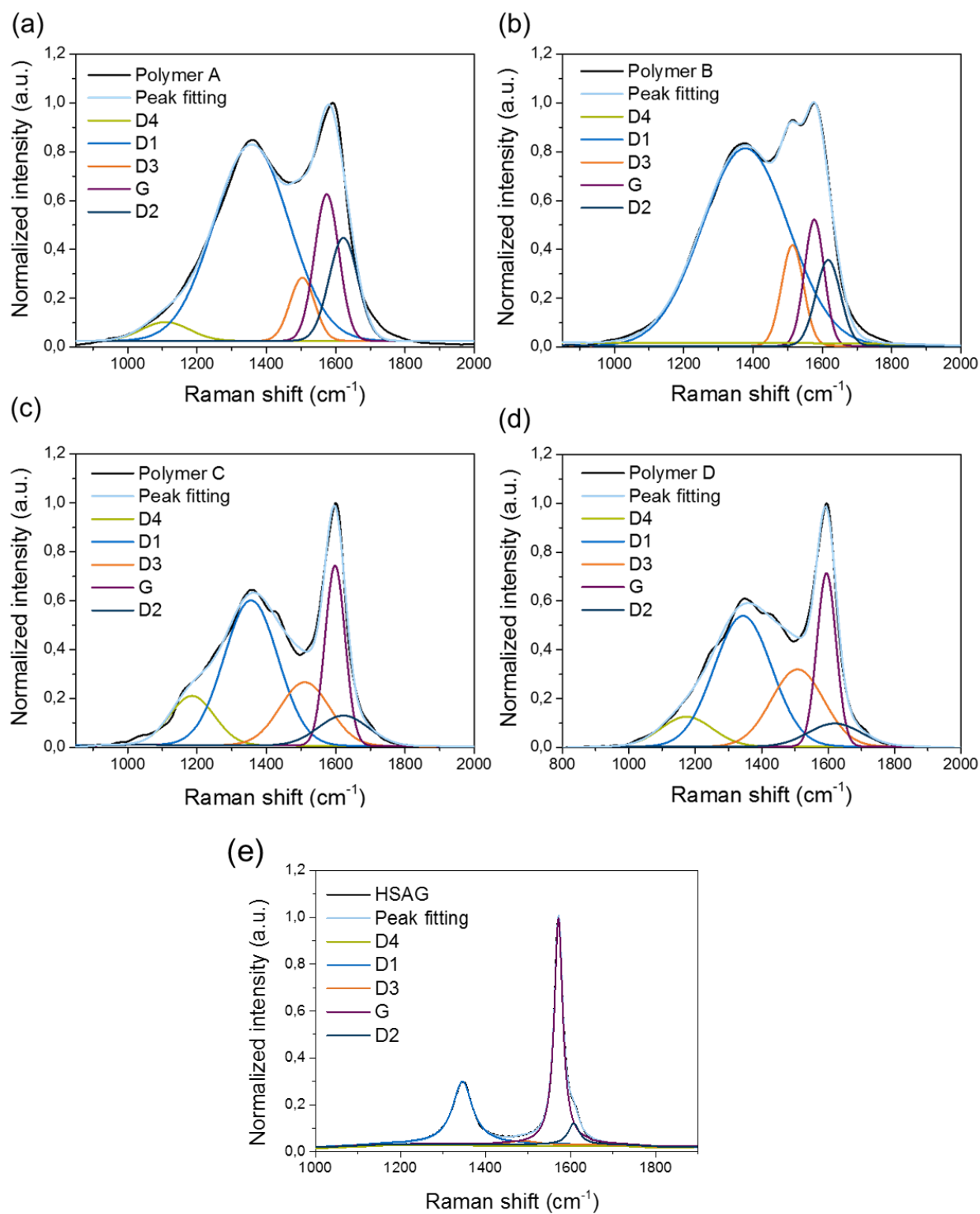
Figure S4-4. Deconvolution of a Raman spectrum of N-modified carbon materials and HSAG.

Table S4-3. Assignment of Raman bands of carbon materials.[1, 2]

Bands	Approx. wavenumber (cm^{-1})	Assignment of bands
G	~1580	Corresponds to an ideal graphitic lattice vibration mode with E_{2g} symmetry.
D1	~1350	Attributed to graphene layer carbon atoms in immediate vicinity of a lattice disturbance like the edge of a graphene layer (graphene layer edges, A_{1g} symmetry).
D2	~1620	Is assigned to a lattice vibration analogous to that of the G band but involving graphene layers at the surface of the graphitic crystal (surface graphene layers, E_{2g} symmetry).
D3	~1500	Originates from the amorphous carbon fraction of soot (organic molecules, fragments or functional groups).
D4	~1200	Is attributed to sp^2-sp^3 bonds or C-C and C=C stretching vibrations of polyene-like structures (disordered graphitic lattice, (A_{1g} symmetry), polyenes, ionic impurities).

Ratio of the D1 and G bands represents the ratio of the defects in the graphene layer

Table S4-4. Sample denotations and comparison of the fit parameters from the peaks fitted in the Raman spectra of N-modified carbon materials and HSAG.[1, 2]

Polymer	Band±	G	D₁	D₂	D₃	D₄	I_D/I_G*	La**
A	Center, cm⁻¹	1574	1358	1622	1504	1108		
	Height	0.60	0.81	0.42	0.26	0.08	1.35	3.22
B	Center, cm⁻¹	1577	1378	1617	1514	1218		
	Height	0.52	0.81	0.35	0.41	0.01	1.55	2.79
C	Center, cm⁻¹	1598	1356	1622	1511	1185		
	Height	5009	4027	838	1761	1364	0.80	5.4
D	Center, cm⁻¹	1595	1344	1619	1508	1173		
	Height	11116	8382	1474	4946	1915	0.75	5.7
HSAG	Center, cm⁻¹	1571	1346	1607	1487	1200		
	Height	0.97	0.27	0.09	0.02	0	0.28	15.6

±Assignment of the Raman bands are indicated in Table S4-3.

*Intensity ratio of D₁ and G.

** Planar microcrystalline size (La) calculated from the intensities of G and D bands on the Raman spectra using Tuinstra and Koening (T-K) equation. $L_a = 4.35 (I_G/I_D)$, nm.[3]
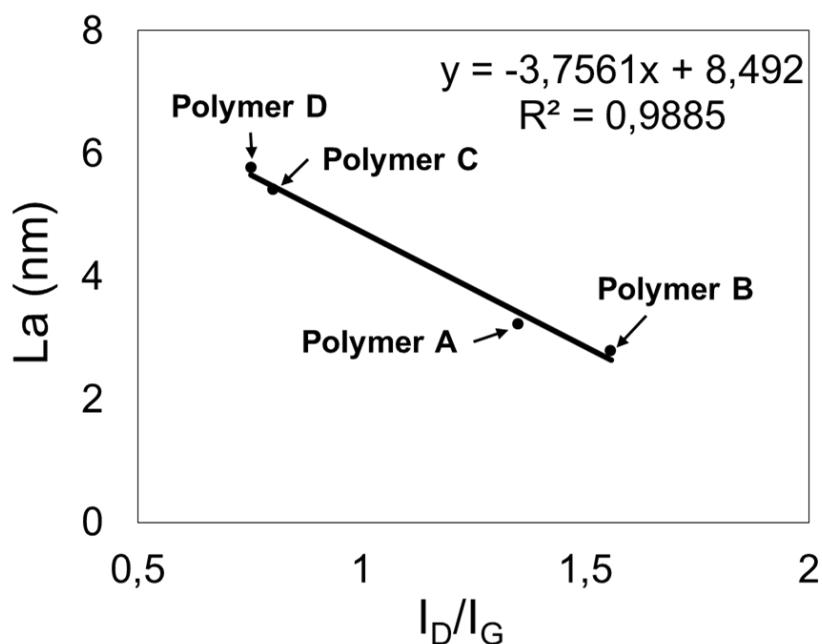
Figure S4-5. Linear correlation between I_D/I_G and La (planar microcrystalline size determined as shown in Table S4-4 and specified in Supplemental Ref. 3) indicating the high crystallinity of the particles. By increasing the aromatic linker, the lateral size of the aromatic units increased as well.

The comparative study of the XRD profiles (recorded on Philips X'Pert Pro diffractometer equipped with an X'celerator module using Cu-Kα radiation and operating at 40 kV/45 mA) of polymer A is presented in Figure S4-6. For the polymerization product of 1,4-dicyanobenzene, polymer A, the XRD pattern of the product displays some intense reflection peaks (Figure S4-2). This observation can be explained by the formation of a crystalline triazine-based organic framework with hexagonal packing of pores. Besides the intense (100) peak at lower angles and two additional peaks (attributable to the (110) and (200) reflections), a broad peak at 24.6 corresponding to an interlayer distance of 3.6 Å for the (001) aromatic sheets is also found. The observed interlayer distance in the case of polymer A is higher than that for non-functionalized graphite (3.3 Å). The increase in interlayer distance is hypothesized to be due to the incorporation of N-atoms into the polymeric carbon sheets. The lateral size of the crystallites are evaluated by Tuinstra and Koening relation (Table S4-4) are found to be in good agreement with that calculated using the Scherrer equations. The average crystallite sizes determined from both XRD and Micro Raman techniques are presented in the Table S4-5.
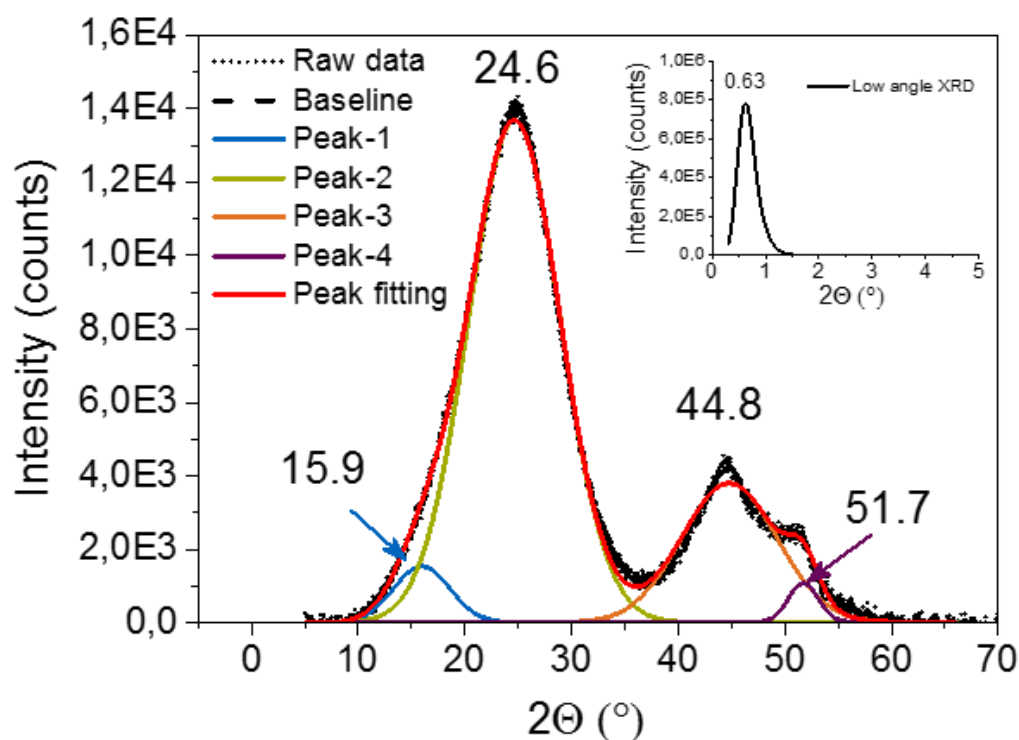
Figure S4-6. X- ray diffraction patterns of polymer A.

Table S4-5. Analysis of low and wide angle XRD pattern.

XRD	Low angle	Wide angle ide angle			
Peak position (2Θ)	0.63	15.9	24.6	44.8	51.7
FWHM (2Θ)	0.411	6.2	10.1	10.6	3.3
Crystallite size (nm)*	40.5	2.68	1.65	1.6	5.16
**d (nm)	14.1	-	0.36	-	-

*XRD Crystallite Size Calculated using Scherrer Formula (Dp = 0.94 λ / $\beta_{1/2}$ cos Θ) where, Dp = Average Crystallite size, β = Line broadening in radians, Θ = Bragg angle, λ = X-ray wavelength. **d value was calculated using bragg`s equation (nλ= 2dsinΘ).
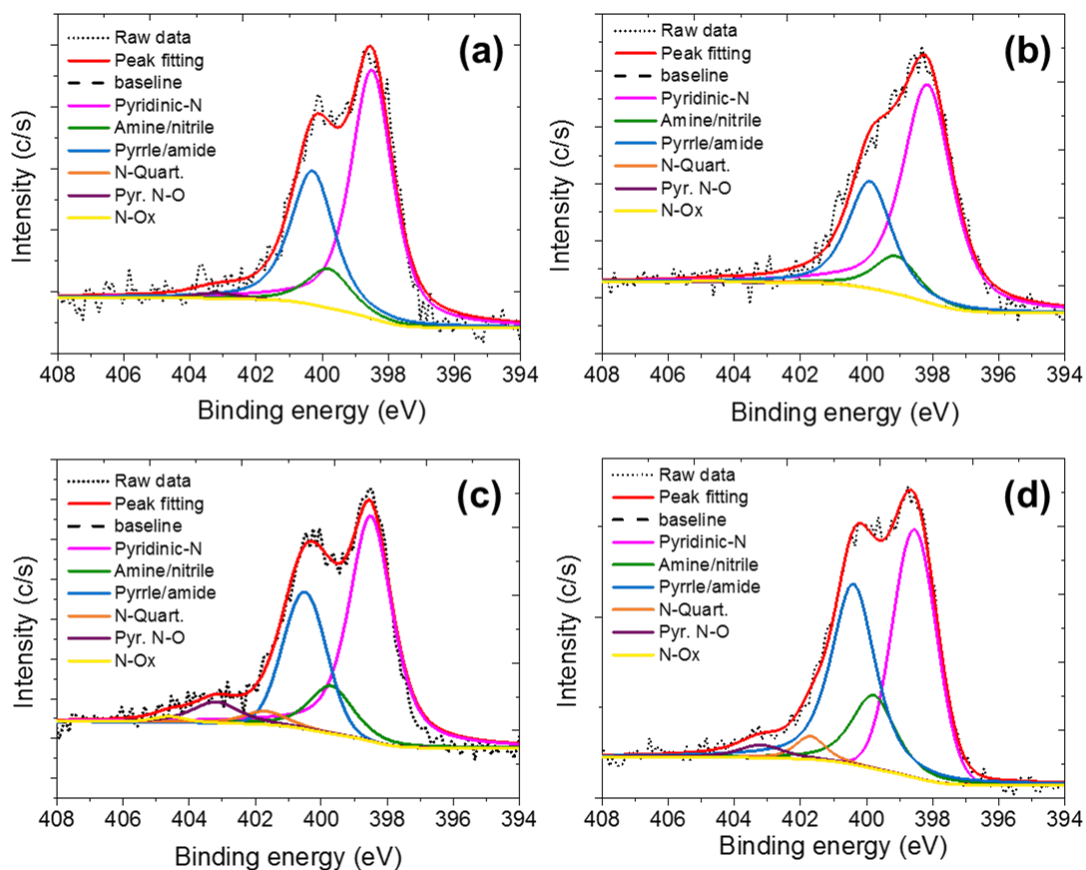
Figure S4-7. N1s narrow scan XPS spectra of N-modified materials synthesized from different precursors: (a) 1,4-dicyanobenzene, (b) tetrachloroterephthalonitrile, (c) 9,10-anthracenedicarbonitrile and (d) 4,4′-biphenyldicarbonitrile.
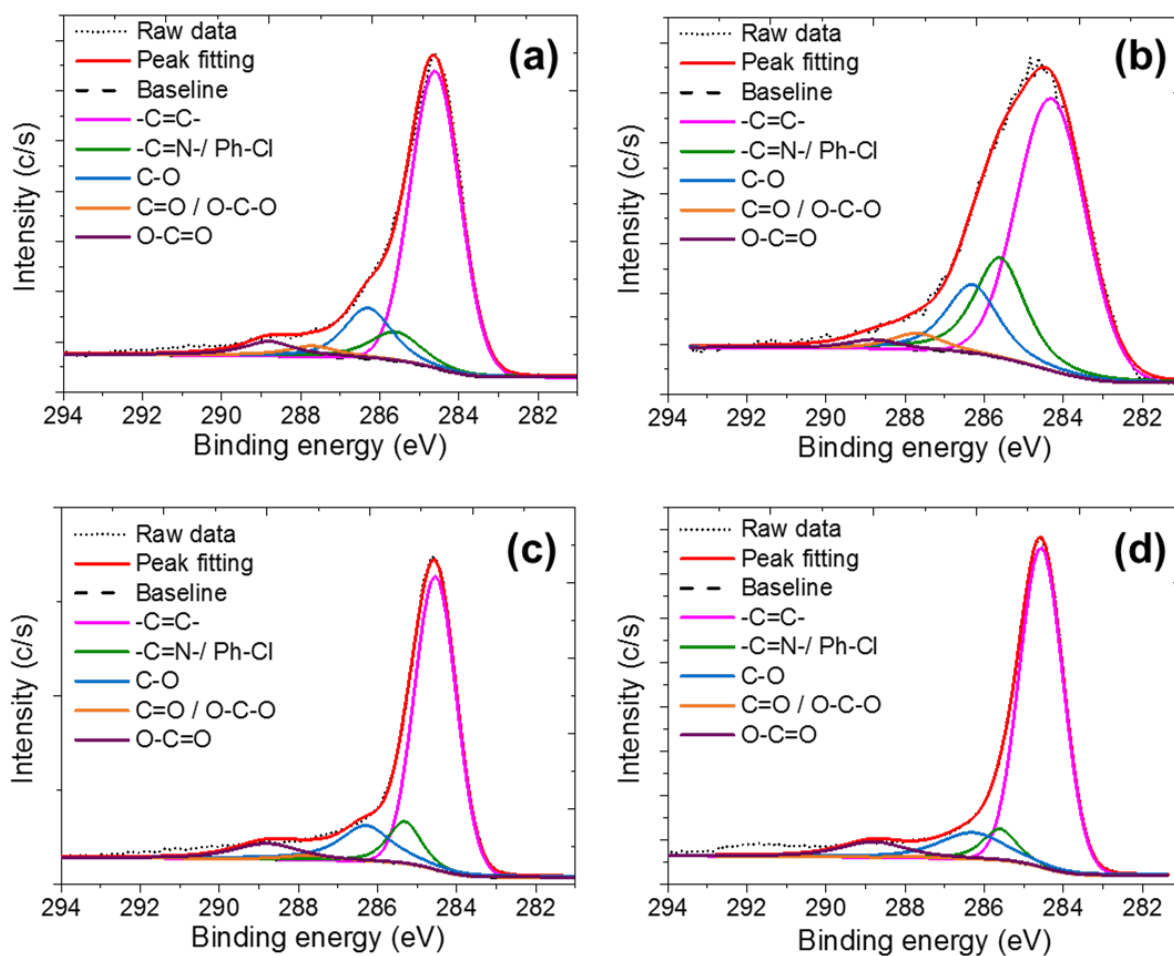
Figure S4-8. C1s narrow scan XPS spectra of N-modified materials synthesized from different precursors: (a) 1,4-dicyanobenzene, (b) tetrachloroterephthalonitrile, (c) 9,10-anthracenedicarbonitrile and (d) 4,4′-biphenyldicarbonitrile.
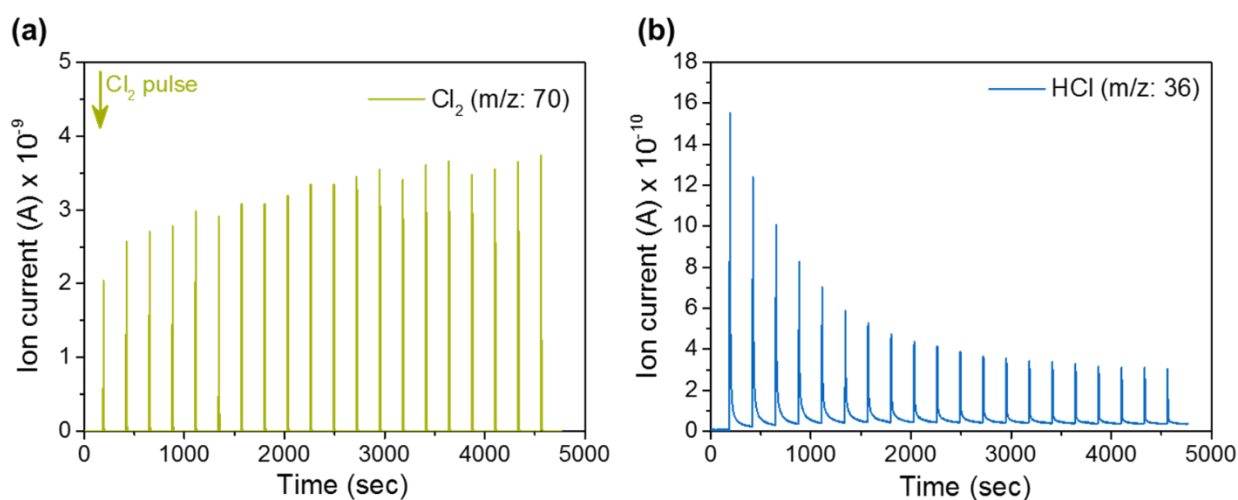
Figure S4-9. Cl$_2$ activation study. Experimental conditions: 20 Cl$_2$ pulses (230 s pulse length, 1.8 µmol Cl$_2$ / pulse), He flow: 10 ml/min, 200 mg of 1,4-dicyanobenzene.
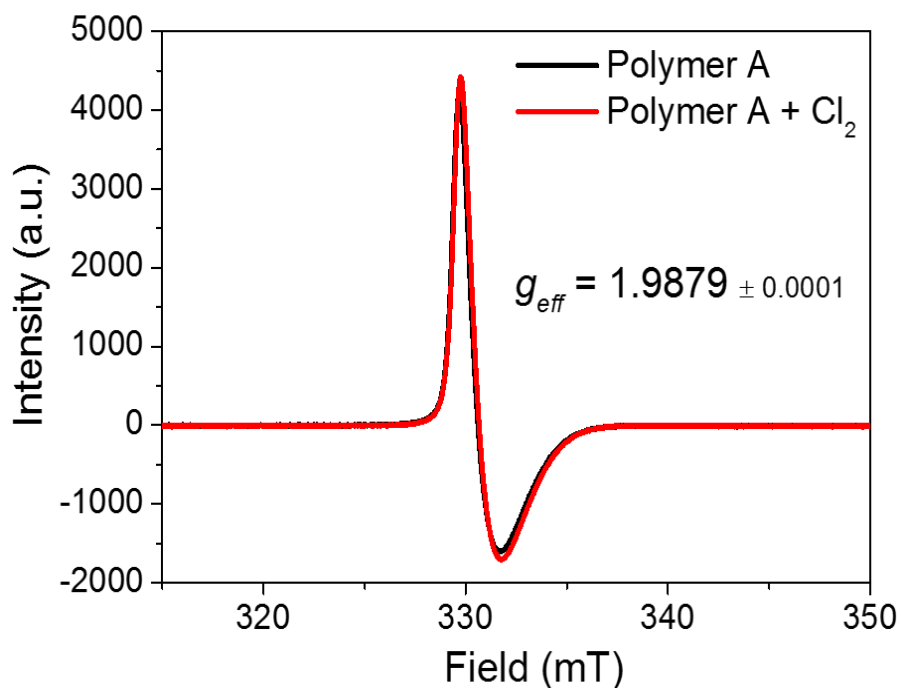
Figure S4-10. In situ ESR spectroscopy of Cl_2 interaction on N-modified carbon.
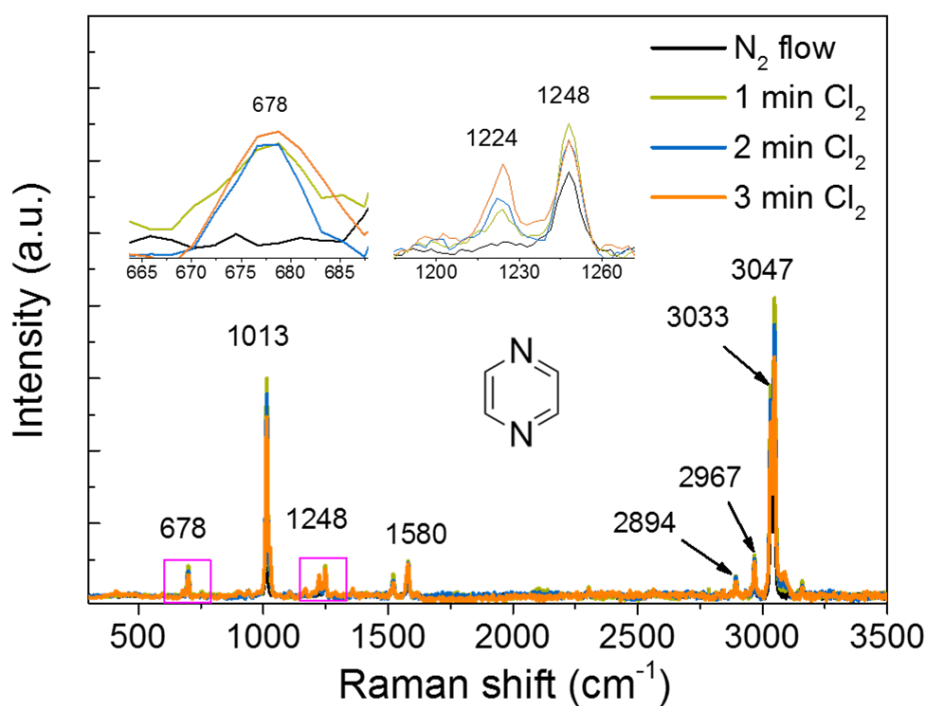
Figure S4-11. In situ Raman spectra of pyrazine before (black) and after Cl_2 (green, blue and orange) addition at 313K.
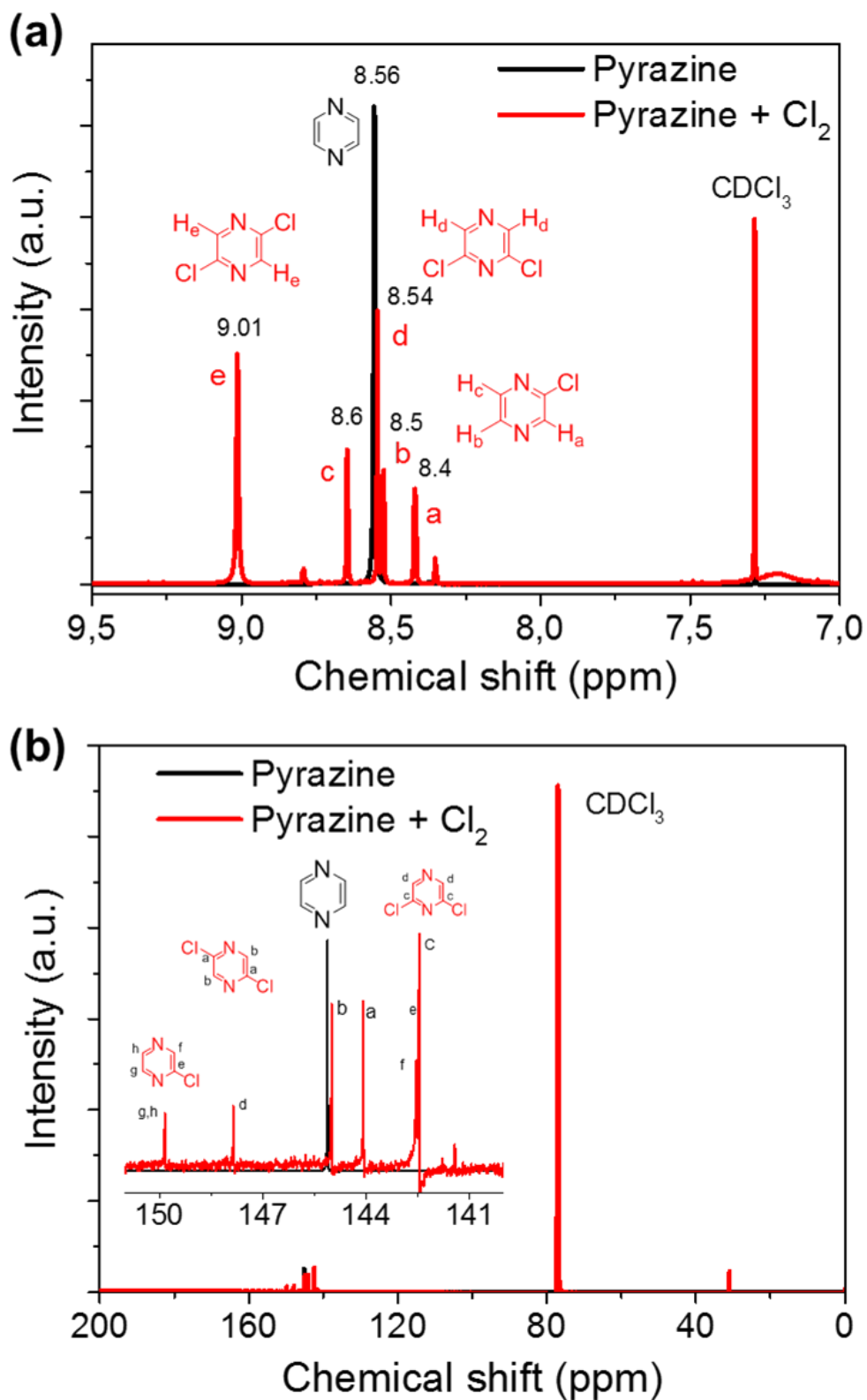
Figure S4-12. ^{1}H and ^{13}C NMR spectra of pyrazine before and after Cl_2 addition at 313K.
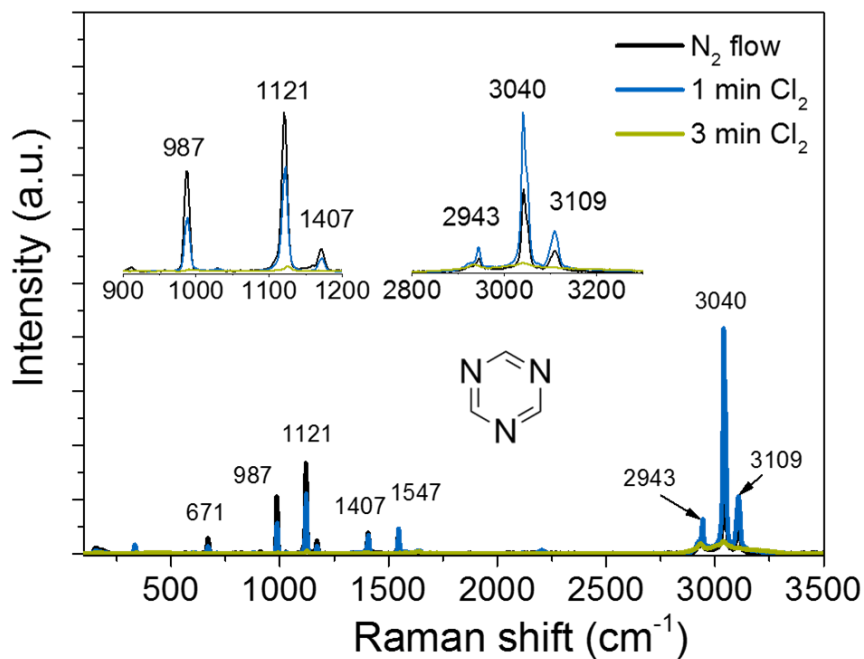
Figure S4-13. In situ Raman spectra of s-triazine before (black) and after Cl_2 (blue and green) addition at 313K.
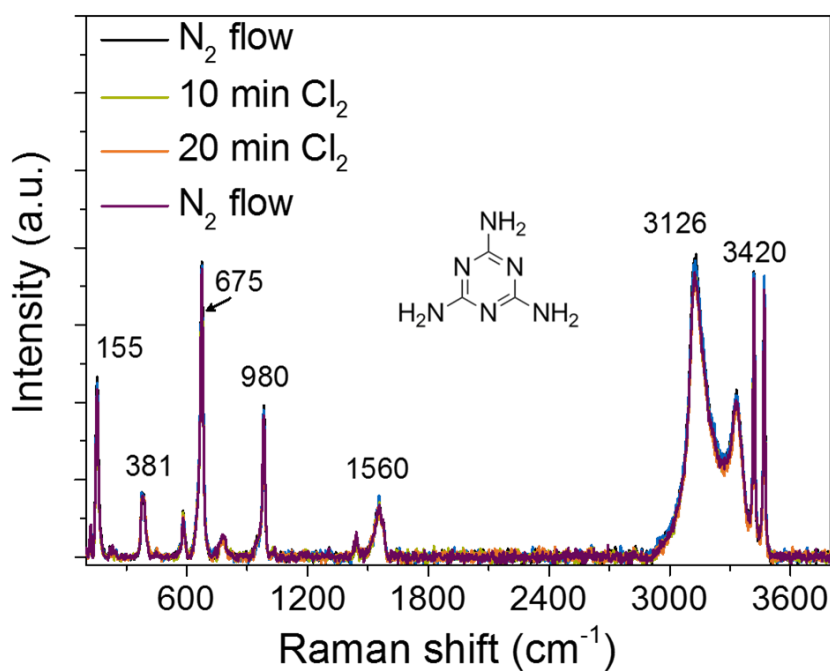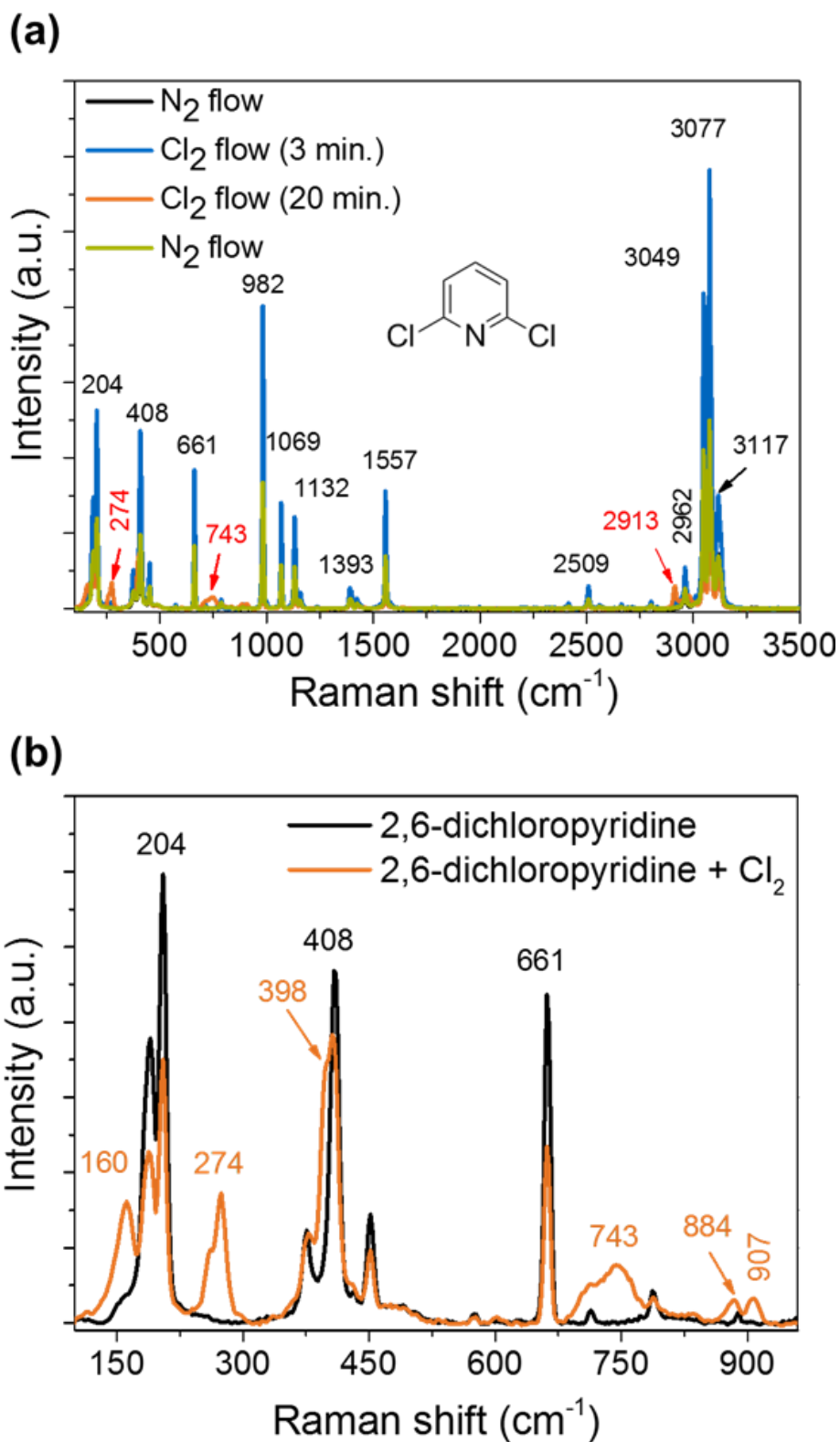

Figure S4-14. In situ Raman spectra of melamine before (black) and after Cl_2 (green, orange) addition at 313K.
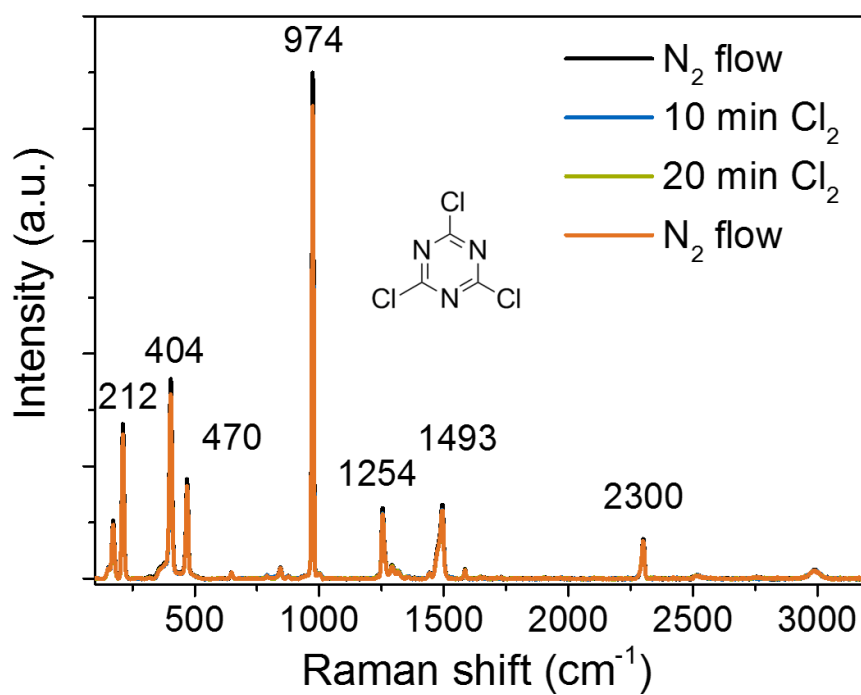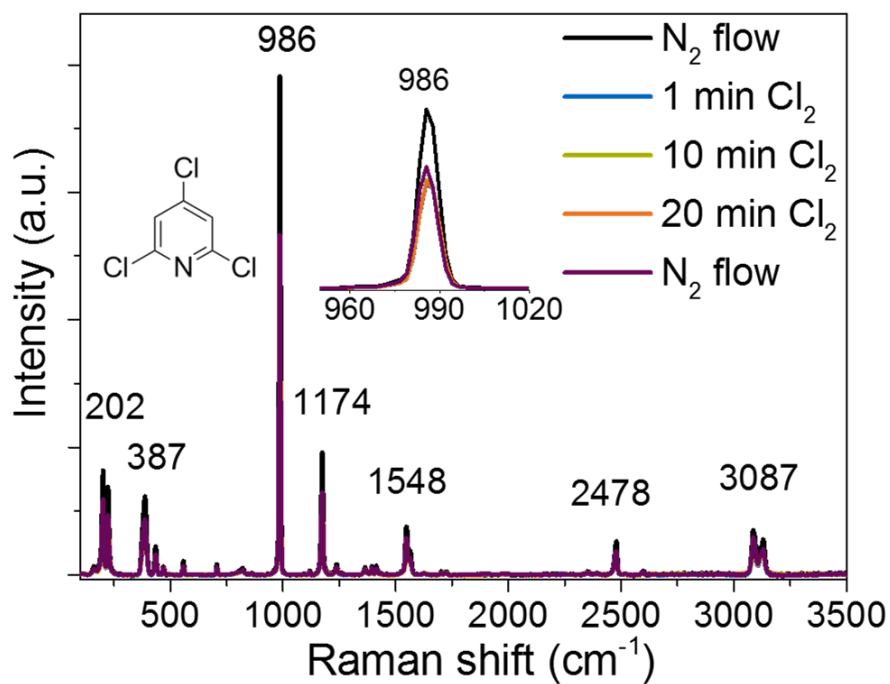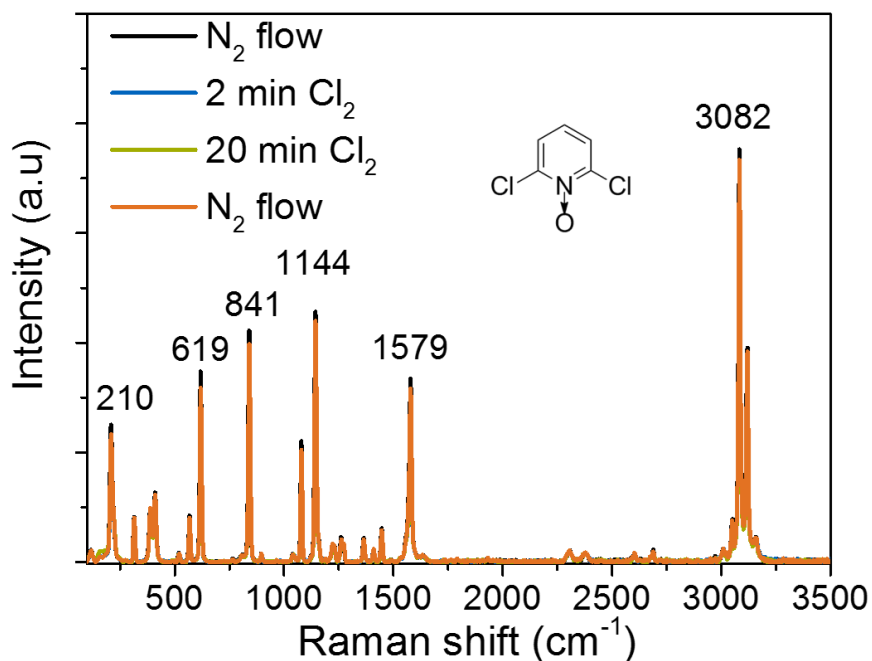
Figure S4-15. In situ Raman spectra of cyanuric chloride before (black) and after Cl_2 addition (blue and green) addition at 313K.

Figure S4-16. In situ Raman spectra of 2,6-dichloropyridine before (black) and after Cl_2 (blue, orange) addition at 313K.

Figure S4-17. In situ Raman spectra of 2,4,6-dichloropyridine before (black) and after Cl_2 (blue, green and orange) addition at 313 K.

Figure S4-18. In situ Raman spectra of 2,6-dichloropyridine N-oxide before (black) and after Cl_2 (blue and green) addition at 313K.
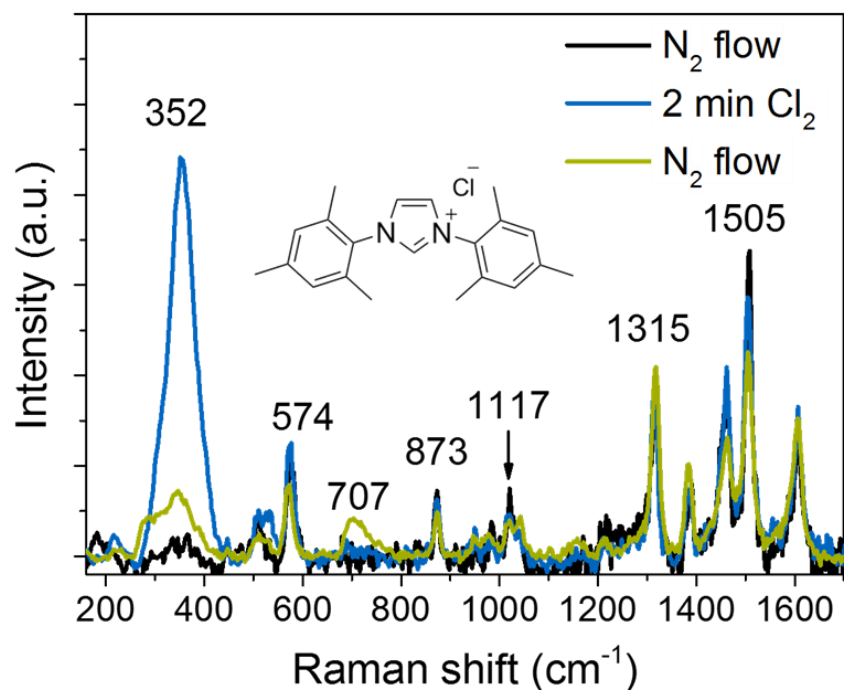
Figure S4-19. In situ Raman spectra of BTIC before (black) and after Cl_2 (blue) addition at 313K.
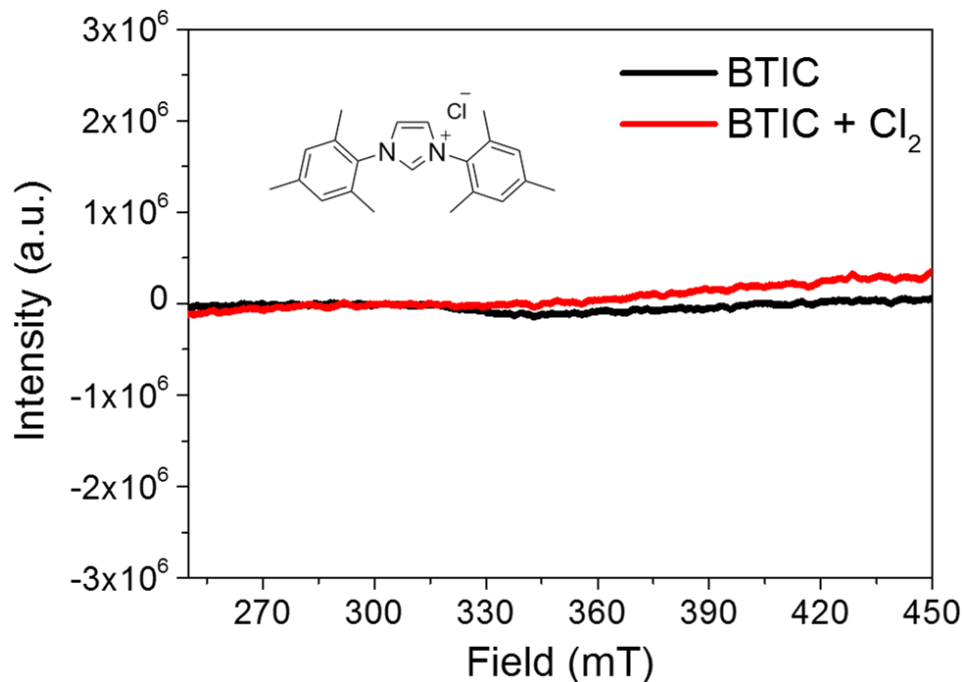

Figure S4-20. ESR spectra recorded from BTIC under inert conditions (black) and in Cl_2 atmosphere (red).
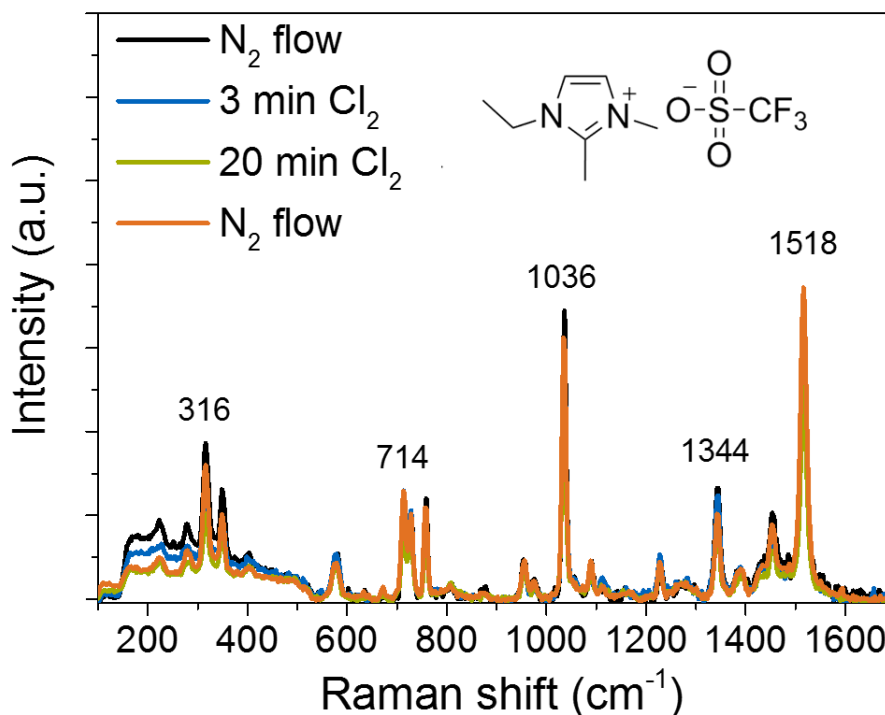
Figure S4-21. In situ Raman spectra of EDITM before (black) and after Cl_2 (blue and green) addition at 313K.

Supplementary reference:

[1]   A. Sadezky, H. Muckenhuber, H. Grothe, R. Niessner, U. Pöschl, *Carbon*, **2005**, *43*, 1731.

[2]   F. Haghseresht, G. Q. Lu, A. K. Whittaker, *Carbon*, **1999**, *37*, 1491.

[3]   A. N. Mohan, B. Manoj, *Int. J. Electrochem. Sci.,* **2012**, *7*, 9537.

Chapter 5

# γ-Alumina catalyzed Cl$_2$ activation and phosgene synthesis

Abstract

The various forms of alumina were tested for the transient phosgene synthesis using a quartz pulse-reactor in conjunction with mass spectroscopic analysis. The catalytic efficiency of aluminum-based catalysts depend on its structure and intrinsic acid/base properties. Kinetic and mechanistic studies indicate that strong Lewis acid sites favor the associative adsorption of Cl$_2$ and the intermediate formation of highly reactive Cl$^{\delta+}$. In comparison to pure AlCl$_3$, γ-Al$_2$O$_3$ exhibits ten times higher catalytic activity of COCl$_2$ synthesis, demonstrating the better stabilization ability of the transiently formed highly active Cl$^{\delta+}$ species on the electron rich surface oxygen. We demonstrate here that γ-Al$_2$O$_3$ is an adequate metal-based highly active catalysts for COCl$_2$ synthesis with remarkable long term operational stability.

5 γ-Alumina catalyzed Cl₂ activation and phosgene synthesis

5.1 Introduction

Polycarbonates have been proved to be one of the most important polymers for daily life.[1,2,3] Their unique features such as light weight, durability and opaqueness makes them exceptionally attractive for a wide range of applications.[1-3] One of the earliest large scale techniques for the synthesis of polycarbonate requiring phosgene ($COCl_2$) as starting material has remained basically unchanged (Scheme 5-1).
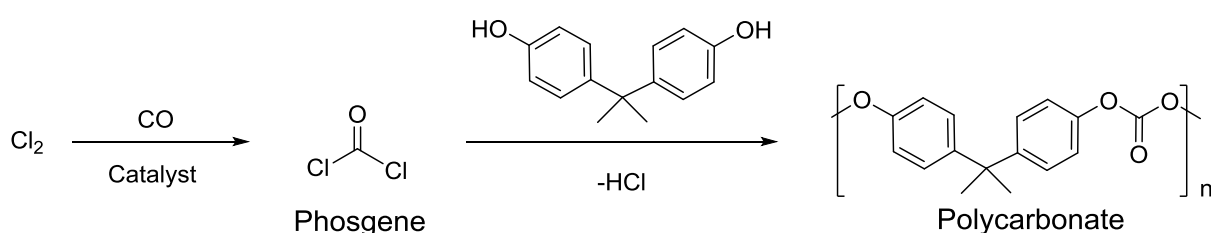
Scheme 5-1. Industrial route for synthesis of polycarbonate.

The conventional production of $COCl_2$ involves the photocatalytic and / or thermal reaction between chlorine (Cl_2) and carbon monoxide (CO).[4,5] The high energy demand of this process restricts, however, its industrial use. Presently, large scale synthesis of $COCl_2$ is based on the reaction of Cl_2 and CO enabled on activated carbon catalyst.[6,7] The presence of multiple sites on heterogeneous surface of activated carbon enable parallel reactions responsible for the irreversible modification of the active catalytic surface as well as for the poor quality of $COCl_2$.[8,9] To overcome this, alternative to the conventional activated carbons, the development of metal based catalysts were targeted to ensure a stable high-quality $COCl_2$ production. In this respect, $AlCl_3$ has been proposed as an alternative active material for high purity $COCl_2$ synthesis under harsh reaction conditions.[10] But, existing $AlCl_3$ based catalytic processes often suffer from serious drawbacks: (a) anhydrous $AlCl_3$ is a hygroscopic, corrosive solid which causes severe problems in waste stream. (b) $AlCl_3$ catalyst forms a stable complex with the organic functional compounds involving disproportionation reactions.[11] Alternative to that, metal oxides have attracted increasing interests as stable catalysts from experimental and theoretical point of view because of their high thermal and chemical stability.[12,13,14] Abundant availability, low cost, and environmental friendliness makes them exceptionally attractive for

the industrial applications.[12-14] A key characteristic of Al_2O_3 material is the great diversity and versatility of their surface chemistry, owing to the presence of different strength of Lewis acidity on Al atom[15] and Lewis basicity on O atom[16] which is strongly dependent on the local bonding environment.

We propose herein, γ-Al_2O_3 as a stable metal based catalyst for selective and large scale $COCl_2$ synthesis under ambient reaction conditions. Combined spectroscopic and reactivity data showed that for a selective and stable $COCl_2$ production high content of strong Lewis acid base pairs are required. Further, spectroscopic evidences were complimented by transient kinetic studies to reveal that the non-dissociative adsorption of Cl_2 resulting in the formation of polarized $Cl^{\delta+}$ fragments are required for the $COCl_2$ formation by a direct reaction of CO.

5.2 Experimental

5.2.1 Materials and reagents

Three aluminum based materials ($AlCl_3$, α-Al_2O_3 and γ-Al_2O_3) are selected for this study. The preexisting catalyst, $AlCl_3$ (≥97 % purity) was received from Merck and used as reference. The alternative proposed oxide based material, α-Al_2O_3 (>99% of purity) and γ-Al_2O_3 (AEROXIDE® Alu C, 99.6 % of purity) were purchased from Sigma Aldrich and Degussa AG, respectively. Traces of organic impurities were removed from both α-Al_2O_3 and γ-Al_2O_3 materials by the thermal treatment conducted at 550 °C for 6 h in O_2 (100 ml/min).

For a comparative study of different thermodynamically stable phases of alumina on the Cl_2 activation during $COCl_2$ synthesis, γ-Al_2O_3 materials (pretreated in O_2 at 550°C) was further thermally treated at 600 to 900 °C in inert gas (N_2, 99.9%) flow (100 ml/min).

Cl_2 (99.5 %), CH_4 (5 vol. % in He) and CO (5 vol. % in He) received from Westfalen AG were used for pulse experiments. However, in situ Raman experiments were performed in dilute Cl_2 (25 vol. % in He) bought from Westfalen AG.

5.2.2 Experimental set-up and safety aspects

The schematic representation of the experimental setup constructed for the Cl_2 activation and CO interaction study is shown in supporting material, Figure S5-1. One major advantage of this setup designed for Cl_2 activation studies is the possibility to use minimal amounts of toxic and

corrosive gases. A six-port valve connected to an on-line mass spectrometer (MS) was used for the automated dosage of Cl_2. All the gaseous residues were neutralized in two interconnected concentrated KOH and Cu^{+2} solution containing bottles. An active carbon containing filter finally accounts for the retention of any generated toxic gaseous intermediates left.

Special attention was paid to the safety issues; two different types of Cl_2 and CO detectors were placed under the fume hood to constantly monitor the Cl_2 and CO concentration at the working place. To avoid contamination with CO, two additional filters for CO entrapment were installed at the outlet of the six-port valve and of the reactor. The maximum amount of $COCl_2$ which could theoretically be formed in the pulse reactor (0.025 ppm) is lower than the permissible exposure limit (0.1 ppm averaged over a work shift of up to 10 hours a day, 40 hours per week with a ceiling level of 0.2 ppm averaged over a 15 min period).[17]

5.2.3 Catalytic Cl₂/CO activation and COCl₂ synthesis

In a typical experiment 100 mg of sample ($\leq$ 80 μm particle size) was placed in a tubular quartz reactor (0.4 mm ID), and thermally treated at 450 °C for 1 h prior to pulse measurements. Multiple Cl_2 pulse (1.8 μmole Cl_2 / pulse, pulse length - 230 seconds) were conducted at 150 °C, in inert gas flow (He, flow rate: 10 ml/min). Gas phase products were analyzed by on-line mass spectroscopy (OMNI star / TM mass-spectrometer) by using the Quadera software from Pfeiffer Vacuum GmbH. The surface bound species were afterwards investigated by temperature program desorption (TPD).

The catalytic test for $COCl_2$ synthesis was studied by performing Cl_2 pulses in 5 vol. % CO containing He atmosphere under similar experimental conditions as described above.

5.3 Catalyst characterization

Textural analysis

Specific surface area and pore volume was determined by N_2 physisorption and Brunauer–Emmett–Teller (BET) using PMI automated Sorptomatic 1990 instrument. Prior to measurement, 200 mg of the samples were pretreated under vacuum (10^{-4} mbar) at 473 K for 2 h. afterwards, the weight of the samples were taken as reference weight and the samples were further cooled to 77 K for N_2 adsorption measurements. Specific surface areas were estimated by applying the BET-formalism. The pore size distribution (PSD) was obtained by applying the

Barret–Joyner–Halenda (BJH) model.[18] While, pore volumes were evaluated from the αs comparative plot with nonporous hydroxylated silica as the reference adsorbent.[19] The presence of microporosity was determined by the t-plot method.[20]

Atomic absorption spectroscopy (AAS)

AAS was used to analyze the purity of Al_2O_3 samples to ensure the absence of transition metal (i.e., Fe and Co etc.) impurities. AAS measurements were carried out using UNICAM-939 atomic absorption spectrometer. Prior to the measurements, 20 to 50 mg of sample was completely dissolved in a boiling mixture of hydrofluoric acid (48 %, 0.5 ml) and nitro-hydrochloric acid (0.1 ml).

Scanning electron microscope (SEM)

Morphology of materials was examined by SEM imaging (JEOL JSM-5900LV, Hitachi S3500N). The SEM was operated at an operational voltage of 10 and 25 kV.

X-ray diffraction (XRD)

The structures of the metal oxides were studied by X-ray diffraction (Philips X'Pert Pro System, λCu Kα = 0.154056 nm, operating at 40 kV/45 mA). The measurements were recorded on the computer with X'Pert Data collector software. Standard measurements were taken by connecting the computer to the spinner on X'Celerator mode. The recorded measurements were between 2 θ angles from 5°-70° with a step size of 0.017° and a scan rate 40 s/step.

Raman spectroscopy

The Raman measurements were performed with a Renishaw Raman spectrometer Series 1000. After calibration of the Raman setup using an Si(111) single crystal the Raman spectra were recorded using the green line of an Ar-ion laser (514.53 nm, 2.41 eV) at elevated temperature under inert conditions. For ex situ measurement the thermally activated (423 K, 1 h, N_2 flow) samples were prepared over glass slits. The final spectra were 1-10 accumulations in a range of $100-4000$ cm^{-1}. Similar conditions were applied for in situ Raman measurements. In situ Raman measurements were performed by placing materials between quartz wool in a tubular quartz reactor (1.62 mm ID). First reference spectra of sample were recorded in N_2 flow at elevated temperature. Subsequently, the surface active species were probed by Cl_2, until a consistent spectrum was achieved. The Cl_2 reversibility on the surface was checked by switching back to inert gas (N_2) flow.

Electron Spin Resonance (ESR) spectroscopy

ESR spectra of N-modified materials were recorded in perpendicular mode on an X-band Joel Jes Fa 200 spectrometer equipped with a cylindrical mode cavity and a liquid helium cryostat. The samples were placed in a quartz tube for ESR measurement in a temperature range of 298−473 K. The experiment was performed using 9.45 GHz, 1mW microwave power. Jes-Fa Series software package (Version 2.2.0) was used for data analysis and simulation.

IR spectroscopy

The information about Lewis acid site was studied by IR spectroscopy using pyridine (Py) (99.8%, Sigma – Aldrich) as probe molecule. IR spectra were recorded using a Bruker IFS 88 (Perkin – Elmer 2000) FT-IR spectrometer operated at a resolution of 4 cm^{-1}. The self-supporting wafers of 0.4 cm ID were prepared by pressing the sample at 10 bar and placing it in a gold sample holder at the center of the furnace, inside the in situ cell connected to the vacuum system. Before the measurement, the samples were activated at 450 °C for 1 h in vacuum (at ~10^{-6} mbar). The adsorption of pyridine was carried out at a partial pressure of 1×10^{-1} mbar using an equilibration time of 30 minutes. After adsorption the physically adsorbed pyridine molecule was degassed at 150 °C for 1 h. IR spectra were collected at 150 °C as an accumulation of 120 scan. To allow the quantitative comparisons of the acid site density, the peak area of before and after Py-adsorption was subtracted using GRAMS-AI software. The concentrations of Brønsted and Lewis acid sites able to retain pyridine at 150 °C were determined using the extinction coefficients and the adsorbance surface of the corresponding bands at around 1540 and 1450 cm^{-1} bands (for PyH$^+$ and PyL), respectively.[21] The quantity of strong acid site concentration was estimated by the spectra recorded after the Py-desorption at 450 °C for 1 h (temperature ramp of 10 °C / min).

The presence of Lewis basic sites in the materials were analyzed by carbon dioxide (CO_2) gas adsorption. IR spectra of adsorbed CO_2 were recorded on a Bruker VERTEX 70 spectrometer at a resolution of 4 cm^{-1} with 64 scans. The materials were activated at 450 °C for 1 h in vacuum and then cooled to 150 °C. They were subsequently exposed to CO_2 by a partial pressure of 1×10^{-1} mbar at 150 °C for an equilibrium time of 30 minutes. The IR spectra were recorded once equilibration was achieved. Further, the stronger basic sites were analyzed after temperature program desorption of CO_2 at 450 °C for 1 h (temperature ramp of 10 °C per min).

Solid state MAS-NMR spectroscopy

^{27}Al MAS NMR spectra of the γ-Al$_2$O$_3$ samples were recorded on a Bruker AV-500 NMR spectrometer. A field strength of 11.7 T and 10 kHz spinning speed was applied by placing samples in 4 mm ZrO$_2$ rotors. NMR-spectra were collected at a frequency of 130.3 MHz with 0.46 μs excitation pulses and 0.25 s recycle times. Al(NO$_3$)$_3$ (δ = -0.54 ppm) was used as a reference for ^{27}Al chemical shifts.

NH$_3$-temperature program desorption (NH$_3$-TPD)

NH$_3$-TPD experiment was performed in six-fold parallel quartz reactor. The catalysts were activated by heating in vacuum to 450 °C (rate 10 °C/min) for 1 h. NH$_3$ (Westfalen AG, ≥99.99 %) was adsorbed at 100 °C with a partial pressure of 1 mbar for 1 h and subsequently the samples were evacuated at 10^{-2}-10^{-3} mbar for 2 h to ensure the total removal of physisorbed NH$_3$ molecules. For the TPD experiments the 6 samples were sequentially heated from 110 °C to 770 °C with a rate of 10 °C/min and the species desorbing were monitored by mass spectrometry (Balzers QME 200). For the better reproducibility of results, in each set of experiments a reference sample (H-ZSM-5 90) with known concentration of acid sites (360 μmol/g) was used for calibrating the MS signal.

5.4   Results and discussions

5.4.1 Physicochemical properties of materials

The textural properties, chemical compositions and acid site concentrations of selected aluminum based materials were determined using N$_2$ physisorption, NH$_3$-TPD, Py-IR and ^{27}Al solid-state NMR. The detailed analysis results of aluminum based materials are summarized in Table 5-1.

**Table 5-1.** Physicochemical properties of AlCl$_3$, α-Al$_2$O$_3$ and γ-Al$_2$O$_3$.

Catalyst	S_{BET} [a] (m^2/g)	V_{pore} [b] (cm^3/g)	D_{pore} [b] (Å)	Lewis acidity (µmol/g)[e]	Al site (%)[c]	
					Al$_{octa}$	Al$_{tetra}$
AlCl$_3$	14.8	0.012	28	n.a[g]	n.a	n.a.
α-Al$_2$O$_3$	3.6	n.d.[f]	n.d.	60	100	-
γ-Al$_2$O$_3$	86.7	0.161	34	83 (91)[d]	65.5	30.3

[a]BET surface area. [b]V$_{meso}$ and V$_{micro}$ correspond to the micro- and mesopore volume of catalysts, respectively. [c]Calculated from ^{27}Al NMR analysis. [d] After adsorption of pyridine at 150 °C and outgassing for 1 h under vacuum. [e]Calculated based on NH$_3$ -TPD experiments within the ± 5 % error. [f]Not detected. [g]Not analyzed.

Depending on the synthesis, origin, structural stability and adjacent atoms of Al, the textural properties of materials varied markedly. In the case of AlCl$_3$, 14.8 m^2/g of specific surface area was determined by N$_2$ adsorption study, however, it was only 3.6 m^2/g for α-Al$_2$O$_3$. In comparison to that, γ-Al$_2$O$_3$ material showed specific surface area about 86.7 m^2/g, which is around 6 times higher than AlCl$_3$. All aluminum based materials were characterized as mesoporous structure (D$_{pore}$ = 28-34 Å) with considerable amount of pore volumes (Table 5-1). In-situ infrared spectroscopy of pyridine adsorbed on γ-Al$_2$O$_3$ was used to differentiate the type and strength of surface Lewis acidity.[22] The infrared spectrum in the range of 1400-1700 cm^{-1} for γ-Al$_2$O$_3$ material before and after the pyridine adsorption is shown in Figure 5-1.
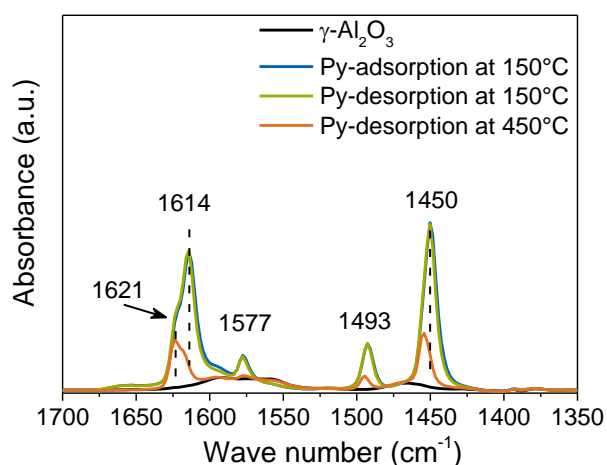
Figure 5-1. In-situ IR spectroscopy of pyridine adsorbed on γ-Al$_2$O$_3$.

The band at 1450 cm^{-1} demonstrates the presence of Lewis acid sites. The three bands at 1577, 1614 and 1621 cm^{-1} points to the existence of three Lewis acid sites with different strength, *i.e.*,

weak, medium and strong (Figure 5-1). The absence of a band at about 1540 cm^{-1} indicating the absence of any relevant number of H$^+$ to form pyridinium ions, which implies that no Brønsted acidity is present.[21] The results obtained from acidity study of γ-Al$_2$O$_3$ by using pyridine as a probe molecule was further confirmed by NH$_3$-TPD measurements (Table 5-1). It is important to note that, employing two different characterization methods (NH$_3$-TPD and Py-IR) similar concentration of accessible Lewis acid sites on γ-Al$_2$O$_3$ (Table 5-1) was determined. It could be because of high mesoporosity of γ-Al$_2$O$_3$ material allow both probed molecules equally to reach the Lewis acid sites. Similarly, the high concentration of Lewis acidity (60 μmol/g) on α-Al$_2$O$_3$ was measured, however, it was about 1.4 times lower than for γ-Al$_2$O$_3$ (Table 5-1).

The presence of Lewis basicity on the γ-Al$_2$O$_3$ was studied by in situ IR-spectroscopy using CO$_2$ as probe molecule.[23] In Figure 5-2, a comparison of the IR spectra of bare γ-Al$_2$O$_3$ is presented next to the spectra of γ-Al$_2$O$_3$, when CO$_2$ was adsorbed at 150 °C and afterward evacuated at 450 °C.
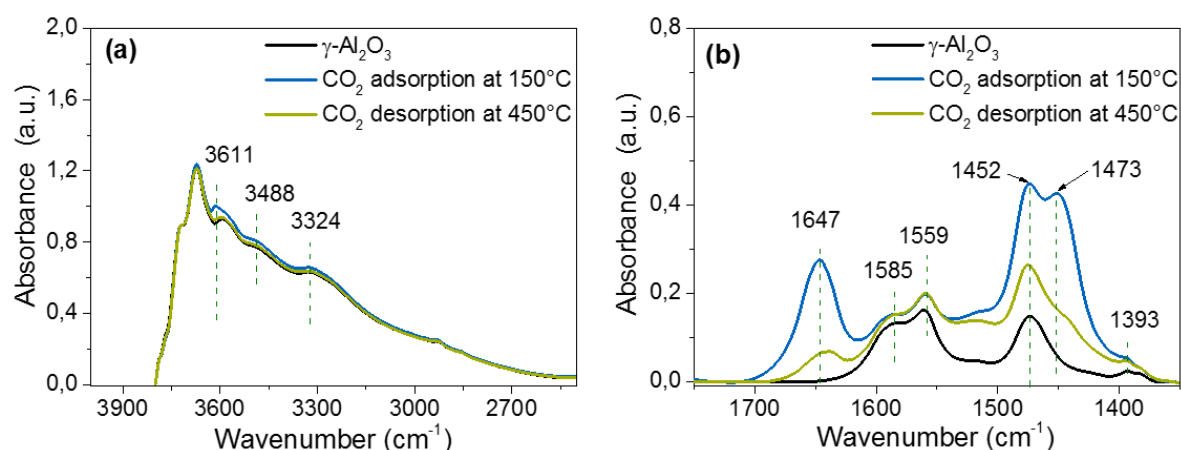
Figure 5-2. IR spectra of γ-Al$_2$O$_3$ recorded before and after CO$_2$ adsorption at 150 °C and following desorption at 450 °C and 0.1 mbar. Spectrum (a) shows the typical fingerprint region of surface OH groups, while in the spectrum (b) the lattice oxygen vibrations are evidenced.

The nature of new bands corresponding to the surface species formation by CO$_2$ adsorption on γ-Al$_2$O$_3$, was assigned based on previous infrared studies of the CO$_2$ / Al$_2$O$_3$ system. On γ-Al$_2$O$_3$ pre-treated at 450 °C, adsorption of CO$_2$ at 150 °C gives rise to three major infrared bands at 1647, 1452 and 1473 cm^{-1} (Figure 5-2 (b)). The band at 3611 is assigned to –OH group stretching vibrations and is less affected by CO$_2$ adsorption / desorption while the other bands are due to unidentate and bidentate bicarbonate species formed on the active alumina surface.[24]

151

Based on the direct comparison with the IR spectrum of KHCO$_3$, the bands at 1647 and 1452-1473 can be assigned to asymmetric C-O and symmetric C-O stretching, respectively, of monomeric bicarbonate species formed by interaction of CO$_2$ with surface hydroxyl groups as schematically indicated in Scheme 5-2.[25,26]
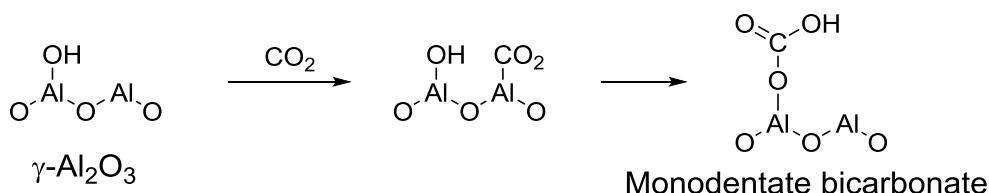
Scheme 5-2. Proposed pathway for bicarbonate formation during CO$_2$ adsorption on γ-Al$_2$O$_3$.

The physisorption of CO$_2$ occurs on the aluminium sites of neighbouring aluminium bearing hydroxyl groups. In the following step, the surface reaction of adsorbed CO$_2$ with –OH groups results in the formation of stable unidentate bicarbonates (Figure 5-2 (b)). Heating under vacuum till 450 °C, parallel decrease in all bicarbonate bands confirmed the reversibility of surface bicarbonate species.

Beside bicarbonate further mono and bidentate carbonates with typical bands at 1585, 1559 and 1393 cm^{-1} are formed on the sites Lewis basic sites of γ-Al$_2$O$_3$. The proposed structure as suggested by Michael P. Rosynek is shown in Scheme 5-3.[26]
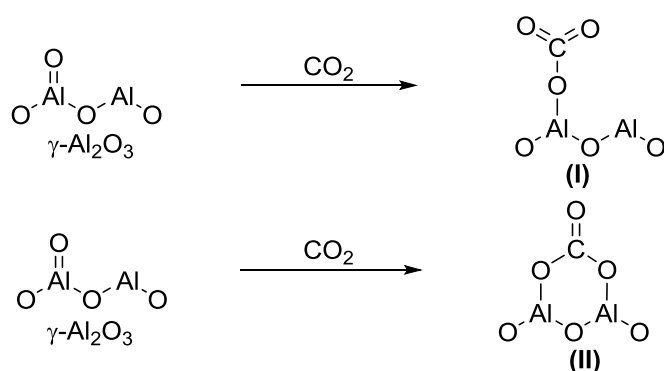
Scheme 5-3. Proposed pathway for the monodentate and bidentate carbonate formation by CO$_2$ adsorption on γ-Al$_2$O$_3$.

In comparison to the γ-Al$_2$O$_3$, the basic sites of α-Al$_2$O$_3$ were similarly probed by CO$_2$. In the case of α-Al$_2$O$_3$, a material bearing no surface hydroxyl groups, did not resulted in the formation of surface stable bicarbonate and carbonate species during CO$_2$ treatment.

Solid state MAS ^{27}Al NMR was employed to characterize the different coordination environment of active sites on γ-Al₂O₃ (supporting information, Figure S5-2). The resonance peak at 67 ppm appears due to the tetrahedrally (tetra) coordinated Al, however, the peak at 10 ppm represent the octahedrally (octa) bound Al.[27] Based on the ^{27}Al-NMR results, as received γ-Al₂O₃ sample contains 65.5 % of octahedrally and 30.3 % of tetrahedrally coordinated Al. However, α-Al₂O₃ showed 100 % octahedrally bounded Al. In the case of solid AlCl₃, –Cl is used as a ligand / coordinating atom, the octahedral Al is stabilized in sheet-like layered cubic close packed framework.[28]

Very defined x-ray diffraction pattern of γ-Al₂O₃ and α-Al₂O₃ confirms the well-defined phase/structure and purity of samples (see supporting information, Figure S5-3). The mean particle size of less than 30 nm for the γ-Al₂O₃ was determined by SEM imaging (see supporting information, Figure S5-4).

Alumina material exist in several metastable crystalline structures such as η-, γ-, δ-, θ-, β-, κ-, χ, and α-Al₂O₃.[29] It have been shown previously, that the different phases of alumina can be achieved by thermal treatment of treatment of well defined γ-Al₂O₃.[30] Therefore, to establish the structure activity relationship, γ-Al₂O₃ was thermally treated under inert conditions from a temperature range of 600 to 900 °C and the obtained materials were characterized by N_2 physisorption and NH_3-TPD. The change in physicochemical properties with structural organization during thermal treatment of γ-Al₂O₃ is summarized in Table 5-2.

Table 5-2. Physicochemical properties of thermally treated γ-Al₂O₃.

Obtained[d]	Treatment	S_{BET} [a] (m^2/g^{-1})	V_{pore} [b] (cm^3/g)	D_{pore} [b] (Å)	Lewis acidity $(\mu mol/g)$[c]
γ-Al₂O₃	As-received	86.7	0.161	34	83
γ-Al₂O₃	N_2, 600 °C	79.5	0.155	36	74
γ/δ-Al₂O₃	N_2, 700 °C	83.3	0.147	31	66
δ-Al₂O₃	N_2, 800 °C	82.4	0.157	30	61
δ/Ө-Al₂O₃	N_2, 900 °C	95.4	0.161	32	45

[a]BET surface area. [b] V_{meso} and V_{micro} correspond to the micro- and mesopore volume of catalysts, respectively. [c] calculated based on NH_3-TPD experiment. [d] Based on literature.[31]

The detailed textural analysis of thermally treated materials revealed the similar specific surface area (~87±8 m²/g), pore volume (~0.154±0.01 cm²/g) and mean pore diameter (~33±3 Å) (see,

Table 5-2). In contrast to that, NH$_3$-TPD experiments showed, the decreased in the concentration of Lewis acid sites with increasing temperature (Table 5-1 and supporting information Figure S5-5). This phenomenon is hypothesized due to the structural transformation and/or reorganization of oxides and hydroxide functional groups.

5.4.2 Cl$_2$ activation study

In order to understand the catalytic activity of aluminum based materials for COCl$_2$ synthesis from Cl$_2$ and CO, it is important to clarify the functional role of electronically different Al atoms at elementary steps. Therefore, the catalytic Cl$_2$ activation study in the presence of γ-Al$_2$O$_3$ has been performed at 150 °C using a pulse quartz reactor connected to a MS analyzer (set-up shown in Supporting information, Figure S5-1). Typical adsorption profiles recorded during Cl$_2$ treatment are presented in Figure 5-3.
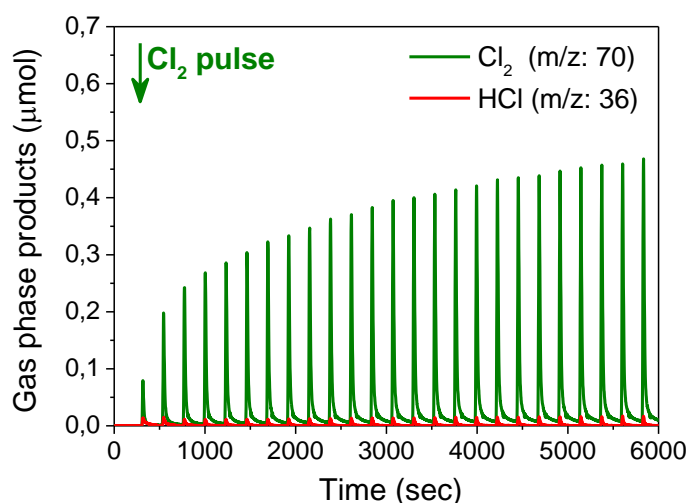
Figure 5-3. Cl$_2$ activation study. Experimental conditions: 50 Cl$_2$ pulses (230 s pulse length, 1.8 µmol Cl$_2$ / pulse), T = 150°C, He flow: 10 ml/min, 100 mg of as received γ-Al$_2$O$_3$.

The adsorption of Cl$_2$ on the active sites located in the selected as received γ-Al$_2$O$_3$ materials is dynamic in nature, involving different types of structures and coordination of Cl$_2$ to the catalyst surface. At the beginning of Cl$_2$ pulses over γ-Al$_2$O$_3$, the material showed the irreversible Cl$_2$ adsorption (14.0 µmol/g, Table 5-3) and small amount of HCl formation (3.0 µmol/g, Table 5-3) following enabled substitution reactions (Figure 5-3). Cl$_2$ (characterized by m/z: 70, Figure 5-3) in the gas phase was, however, detected in the first applied pulse over γ-Al$_2$O$_3$, steady state equilibrium is achieved only after approx. 4000 sec. In the case of γ-Al$_2$O$_3$ the irreversible

addition of Cl$_2$ is hypothesized to occur at the more reactive, at structural and topological defect sites and at coordinatively unsaturated positions. Based on the previous studies on the chlorination of Al$_2$O$_3$, the reactions shown in equation 5-1 and 5-2 can be proposed for irreversible Cl$_2$ addition to γ-Al$_2$O$_3$, where arrows are indicating the preferred bond cleavage.[32,33] It was interesting to note that during the experiments conducted in the pulse reactor, the expected HOCl (m/z: 52) was not detected by MS analysis.

[5-1]

[5-2]
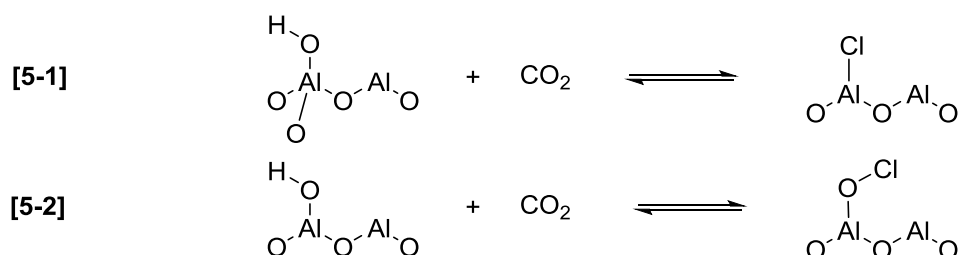
The irreversible Cl$_2$ interactions result in aluminum bonded Cl species e.g. [Al−Cl]$^{+2}$ on the surface of γ-Al$_2$O$_3$ (equation 5-1). The small amount of HCl formed (3.0 μmol/g, Table 5-3) proceeds by the reaction of Cl$_2$ with surface bound -OH groups (equation 5-2). For a better understanding of underlying Cl$_2$ reactions with aluminum based materials, the results from Cl$_2$ pulse experiment on AlCl$_3$ and α-Al$_2$O$_3$ are presented next to γ-Al$_2$O$_3$ in Table 5-3.

Table 5-3. Summary of Cl$_2$ activation study on selected aluminum based materials at 423 K.

Material	Irreversible Cl$_2$ interaction (μmol/g)	HCl formation (μmol/g)
AlCl$_3$	0	0
α-Al$_2$O$_3$	2.0	1.0
γ-Al$_2$O$_3$	14.0	3.0

In comparison to the γ-Al$_2$O$_3$, well-defined AlCl$_3$ material is quite stable in Cl$_2$ atmosphere at 150 °C towards surface chlorination (see supporting information, Figure S5-6, Table 5-3). Irreversible Cl$_2$ adsorption and HCl formation was not observed. But, α-Al$_2$O$_3$ material showed about 2 μmol/g of irreversible Cl$_2$ interaction and only 1 μmol/g of HCl formation. The amount of total Cl$_2$ uptake on γ-Al$_2$O$_3$ was found about 7 times higher than α-Al$_2$O$_3$. This might be due to the presence of higher amount of terminating / extra-framework sites on γ-Al$_2$O$_3$ (5.9 mmol / g for γ-Al$_2$O$_3$ while no extra-framework alumina sites were found for γ-Al$_2$O$_3$ as evidenced by

^{27}Al MAS NMR). Lower chlorination degree of α-Al$_2$O$_3$ compared to γ-Al$_2$O$_3$ is in line with previous studies.[34]

The change in surface properties in terms of restructuring and chemical nature of active sites during Cl$_2$ interaction was characterized at macroscopic as well as microscopic level by using XRD, SEM, IR spectroscopy using probe molecules such as pyridine and CO$_2$ and solid state ^{27}Al MAS-NMR. XRD pattern and SEM images of chlorinated γ-Al$_2$O$_3$ were identical to the as-received γ-Al$_2$O$_3$ confirming that Cl$_2$ interaction did not induce any change in well-ordered crystalline phase (see supporting information, Figures S5-7 and S5-8).

The change in the Lewis acidity due the surface *Al-Cl bounded species (as proposed in Equation 5-1) of the γ-Al$_2$O$_3$ after chlorination was determined by probing the active site with pyridine followed by the changes in IR-spectroscopy. The amount of Lewis acidic sites in γ-Al$_2$O$_3$ and chlorinated γ-Al$_2$O$_3$ were normalized to the weight of samples for the correct comparison (Figure 5-4).

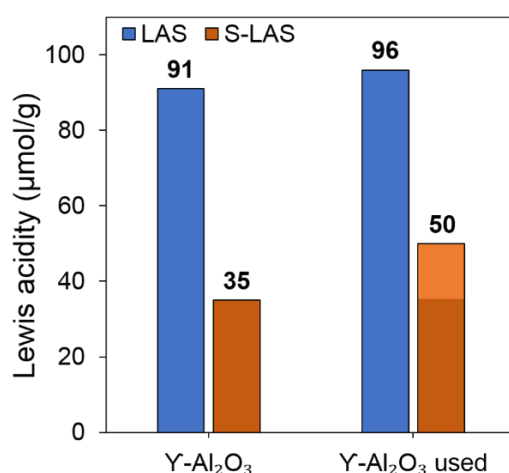**Figure 5-4**. Comparisons of Lewis acidic site of γ- Al$_2$O$_3$ and γ- Al$_2$O$_3$ + Cl$_2$.

The total concentration of Lewis acid sites determined by Py-IR measurements was estimated very similar (93 ± 3 μmol/g) in amount after chlorination of γ-Al$_2$O$_3$ in comparison to the as-received γ-Al$_2$O$_3$ material. The similar amount of the total Lewis acid sites (LAS) indicating that the aluminum sites are not affected during Cl$_2$ treatment of γ-Al$_2$O$_3$ at 150 °C. However, an increase in the strong Lewis acidity (S-LAS) by about 1.4 times after chlorination of γ-Al$_2$O$_3$ was due to the formation of *Al–Cl surface functional groups. This was due to higher electron withdrawing ability of Al bonded Cl atoms compared to surface -OH groups. [35]

Proposed equation 5-2, suggests the formation of *Al-O-Cl type of functional groups by Cl_2 interaction with γ-Al_2O_3. However, this type of species have basic character and its presence and the chemical nature has been characterized by the use of CO_2 as probe molecule. In situ IR spectroscopy was adopted to monitor the CO_2 adsorption on chlorinated γ-Al_2O_3 surface. Direct comparison of the IR spectra of the γ-Al_2O_3 before and after catalysis (Figure 5-5), reveal that during Cl_2 treatment various irreversible transformations as proposed in equation 5-1 and 5-2 occur. On the new sites of γ-Al_2O_3 catalyst, CO_2 is only weakly adsorbed (Figure 5-5).
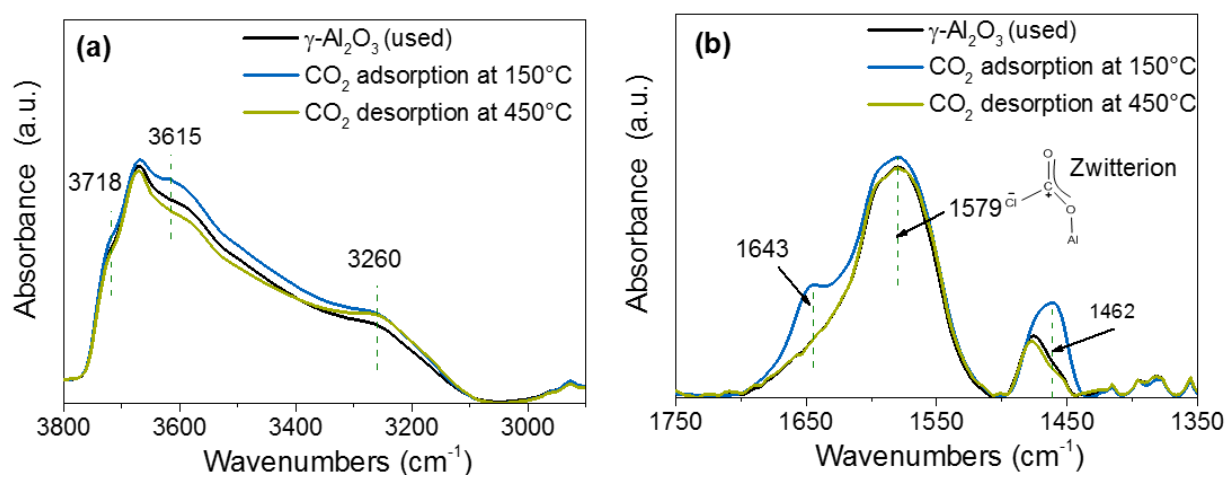

Figure 5-5. In-situ IR spectroscopy of CO_2 adsorption and desorption using chlorinated γ-Al_2O_3.

Upon CO_2 addition at partial pressure (0.1 mbar) to a chlorinated γ-Al_2O_3 sample showed the formation of three new bands at 1643, 1579 and 1462 cm⁻¹, corresponding to the new surface species formation. Based on the sift in the band position compared to bare surface CO_2 adsorption, the two bands at 1643 and 1462 cm⁻¹ could be assigned to the chlorine containing $ClCO_3^{-1}$ specie while the band at 1579 cm⁻¹ was due to the mono-dentate zwitterion formation on the surface as indicated in following chemical equations shown in Scheme 5-4.
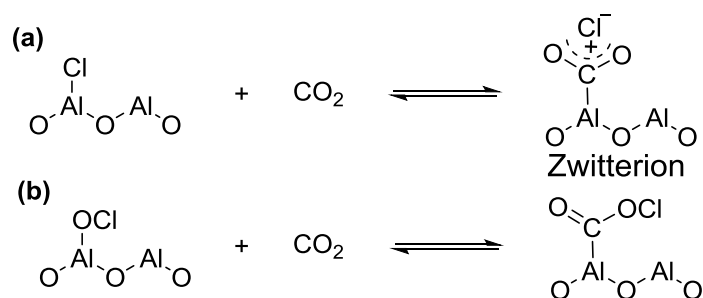

Scheme 5-4. Proposed species formation on chlorinated γ-Al_2O_3 by CO_2 adsorption.

However, the surface hydroxyl groups were hardly affected by CO_2 adsorption on chlorinated γ-Al_2O_3.

The TPD after CO_2 adsorption confirmed the significant reversibility of new species formed on the surface on chlorinated γ-Al_2O_3. CO_2 adsorption on γ-Al_2O_3 (before and after chlorination) gave further the evidences for the reorganization of the surface functional groups and formation of new *Al−O−Cl and *Al−Cl stable surface groups during catalysis.

Magic angle spinning ^{27}Al NMR studies of γ-Al_2O_3 after chlorination showed the decrease by ~3 % in tetrahedrally coordinated Al and a concomitant increase by ~3 % in octahedrally coordinated Al atoms during Cl_2 adsorption (supporting information, Figure S5-9) indicating the irreversible Cl_2 interaction with the tetrahedral Al sites and the consecutive formation of octahedrally coordinated Al sites. This would also count for the increase in strong Lewis acidity following catalysis.
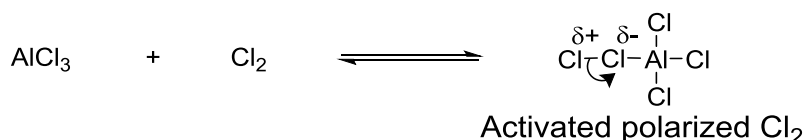
After the saturation of those reactive sites for Cl_2 adsorption, a reversible interaction and formation of reactive chlorine intermediate (surface activated Cl_2 in dynamic equilibrium with gas phase Cl_2) was observed (Scheme 5-5).

Activated polarized Cl_2
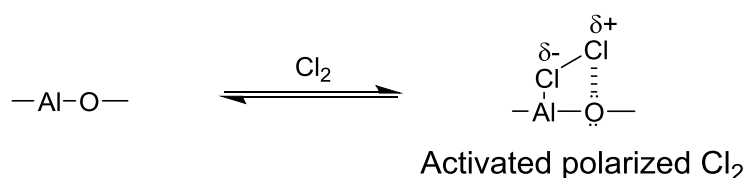
Scheme 5-5. Schematic proposed representation of activated Cl_2 on Al_2O_3 materials.

Reversibly Cl_2 is activated on Lewis acid based pairs of γ-Al_2O_3 and led to the formation of reactive polarized Cl_2 species. Polarized Cl_2 is a charged molecule, stabilizing partial positive and negative charges on both Cl atoms. In addition, the bridged oxygen atoms stabilizing high electron density have ability to interact with electron positive species. Therefore, the formed reactive $Cl^{\delta+}$ species is preferentially stabilized on the electron rich neighboring oxygen atoms (Scheme 5-5). However, during chlorination, the concomitant, in situ generation of electrophilic oxygen sites can not be excluded.[36]

In the case of $AlCl_3$, the Cl_2 activation also occurs on the Al atoms with Lewis acid character but due to the absence of any electron rich surface, no further stabilization of the reactive $Cl^{\delta+}$ species can occur (the schematic representation shown in Scheme 5-6).

$$AlCl_3 \quad + \quad Cl_2 \quad \rightleftharpoons \quad \overset{\overset{Cl}{|}}{\underset{\underset{Cl}{|}}{\overset{\delta+ \;\; \delta-}{Cl \overset{\curvearrowright}{Cl-Al-Cl}}}}$$

Activated polarized Cl₂

Scheme 5-6. Proposed Cl₂ activation on AlCl₃.

In an attempt to provide the more comprehensive details on the mechanism of reversible Cl₂ activation processes, in situ Raman spectroscopy was employed. Raman spectroscopy is particularly know as a very sensitive technique for detection of polarization molecules.[37] Preforming Raman spectra of activated γ-Al₂O₃ in inert condition at 150 °C showed the absence of Raman active bands (Figure 5-6).

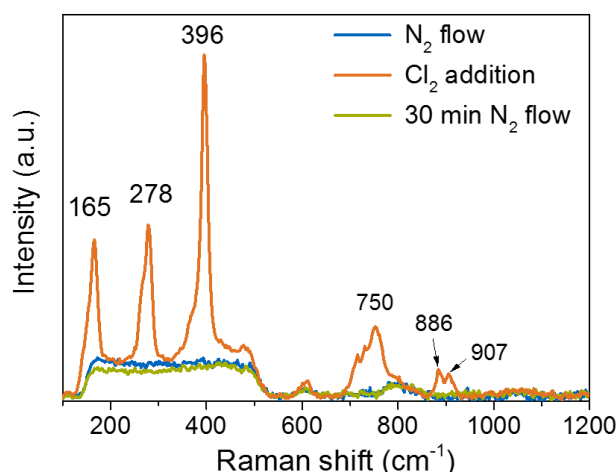**Figure 5-6.** In situ Raman spectra of γ-Al₂O₃ contacted with Cl₂ at 150 °C.

In the presence of Cl₂, the reversible intense characteristic bands formation were observed in the range of 100-1000 cm^{-1}. These new bands were totally distinct from the free gas phase Cl₂ band at 540 cm^{-1}, which was not observed under experimental conditions. Analyzing carefully the new Raman bands, we proposed that the most intense band at 396 cm^{-1} is due to the symmetrical mode vibration of polarized Cl₂. The low energy bands at 278 and 165 cm^{-1} are attributed to the bending modes vibrations (depolarized). The weak bands at 886 an 907 cm^{-1} can be assigned to the Fermi resonance with an overtone or a combination tone. A broad band at 750 cm^{-1} is due to the weak *Al and Cl₂ interaction. Typical patterns of activated Cl₂ were similar to those obtained in the presence of a well-defined 2,6-dichloropyridine material, a model molecule which can also stabilize a Lewis acid character of carbon at para position.[38] The nature of activated Cl₂ species and their reactivity was further investigated by using CH₄ as a probe molecule. The multiple chlorine substitution of strong C*-H of CH₄ is known as a

radical reaction.[38] The formation of chlorinated CH_4 derivatives *e.g.* $CH_{4-n}Cl_n$ were carefully analyzed and compared with non-catalytic radical chain reaction (Figure 5-7).

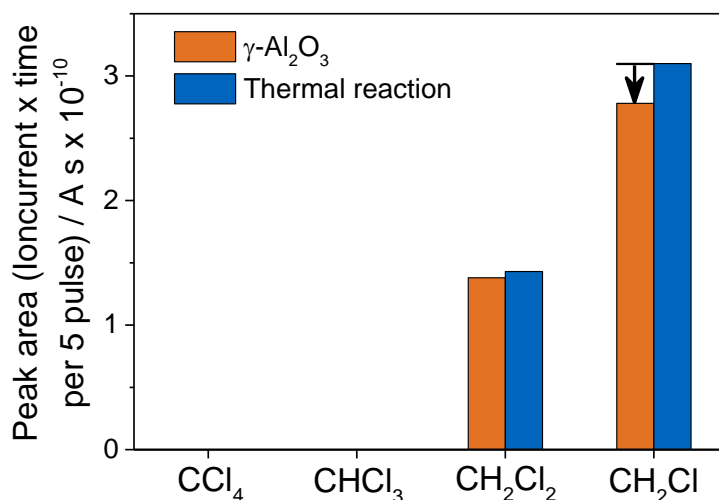**Figure 5-7.** Probing activated Cl_2 with CH_4. Experimental conditions: 100 pulses (230 s pulse length, 1.8 μmol Cl_2 / pulse), 5 vol. % CH_4 in He flow: 10 ml/min, T = 423 K, 100 mg of Al_2O_3. Chlorinated CH_4 derivatives were analyzed by MS as CCl_4 (m/z: 117), $CHCl_3$ (m/z: 83), CH_2Cl_2 (m/z: 49), CH_3Cl (m/z: 50).

The close examination of C-H functionalized CH_4 derivatives formed on $γ$-Al_2O_3 showed no change in amount compared to the thermal reaction (Figure 5-5). The formation of CH_3Cl and CH_2Cl_2 was due to the thermally accessible Cl radicals at 150 °C. The lower amount of CH_3Cl detected in the presence of $γ$-Al_2O_3 compared to the thermal reaction was due to the competitive adsorption of chlorinated hydrocarbons with Cl_2.

In-situ ESR spectroscopy was further employed to understand the electronic character of activated Cl_2. ESR spectroscopy is a very sensitive technique for radical detection. In time resolved ESR spectroscopic study of Cl_2 to $γ$-Al_2O_3 did not induce any change in ESR spectra. This experiment clearly evidenced that no radicalic species are formed during long exposure of Cl_2 on $γ$-Al_2O_3.

Similarly, the extensive Cl_2 activation study on $α$-Al_2O_3 and $AlCl_3$ using in-situ Raman and ESR spectroscopies, confirmed the ionic type of reversibly activated surface species formation as proposed in Scheme 5-5 and Scheme 5-6.

5.4.3 CO activation study

CO interaction was studied on one adequated aluminum based material, γ-Al_2O_3 using pulsed experiments together with in situ IR spectroscopic measurements (Figure 5-8).
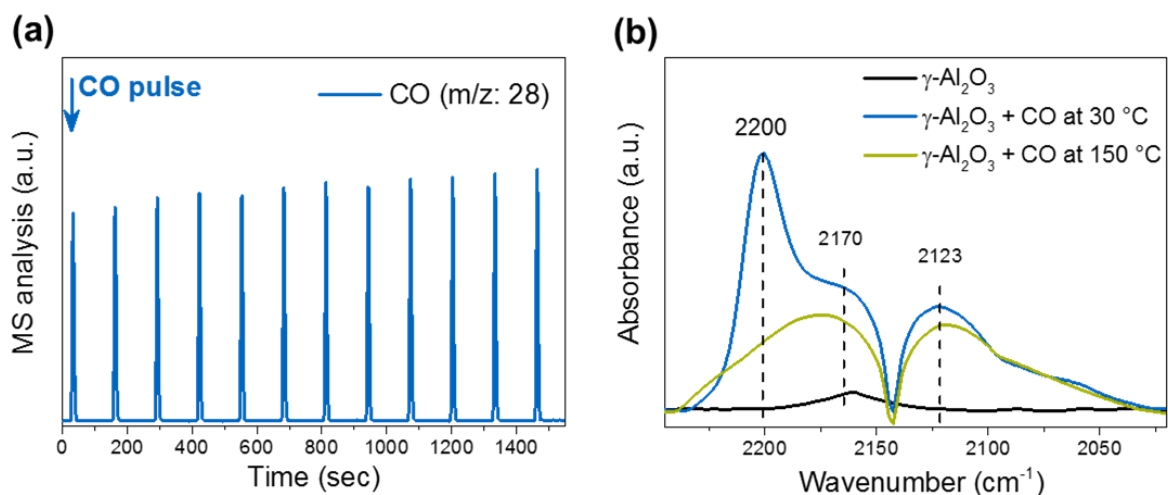

Figure 5-8. CO interaction study on γ-Al_2O_3, (a) transient MS analysis, (b) in situ IR spectroscopy.

By the repetitive CO additions combined with in situ IR spectroscopy, a weak reversible interaction of CO with γ-Al_2O_3 was observed (Figure 5-8). MS analysis of CO pulses showed only CO in gas phase however, no other gas phases products were detected (Figure 5-8a). However, in situ IR spectroscopic results of CO adsorption at partial pressure of 10 mbar on γ-Al_2O_3 at 30 °C, showed three overlapping bands in the C=O stretching region (Figure 5-8b). Based on previous CO adsorption studies[40,41], two bands at 2200 and 2170 cm^{-1} are assigned to the CO adsorption on octahedrally and tetrahedral coordinated Al sites, respectively. The shift in the band positions on differently coordinated Al sites can be explained by the electron back donation capability of the neighboring oxygen atoms to CO. Higher the coordination number, the lower electron back donation is expected. Based on previous study, the band at 2123 cm^{-1} was assigned to the *Al-OH·····CO interactions.[41] Note that the hydroxyl bound CO feature is rather broad on γ-Al_2O_3 sample because of different type of hydroxyl groups on surface. By increasing the temperature from 30 to 150°C, IR band at 2200 cm^{-1} decreased, however, the other bands were quite stable (Figure 5-8b).

Temperature program desorption after CO adsorption on γ-Al_2O_3 evidenced the absence of any oxygen surface species formation during CO interaction.

5.4.4 Mechanistic study for COCl₂ synthesis on aluminum based materials

The complex Cl_2 activation during $COCl_2$ formation was studied on three aluminum based materials having different structural and textural properties at 150 °C. The pulse experiment result when γ-Al_2O_3 is used as catalyst to enable the $COCl_2$ formation from Cl_2 and CO is presented in Figure 5-9.
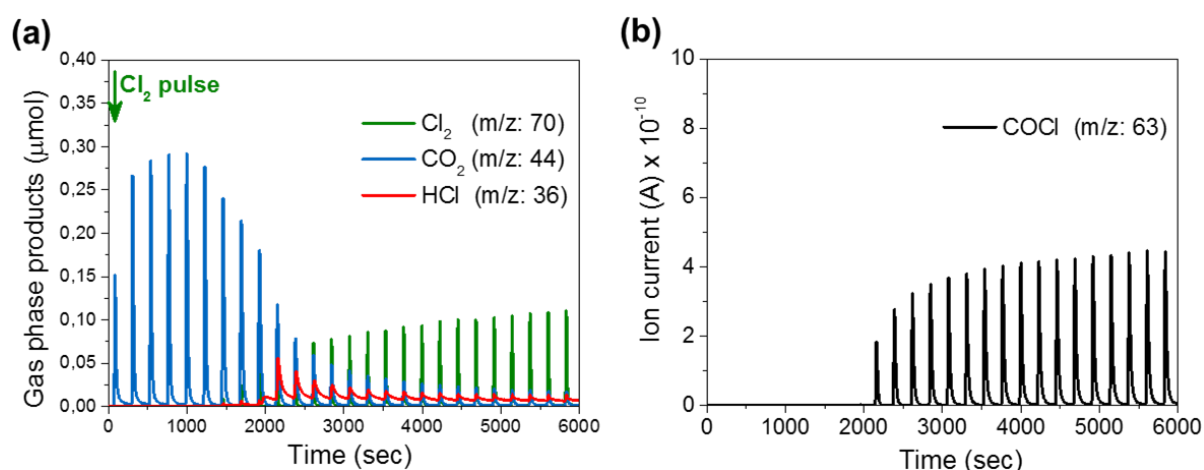

Figure 5-9. (a) Cl_2 adsorption at 473 K in 5 vol. % CO and (b) $COCl_2$ synthesis. *Experimental conditions*: 50 Cl_2 pulses (230 s pulse length, 1.8 μmol Cl_2 / pulse), 5 vol. % CO in He flow: 10 ml/min, 100 mg of γ-Al_2O_3.

First Cl_2 pulse under isothermal condition showed the complete irreversible uptake of Cl_2 (21.6 μmol/g) and formation of CO_2 (148 μmol/g) and HCl (75 μmol/g). The formation of CO_2 in the gas phase was due to the carbonization reaction occurring on the most reactive sites (structural and topological defects) of γ-Al_2O_3. The observed phenomenon is in line with previous studies of Cl_2/CO interaction on γ-Al_2O_3.[36] The proposed reaction for the formation of CO_2 is presented by Scheme 5-7.[36]
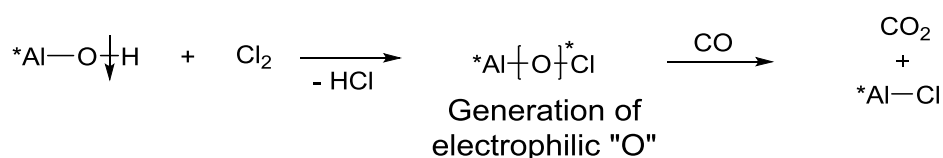
Scheme 5-7. Proposed pathway for CO_2 formation on γ-Al_2O_3 in the presence of Cl_2 and CO.

In the concomitant presence of Cl_2 and CO, Cl_2 adsorption on γ-Al_2O_3 led to the formation of surface stabilized electrophilic oxygen atoms. In the following step, the reaction of CO (which has nucleophilic character) and reactive electrophilic oxygen atoms results in the formation of CO_2 (Scheme 5-7). HCl and CO_2 formation at the beginning of Cl_2 pulses in CO atmosphere on structurally different aluminum based materials is summarized in Table 5-4.

Table 5-4. Summary of Cl_2 activation study under CO atmosphere over aluminum based materials at 150 °C.

Catalysts	HCl formation (µmol/g)	CO₂ formation (µmol/g)	CO₂/HCl
$AlCl_3$	0	0	0
α-Al_2O_3	0.08	0.44	5.5
γ-Al_2O_3	74.90	147.70	2.0

Different amount of HCl and CO_2 formation on different aluminum based materials were shown by transient MS analysis. High amount of HCl (74.9 µmol/g) and CO_2 (147.7 µmol/g) was detected from γ-Al_2O_3, which was much higher (~ 900 times of HCl and ~300 times of CO_2) compared to α-Al_2O_3. However, no HCl and CO_2 was observed using $AlCl_3$.

Following the saturation of these reactive sites, Cl_2 interacts reversibly in the dynamic equilibrium with surface active sites located at framework alumina (Scheme 5-5). The reversibly activated Cl_2 in the concomitant presence of CO leads to $COCl_2$ formation (see in Figure 5-9(b)). Interestingly, γ-Al_2O_3 catalyzed $COCl_2$ formation occurs in the presence of free gas phase Cl_2 in the reaction environment. This type of $COCl_2$ formation profile is very similar to the carbon catalyzed $COCl_2$ synthesis.[42]

Further, the activity for $COCl_2$ synthesis of different aluminium atom based materials was compared and presented in Figure 5-10.
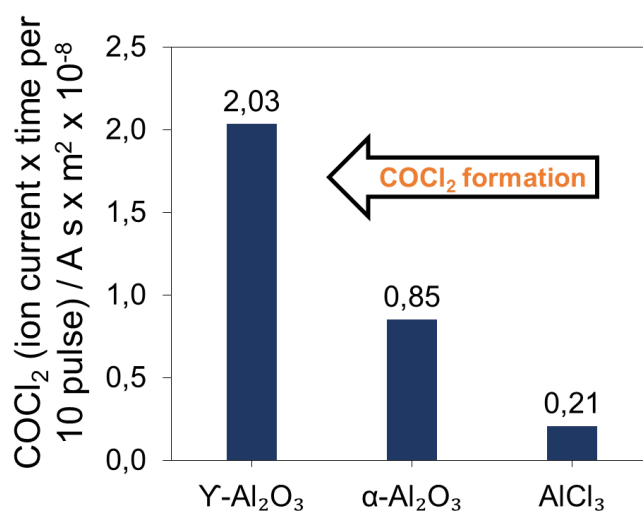
Figure 5-10. Comparisons of phosgene formation on aluminum based materials. Experimental conditions: 50-100 Cl_2 pulses (230 s pulse length, 1.8 µmol Cl_2 / pulse), 5 vol. % CO in He flow: 10 ml/min, 100 mg of material.

Using the reference material, $AlCl_3$ was found catalytically active for $COCl_2$ synthesis. However, changing the ligands in the first coordination sphere of alumina, the activity was drastically improved. In comparison to $AlCl_3$, α-Al_2O_3 showed about 5 times higher activity while in case γ-Al_2O_3 the activity for $COCl_2$ synthesis was further enhanced. Approximately ten times higher rate of $COCl_2$ formation on γ-Al_2O_3 compared to pure $AlCl_3$ was detected indicating the better stabilization ability of the transiently formed highly active $Cl^{\delta+}$ species on the electron rich surface oxygen of γ-Al_2O_3, as proposed in Scheme 5-5.

The structure activity relationship was further established by using structurally different alumina phases, obtained by thermal treatment of γ-Al_2O_3 materials (Table 5-2). By the use of thermally calcined materials it is possible to better understand the structural requirement for efficient $COCl_2$ synthesis. Therefore, the catalytic activity for $COCl_2$ production on structurally different aluminas was compared with their structural properties and presented in Figure 5-11.
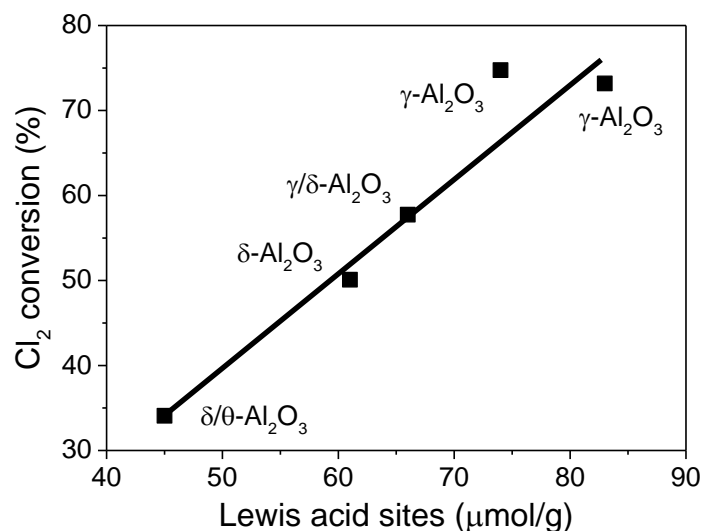
Figure 5-11. Effect of γ-Al₂O₃ thermally calcination at different temperature on Cl₂ conversion and byproducts formation. Experimental conditions: 140 Cl₂ pulses (230 s pulse length, 1.8 µmol Cl₂ / pulse), 5 vol. % CO in He flow: 10 ml/min, 100 mg of material.

The catalytic activity for $COCl_2$ formation was not affected by the thermal treatment till 600 °C. This was not a surprising result since the physicochemical properties of the material were similarly unaffected till 600 °C. Whereas the high temperature treatment (≥ 700 °C) of γ-Al₂O₃ material showed drastic decrease in Cl₂ conversion and subsequent $COCl_2$ formation. Notably, a good correlation was observed between catalytic activity and Lewis acid sites of materials (Figure 5-11). The linear dependency between Cl₂ conversions with concentration of Lewis acid sites confirmed the location of the active sites on Lewis acid base pair on aluminas.

5.4.5 Mechanistic interpretations

The results obtained from the spectroscopic analysis and reaction data is used to propose the $COCl_2$ synthesis mechanism on γ-Al₂O₃. The proposed reaction cycle is shown in Scheme 5-8.
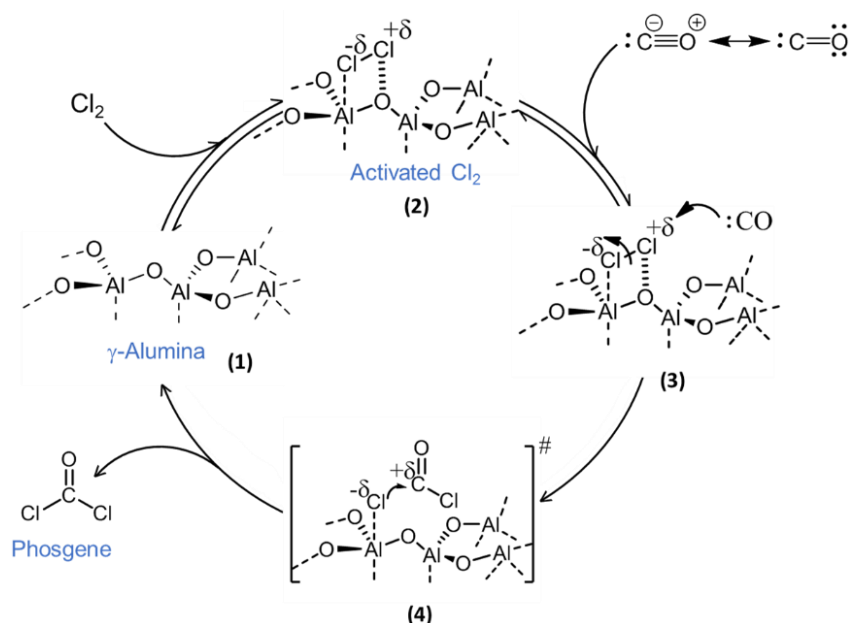
Scheme 5-8. Proposed mechanism of γ-Al$_2$O$_3$ catalyzed phosgene synthesis.

Cl$_2$ is activated on the framework Al-O (Lewis acid-base pair) and forms an activated Cl$_2$ with ionic character (**2**). The highly reactive Cl$^{\delta+}$ species is further stabilized on the electron rich adjacent Lewis basic oxygen atoms. In the second step, CO acting as a nucleophile reacts with the electrophilic Cl$^{\delta+}$ resulting in the formation of [COCl]$^{\delta+}$ (acyl chloride) in the intermediate step. The recombination of [COCl]$^{\delta+}$ and surface physisorbed Cl$^-$ gives COCl$_2$. The proposed reaction sequence is in line with the observed reaction order of one (shown in Table 5-5) for Cl$_2$ and CO.

Table 5-5. Comparisons of activation energy for COCl$_2$ synthesis on different catalysts.

Catalysts	Ea^a [kJ/mol]	Reaction order for Cl$_2$ and CO	Reference
γ-Al$_2$O$_3$	26	1	This work
AlCl$_3$	29	1	This work
Activated carbon	56	1	[43]

^{a} ± 2 kJ/mol.

The apparent activation energies for COCl$_2$ synthesized by the reaction of Cl$_2$ and CO were evaluated from the effect of temperature on the COCl$_2$ formation rates for two aluminum based catalysts and compared with conventional carbon materials (Table 5-5). From the slope of the Arrhenius plots it was determined that COCl$_2$ formation had different apparent activation

energies over the two catalysts with the value for γ-Al$_2$O$_3$ being lower than that of AlCl$_3$ (Table 5-5). This explains the reason for the higher effectiveness of γ-Al$_2$O$_3$ than AlCl$_3$ for COCl$_2$ synthesis. Overall, the apparent activation energy experimentally determined for the two most significant aluminum based materials (shown in Table 5-5) was considerably lower (25-30 kJ/mol) than the one measured for conventional activated carbon (56 kJ/mol[43]) clearly indicating the subtle effect of the local environment of the active sites on the structure and energy of the transition state. In general, aluminium based materials have electron withdrawing ability due to the vacant π-orbitals, with enhanced adsorption and activation abilities. The selective associative adsorption of Cl$_2$ on these sites results in the favored intermediate formation of active ionic chlorine species preferentially stabilized on surface basic oxygens. In the next step, active chlorine intermediates interact with CO and lead to the stable formation of COCl$_2$.

5.5   Conclusions

Detailed characterization of γ-Al$_2$O$_3$ material showed the presence of acidic as well as base sites. Only Lewis acid sites were evidenced using pyridine as probe molecule, however, Brønsted acid sites were absent. Thermal treatment of γ-Al$_2$O$_3$ showed the surface reorganization and reduction of Lewis acidic sites. Increasing the temperature above 800 °C a drastic decrease in Lewis acidity of evidenced. Kinetic study on different aluminum based materials showed the importance of Lewis acid base sites in activation of Cl$_2$. Combining in situ Raman with EPR spectroscopy, the formation of polarized Cl$_2$ species was proved. Using various model materials, it was possible to experimentally show, a better stabilization of reactive Cl$^{\delta+}$ intermediate on electron rich oxygen atoms.

5.6 References

[1]   D. J. Brunelle, M. Korn, *Advances in Polycarbonates, American Chemical Society,* **2005.**

[2]   W. F. Christopher, D. W. Fox, *Polycarboantes, Reinhold Publishing Corporation, New York*, **1962**, 16-18.

[3]   J. A. King, *Synthesis of Polycarbonates*, *Handbook of Polycarbonate Science and Technology*, Marcel Dekker Inc. New York, **2000**.

[4]   M. Bodenstein, *Chem. Rev.*, **1930**, *7*, 225.

[5]   M. Bodenstein, S. Lenher and C. Wagner, *Z. Phys. Chem., Abt. B*, **1929,** 3, 459.

[6]   C. J. Mitchell, W. v. d. Borden, K. v. d. Velde, M. Smit, R. Scheringa, K. Ahrikaa, D. H. Jonesa, *Catal. Sci. Technol.* **2012**, *2*, 2109.

[7]   R. H. Atkinson, C. T. Heycock, W. J. Pope, *J. Chem. Soc.,* **1920**, 117, 1410.

[8]   P. Serp, J. L.Figueiredo, *Carbon Materials for Catalysis*, John Wiley & Sons, Inc. **2009**.

[9]   W. V. Cicha, L. E. Manzer, *US6022993 A*, **1996**.

[10]   H. Eckert, B. Gruber, J. Auerweck, *US20020065432 A1*, **2002**.

[11]   C. W. Montgomery, N. W. Franke, *US2380703 A*, **1945**.

[12]   L. E. Campbell, L. R. Johnson, *US 3904553 A*, **1975**.

[13]   M. Huynh, D. K. Bediako, D. G. Nocera *J. Am. Chem. Soc.* **2014**, *136*, 6002.

[14]   G. Zu, J. Shen, W. Wang, L. Zou, Y. Lian, Z. Zhang, B. Liu, F. Zhang *Chem. Mater.*, **2014**, *26*, 5761.

[15]   M. Digne, P. Sautet, P. Raybaud, P. Euzen, H. Toulhoat, *J. Catal*., **2004**, *226*, 54.

[16]   M. Digne, P. Sautet, P. Raybaud, P. Euzen, H. Toulhoat, *J. Catal*., **2002**, *211*, 1.

[17]   American Conference of Governmental Industrial Hygienists: "Phosgene", Documentation of the Threshold Limit Values for Substances in Workroom Air (3rd ed., 2nd printing), Cincinnati, **1974**.

[18]   E. P. Barrett, L. G. Joyner, P. P. Halenda, *J. Am. Chem. Soc.* **1951**, *73*, 373.

[19]   . J. Gregg, , S. W. S. Kenneth, *Adsorption Surface Area and Porosity* ed. 2, Academic Press Inc.,U.S., London, **1982**.

[20]   B. C. Lippens, J. H. Deboer, *J. Catal.* **1965,** 4, 319.

[21]   J. A. Lercher*, Reaction Kinetics and Catalysis Letters,* **1982**, *20*, 409.

[22]   E. P. Parry, *J. Catal*., **1963**, *2*, 371.

[23]   S. D. Jackson, J. S. J. Hargreaves, *Metal Oxide Catalysis*, Wiley, **2008**.

[24]   C. Morterra, A. Zecchina, S. Coluccia, A. Chiorino, *J. Chem. Soc., Faraday Trans.* **1977**, *73*, 1544.

[25]   N. D. Parkyns, *J. Chem. Soc. A*, **1969**, *410*.

[26]   M. P. Rosynek, *J. Phys. Chem.*, **1975**, *79*, 13.

[27]   T. R. Lopes, G. R. Gonçalves, E. Barcellos, M. A. Schettino, A. G. Cunha, F. G. Emmerich, J. C. C. Freitas, *Carbon*, **2015**, *93,* 751.

[28]   A. F. Wells, *Structural Inorganic Chemistry*, Oxford, UK, **1984.**

[29]   J. F. Shackelford, R. H. Doremus, *Ceramic and Glass Materials: Structure, Properties and Processing*, Springer: New York, USA, **2008.**

[30]   Y. Kato, K. I. Shimizu, N. Matsushita, T. Yoshida, H. Yoshida, A. Satsuma, T. Hattori *Phys. Chem. Chem. Phys.,* **2001**, *3*, 1925.

[31]   A. Boumaza, L. Favaro, J. Le´dion, G. Sattonnay, J. B. Brubach, P. Berthet, A.M. Huntz, P. Roy, R. Tetot, *J. Solid State Chem.* **2009**, *182*, 1171.

[32]   M. C. Rohner, V. K. Sharma, W. Richarz, *Chem. Eng. Technol.,* **1989**, *12*, 27.

[33]   M. Digne, P. Raybaud, P. Sautet, D. Guillaume, H. Toulhoat *J. Am. Chem. Soc.* **2008**, *130*, 11030.

[34]   D. J. Âdelman, PhD Thesis, *Kinetics of coal fly ash chlorination by phosgene*, **1984**.

[35]   A. Melchor, E. Garbowski, M. V. Mathieu, M. Primet, *J. Chem. Soc., Faraday Trans.* **1986**, *82*, 1893.

[36]   M. C. Rohner, V. K. Sharma, W. Richarz, *Chem. Eng. Technol*. **1989***, 12,* 27.

[37]   E. L. Ru, P. Etchegoi, *Principles of Surface-Enhanced Raman Spectroscopy: and related plasmonic effects*, Elsevier, **2009**.

[38]   N. K. Gupta, E. E. Ember, J. A. Lercher, *Unpublished result*.

[39]   G. Czako, J. M. Bowman, *J. Chem. Phys.* **2012**, *136*, 044307/1.

[40]   T. Theophile, *Infrared Spectroscopy – Materials Science, Engineering and Technology*, InTech, **2012**.

[41]   J. Szanyi, J. H. Kwak, *Phys. Chem. Chem. Phys*. **2014**, *16*, 15117.

[42]   N. K. Gupta, E. E. Ember, J. A. Lercher, Unpublished result.

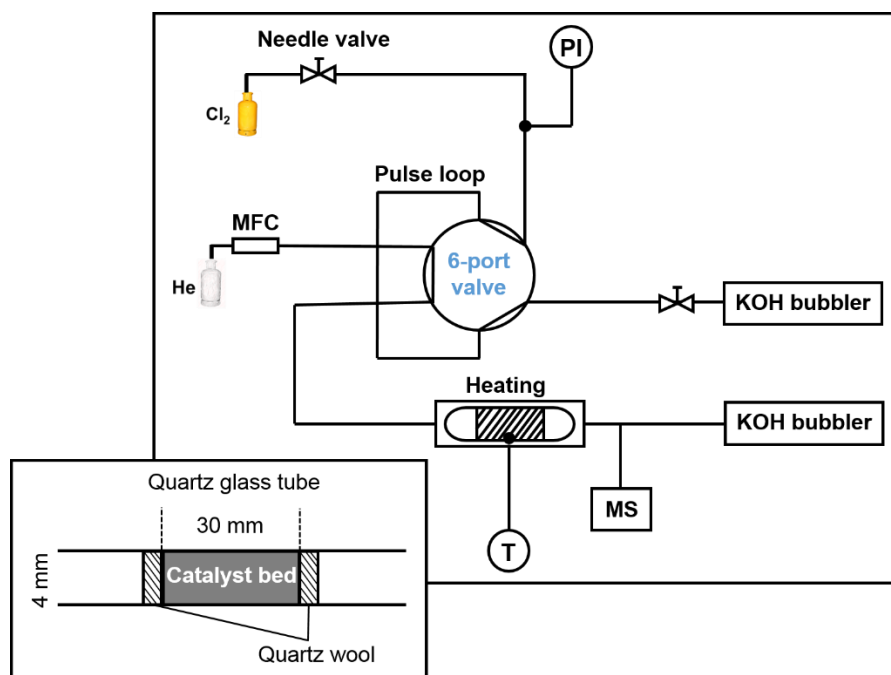[43]   Presented in Chapter 2.

5.7   Supporting information

Figure S5-1. Pulse set-up for Cl$_2$ interaction and COCl$_2$ synthesis study. (PI = pressure indicator, MFC = mass flow controller, MS = Mass spectrometer, T = temperature controller)
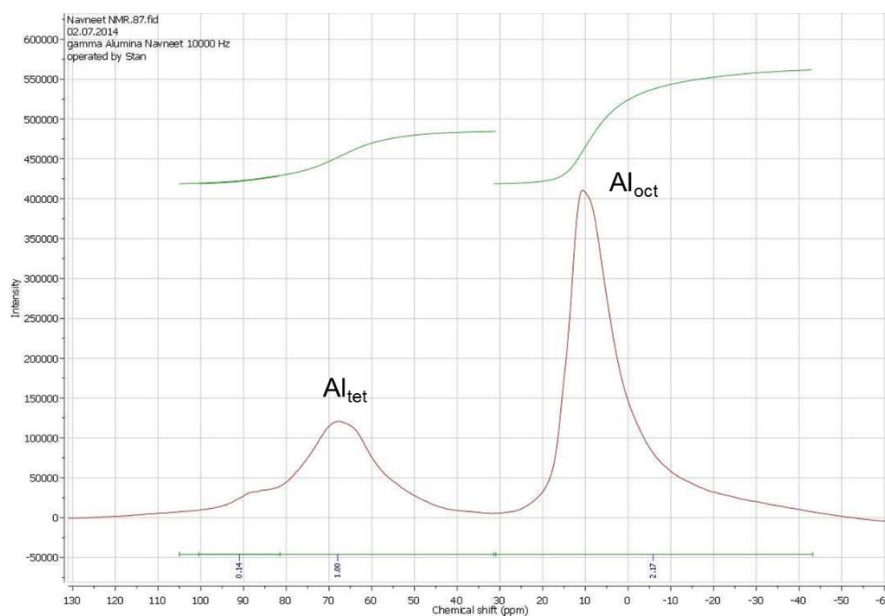

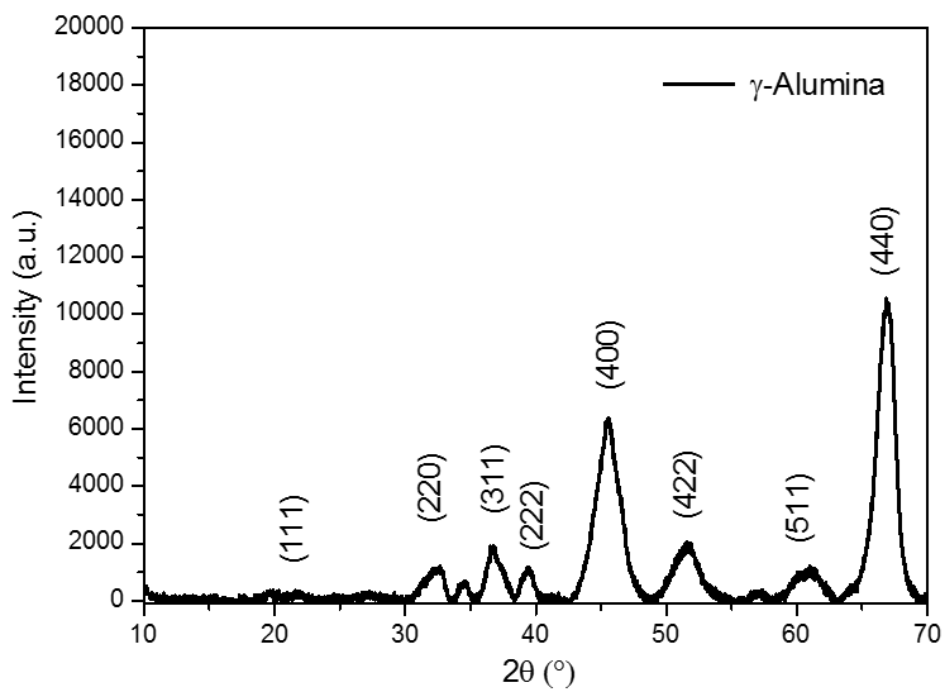
Figure S5-2. MAS ^{27}Al-NMR of fresh γ-Al$_2$O$_3$.
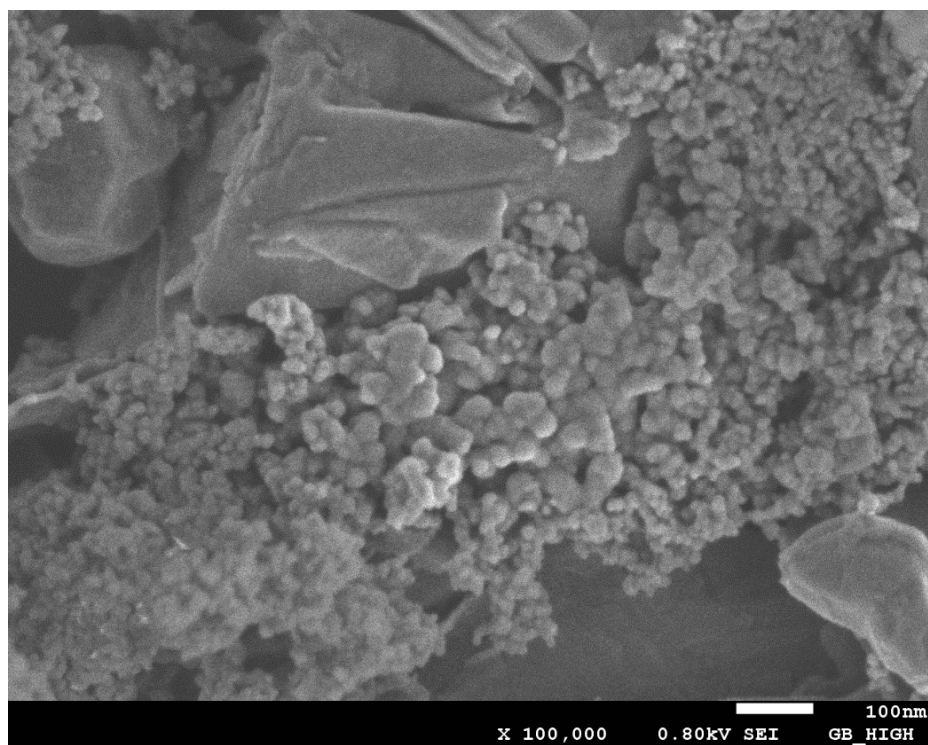
Figure S5-3. Powder X-ray diffraction

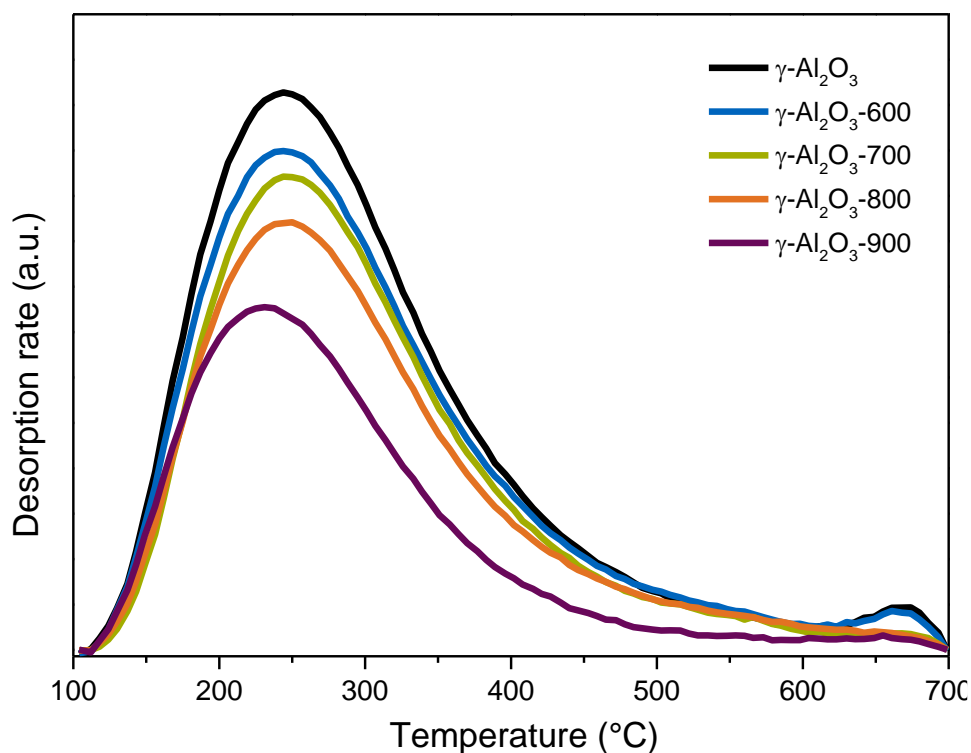**Figure S5-4**. SEM image of fresh γ-Al_2O_3.

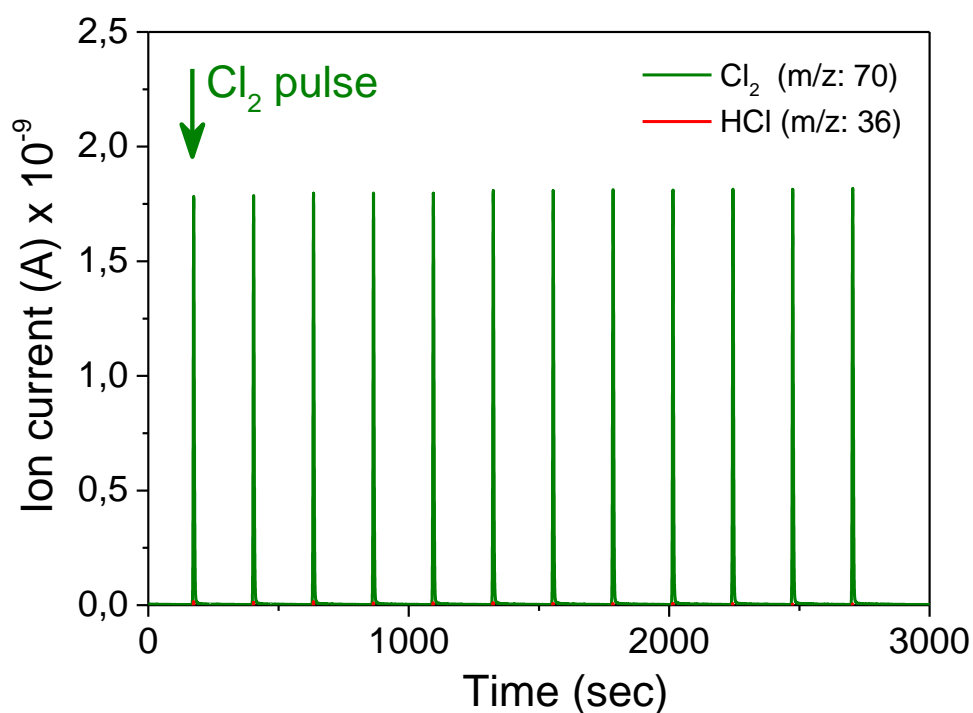**Figure S5-5**. NH_3-TPD of calcined γ-Al_2O_3 materials.

Figure S5-6. Cl_2 activation study on $AlCl_3$ material. Experimental conditions: 25 Cl_2 pulses (230 s pulse length, 1.8 µmol Cl_2 / pulse), He flow: 10 ml/min, 100 mg of $AlCl_3$.

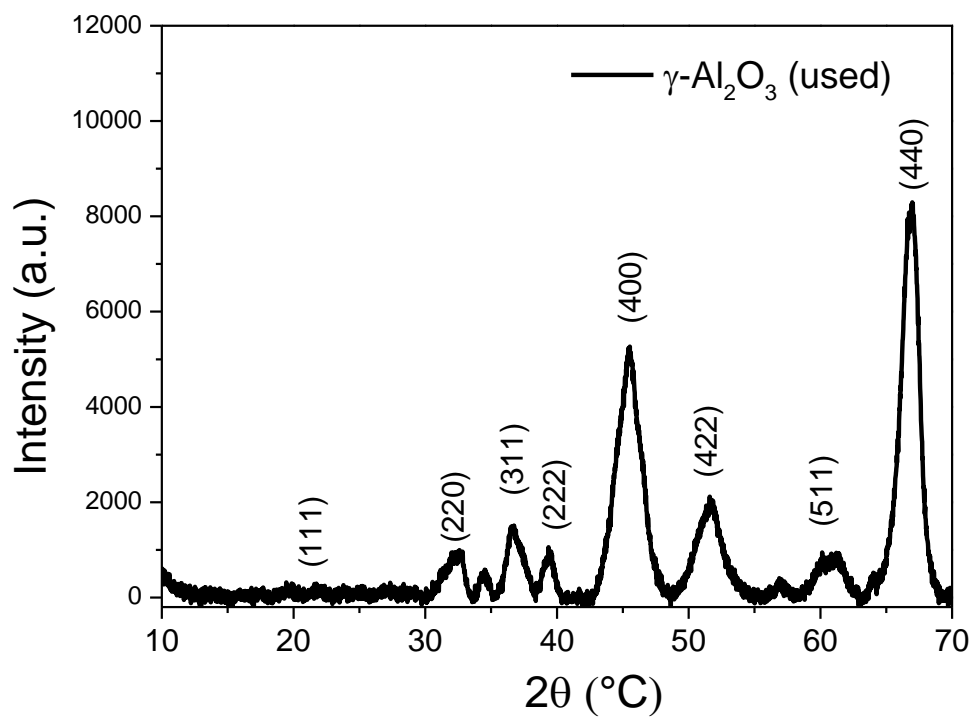**Figure S5-7**. Powder X-ray diffraction patterns of chlorinated γ-Al₂O₃.
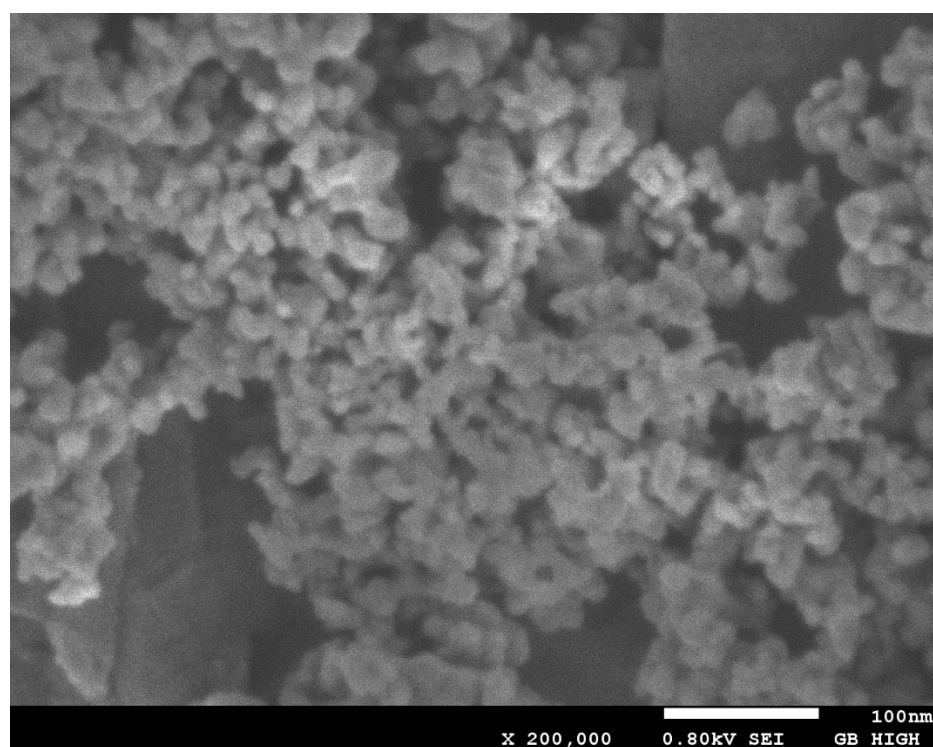
Figure S5-8. HR-SEM image of chlorinated γ-Al₂O₃.
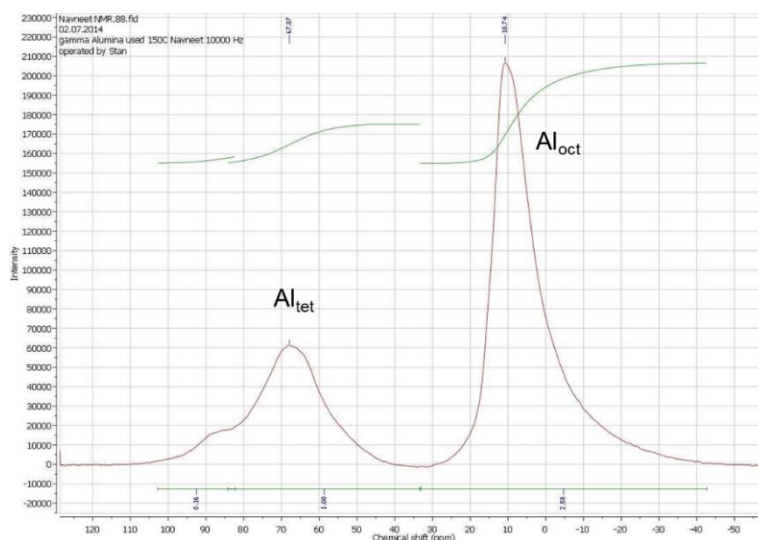
Figure S5-9. MAS ^{27}Al-NMR of chlorinated γ-Al$_2$O$_3$.

S5-1. Influence of catalyst amount on COCl₂ formation

The catalyst amount is one of the main technological parameters in phosgene production process. In this study, the effect of catalyst amount (50-150 mg) on the Cl$_2$ and CO reaction for COCl$_2$ synthesis process at 150 °C were conducted and summary is presented in Figure S5-10.

Figure S5-10. Effect of catalyst amount on phosgene formation (blue-COCl$_2$ formation, yellow- Cl$_2$ conversion).

The obtained results demonstrated, the linear increase in catalytic COCl$_2$ formation with increasing the catalyst amount from 25 mg to 100 mg.

Chapter 6

Summary

&

Zusammenfassung

6 Summary & Zusammenfassung

6.1 Summary

Polycarbonates are an important class of high performance polymers, which can be directly synthesized from DPC. In this respect, innovative and safer pathways 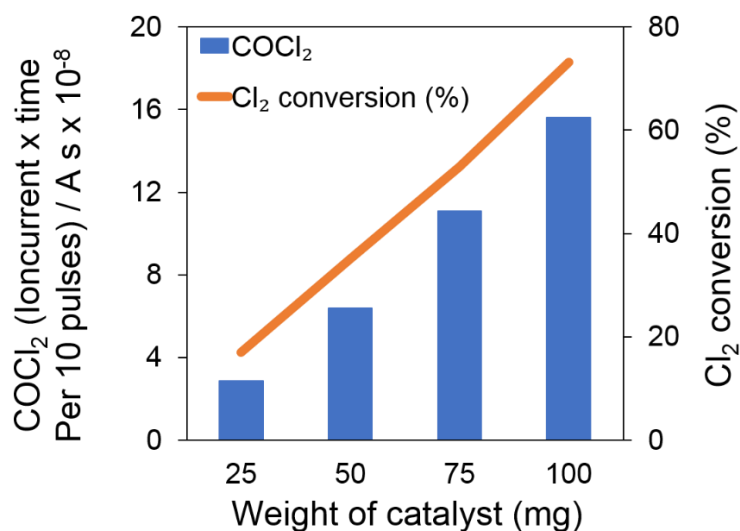for sustainable DPC production required a good understanding on the complex chemical reaction network. In turn DPC synthesis proceeds by using $COCl_2$ as a reactive building block.

In industry, large scale $COCl_2$ is synthesized over activated carbon as metal-free catalyst since it is not only cheap but also highly active. One characteristic of the surface of a typical carbon catalyst is the heterogeneous distribution of various active sites responsible for parallel running side reactions. The low material stability and product selectivity under reaction conditions render their application for the stable transient $COCl_2$ production. Therefore, to gain a fundamental knowledge on the active sites and enabled reactive intermediates, a rigorous kinetic and mechanistic study on the reaction between Cl_2 and CO was carried out. Detailed characterization of active industrial carbon materials showed the presence of various active sites such as, zig-zag and arm-chair edges, defects, paramagnetic sites, reactive N- and O- containing functional groups and curved surfaces containing sp^2/sp^3 mixed hybridized carbons. To study their contribution in catalysis, a pulse reactor with online MS analysis was designed. Comparative studies using various model carbon materials showed that irreversible as well as reversible Cl_2 interactions are enabled at mild reaction conditions. Irreversible Cl_2 interaction occurred at the most reactive sites led to the undesired chemical modification of the active surface. However, reversible weak interaction was found to be crucial for catalysis. To show the possible interactions and followed catalysis over curved surface moieties of activated carbon C_{60} fullerene was selected as well-defined model catalyst. Mechanistic studies on C_{60} enabled Cl_2 and CO reaction reveled the carbon atoms distorted from sp^2 coordination in non-planar carbon units are able to generate active Cl_2 species of radical character for CO reaction. The transiently generated radicalic Cl_2 species were experimentally tested by using CH_4 as probe molecule. Compared to the thermal enabled reactions, C_{60} material showed higher amount of $CH_{4-n}Cl_n$ products formation *via* a radical chain mechanism. Theoretical studies combined with experimental results suggest that the stable $COCl_2$ synthesis requires a carbon catalysts with considerable surface strain to form the critical reversible surface bound radical $[C_{60}\cdots Cl_2]$ species.

Further, one of the main achievements was to experimentally show that by N-modification a highly stable carbon catalyst can be designed for the transient $COCl_2$ formation. It was shown, that the incorporation of N- functionalities with electron withdrawing abilities in heterocyclic moieties, which are stabilized by resonance with the π-electron system, will preferentially contribute to the formation and stabilization of new electron deficient active carbon sites with enhanced adsorption and Cl_2 activation abilities. The selective adsorption of Cl_2 on these sites resulted in the favored intermediate formation of active ionic chlorine species able to further interact with CO and lead to the stable formation of $COCl_2$. Using N-modified materials the by-products formation was during $COCl_2$ production under detection limit.

It was similarly important to search for alternative metal-based catalysts for stable $COCl_2$ production. Comparative studies on various metals have shown that γ-Al_2O_3 is an adequate catalyst for Cl_2 and CO reaction for stable $COCl_2$ production. Using different crystallization phases and morphologies of Al_2O_3, $COCl_2$ formation is altered. It was possible to show that, the Lewis acid sites of alumina have the ability to activate gaseous Cl_2 and to generate reactive $Cl^{\delta+}$ species for CO reaction.

In summary, deeper characterization and identification of active sites of conventional carbon catalyst enabled the development of highly active and stable metal-free and metal-based catalysts for selective $COCl_2$ synthesis.

6.2 Zusammenfassung

Polycarbonate, die direkt aus DPC synthetisiert werden können, stellen eine wichtige Klasse von Hochleistungspolymeren dar. Für innovative und sichere Wege zur nahhaltigen DPC Produktion sind daher ein tiefgreifendes Verständnis des komplexen chemischen Reaktionsnetzwerkes nötig. Die DPC Synthese wiederrum verläuft unter der Verwendung von $COCl_2$ als reaktiver Synthesebaustein.

Großindustriell, wird $COCl_2$ mittels Aktivkohle als metallfreier Katalysator hergestellt, da diese nicht nur günstig sondern auch hochaktiv ist. Ein wichtiges Charakteristikum der Oberfläche eines typischen Kohlenstoff Katalysators ist die heterogene Verteilung von verschiedenen aktiven Zentren, die auch für gleichzeitig ablaufende Nebenreaktionen verantwortlich sind. Sowohl die geringe Materialstabilität, als auch die geringe Produktselektivität erschweren Ihre Anwendung für eine stabile, transiente $COCl_2$ Produktion. Um grundlegende Kenntnisse über die aktive Zentren und beteiligte reaktive Zwischenprodukte zu erhalten, wurde daher eine detaillierte kinetische und mechanistische Untersuchung der Reaktion zwischen Cl_2 und CO durchgeführt. Eine akurate Charakterisierung von aktiven und in der Industrie verwendeten Materialien zeigte, dass verschiedene aktive Zentren wie zick-zack und „arm-chair" Kanten, Fehlstellen, paramagnetische Zentren, reaktive N- und O- haltige funktionelle Gruppen und gebogene Oberflächen mit einer Mischung aus sp^2/sp^3 hybridisierten Kohlenstoffatomen vorhanden sind. Um ihre Beteiligung in der katalytischen Reaktion zu untersuchen wurde ein Pulsreaktor mit online MS entworfen. Ein direkter Vergleich von verschiedenen Kohlenstoffmodellmaterialien zeigte, dass unter milden Reaktionsbedingungen sowohl irreversible als auch reversible Cl_2 Wechselwirkungen stattfinden. Die irreversible Wechselwirkung von Cl_2 fand zuerst an den reaktivsten Zentren statt und führte zu einer ungewünschten chemischen Modifikation der aktiven Oberfläche. Die reversiblen schwachen Wechselwirkungen jedoch stellten sich als ausschlaggebend für die Katalyse heraus. Um die möglichen Wechselwirkungen und katalytische Wirkung von gebogenen und aktiven Kohlenstoffoberflächen aufzuzeigen wurde das C_{60} Fulleren als wohldefinierter Modelkatalysator ausgewählt. Mechanistische Untersuchungen der Reaktion von C_{60} mit Cl_2 und CO demonstrierten, dass sp^2 verzerrte Kohlenstoffatome der nicht-planaren Kohlenstoffeinheiten, zur Bildung radikalische aktive Cl_2 Spezies führen können. Durch die Verwendung von CH_4 als Probenmolekül konnten die generierten kurzlebigen radikalischen Cl_2 Spezies experimentell erprobt werden. Verglichen mit den thermisch initiierten Reaktionen, weist C_{60} Fulleren eine höhere $CH_{4-n}Cl_n$ Bildung, die über einen radikalischen

Kettenmechanismus läuft, auf. Die Kombination von theoretischen Untersuchungen mit experimentellen Ergebnissen deutet darauf hin, dass die stabile $COCl_2$ Synthese einen Kohlenstoffkatalysator mit einer erheblichen Oberflächenkrümmung benötigt um für die katalyse entscheidenden radikalischen $[C_{60}\cdots Cl_2]$ Spezies, die reversibel an der Oberfläche gebunden sind, zu bilden. Eines der Haupterrungenschaften war es experimentell zu demonstrieren, dass durch das Einbringen von N Atomen ein hochstabiler Kohlenstoffkatalysator für die $COCl_2$ Synthese dargestellt werden kann. Dabei zeigte sich, dass über das π-System resonanzstabilisierte und elektronenziehende N Funktionalitäten in heterozyklischen Teilen bevorzugt zur Bildung und Stabilisation neuer Kohlenstoffzentren mit Elektronenmangel beitragen. Diese Zentren beschleunigen (dann) die Adsorption und Cl_2 Aktivierung. Die selektive Adsorption von Cl_2 an diesen Zentren führt zu einer favorisierten Zwischenproduktbildung der aktiven ionischen Clorspezies, welche im Weiteren mit CO interagiert und zur Bildung von $COCl_2$ führt. Bei der Verwendung von N modifizierten Materialien konnten keinerlei Nebenprodukte bei der $COCl_2$ Produktion nachgewiesen werden. Desweitern war es wichtig Alternativen für die stabile $COCl_2$ Herstellung mittels Metallkatalysatoren zu finden. Bei einer Vergleichsstudie verschiedener Metalle stellte sich γ-Al_2O_3 als ein adäquater Katalysator für die Reaktion von Cl_2 und CO zu $COCl_2$ dar. Dabei ändert sich die $COCl_2$ Bildung abhängig von der verschiedenen Kristallisation und Morphologie von Al_2O_3. Es konnte gezeigt werden, dass die Lewis Säurezentren des Aluminiumoxid fähig sind Chlorgas zu aktivieren und reaktive $Cl^{\delta+}$ Spezies zu bilden.

Zusammenfassend wurde durch die genaue Charakterisierung und Identifikation der aktiven Zentren von konventionellen Kohlenstoffkatalysatoren hoch aktive und stabile metallfreie und metallhaltige Katalysatoren für die $COCl_2$ Synthese entwickelt.

7   Curriculum Vitae

Navneet Kumar Gupta was born in small town of Uttar Pradesh in India. After completing his higher secondary schooling in his hometown, in 2005, he moved to New Delhi, India for university education. He received his Bachelor of Science degree in Chemistry (Hons) form ARSD College, University of Delhi, India. To strengthen the organic chemistry knowledge he joined Department of Chemistry, University of Delhi for M. Tech. degree in "Chemical Synthesis and Process Technologies" in August 2008. To deepen his education in field of materials and engineering he joined the group of Prof. Kohki Ebitani at School of Material Science, Japan Advanced Institute of Science and Technology, Japan for his master thesis. He graduated there in Materials Science with the highest distinctions. In continuation of his study, in 2011, he joined the research group of Prof. Johannes A. Lercher at Chair of Technical Chemistry, Technical University of Munich, Germany for PhD degree on topic entitled "Innovative Pathways for Sustainable Diphenyl Carbonate Production".

8 List of Publications

1. **N. K. Gupta**, S. Nishimura, A. Takagaki and K. Ebitani *Green Chem.*, **2011**, 13, 824. Hydrotalcite-supported gold-nanoparticle-catalyzed highly efficient base-free aqueous oxidation of 5-hydroxymethyl furfural into 2, 5-furandicarboxylic acid under atmospheric oxygen pressure.

2. G. Centi, K. Barbera, S. Perathoner, **N. K. Gupta**, E. E. Ember and J. A. Lercher *ChemCatChem*, **2015**, *7*, 3036 – 3046. (*a special issue on carbon in catalysis*) Onion-like graphene carbon nanospheres as stable catalysts for CO and CH_4 chlorination.

3. **N. K. Gupta**, A. V. Pashigreva, E. Pidko, E. Hensen, L. Mleczko, S. Roggan, E. E. Ember and J. A. Lercher *Accepted for publication in Angew. Chem. Int. Ed.* Bent carbon surface moieties as active sites on carbon catalysts for phosgene synthesis.

4. **N. K. Gupta**, E. E. Ember, G. L. Haller and J. A. Lercher *Submitted for publication in ACS Catal.* N-modified carbon nanomaterials as stable non-metal catalysts for phosgene synthesis.

5. **N. K. Gupta**, B. Peng, E. E. Ember and J. A. Lercher *Manuscript in preparation* γ-Al_2O_3 catalyzed Cl_2 activation and phosgene synthesis.

6.   B. Peng, **N. K. Gupta**, G. L. Haller, E. E. Ember, J. A. Lercher *Manuscript in preparation* Rate enhancement of dimethyl carbonate formation from methanol and CO_2 over ZrO_2-based catalysts by heteroatom doping and its mechanistic insights.

7. B. Peng, **N. K. Gupta**, E. E. Ember, J. A. Lercher *Manuscript in preparation* Towards mechanistic understanding on transesterification between phenol and dimethyl carbonate over MoO_3 catalysts.

8. C. B. Himmelsbach, **N. K. Gupta**, E. E. Ember, J. A. Lercher *Manuscript in preparation* Mechanistic insight into metal free O_2 activation and C-H bond functionalization.